UNIVERSIDAD COMPLUTENSE DE MADRID

FACULTAD DE CIENCIAS FÍSICAS
Departamento de Astrofísica

TESIS DOCTORAL

Espectroscopía en el infrarrojo lejano para la región OMC-2: optimización del procesado de datos y análisis físico

Far infrared spectroscopy of the OMC-2 region: optimization of the data processing and physicazl analysis

MEMORIA PARA OPTAR AL GRADO DE DOCTOR

PRESENTADA POR

Beatriz María González García

Director
Roland Vavrek

Madrid, 2016

DEPARTAMENTO DE ASTROFÍSICA

Universidad Complutense de Madrid

ESPECTROSCOPÍA EN EL INFRARROJO LEJANO PARA LA REGIÓN OMC-2

OPTIMIZACIÓN DEL PROCESADO DE DATOS
Y ANÁLISIS FÍSICO.

FAR INFRARED SPECTROSCOPY OF THE OMC-2 REGION

OPTIMIZATION OF THE DATA PROCESSING
AND PHYSICAL ANALYSIS.

Memoria que presenta

Beatriz María González García

para la obtención del título de
Doctora en Ciencias Físicas

Tesis dirigida por

Dr. Roland Vavrek

EUROPEAN SPACE ASTRONOMY CENTER
4 de Noviembre de 2015

A mi Familia,
por Tierra, Mar y Aire,
en especial a mis padres,
Beatriz y Jose Ramón

Agradecimientos

Puede que me falle la memoria, pero el agradecimiento es inmenso a todas las personas con las que he compartido este tiempo de mi tesis. Gracias a vosotros por darme vuestro agua del conocimiento y abrigo en el camino.

I want to start, of course, by my thesis supervisor, Dr. Roland Vavrek, who accepted to get on board with me in this adventure and guide me in the way. We spent days and months working long hours looking for the most appropriate method to obtain the best data processing method for the HOPS data, and finally, we found it. His vision of simulations made this work more complex at the time that more interesting and complete. Thanks a lot to him for giving me the opportunity to be part of the HOPS team.

From the HOPS team, lead by Dr. Tom S. Megeath, I discovered how the oceans and kilometres of distance do not prevent an unlimited collaboration as much as time permitted. In addition to Dr. Megeath, special mention in the team to Dr. Manoj. P, Dr. Dan Watson, Dra. Amy Stutz and Dra. Mayra Osorio. Without their suggestions the scientific analysis of this work would not be so complete. Thanks a lot to all of them for answering my doubts any day at any time. My full admiration and gratitude to them. Thanks as well to Ana Karla Díaz-Rodrıguez, PhD student of Dra. Osorio, for her help at the PACS /VLA data comparison.

Importantes atalayas en mi camino han sido la Dra. Katrina Exter y el Dr. Miguel Sánchez-Portal. También han sido reveladoras la multitud de charlas con la Dra. Carmen Sánchez-Contreras, el Dr. Pablo Rivière-Marichalar y el Dr. Guillen Anglada. Su incondicional apoyo profesional y personal han consolidado mi amistad, respeto y agradecimiento hacia ellos para siempre.

Also admiration and gratitude to the PACS team (at the Intrument Control Centers and Herschel Science Center) for all their explanations to the doubts that the PACS data and its algorithm brought with them. Special mention for their support to Dra. Katrina Exter, Dr. Jeroen de Jong, Dra. Sara Regibo, Dr. Pierre Royer and Dr. Juergen Schreiber.

Por supuesto admiración y agradecimiento a mis valoradores externos: Dra. Belén Tercero y Dr. Benjamín Montesinos. Su inmensa profesionalidad combinada con su abrumadora humanidad les hace únicos.

Agradecimiento también hacia ISDEFE y al Dr. Leo Metcalfe, por haber apoyado mi cruzada con lo que ello llevaba.

Por supuesto, no quiero dejar de mencionar a personas clave gracias a las que la luz volvió cuando la noche se hizo oscura: Dr. Miguel Sánchez-Portal, Dr. Pedro García-Lario, D.Javier Delgado, Dra. María Santos-Lleo y D. Ramón Muñoz.

El centro LAEFF en tiempos, ahora CAB, siempre ha sido para mí un paraíso de acogida y conocimiento compartido, y por ello, os estoy inmensamente agradecida. Me acogieron como una más cuando empecé en el año 2000 a trabajar con el Dr. Enrique Solano y, después, en el 2005 con la Dra. María Rosa Zapatero-Osorio, con los que aprendí tanto. Gracias a Dr. Irene Pintos por toda su ayuda con el template de latex y derivados.

También una inmensa gratitud hacia los operadores y analistas del equipo (CSG) en ESAC y hacia mis compañeros desarrolladores de Herschel (Jeroen de Jon, Javier Diaz y Jaime Saiz) y Dr. Albert Domingo Garau, ambos me han ofrecido su ayuda cuando las máquinas o el código se imponían en mi cruzada.

No puedo dejar de acordarme del lugar donde empecé. Me refiero a ese templo de sabiduría que es la Facultad de Ciencias Físicas de la Universidad Complutense donde disfruté, y también sufrí, y, sobre todo, evidentemente, al Claustro de profesores que forjaron mi mente y me enseñaron a amar la Astrofísica. En especial agradecer a la Dra. Elisa de Castro y al Dr. Jesús Gallego y a D. Pedro y D. Eugenia de las de Secretaría de Físicas, por toda su ayuda con los trámites del doctorado.

Especiales han sido también para mí los buenos ratitos con mis amigas de ESAC: Pilar, Mónica, Nana, Rocío G. y Rocío F., Merche y Alba. Muchísimas gracias por todos ellos.

En este turno de agradecimientos no puedo olvidar a mi familia, la cual me ha apoyado incondicionalmente en éste, mi sueño.

Empezando por mis padres (Beatriz y Jose Ramón), ejemplo diario de capacidad de sacrificio por aquéllo que merece la pena y generosidad sin límite hacia aquéllos que quieren: su familia. A mis hermanos: José Dionisio (mi super hermano mayor) y Juan Miguel (mi super hermanito pequeño), profesionales punteros en sus campos y con excelente formación, son, sin duda, mis modelos a seguir. Sus buenos consejos, junto los de mis padres, y su compañía me permiten enfrentarme a los temporales con la mejor de mis sonrisas y la seguridad de salir adelante. Ellos, junto a sus mujeres (Gloria y Mónica), han dado luz a las estrellas más brillantes de mi firmamento: Jaime (mi increíble ahijado), Candela, Juan y Claudia, que sólo con estar me arrancan sonrisas.

Las adversidades, que han podido suceder, se han hecho mucho más pequeñas gracias a todos estos angelitos que, a momentos, me han sostenido.

No quiero olvidar a mis grandes amigas: Thais, Carmen y Carlota.

Gracias a todos.

Figura 1: Snapshot from a youtube video edited by Marcelo Lacava, www.inknowation.com

Resumen en español

Esta tesis presenta el trabajo realizado con el fin de conocer mejor la región OMC-2, que se encuentra en el complejo de formación estelar Orion A de la Galaxia, a través de los datos tomados con el satélite Herschel.

Los datos de este trabajo pertenecen al programa HOPS (*Herschel Orion Protostar Survey*), un programa clave de tiempo abierto tomado con el satélite Herschel, liderado por el Dr. T. S. Megeath. El objetivo de este programa es responder a las cuestiones clave que conciernen a la formación estelar de estrellas de baja masa y de masa intermedia. Para este estudio, la región de Orión es un lugar óptimo por su proximidad ~420 pc, (Menten et al. 2007) y la variedad de entornos en las que nacen estrellas en ella.

El programa de observación de HOPS tomó imagenes y espectros con los instrumentos PACS y SPIRE, para objetos clasificados como protoestrellas por el satélite *Spitzer*. De ellas, 298 fueron observadas con la cámara PACS en las bandas 70 y 160 μm, mientras que para 36 protoestrellas se tomaron espectros en el rango espectral 50-210 μm , también con el instrumento PACS. Para dos de estos targets se tomaron mapas espectroscópicos de SPIRE de alta cobertura.

La combinación de fotometría de campo profundo, espectroscopía de amplio rango espectral y mapas espectrales hacen de este programa un legado único para el estudio de la formación estelar. La estrategia observacional para las observaciones espectroscópicas de PACS han sido un compromiso entre la eficiencia observacional y el retorno científico. Un subconjunto de 4 objetos de la muestra espectroscópica de HOPS/PACS fue observada en modo mapa en el rango 55-210 μm , entre las que se incluye la región OMC-2 tratada en esta tesis.

El primer reto en esta tesis fue la optimización del procesado de datos estándar para los datos espectroscópicos de la muestra HOPS tomados con el instrumento PACS. Estos datos corresponden a dos áreas más pequeñas de la región OMC-2, cada una observada con un modo diferente. El objeto OMC-2 FIR 3 ha sido observado como un mapa de alta cobertura, obteniendo para él mapas espectrales con un muestreo Nyquist. El objeto FIR 4 fue observado en una posición fija. Una cantidad significativa de este trabajo ha consistido en encontrar el método óptimo para combinar y procesar ambas regiones y ambos tipos de observación en un modo único y homogéneo para facilitar el análisis de la región en conjunto, para ser capaz de caracterizar la morfología y la interacción entre componentes.

Hemos aplicado las simulaciones de datos híbridos, combinando la información del apun-

tado del satélite con datos simulados de distribución de flujo, que permite optimizar los parámetros para la selección y parametrización de las técnicas de reconstrucción.

Nuestra optimización de las técnicas de reconstrucción, en concreto de *drizzle*, para mapas espectrales de alta cobertura, han sido adoptados en ambos entornos: el procesado estándar (*SPG*) y el entorno HIPE (*Herschel Interactive Processing Environment*). El método de procesado de los datos de HOPS puede ser fácilmente adoptado para otros datos observados por Herschel, que podrá ser usado por la comunidad científica para generar los productos de Legado del Archivo de Herschel.

En el siguiente paso del procesado, hemos ajustado los cubos espectrales (RA, Dec, longitud de onda) para obtener mapas de línea de flujos para líneas de estructura hiper-fina ([O I], [C II]), líneas moleculares de CO, H_2O y OH. Obtenemos $\sim$ 60 mapas de líneas de flujo y sus correspondientes mapas de signal-a-ruido. Ésta es la mayor base de datos de líneas de emisión en el infrarrojo lejano 55-210 μm observadas para una región de formación estelar de masa intermedia. Hemos optimizado el método de extracción de flujo con el fin de obtener flujos integrados bajo la línea de segmentos morfológicos específicos en la región de OMC-2.

El segundo reto de este trabajo ha sido el modelado de la región OMC-2, permitiéndonos describir los objetos FIR 3 y FIR 4 y sus interacciones. Ambas fuentes dominan la emisión tanto el contínuo (que traza el polvo) como la de línea (que traza el gas) en la región de OMC-2.

Hemos llevado a cabo un análisis de las líneas hiperfinas ([O I], [O III] and [C II]). El mapa de la línea de emisión de [O I] revela la presencia del primer jet detectado para una protoestrella de masa intermedia. La densidad electrónica derivada del mapa de cociente de líneas [O I] 63 /145 μm decrece de 7.4 a 4.8 , lo cual parece indicar que el jet bipolar es originado por FIR 3, con uno de sus lóbulos apuntando en la dirección de FIR 4. Estos resultados confirman las conclusiones de estudios previos por Reipurth et al. (1999) y Shimajiri et al. (2008). Podemos ver signos de interacción del jet con el material que rodea a FIR 4 en todas los trazadores de CO y H_2O que no parecen ser interpretados por evolución del objeto FIR 4 por sí mismo.

Comparando nuestros resultados con previos [O I] jets detectados para protoestrellas de baja masa (Nisini et al. 2015), la pérdida de masa de FIR 3 que hemos medido se sitúa entorno a $\sim$ a 10 veces mayor que la típica pérdida de masa de sus compañeras menos masivas (1-4 $\times 10^{-7}$ $M_\odot$ yr^{-1}). La pérdida de masa de FIR 3 (5.4 $\times 10^{-6}$ $M_\odot$ yr^{-1}) medida excede hasta el mayor valor de pérdida de masa detectado para un objeto de baja masa (HH 46), la cual es de (2-4 $\times 10^{-6}$ $M_\odot$ yr^{-1}(Nisini et al. 2015)). Esta idea es consistente con la idea de que las protoestrellas de masa intermedia generan jets más potentes que los de sus compañeras *Class 0* de baja masa.

Por comparación de los cocientes de línea de CO, obtenidos en esta tesis, con una red de modelos (Neufeld 2012) generados para el rango de densidades 10^2-10^{12} cm^{-3} y temperaturas 100 - 5000 K, obtenemos, para una única componente en NLTE, altas temperaturas (T $\geq$ 2500$-$5000 K) y bajas densidades ($n(H_2) \leq 2.5\times10^4$ cm^{-3}) a lo largo del jet (González-García et al, 2015, submitted). Estos valores de temperatura y densidad

han sido reportados en la literatura para otras regiones de formación estelar (Kaufman & Neufeld 1996; Neufeld et al. 2014). Sin embargo, una solución diferente puede también explicar nuestros resultados, basado en los diagramas rotacionales de CO, por medio de una solución que requiere 3-4 diferentes componentes de temperatura en LTE con el gas que les rodea. Esta solución también ha sido reportada en la literatura para otras regiones de formación estelar (Herczeg et al. 2012; Goicoechea et al. 2012; Karska et al. 2013, 2014).

Nuestros resultados sugieren que el gas molecular se calienta a medida que se mueve de FIR 3 a FIR 4. Esto puede indicar que choques no disociativos, responsables del calentamiento del gas molecular, son más intensos hacia la zona sur-este del jet, cerca de la posición de FIR 4, el cual parece coincidir con la posición terminal de un choque producido por el jet de FIR 3. Estas altas velocidades de choque ($v_s \geq 25$ km/s) podrían ser capaces de arrancar el oxígeno en los mantos helados de los granos de polvo de la envoltura de las protoestrellas, y convertirlo, rápidamente, en vapor de agua a través de la reacción endotérmica neutral-neutral.

Una de las posibilidades que podría suceder es que, si todo el oxígeno que no es atrapado para formar CO fuera convertido en H_2O, podríamos esperar una abundancia de agua de 1.2 veces la del CO, $n(H_2O)/n(CO) = 1.2$, (van Dishoeck et al. 2013; Neufeld et al. 2014). Sin embargo, las abundancias que medimos de H_2O respecto a CO son más bajas, ~ 0.4. Estos valores de abundancias también son reportadas en trabajos previos (van Dishoeck et al. 2013; Karska et al. 2014).

Finalmente, hemos combinado nuestros resultados con datos del equipo HOPS, tomados con *Spitzer*, APEX y VLA, con el objetivo de caracterizar lo mejor posible la región OMC-2 y poder construir nuestro propio modelo para describirla. La alta resolución de las imágenes centimétricas del VLA así como de APEX para la línea CO (6-5) también parecen confirmar que el origen del jet es FIR 3, con una estructura en la dirección de FIR 4. Las imágenes de *Spitzer*/IRAC a 4.5 μm muestran la extensión NE del jet bipolar, la cual queda fuera del campo de visión de los datos espectroscópicos tomados con PACS.

Abstract

This PhD thesis presents the work performed to better understand the OMC-2 region, in the Orion A complex star-forming region in the Galaxy, by using the Herschel satellite data. We have contributed to the optimisation and calibration of the data processing required for the scientific analysis of the data.

The data of this work belongs to the HOPS programme (*Herschel Orion Protostar Survey*), a Herschel Open Time Key Programe lead by Dr. T. S. Megeath. The objective of the program is to answer to key questions concerning low and intermediate-mass star formation. The Orion region is an optimal place for this study due to its proximity ~420 pc, (Menten et al. 2007) and its variety of environments where stars form.

The HOPS observing programme performed imaging and spectroscopy with the PACS and SPIRE instruments for *Spitzer* identified protostars. 298 protostars were imaged with the PACS camera at 70 and at 160μm bands and 36 protostars in full range spectroscopy from 50-210 μm with the PACS instrument. For two of these targets, SPIRE spectrometer mapping observations with full sampling were performed.

The combination of deep photometry, full range spectroscopy and spectral imaging makes the programme an unique legacy for star formation studies. The optimised observing strategy for the HOPS PACS spectroscopic sample was a trade off between observing efficiency and science return. A subset of 4 objects of the PACS spectroscopy sample has been observed in mapping mode for the range 55-210 μm , included the OMC-2 region.

The first challenge in this PhD was the optimisation of the standard spectroscopy data processing pipeline for the HOPS data collected by the PACS instrument. These data correspond to two smaller areas in the OMC-2 region, collected with different observing modes. The OMC-2 FIR 3 have been observed as an oversample raster, providing Nyquist sample spectral maps of the target, and FIR 4 was observed as a single pointing mode. A significant amount of this work consists of finding the optimal method for combining and processing both regions and both type of observations in a single and homogenous way to facilitate the analysis of the region as a whole, to be able to characterise the morphology and interactions among components.

We applied simulations of hybrid data combining pointing information from the spacecraft with simulated flux distribution which allows to optimise parameters for the selection and parametrisation of the reconstruction techniques.

Our optimised used of the *drizzle* reconstruction technique for oversampled spectral maps

has been adopted in both: the Herschel standard processing generation (*SPG*) and the HIPE environment (*Herschel Interactive Processing Environment*). The complete HOPS processing pipeline can be easily adopted for other data observed by Herschel, which can be used by the community to generate products for the Herschel Legacy Archive.

In the next step of the processing we fit the spectral cubes (RA,Dec,wavelength) to obtain line flux maps for fine structure lines ([O I], [C II]), molecular lines of CO, H_2O and OH. We obtained $\sim$ 60 line flux maps and their corresponding signal-to-noise maps. This is so far the largest database of far-infrared emission lines observed in the 55-210 μm range for an intermediate mass star forming region. We optimised the flux extraction method to obtain integrated line fluxes of specific morphological segments of the OMC-2 region.

The second challenge of this work was modelling the OMC-2 region, allowing us to describe the FIR 3 and FIR 4 objects and their interactions. These sources dominate both the continuum (dust) and line (gas) emission of the OMC-2 region.

We have carried out an analysis of the fine-structure lines ([O I], [O III] and [C II]). The [O I] line emission maps revealed the presence of the first ever detected protostar jet from an intermediate mass protostar. Electron densities decreasing from 7.4 to 4.8 derived from the [O I] 63 /145 μm line ratio map indicate that the bipolar jet is driven by FIR 3, with one of the lobes pointing in the direction of FIR 4. These results confirm conclusions in earlier studies by Reipurth et al. (1999) and Shimajiri et al. (2008). We see signes of interaction of the jet with the material that surrounds FIR 4 in all main CO and H_2O tracers which seems not to be interpreted as an evolutionary signature of the object by itself.

Comparing to [O I] jets previously characterised (Nisini et al. 2015) for low-mass protostars, the FIR 3 mass-loss rate we measured is about $\sim$10 times higher than typical mass-loss rates observed for their low-mass counterparts (1-4 $\times 10^{-7}$ $M_\odot$ yr^{-1}). The FIR 3 (5.4 $\times 10^{-6}$ $M_\odot$ yr^{-1}) mass-loss rate we here measured exceeds even the highest value previously detected for the HH 46 object (2-4 $\times 10^{-6}$ $M_\odot$ yr^{-1}(Nisini et al. 2015)). This is consistent with the idea that they drive more powerful jets than their low-mass Class 0 counterparts.

By comparison of the CO line ratios, obtained in this PhD thesis, to a grid of models (Neufeld 2012) generated for the range of densities 10^2-10^{12} cm^{-3} and temperatures 100 - 5000 K, we measured for a single component in NLTE, high temperatures (T$\geq$2500-5000 K) and low densities ($n(H_2) \leq 2.5\times10^4$ cm^{-3}) through the jet (González-García et al, 2015, submitted). These values of temperature and densities have been reported in the literature for other star-forming regions (Kaufman & Neufeld 1996; Neufeld et al. 2014). However a different solution could explain our results as well, based on the CO rotation diagrams, which require 3-4 different temperature components that are in LTE with the surrounding gas. Also this solution has been reported in literature for other star forming regions (Herczeg et al. 2012; Goicoechea et al. 2012; Karska et al. 2013, 2014).

Our results suggest that the molecular gas gets hotter as we move from FIR 3 to FIR 4. This could indicate that non-dissociative shocks, responsible for the heating of the molecular gas, are stronger towards the south-west part of the jet, at the location of FIR 4, which

coincides with the position of the terminal shock produced by the jet from FIR 3. These high speed shocks ($v_s \geq 25$ km/s) could be able to sputter the oxygen at the icy mantles in the dust grains from the protostar envelopes, and turn them rapidly into water vapour through an endothermic neutral-neutral reaction.

One of the possibilities that could happen is that, if all the oxygen that were not used for the CO were converted into H_2O, we would expect a water abundance of 1.2 times the one from the CO, $n(H_2O)/n(CO) = 1.2$, (van Dishoeck et al. 2013; Neufeld et al. 2014). However we measure lower abundance value of H_2O respect to CO, of ~ 0.4. Such low values also have been measured in previous studies (van Dishoeck et al. 2013; Karska et al. 2014).

Finally, we have combined our results with data from the HOPS team collected with Spitzer, APEX and VLA, with the purpose of better characterising the OMC-2 region and to build our own model. The high spatial resolution VLA centimetre continuum images as well as the APEX CO (6-5) data confirm the origin of the FIR 3 jet, which exhibit a structure towards FIR 4. Spitzer/IRAC 4.5 μm imaging shows the NE extent of the bipolar jet which is not sampled by the PACS spectroscopy data.

Contents

Agradecimientos **iii**

Resumen en español **vii**

Abstract **xi**

Acronyms **xix**

List of figures **xix**

List of tables **xxxiii**

1 Star formation in a nutshell **3**
1.1 Classification of protostars 6
1.2 Outflows and Jets 12
1.3 Tracers of star formation regions 16
1.4 The Orion star-forming region 21
1.4.1 The OMC-2 region 24
1.5 Motivation and Objectives of this PhD thesis 27

2 The Herschel Space Observatory **31**
2.1 Herschel mission overview 31
2.2 The PACS instrument 35
2.3 Observing with PACS photometer 37
2.4 Observing with the PACS spectrometer 39
2.4.1 Beam-modulation techniques 39
2.4.2 Spatial sampling 43
2.5 The SPIRE instrument 44
2.5.1 Observing with SPIRE spectrometer 46
2.5.2 Pointing mode 48
2.5.3 Spatial sampling 49
2.5.4 Flux calibration accuracy 50
2.6 The HIFI instrument 50

3 The Herschel Orion Protostar Survey (HOPS) **53**
3.1 Scientific motivation 53

3.2 Results from the Herschel Orion Protostar Survey . . . 55
3.2.1 PACS Bright Red sources . . . 56
3.2.2 The modelling of CO emission from protostellar cores . . . 58
3.2.3 Modelling SEDs of the protostars in the OMC-2 region . . . 60
3.3 Data processing and analysis of the HOPS spectroscopic sample . . . 61

4 Calibration and data processing pipelines 65
4.1 The Herschel Interactive Processing Environment . . . 65
4.2 The PACS photometer pipeline for the OMC-2 region . . . 66
4.2.1 Standard Herschel PACS data reduction for scan map observations 67
4.2.2 Evolution of data processing pipelines from HIPE 8.0 data to HIPE 12.1 data . . . 68
4.3 The PACS spectrometer pipeline . . . 68
4.3.1 Standard Herschel PACS data reduction for unchopped range observations . . . 70
4.3.2 Evolution of data processing pipelines from HIPE 8.0 to HIPE 12.1 74
4.4 The SPIRE spectrometer pipeline for the OMC-2 region . . . 76

5 Spectral cube reconstruction techniques 79
5.1 Construction of the spectral grid . . . 79
5.2 Naive reconstruction (specProject) algorithm . . . 80
5.3 Drizzling algorithm . . . 81
5.3.1 Application to PACS spectrometer data . . . 83
5.4 Interpolation with the Delaunay triangulation algorithm . . . 84
5.5 Comparison of the three methods . . . 86

6 The optimization of the drizzle algorithm for oversampled maps 87
6.1 Input parameters for the drizzle algorithm . . . 88
6.2 Drizzle parameter optimization baseline . . . 90
6.3 Drizzle parameter optimisation results . . . 91
6.4 Testing of optimal drizzling on RDor . . . 92

7 Optimisation of standard data processing pipeline for the HOPS OMC-2 data. 97
7.1 Standard pipeline reduction of unchopped range spectroscopy data . . . 98
7.2 Areas of concern for performance improvements . . . 99
7.3 Data processing from Level 0 to Level 1 . . . 103
7.4 Data processing from Level 1 to Level 2 . . . 107
7.5 Optimal reconstruction of the spectral cubes for the OMC2 region . . . 109

8 HOPS spectroscopy legacy products 115
8.1 Fitting of emission lines and continuum . . . 115
8.1.1 Line fitting . . . 115
8.1.2 Continuum fitting . . . 117
8.2 Turning fitting results into maps . . . 119
8.2.1 CO emission line maps . . . 119

8.2.2 H_2O emission line maps . . . 127
8.2.3 Fine Structure emission line maps . . . 132
8.3 Extracting the source fluxes from the maps . . . 134
8.3.1 Analysis the morphology of the source . . . 134
8.3.2 Identification of the proper aperture radius where to measure the flux for the OMC-2 targets . . . 136
8.3.3 Comparison of the CO fluxes from our line maps with those measured byManoj et al. (2013) for the target HOPS108 . . . 137
8.3.4 Beam correction factors per aperture per band . . . 139

9 The morphology of protostellar sources in OMC-2 143
9.1 Methodology to contain possible extended emission . . . 143
9.2 Applying the method to OMC-2 data . . . 145
9.3 Interpretation of the results . . . 145

10 Far-IR fine structure line emission from the OMC-2 region 151
10.1 Relevance of fine structure lines for physical analysis of protostars . . . 152
10.2 Analysis and Results of fine-structure line maps . . . 153
10.2.1 The jet morphology . . . 154
10.2.2 Excitation conditions in the jet . . . 154
10.2.3 Mass-loss rates from jets . . . 155
10.2.4 Extended emission from PDRs . . . 157
10.2.5 Mass limit on the ionised gas from [OIII] 88.4 μm non-detection 159
10.3 Discussion on the analysis of the fine structure lines . . . 160

11 Far-IR CO and H_2O emission from the OMC-2 region 161
11.1 Introduction to molecular spectroscopy on the OMC-2 region . . . 161
11.2 Analysis of the CO and H_2O line maps . . . 162
11.2.1 Modelling of the CO emission tracing the jet . . . 162
11.2.2 H_2O/CO abundance ratio in the jet . . . 163
11.3 Discussion on the study of the CO and H_2O lines . . . 164
11.3.1 Physical conditions in the molecular jet from FIR 3 . . . 164
11.3.2 Water abundance behind outflow shocks . . . 164
11.4 Conclusions . . . 165

12 Data synergies and future studies 171
12.1 HOPS VLA data from the OMC-2 region . . . 171
12.2 VLA/PACS data cross-match . . . 173
12.3 Future Work . . . 178

13 Summary and Conclusions 179
13.1 Technical achievements . . . 179
13.2 Scientific results . . . 180

A Basic equations of star formation theory 183
A.1 Bonnor-Ebert mass calculation . . . 183

A.2 Bolometric temperature definition 183
A.3 Luminosity of a protostar 184
A.4 Protostar envelope mass 184
A.5 Escape velocity 184
A.6 Mass loss rate from [O I] 63.2 μm 185

B Optimization of Drizzle parameters **187**

C Electron temperature and density **199**
C.0.1 Calculation of electron density 200

D Error budget **203**

Bibliography **213**

List of Figures

1 Snapshot from a youtube video edited by Marcelo Lacava, www.inknowation.com v

1.1 Clumps form clusters, cores for stars. 4
1.2 Taurus B211/3 filament detected by SPIRE at 250 μm . Image adapted from **?**. 6
1.3 Overview of star and planet formation. Taken from (Greene 2001). 7
1.4 Classification of the protostars based on the SED distribution. Image adapted from Furlan et al (2015). 8
1.5 Classification of the protostars based on *(left)* the envelope mass of the protostar and (*right*) based on the bolometric temperature and L_{smm}/L_{bol}. (*Left*) image taken from Schulz et al (2005) and (*right*) image he talk given by Michel Dunham and Amelia Stutz at the meeting Protostars and Planets VI, Heidelberg, July 15-20, 2013. 9
1.6 Spectral energy distribution of protostars identified as VELLOs and PBRs and their location in the L_{bol} vs. T_{bol} diagrams. Figures from the talk given by Michel Dunham and Amelia Stutz at the meeting Protostars and Planets VI, Heidelberg, July 15-20, 2013. 10
1.7 Evolution of protostars from Prestellar core to Class 0 protostar. Image collected from the talk given by Michel Dunham and Amelia Stutz at the meeting Protostars and Planets VI, Heidelberg, July 15-20, 2013 10
1.8 Evolution of protostars from Class I protostar to star in the PMS . Image collected from the talk given by Michel Dunham and Amelia Stutz at the meeting Protostars and Planets VI, Heidelberg, July 15-20, 2013. 11
1.9 Bipolar molecular outflow cartoon from Snell et al. (1980) taken from Guillem Anglada (1996). 13
1.10 This image of the Herbig-Haro Object HH 46/47 is a composition of radio observations (Atacama Large Millimeter/submillimeter Array) combined with visible observations (ESO's New Technology Telescope). The ALMA observations (lower right in orange and green) revealed a large energetic jet, driven by a new born star, moving away from us. This emission is not detected in the visible range as is hidden by the dust and gas in the region. ESO NNT observations (upper left in pink and purple) shows the visible part of the jet, streaming partly toward us .Image adapted from http://www.space.com/22428-amazing-star-birth-photos-alma-telescope.html 14

1.11 Structure of the working surface in a variable jet (schematic). Gas of density ρ_1 and speed V_1, emitted by a star on the left, encounters a flow with density ρ_2 and lower speed V_2. The large value of pressure P_{high} in the intershock region expels material into the cocoon. Both the Mach disk and the bowshock travel at the speed V_{pulse}, intermediate between V_1 and V_2. Image from Stahler & Palla (2005). 16
1.12 Star-forming regions tracers. Image adapted from the Schulz (2005). . . . 17
1.13 The spectrum of the Galactic Center region, Sgr A West. Image adapted from Watson (1985) 19
1.14 Detection of molecules in the different positions of the protostar. Image taken from van Dishoeck et al. (2011) 20
1.15 The Orion region. Credits: far-infrared: ESA/Herschel/PACS/SPIRE/Hill, Motte, HOBYS Key Programme Consortium; X-ray: ESA/XMM-Newton EPIC/XMM-Newton-SOC/Boulanger. 22
1.16 CO J=1-0 image showing the Orion A and B clouds using colours to represent Doppler shifts (blue for V_{LSR} = 0 to 5 km/s, green for V_{LSR} = 5 to 10 km/s, and blue for V_{LSR} = 10 to 15 km/s). Data collected with the 7-m radio telescope on Crawford Hill in Holmdel, NJ. (Bally 1989; Bally et al. 2000). 23
1.17 (*left*) OMC-2 region observed by Gatley et al. (1974) and (*right*) by Chini et al. (1997). 24
1.18 Combination of Spitzer and Herschel images of the OMC-2 region taken from Furlan et al. (2014). IRAC 3.6, 4.5, 5.8, and 8.0 μm, MIPS 24 μm, PACS 70 and 160 ,μm SABOCA 350 μm, and LABOCA 870 μm images of the region around OMC-2 FIR 4 (SOF 3, HOPS 108). At 24 μm the saturated sources to the north, south, and southwest are OMC-2 FIR 3 (SOF 2N, HOPS 370), OMC-2 FIR 5 (SOF 4, HOPS 369), and SOF 5 (HOPS 368), respectively. The crosshairs show the position of FIR 3 and FIR 4. 26

2.1 The Herschel satellite 32
2.2 The Herschel transitional and operational orbits 34
2.3 The Herschel instruments at the focal plane 34
2.4 The PACS optical path (figure collected from the PACS Observer's Manual) 35
2.5 The PACS photometer filters. Figure collected from Poglitsch et al. (2010). 35
2.6 The IFU concept. Image adapted from http://ifs.wikidot.com/what-is-ifs . 36
2.7 PACS spectrometer slicing concept. Image collected from the PACS Observer's Manual. 37
2.8 Representation of the scan map technique. Figure collected from the PACS Observers Manual 38
2.9 *Up:* relation between grating angle and the wavelength at the PACS spectrometer instrument. *bottom:* nominal and parallel ranges between the blue and red channels. Image from the PACS Observer's Manual. 40

2.10 Setup of a typical PACS spectrometer (*top*) for chop/nod mode observations, (*bottom*) for unchopped mode observations. Figures from the PACS Observer's Manual. 41
2.11 *Left:* PACS line sensitivity and *Right:* PACS continuum sensitivity. Images from the PACS Observer's Manual. 42
2.12 Spatial distribution of the PACS beam at 62 μm and 150 μm with the footprint of the IFU over plotted. Figure from the PACS Observer's Manual. 43
2.13 The SPIRE optical path. Figure adopted from *The Spectral and Photometric Imaging Receiver (SPIRE) Handbook*, HERSCHEL-DOC-0798 . . 44
2.14 The SPIRE photometer instrument. Figure from the SPIRE Handbook. . 45
2.15 A schematic of the Mach-Zehnder Fourier transform spectrometer. Figure adopted from the SPIRE Observers's Manual 45
2.16 The SPIRE spectrometer instrument. Figure from the SPIRE Handbook. 46
2.17 Explanation of raster pointing technique 48
2.18 Footprint of the SPIRE detector arrays for sparse (left image), intermediate (centered image) and full spatial sampling (right image) modes. Figure taken from SPIRE Handbook. 49
2.19 The HIFI optical path 50
2.20 Superposition of upper (red) and lower (blue) sideband spectra for DBS spectra for the Orion cloud at 807.0 GHz. Image adopted from the HIFI Observer's manual 51

3.1 HOPSTeam logo 53
3.2 Spectral Energy Distribution of a typical YSO overlaid with the range of sensitivity exhibited by different experiments from the near-infrared to submillimetric wavelengths. 54
3.3 (*left*) YSO targets observed by HOPS and (*right*) zoom on the region marked as a box in the *left* image, which contains the OMC-2 region. Both figures were collected from a talk given by T. S. Megeath, the HOPS team P.I. 55
3.4 *Top* shows a composition of images collected by the HOPS programme at the position of the PBR object NGC2068 093005. This object is detectable only from 70 μm onwards. Therefore is one of the new protostars identified by Herschel. *Bottom*) image show the spectral energy distribution of this target peaking at 160 μm (Herschel range). Image adopted from Stutz et al. (2013) 56
3.5 Identification of the new PBRs objects in the Orion Molecular Cloud. Image adopted from Stutz et al. (2013) 57
3.6 Identification of the lines in the PACS range for a set of protostars from the Herschel Orion Protostar Survey. Image taken from Manoj et al. (2013). 58
3.7 (*Left*) rotation diagram for the HOPS 108 (FIR 4) target , where at least three components can be derived and *right* the estimated gas temperature and densities comparing observed results to Neufeld (2012) grid of model. Images adopted from Manoj et al. (2013). 59

3.8 Total luminosity of the CO lines detected within the PACS wavelength range with S/N > 3σ as a function of L_{bol}, T_{bol}, and envelope density (ρ_1). Image adopted from Manoj et al. (2013). 59

3.9 (*Left*) SEDs of HOPS 370 and (*right*) of HOPS 108, taken from Furlan et al. 2015. 60

3.10 PACS 70 μm image of the HOPS sample for the OMC-2 region. Overplotted the footprint of the PACS spectrometer observations for HOPS 370 (top) a 3×3 raster and HOPS 108 (bottom) a staring observation. 62

4.1 Level 0 for one of the HOPS observations from this thesis (1342227764). Step (4) in the process. Y axis is digital units (i.e, instrumental) and x axis is readouts, i.e: a simple counter of data points. 70

4.2 Data structure at step (11) of the pipeline applied from Level 0 to Level 0.5. The data units are in Volts per second. The data at value zero are bad data, which will are masked by the pipeline. 71

4.3 Data structure at state (6) of the pipeline applied from Level 0.5 to Level 2, just before the FlatFielding task. Each color is the spectrum from a different spatial pixel of the central spaxel (module 12). It is clear that the different pixel-spectra have offsets with respect to each other correct for this. 73

4.4 Data after flat-fielding now.The different coloured spectra now lie on top of each other: compare to Fig. 4.3. The red part of the spectrum has been cut as these data could not be calibrated at the time of our data reduction. 73

4.5 A spectrum from one spaxel of one raster position for the same observation shown in the previous plots. Blue curve are the on-source data and green are the off-source data. The brown spectrum is the on-off. This is the result of running the standard pipeline script for unchopped raster observations. 74

4.6 Comparison of the spectrum for the PACS central spaxel, from a PACS rebinned cube, between HIPE 8 and HIPE 12. 75

4.7 Comparison of the spectrum for the central module from a PACS Level 1 cube, when applying different off subtraction methods in HIPE 12.1 (calibration version 65). 76

5.1 Explanation of *oversample* and *upsample* concepts, applied for the generation of the spatial and spectral grids (figure from S.Regibo, 2014) 81

5.2 Description of the drizzle algorithm(Regibo 2012) 82

5.3 Nyquist sampling definition wavelengths. 84

5.4 (*let*) The concept of applying the Delaunay triangulation. Figure from the PACS Data Reduction Guide for spectrometer data.(*right*) This drawing illustrates that specInterpolate can not be used for observations with dense spatial sampling. Blue dots are the central spaxels for a raster observation. If the output spaxels are set too large (red squares) then the 3 input positions (orange triangles), chosen by the Delaunay algorithm, all inside a single spaxel (red square). This means not all the FoV covered by a single spaxel is included in the interpolation. The SNR of the result will hence suffer. 85

6.1 The overlap of two nod positions for chop/nod observations it is not exact. This could cause a "blurring" effect in the drizzle cubes. 88

6.2 Explanation of drop size and shrinking factor at the drizzle algorithm (figure from Regibo (2012). 88

6.3 Explanation of *oversample* and *upsample* concepts, applied at the generation of the spectral grids. Figure from Regibo (2012) 89

6.4 Illustration of the effect of drizzling on the cross-section of a Gaussian beam profile. We plot the input Gaussian and those which are convolved with the spaxel size rebinned to the output pixel size. 90

6.5 (*left*) the impact of a strong shrinking (pixfrac=0.1) in the final map may cause holes, (*right*) spatial distribution for pixfrac from 0.1 to 1 for the selected oversample and upsample values (3,2) and comparison to specProject result on the same data. 93

6.6 FWHM of the projected Gaussian source obtained from drizzle maps versus *pixfrac* for the different set of (oversample, upsample) values selected 94

6.7 Comparison of line maps for a point source (RDor) in a drizzled cube generated with spatial grid parameters (oversample=3, upsample=2) and pixfrac (from left to right) of 0.4, 0.6, 0.8 and 1.0. 95

6.8 Comparison of line maps for a point source (RDor) in a drizzled cube generated with spatial grid parameters (oversample=3, upsample=2) and pixfrac (from left to right) of 1.0 compared to line map generated with specProject (right). 95

7.1 Colours represent signal from the subsequent spectral up-down scans obtained from module 12 pixel 3 of the blue spectrometer array. In one upscan (black curve) the pixel has been hit by a high-energy particle which caused the glitch in signal and the following trend in response. 99

7.2 (yellow curve) RSRF residuals are reproducible over a large number of observations (the dots). The amplitude of repeating patterns accounts for ~1.5% of un-calibrated flux modulation in band B2B, and ~1.0% in band R1. 100

7.3 Measured noise performance from HOPS spectroscopy data on spaxel 12. Plots of the continuum RMS values versus wavelength. On-source observations (red line) exhibit a significantly higher noise than Off-source observation (blue line), due to the presence of strong spectral lines, pointing jitter, slit illumination effects and probably due to flux-dependent variation in the RSRF residuals. The measured performance, however, exceeds the predicted performance. 102

7.4 Common de processing from Level 0 to Level 1 products. 103

7.5 Different processing from Level 1 to Level 2 products depending on the observing strategy. 104

7.6 Examples of the continuum subtraction. The specBaselineEstimator task applies a multi-resolution wavelet based method which can iteratively estimate the baseline level even in spectra which contain a variety of dominating frequencies. Upper panel, areas of emission lines are zoomed on, Bottom panel, the entire R1 red band spectrum. 106

7.7 Comparison, for a single slice of the Pacs Level2 cubes at 63 μm , of the spatial distribution for (top) specProject cubes, (middle) drizzled cubes and (bottom) specInterpolated cubes. At each one of these images, (left images) show the reconstruction for an output pixel size of 3 $''$and (right images) for 1.4 $''$. Upper part of the data is oversampled and lower part is under-sampled. 111

7.8 Flux comparison per pixel at the line maps generated from specProject cube and for the drizzle cubes at this work. (*Top*) image for [OI] 63 μm line map and (*middle*) image for the [OI] 145 μm line map. The comparison at the line maps with output pixel size of 3$''$is represented with blue dots and for those of 2$''$pixel size with green dots. (*Bottom*) image perform a similar comparison between specProject and drizzle for shrinking factors of 60 % (blue dots) and 100 % (pink dots) 112

7.9 *(Top)* The [O I] 63 μm line map generated with Drizzle and specInterpolate for 2$''$. *(Middle)* The [O I] 63 μm line map generated with Drizzle and specInterpolate for 3$''$. *(Bottom)* The [O I] 63 μm line map generated with specProject and specInterpolate for 3$''$. 113

8.1 Comparison of line maps generated for the different fitting methods for a bright line: (*left*) method 1: fitting spaxel by spaxel in a loop obtaining the model (Gaussian + zero order polynomial) for a spaxel and passing it as input for the fitting of the neighbour pixel, (*middle*) method 3: automatic selection of the reference spaxel and applying to it a model (Gaussian + zero order polynomial) which later will be passed it as input for fitting the rest of the cube with the Multifitter task and (*right*) method 4: same as method 3 using the GUI task. 116

8.2 Comparison of line maps generated for the different fitting methods for a faint line: (*left*) method 1: fitting spaxel by spaxel in a loop obtaining the model (Gaussian + zero order polynomial) for a spaxel and passing it as input for the fitting of the neighbour pixel and (*right*) method 3: automatic selection of the reference spaxel and applying to it a model (Gaussian + zero order polynomial) which later will be passed it as input for fitting the rest of the cube with the Multifitter task. 117

8.3 Integrating flux extracted for 7″radius around the HOPS 108 (blue) and HOPS370 (red) target. 118

8.4 Line flux maps of CO transitions detected in the OMC-2 regions for the emission lines CO (4-3), CO (5-4), CO (6-5), CO (7-6), CO (8-7) and CO (9-8). From CO (4-3) to CO (8-7) the lines were detected with the SPIRE SLW detector and CO (9-8) with SSW detector. The star symbols represent the OMC-2 FIR 3 target (top) and OMC-2 FIR 4 target (bottom). 120

8.5 Line flux maps of CO transitions detected in the OMC-2 regions for the emission lines from detected from SPIRE SSW from CO (10-9) to CO (13-12) and from PACS from CO (14-13) to CO(15-14). See the difference of field of views between SPIRE and PACS maps. The star symbols represent the OMC-2 FIR 3 target (top) and OMC-2 FIR 4 target (bottom). 121

8.6 Line flux maps of CO transitions detected by PACS in the OMC-2 regions for HOPS 370 (FIR 3) and HOPS 108 (FIR 4) for the emission lines of CO (16-15), CO (17-16), CO (18-17), CO (19-18), CO (20-19) and CO (21-20). The star symbols represent the OMC-2 FIR 3 target (top) and OMC-2 FIR 4 target (bottom). 122

8.7 Line flux maps of CO transitions detected by PACS in the OMC-2 regions for HOPS 370 (FIR 3) and HOPS 108 (FIR 4) for the emission lines of CO (22-21), CO (23-22), CO (24-23), CO (25-24), CO (28-27) and CO (29-28). 123

8.8 Line flux maps of CO transitions detected by PACS in the OMC-2 regions for HOPS370 (FIR3) and HOPS108 (FIR4) for the emission lines of CO (30-29), CO (31-30), CO (32-31), CO (33-32), CO (34-33) and CO (35-34). The star symbols represent the OMC-2 FIR 3 target (top) and OMC-2 FIR 4 target (bottom). 124

8.9 Line flux maps of CO transitions detected by PACS in the OMC-2 regions for HOPS370 (FIR3) and HOPS108 (FIR4) for the emission lines of CO (36-35), CO (37-36), CO (38-37), CO (39-38), CO (40-39) and CO (41-40). The star symbols represent the OMC-2 FIR 3 target (top) and OMC-2 FIR 4 target (bottom). 125

8.10 Line flux maps of CO transitions detected by PACS in the OMC-2 regions for HOPS370 (FIR3) and HOPS108 (FIR4) for the emission lines of CO (42-41), CO (43-42), CO (44-43) and CO (45-44). The star symbols represent the OMC-2 FIR 3 target (top) and OMC-2 FIR 4 target (bottom). . 126

8.11 Line maps of the *16 ortho-* H_2O detections at the OMC-2 regions. The stars identify OMC-2 FIR3 (top) and OMC-2 FIR4 (bottom). The lines from top left to bottom right are those at the wavelengths: 180 μm , 179.5 μm , 174.6 μm and 160.5 μm 127
8.12 Line maps of the *16 ortho-* H_2O detections at the OMC-2 regions. The stars identify OMC-2 FIR3 (top) and OMC-2 FIR4 (bottom). The lines from top left to bottom right are those at the wavelengths: 156.26μm (blended with *para-* H_2O detections at 159.19 μm), 113.53 μm , 108 μm , 96.62 μm , 78.74 μm and 77.08 μm 128
8.13 Line maps of the *16 ortho-* H_2O detections at the OMC-2 regions. The stars identify OMC-2 FIR3 (top) and OMC-2 FIR4 (bottom). The lines from top left to bottom right are those at the wavelengths: 74.94 μm , 71.94 μm , 66.09 μm , 65.16 μm , 63.32 μm and 58.69 μm 129
8.14 Line maps of the *16 para-* H_2O detections at the OMC-2 regions. The stars identify OMC-2 FIR3 (top) and OMC-2 FIR4 (bottom). The lines from top left to bottom right are those at the wavelengths: 138.52 μm , 125.35 μm , 96.62 μm , 89.98 μm , 83.28 μm and 82.03 μm 130
8.15 Line maps of the (*left*) *16 para-* H_2O at 67.08 μm , 63.45 μm and 59.98μm .131
8.16 Line maps of the (*left*) [O I] at 63 μm , (*middle*) [O I] at 145 μm and (*right*) [CII] at 157 μm 133
8.17 The image show the contours levels (75%, 50% and 25% the maximum flux) of the flux distribution line map, generated from specInterpolate cubes with 3 ″spaxel, for a point source (RDor) overlaid with the line map generated with the same technique for HOPS108. 136
8.18 Comparison of our flux measurements from the CO line maps detected in the PACS range (J_{up} = 42-14) versus those from Manoj et al. (2013). . . . 138
8.19 Beam correction factors to apply to the aperture photometry values calculated from PACS line maps with pixel size of 0.5″for the set of wavelengths delivered at the PACS calibration website (55μm , 62μm , 68μm , 75μm ,84μm , 94μm ,125μm ,136μm ,145μm , 150μm ,168μm and 187μm).142

9.1 Line and continuum emission for the [O I] 63 μm maps generated at this work. The coordinate axis just indicate the shift in (RA,Dec) respect to the HOPS 370 target (the northern one at these maps). (*Top left*) image is a smoothed display of the line maps calculated in this work, with a colour scale that allows to better see the different flux levels (in W/m^2 units), (*top right*) shows the continuum maps generated in this work with the same colour scale (*bottom left*) shows the sum of line-plus-continuum map (in W/m^2 units) and (*bottom right*) shows the flux distribution of comparing the line and continuum maps for the same line following Podio et al. (2012) method (i.e. residual maps). 146
9.2 Same than Fig. 9.1 but applied to the OH maps at 84 μm 147
9.3 Same than Fig. 9.1 but applied to the H_2O maps at 113 μm 148
9.4 Same than Fig. 9.1 but applied to the OH maps at 119 μm 149
9.5 Same than Fig. 9.1 but applied to the H_2O maps at 179 μm 150

10.1 *(Left)*: The [O I] 63 μm line map of the OMC-2 region, *(middle)*: the narrow ridge like emission component obtained after subtracting the extended emission background component *(right)*: the extended emission component extracted by fitting a 2D third order polynomial to the line map. The positions, sizes, and names of the line flux aperture measurements listed in Table 10.1 are indicated. The residual background was measured within an aperture of the same radius 9″away from the jet, as shown in the figure. 153

10.2 [O I] 145 μm map *(left)* and [O I] 63 / [O I] 145 line ratio map before *(middle)* and after PDR subtraction (*right*). 154

10.3 [O I] 63 μm line emission from our maps (white contours; levels = 1, 2 & 3 $\times 10^{-16}$ Wm^{-2}/pixel) with the FOV outlined in green *(left panel)*. The blue (-10 to 9 km s^{-1}) and red (14 to 30 km s^{-1}) wings of the CO 6-5 (from the APEX observations) values are the blue and red contours in the *right panel*. Both are overlaid on the 4.5 μm image, which shows the jet extending to the north-east. 155

10.4 The [O I] and [C II] line ratio maps of the OMC-2 region: *left* panel shows the [O I] 63 μm / [C II] 158 μm map and the *right* panel shows he [O I] 63 μm / [O I] 145 μm map. All line ratios are calculated at matched angular resolution. 157

10.5 *(Left)* Observed [O I] 63.2/145.5 (blue) and [O I] 63.2/[C II] 157.7 line ratio (green) contours compared to expectations for a single-component model. The observed ratios for the regions immediately outside the FIR 3 jet are indicated with heavy solid contours, and the ± 1 σ band by dashed contours. Thin contours indicate the same line ratios, covering the plotted range of density and temperature, with logarithmically-spaced contours. The families of curves intersect near n_e = 10^4 cm^{-3} and T = 130 K, which lie in the ranges common for photodissociation regions in the Orion molecular-cloud complex. *(Right)* [O I] 63.2/145.5 intensity ratios observed along the jet plotted as heavy blue curves: FIR 4 (shortest dashes), FIR 3 (solid), SW/NE of FIR 3 (medium/long dashes). At high temperatures the intensity ratios would indicate electron density in the range 5×10^4 - 8×10^4 cm^{-3}. 158

10.6 PACS spectra centred around FIR 4 at the wavelength of the [O III] line, 88.36 μm , shows no-detection. The strong line that appears in the range is the CO (30-29) emission line, at 87.190 μm. 159

11.1 CO (J = 17 $\rightarrow$ 16) *(left)* and H_2O ($7_{0,7} \rightarrow 6_{1,6}$) *(right)* line maps of the OMC-2 region. The positions, sizes, and names of the line flux aperture measurements listed in Table 11.1 are indicated. 162

11.2 *(Left)* Rotational diagrams for CO from an isothermal medium that best fits the observations (solid red line). Downward arrows indicate upper limits to the fluxes of the CO lines which are blended with a nearby line. Open circles correspond to 3 σ upper limits for the non-detections. *(Right)* Reduced-χ^2 contours for T and $n(H_2)$. The star symbol marks the minimum. The contours corresponding to 68.3% (blue), 95.4% (green) and 99.7% (red) confidence levels are shown. 167

11.3 The model predictions of o-H_2O ($7_{0,7} \rightarrow 6_{1,6}$) to CO ($J = 17 \rightarrow 16$) line ratio as a function of $n(H_2)$ for various temperatures (color coded) and for a CO optical depth parameter of $log[N(CO)/dv] = 15.5$. Different panels correspond to the abundance ratio, $n(o\text{-}H_2O)/n(CO) = 3.16$, 1.0, 0.32, 0.1, 003 and 0.01. The observed ratios at the 4 positions along the jet are shown as gray bars, with the spread corresponding to uncertainties. For the $n(H_2)$ and T inferred from the best fit models for CO emission, the observed line ratios indicate $n(o\text{-}H_2O)/n(CO)$ between 1 and 0.32 . . 169

11.4 Same as in Figure 11.2, but for a CO optical depth parameter of $log[N(CO)/dv] = 16$. 170

12.1 VLA map at 3cm at C configuration. Contours presented from [-3,3,6,9,15,21] $\times \sigma$, being $\sigma = 0.008$ mJy/Beam. The color scale also corresponds to the 3 cm emission. Beam size represented at the bottom left side of the image. 172

12.2 Combination of VLA 3cm data with the PACS [C II] at 157 μm line (*left*) and (*continuum*) maps. PACS data is presented in the background and the VLA as contours. Images generated by A.K.Diaz and passed as private communication. 174

12.3 Combination of VLA 3cm data with the PACS [O I] 63 and 145 μm line maps. PACS data is presented in the background and the VLA as contours. Images generated by A.K.Diaz and passed as private communication. 175

12.4 Combination of VLA 3cm data with a sample of the PACS OH line maps. PACS data is presented in the background and the VLA as contours.Images generated by A.K.Diaz and passed as private communication. 176

12.5 Combination of VLA 3cm data with a sample of the PACS CO and H_2O line maps. PACS data is presented in the background and the VLA as contours.Images generated by A.K.Diaz and passed as private communication. 177

13.1 Our toy model of the OMC-2 region. In green there is the narrow jet structure, driven by FIR 3, that extends north-east and south-west. This impact with the cold cloud where FIR 4 is forming, very close to FIR 4 but maybe to exactly in the same position. Along the outflow there is detected CO and H_2O emission. The four apertures on which the fluxes were measured for the line maps generated in this work are shown. The extended emission that we see at [C II] line maps, is also shown. 182

B.1 This figure shows, two short ranges (in the blue band) of unchopped raster observation of the target HOPS85, the difficulty of identifying by visual comparison, the optimal drizzle parameters for the On-source (left) and at On-source, off subtracted (right) observations. The blue curve is the result of applying specProject to the raster observation and the black and red curves the selection of different upsample, oversample values. 187

B.2 188

B.3 This figure shows the different flux distributions along a cross section, of an input Gaussian flux distribution to which specProject and drizzle (for upsample=[1,2,3] and pixfrac=[0.1,0.2.0.3,..,0.9]) have been applied. The observation on which the simulated flux was applied is obsid xxx, and we used the pointing information from this oversample raster observation . . 189

B.4 This table shows the resultant FWHM obtained from fitting a Gaussian to each of the flux distributions mentioned at figure B.3. Green colour represent the Gaussian distribution at the central pixel and blue colour represent the specProject distribution (in line to Fig B.3). We identified optimum parameter those (upsample, pixfrac) parameters which flux distribution have a FWHM closer and smaller to the FWHM from the PSF at that wavelength 189

B.5 This figure shows the resulting images from our simulation (Fig. B.3 and B.4) for a short range around 181 μm. From left to right they are: the expected flux distribution (green), specProject flux distribution (blue), drizzle flux distribution for those parameters that best match the FWHM of the beam (red), drizzle flux distribution for those parameters that worst match the FWHM of the beam (black) 190

B.6 This figure shows the same analysis than Fig. B.4 and B.5 for a short range around 68 μm. 190

B.7 This figure shows the same analysis than Fig. B.6 but for a fixed oversample factor = 3, upsample =[1,2,3] and pixfrac=[0.1,...,1.0]. 191

B.8 This figure shows the comparison of applying drizzle (with the optimum input parameters identified at that wavelength) and specProject for two short ranges of the observation xxx (~ 2 μm centered at 181 μm (top) and 63 μm (bottom). The same WCS created by specProject (for an output pixel of 3$''$) was used for the generation of drizzle cubes. The continuum was not subtracted from the Pacs Level 1 cubes, and the uncertainty in the continuum for unchopped range modes did not show any obvious identification. 192

B.9 This figure shows, in similar lines as previous images, the flux distribution along a cross section for 2 simulated Gaussians with different intensity levels (left image). As before, the resultant FWHM from firing the flux distribution with two Gaussians is calculated (right table). At the bottom part of this figure, there are the maps, centered at 181 μm, showing the flux distribution of the cubes from the expected flux (magenta frame), the specProject algorithm (blue frame), the drizzle cube generated with input parameters that best fit the PSF (red) and the drizzle cube generated with input parameters that worst fit the PSF (black). 193
B.10 The same study than Fig. B.9 have been done for 63 μm. Here there are displayed the maps, centered at 63μm, which show the flux distribution of the cubes from the expected flux (magenta frame), the specProject algorithm (blue frame), the drizzle cube generated with input parameters that best fit the PSF (red) and the drizzle cube generated with input parameters that worst fit the PSF (black). 193
B.11 Comparison of the impact on the data by using the spacecraft attitude information considering 25 sky positions (the center position of each of the 25 spaxel) or 400 sky positions (different positions for each of the 16 spectral pixels at each of the 25 spaxels). 194
B.12 Comparison of the flux distribution along the two cross sections for a single pixel position , when considering 25 or 400 positions per raster position. 194
B.13 Comparison of the flux distribution along the two cross sections for a single pixel position, considering the 400 positions, when applying and not applying transient corrections. 195
B.14 Comparison of the spatial distribution of the drizzle cubes, generated at 68 μm for several (oversample, upsample) combinations and for the 9 possible pixfrac values (from 0.1 to 0.9). Also specProject, within a blue frame, generated with the same WCS is displayed for comparison. From top left to bottom right the plots represent (oversample=3, upsample=3), (oversample=3, upsample=2), (oversample=3, upsample=1), (oversample=2, upsample=3), (oversample=2, upsample=2) and (oversample=2, upsample=1) 196
B.15 Comparison of the spatial distribution of the drizzle cubes, generated at 181μm for several (oversample, upsample) combinations and for the 9 possible pixfrac values (from 0.1 to 0.9). Also specProject, within a blue frame, generated with the same WCS is displayed for comparison. From top left to bottom right the plots represent (oversample=3, upsample=3), (oversample=3, upsample=2), (oversample=3, upsample=1), (oversample=2, upsample=3), (oversample=2, upsample=2) and (oversample=2, upsample=1) 197

List of Tables

2.1 Detail of the Herschel instruments at the focal plane 33
2.2 Essential properties of the PACS photometer AOTs 39
2.3 Essential science performance properties of the PACS spectrometer 42
2.4 Capabilities of the SPIRE spectrometer for sparse sampling 46
2.5 Spectral resolution for SPIRE sparse sampling, from SPIRE Spectrometer PointSource ReleaseNote 48
2.6 Calibration accuracy for the SPIRE intermediate and full sampling, from SPIRE Spectrometer Mapping ReleaseNote 50
2.7 HIFI frequency coverage and band allocation. Table adopted from HIFI Observer's Manual 52

3.1 Log of PACS photometer observations 63
3.2 Log of PACS and SPIRE spectroscopic observations. The rasters observations are reported as $n \times m$, which are step number times step size. . . . 63

6.1 Set of input parameters used for the drizzle optimisation process at the blue (68 μm) and red (181μm) wavelengths 91

7.1 Drizzle Ids in which the complete PACS long-range was divided from Level 1 onwards 108

8.1 *c9/c1* comparison from the peak of CO lines detected in the HOPS108 spectra. 135
8.2 Fluxes extracted for several aperture radii for HOPS108 and HOPS370 from the line maps of [O I] at 63 μm and [O I] at 145 μm 137
8.3 Fluxes extracted for several aperture radii for HOPS108 and HOPS370 from the line maps of CO (16-15) at 162.8 μm and CO (20-19) at 130.37 μm 137
8.4 Fluxes extracted from the CO line maps generated by this work for HOPS 108 within an aperture of 6.5″radius versus those reported by Manoj et al. 2013. 140
8.5 Differences in our processing versus Manoj et al. (2013). 140
8.6 Fluxes extracted from the rebinned cubes from the pointed observation of HOPS 108 from the central spaxel, with point source correction from us versus those reported by Manoj et al. (2013). 141

8.7 Fluxes extracted from the central spaxel of the rebinned cubes of HOPS 108, without and with point source correction compared to the flux from table 8.6 for 13 ″. 141

10.1 Observed properties of the [O I] jet from FIR 3 156

11.1 CO line fluxes extracted from the line map within the same four apertures used for the [O I] analysis, with 9″ radius. 166
11.2 Physical parameters of the CO emitting gas from modeling 166
11.3 H_2O line fluxes extracted from the line map within the same four apertures used for [O I], for aperture radius of 9″. 168

Outline

Imaging and spectroscopy data obtained on the OMC-2 region from the HOPS sample have been processed, analysed and interpreted in the thesis along the following structure:

In the first chapter the elementary components of the star formation process are introduced and the importance of a far-infrared space mission in the context of star formation studies is illustrated.

The second chapter describes the Herschel Space Observatory, following by an outline of its science instruments and their observing modes.

The third chapter explains the scientific motivation of the HOPS programme, describing our optimal use of PACS observing techniques that allow us to detect IR radiation from our densely populated area of young stellar objects.

In chapter 4 we give a technical description of the standard calibration and data processing pipelines of the SPIRE and PACS data of the HOPS program.

Chapter 5 contains an overview of the spectral mapping reconstruction techniques available to PACS spectrometer users in the Herschel Interactive Processing Environment (HIPE).

Chapter 6 describes the method done by first time in this PhD thesis to identify the optimal parameterisation to be applied to the drizzling cube reconstruction algorithm when applied to oversampled PACS spectral mapping data. Our findings have been adopted as the standard processing, in HIPE, being now available for all the Herschel users.

Chapter 7 illustrate our optimisation of the unchopped spectroscopy data processing pipeline to create the HOPS legacy products of the OMC-2 region.

Chapter 8 provides an inventory of the legacy products, generated in a unique way by this work, including spectral line- and continuum maps as well as line ratio maps. In this chapter, we describe our investigation of the optimal flux extraction techniques applied to our HOPS spectral cubes, and the uncertainties associated with the resulting spectral map products. Comparison with data reduction results provided in previous studies on the HOPS 108 source is also provided here. At the end of the chapter, we present our choice of technique to extract integrated fluxes from morphological segmented regions on the OMC-2 line maps.

Chapter 9 analyses the technique that we applied to investigate the spatial correlation between continuum and line emission peaks, in order to see whether or not there is extended emission in the different species ([O I], [C II], CO, H_2O ,OH) of the OMC-2 region. This comparison was a first approach to the data, the deeper analysis done in chapters 10 and 11.

Chapter 10 provides the analysis and scientific interpretation of the fine structure line data ([O I], [O III] and [C II]). We model the fundamental physical properties of the region, identify the origin of the [O I] jet, and describe the nature of the bright line emission towards the FIR 4 source.

Chapter 11 details the modelling of CO and H_2O molecular transitions detected in the OMC-2 region, in particular the physical conditions in the molecular gas along the jet driven by FIR 3. We compare the H_2O-to-CO abundance measured behind the outflow shocks and provide some explanations for those values.

Synergies with VLA data for future interpretation are discussed in Chapter 12 and summary and conclusions are provided in Chapter 13.

1

Star formation in a nutshell

Among several outstanding open issues in modern astrophysics, one of the main concerns is a thorough understanding of how stars and planetary systems form. The OMC-2 region is a star forming region of low- and intermediate star formation. For that reason here we introduce some star formation processes.

Star formation is an universal process which mostly takes place in the disks of galaxies (including our own Milky Way) and particularly in the spiral arms, where gravitational instabilities and colliding flows of gas form bound structures of $\sim 10^7\ M_\odot$ from the diffuse interstellar medium (ISM) (McKee & Ostriker 2007).

The formation of low-mass stars has been observed in isolated low-mass cores of $T_K \sim$ 10 K, densities of $\sim 10^3$ cm^{-3} and radii of $\sim$ 0.04 pc, as well as in dense clusters. The formation of high-mass stars is more commonly to be observed in clusters, at $T_K \sim 30$ K, densities of $\sim 10^6$ cm^{-3} and radii of $\sim$ 0.2 pc (Mardones 2003).

Current low-mass star formation theories largely rely on the work of Larson (1969) and Shu et al. (1987), which consider that star formation follows different stages. The first stage occurs when the molecular cloud fragments into smaller clouds and clumps within them, due to the combination of high level of turbulence in the ISM and gravity. The highly supersonic turbulences inside the clouds are responsible for creating a wide range of densities and, therefore, clumps (and cores, see Fig. 1.1) of different sizes and masses. Turbulence processes are not well understood yet, but seem to be key in star formation (Federrath & Klessen 2012). Magnetic fields also the may play an important role in the lifetime of the cores and their collapse phases.

During the first stage, the combination of forces (turbulence, perturbations, magnetic,

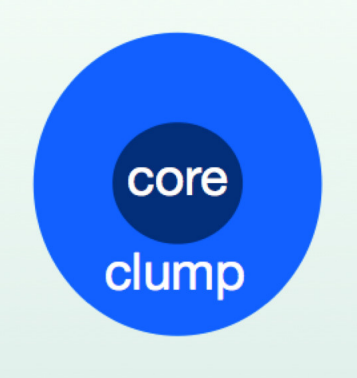

Figure 1.1: Clumps form clusters, cores for stars.

thermal pressure and gravitation) are compensated and the cores can not collapse (Mouschovias 1991; Shu et al. 1987). It will be later, due to not well understood mechanisms, when cores become more unstable to collapse (Larson 1969; Nakano 1998; Mouschovias 1991; Bonnell et al. 1997; Crutcher 1999). Larson (1969) considered that this initial collapse is being generated by a density gradient which follows the expression $\rho \propto r^{-2}$, with a strong concentration of matter in the centre of the core. The studies of Whitworth & Summers (1985a); Blottiau et al. (1988); Foster & Chevalier (1993) concentrate in the central part of the core (the densest within a small radii) independent from initial conditions.

Evolution continues and, at some point, the centre of the core becomes opaque and hydrostatic. It is then that we consider that a protostellar object has formed (Larson 1969; Boss & Yorke 1995; Bate 1998). At this stage the main accretion phase of the central object takes place and the mass of the star ($M_\star$) will be defined. The accretion of mass is done from the shocks of the surrounding infalling envelope (of mass M_{env}) and those generate a rotating internal accretion disk, which transports the angular momentum outwards and warms up the central object in the process. This stage receives the name of an accreting protostar (Andre et al. 2000), where $M_\star \ll M_{env}$ and the accretion luminosity is $L_{acc} \sim GM_\star \dot{M}_{acc}/R_\star$, where G is the universal gravitational constant, $\dot{M}_{acc}$ the mass accretion rate and $R_\star$ the star radius.

The main accretion phases are connected to powerful mass ejections where a small fraction of the infall material is released. They occur as powerful winds driven from the surface of the disk, as a result of magneto-centrifugal forces, to release angular momentum (Bachiller 1996; Konigl & Pudritz 2000). The regions of the wind closest to central star are the most ionised and therefore the most affected by magnetic stresses, defining a collimated jet-like structure. As the disk is wide, the wind from the disk can sweep up a huge amount of ambient gas into a massive molecular outflow, reducing the net efficiency of the star formation to one third (McKee & Ostriker 2007).

The process of accreting and releasing mass continues until the central object achieves 90% of its final mass During the pre-main-sequence (PMS) phase, the star evolves, at almost a fixed mass, following the Kelvin-Helmholtz contraction timescale (Baraffe et al. 2015).

During the protostar accretion phase, for stars more massive than 0.1 $M_{\odot}$ the deuterium is burnt, while for stars more massive than 8 $M_{\odot}$ already hydrogen is burnt (Palla & Stahler 1991).

Low- and intermediate-mass stars are believed to form in cores which may be described as unstable *Bonnor-Ebert*[1] spheres supported by thermal gas pressure, whereas massive stars form in turbulent cores (Bonnor 1956; Ebert 1957). These massive and luminous stars ionise the gas, leading to the formation of HII regions that expand into the ambient cloud at typical velocities of 10 km/s, which may cause the loss of cloud mass by evaporation. The destruction of the cloud delivers low and intermediate mass stars at a typical star-formation efficiency of 5 %. The likely reason of this low value is because only a few percent of the gas become dense enough to overcome the turbulence and collapse into stars.

Theoretically, for an infalling isothermal envelope at T $\sim$ 10 K, an accretion rate of $1.6{\times}10^{-6}$ $M_{\odot}$ yr^{-1}would be expected. In this case, to form a $1M_{\odot}$ star would last $\sim 7{\times}10^{5}$ yr. More detail calculations for spherical collapse (Hunter 1977; Whitworth & Summers 1985b; Ogino et al. 1999) consider that there is an initial rapid accretion, which lasts $\sim 10^{4}$ yr and during half of which the envelope is accreted. The rest is accreted over a 10^{6} years timescale. However, from the observational measurements these accretion rates are not well constrained. When the protostar core temperature exceeds $\sim 10^{6}$ K is when the protostar becomes a main sequence star (Schulz 2005).

Even when we have described in an easy way the steps related to low-mass star formation, there are many physical processes involved which are not well understood yet (Krumholz 2011): supersonic turbulent plasma, magneto-hydrodinamic processes, gravity and radiative processes, chemical processes (formation and destruction of molecules and dust grains) changing the thermodynamic of the gas and the ionisation state and strongly affecting how the gas couples with the magnetic fields. Therefore observations of a variety of star-formation regions are required to achieve an unified theory of star formation (Krumholz 2011).

As mentioned in Dunham et al. (2014), the modern understanding of low-mass star formation processes is a combination of theorical work and empirical classification scheme for dense rotating and collapsing cores (Shu et al. 1987; Adams et al. 1987; Wilking et al. 1987; Kenyon et al. 1993).

Herschel results (André et al. 2010; Könyves et al. 2010; Arzoumanian et al. 2011) reveals "universal" filamentary structure in the cold ISM and suggest that star formation occurs in two main steps:

- First: The filaments form in the cold ISM, probably as a dissipation of the magnetohydrodinamic (MHD) turbulence, where cores form (see SPIRE map of Fig. 1.2).
- Second: The densest filaments then fragment into prestellar cores via gravitational

[1] *Bonnor-Ebert mass:* For a static isothermal cloud without magnetic field with a given surface pressure, the critical mass M_{cr}, which is the maximum mass for the cloud in hydrostatic equilibrium (stable or unstable) - is the Bonnor-Ebert mass (Bonnor 1956; Ebert 1957).

instability above a critical (column) density threshold of 150 $M_{\odot}$pc^{-2}, $A_V \sim 8$, $n_{H2} \sim 2 \times 10^4$ cm^{-3}.

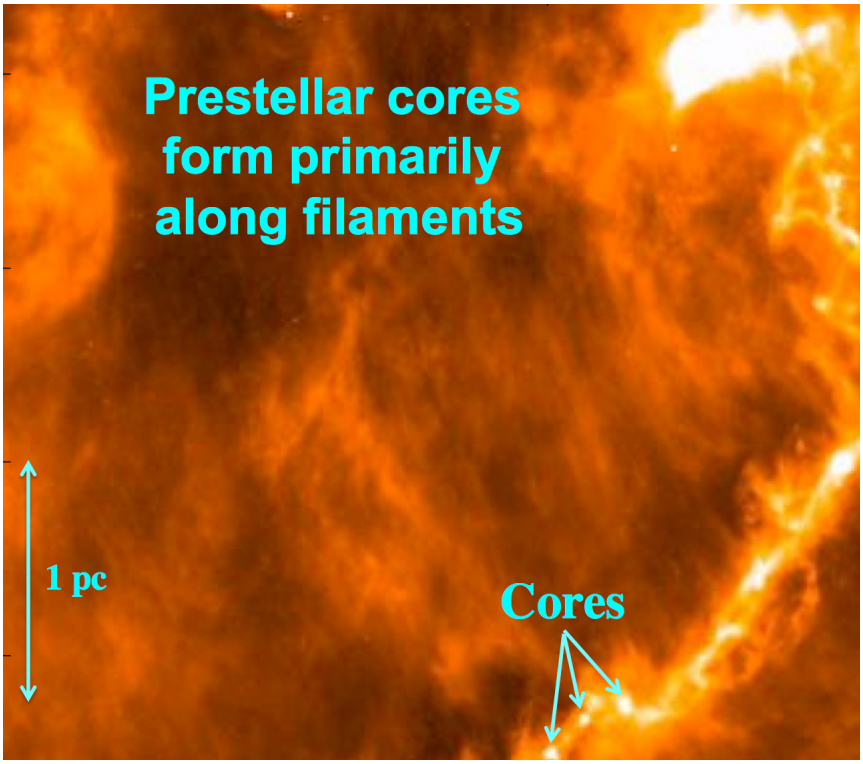

Figure 1.2: Taurus B211/3 filament detected by SPIRE at 250 μm . Image adapted from **?**.

The different protostar evolutionary stages were reviewed by Dunham et al. (2014) based on *Spitzer* and *Herschel* observations at the Protostars and Planets IV conference held in Heidelberg on 16th July 2013. We describe them in the next section.

1.1 Classification of protostars

The two targets from this study OMC-2 FIR 3 and FIR 4 are protostars in different evolutionary stages. We consider appropriate to add some information about these stages.

The formation of a star and its planets, as shown in Fig. 1.3 taken from Greene (2001), start from a giant molecular cloud that fragments into dense cores which collapse (images *a* to *b*). As a result a protostar is generated (image *c*) which evolves over time to the main sequence phase, first by ejecting the envelope at the T Tauri phase and evolving its disk to debris disk from where planets may form.

Our work focuses on two objects in the protostar phase (image *c*) which are embedded in the infalling material from their envelopes (of 5000 AU), and accreting mass onto their disks, part of which could be released as bipolar outflows.

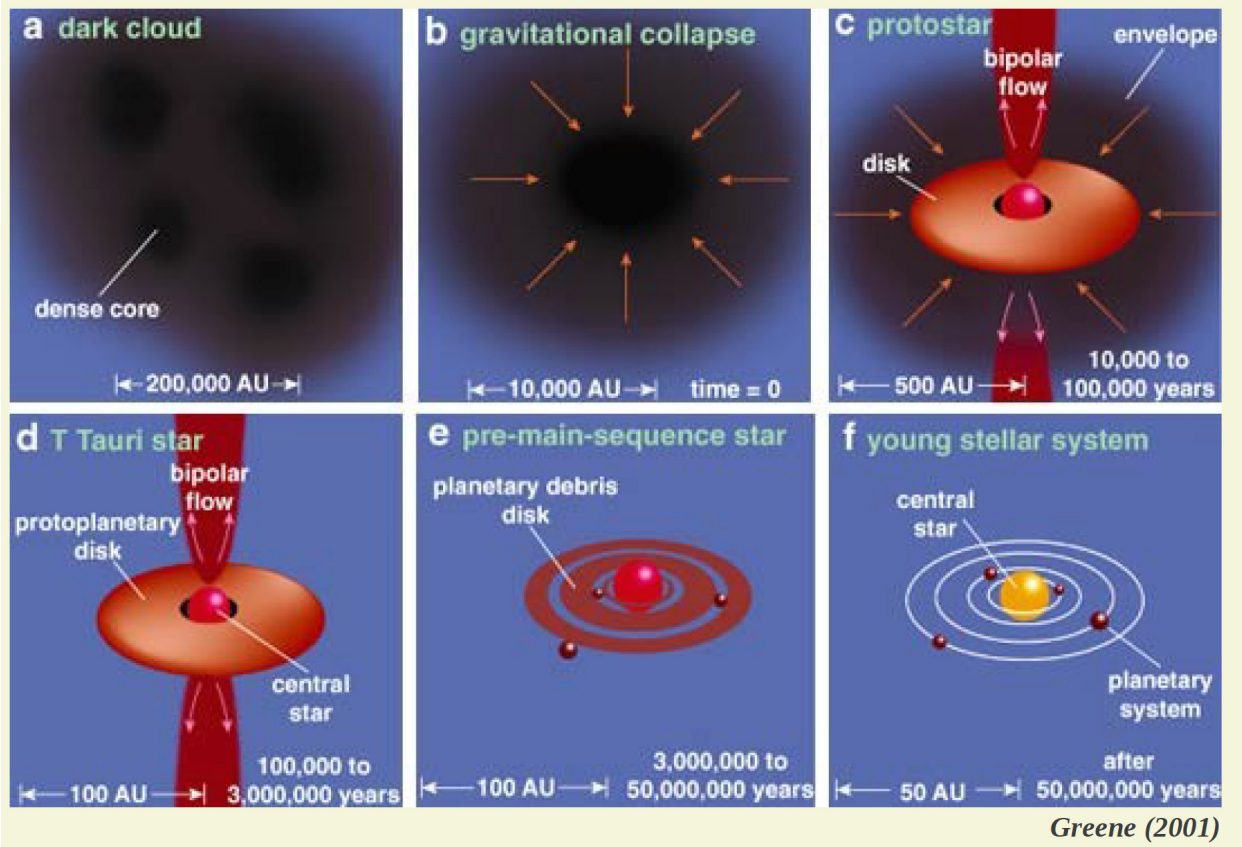

Figure 1.3: Overview of star and planet formation. Taken from (Greene 2001).

Lada & Wilking (1984) and Lada et al. (1987) formulated a classification of young stellar objects (YSO) from an analysis of the morphology from the 1-100 μm spectral energy distributions (SED) of the core of the ρ Ophiuchi dark cloud. Greene et al. (1994) added a fourth class, named "flat-SED", and Andre et al. (1993) identified a fifth class called Class 0. Fig. 1.4 shows the different spectral energy distribution for the protostar phase. Therefore, the complete classification of YSO, ordered in evolutionary stages is :

- **Class 0:** 0.5 % of luminosity emitted in the SED peaks for $\lambda \geq 350$ μm .
- **Class I:** $\alpha_{IR} \geq 0.3$, (α_{IR} is the spectral index)
- **Flat-SED:** $0.3 < \alpha_{IR} < -0.3$
- **Class II:** $-1.6 < \alpha_{IR} < -0.3$,
- **Class III:** $\alpha_{IR} < -1.6$,

Class I objects have large IR excesses associated with thermal emission from dust in large circumstellar envelopes. They are considered to be evolved protostars of 1-2 $\times$ 10^5 yr (Barsony & Kenyon 1992; Greene et al. 1994; Kenyon & Hartmann 1995) surrounded by a disk and a circumstellar envelope ($\geq$ 0.1 - 0.3 $M_{\odot}$). Much lower IR excesses are detected in Class II and even less in Class III objects, which are also called "weak" and "classical" T Tauri stars. They are surrounded by a disk, optically thin in Class II and and optically

thick in Class III. Neither Class II nor Class III have a dense circumstellar envelope. To identify Class 0 objects require indirect measurements, such as detection of a compact radio continuum emission, a collimated CO outflow, or an internal heating source. Their spectral energy distribution emulates a black body of 15-30 K, which traces the dust from the circumstellar envelope instead of the disk. Class 0 objects can also be identified for the submillimeter-to-bolometric luminosities ratio ($\sim L_{smm}/L_{bol}$) ≥ 0.05.

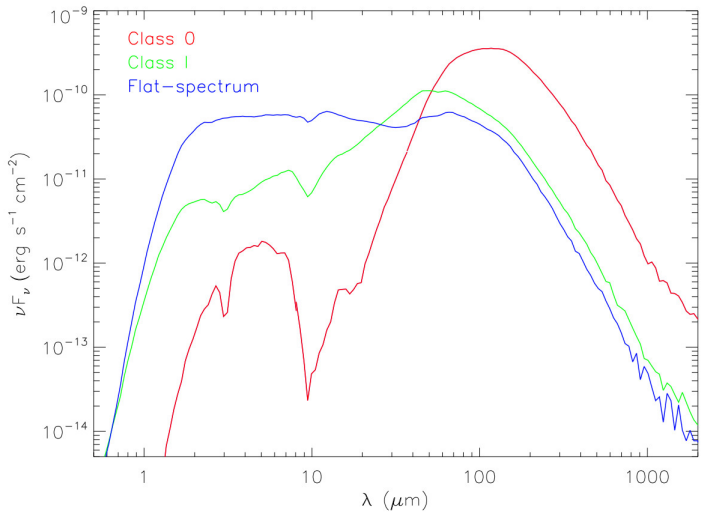

Figure 1.4: Classification of the protostars based on the SED distribution. Image adapted from Furlan et al (2015).

A protostar could be a Class 0 object, a Class I object or a Flat spectrum object (see Fig. 1.4). Inclination with respect to the line of sight may affect the proper classification of the source, as a Class I object could look like a Class 0 object when observed at high inclinations because of the extinction (Ercolano & Koepferl 2014).

Bontemps et al. (1996) found that outflows from Class 0 objects are an order of magnitude stronger than those from Class I, but recent findings from Manoj et al. (2013) find no difference in the CO luminosity once the dependence with the bolometric luminosity is accounted.

Other ways to classify YSOs are based on the circumstellar mass ($M_{c\star} = M_{env} + M_{disk}$), which is dominated by the mass from the envelope (M_{env}) for Class 0/Class I types and decreasing by a factor of 5-10 on average from one YSO type to the other (Terebey et al. 1993; Andre et al. 2000). In similar lines, Saraceno et al. (1996) proposed classification by diagrams (L_{smm} - L_{bol}); (M_{env} - L_{bol}) or T_{bol} diagrams, as shown in Fig. 1.5. A Class 0 object has $T_{bol} < 70$ K, a Class I object 70 K $< T_{bol} <$ 650 K, and a Class II object 650 K $< T_{bol} <$ 2800 K (Chen et al. 1995).

In general, both Class 0 and Class I YSO are within a dense *envelope+disk* system, very well detected in the far-IR continuum, where the optical and near-IR emission from the *star+disk* system are absorbed and re-emited in the far-infrared by the envelope. Therefore, at far-infrared and submilimeter wavelengths, when the medium is optically thin,

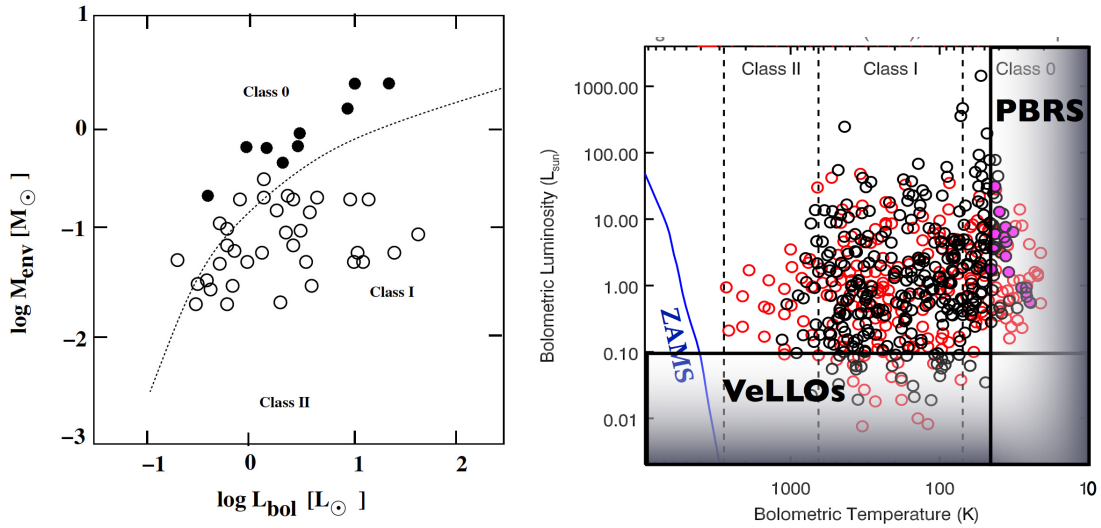

Figure 1.5: Classification of the protostars based on *(left)* the envelope mass of the protostar and (*right*) based on the bolometric temperature and L_{smm}/L_{bol}. (*Left*) image taken from Schulz et al (2005) and (*right*) image he talk given by Michel Dunham and Amelia Stutz at the meeting Protostars and Planets VI, Heidelberg, July 15-20, 2013.

where the different type of objects can be better differentiated. From the analysis performed by Dunham et al. (2014), there is a 81% of agreement on the classification assignments when using the T_{bol} and the L_{smm}/L_{bol} diagrams.

Many surveys to spectrally characterise YSOs have been carried out by the Spitzer telescope in the 3-160μm range: i.e. Werner et al. (2004); Evans et al. (2003, 2009) who studied ~100 isolated dense cores in seven large nearby molecular clouds, Dunham et al. (2013), who covered eleven additional nearby clouds, and the Spitzer surveys of Orion (Megeath et al. 2012) and Taurus (Rebull et al. 2010). Also recent surveys carried out by the Herschel satellite (Pilbratt et al. 2010) in the 55-670 μm range, such as those of André et al. (2010); Fischer et al. (2013); Manoj et al. (2013); Stutz et al. (2013). From all of these surveys we know better now the characteristics of the different protostar phases and also are aware of new classes such as Very Low Luminosity Objects (VeLLOs) (Dunham et al. 2008) and the PACS Bright Red Sources (PBRS) Stutz et al. (2013), these last one detected by Herschel/PACS by first time. Their SEDs and location at the L_{bol} vs/ T_{bol} diagrams can be seen in Fig. 1.6.

The Evolution of the SED during the evolution of the protostar is shown at Fig. 1.7 and 1.8.

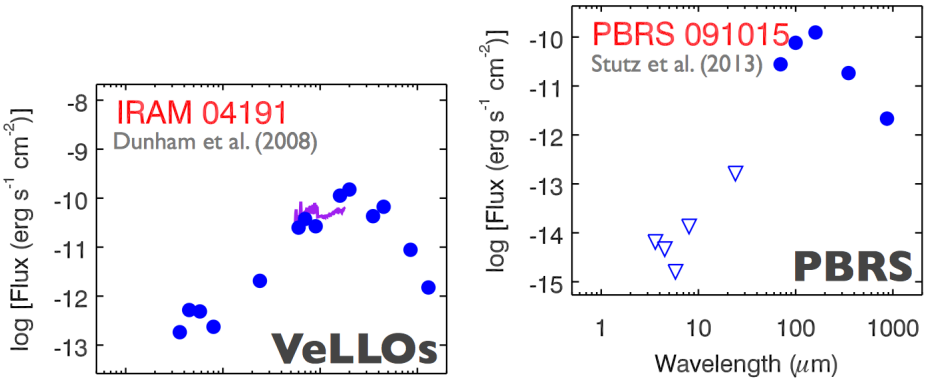

Figure 1.6: Spectral energy distribution of protostars identified as VELLOs and PBRs and their location in the L_{bol} vs. T_{bol} diagrams. Figures from the talk given by Michel Dunham and Amelia Stutz at the meeting Protostars and Planets VI, Heidelberg, July 15-20, 2013.

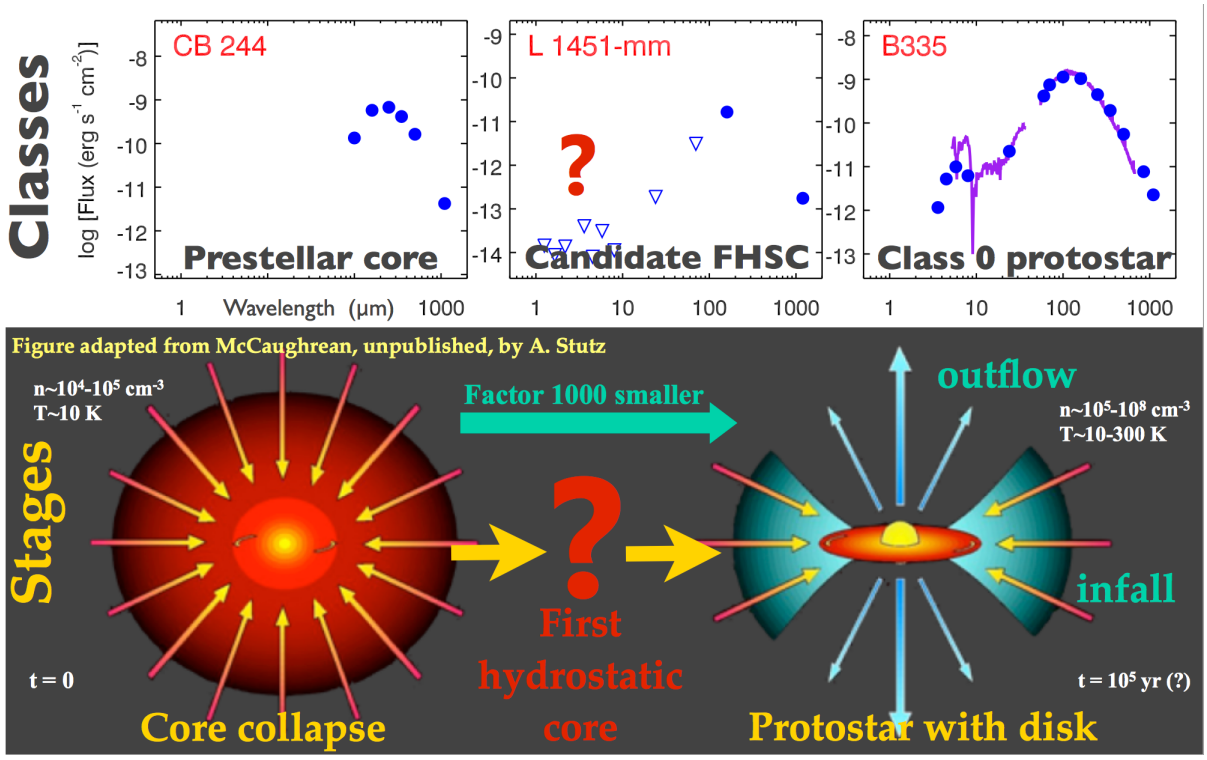

Figure 1.7: Evolution of protostars from Prestellar core to Class 0 protostar. Image collected from the talk given by Michel Dunham and Amelia Stutz at the meeting Protostars and Planets VI, Heidelberg, July 15-20, 2013

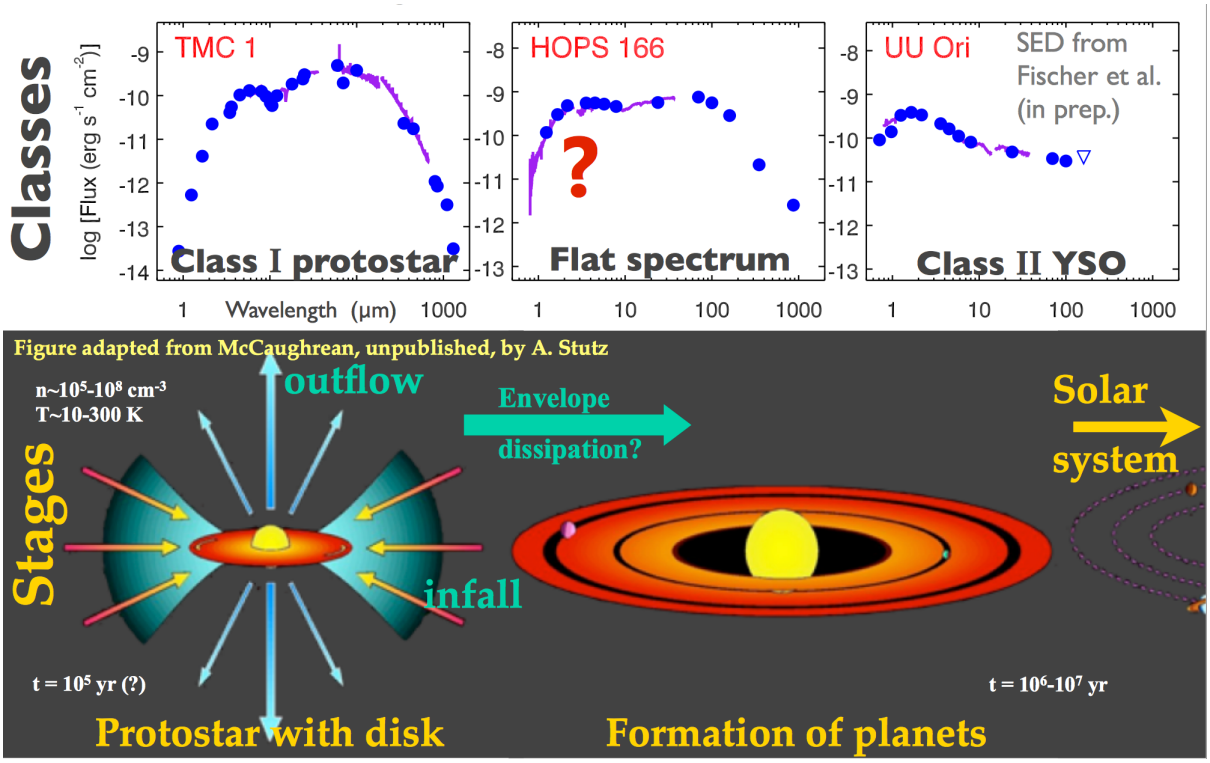

Figure 1.8: Evolution of protostars from Class I protostar to star in the PMS . Image collected from the talk given by Michel Dunham and Amelia Stutz at the meeting Protostars and Planets VI, Heidelberg, July 15-20, 2013.

1.2 Outflows and Jets

One of the targets in this study OMC-2 FIR 3 is driving a jet/outflow. For that reason here we introduce some information about jets/outflows.

Mass ejections in the form of outflows and jets may occur at various stages of star formation, as a response to the infalling material from the envelope onto a protostar.

During the protostar phase, as a result of the rotation of the molecular cloud as it collapses, a disk is formed around the protostar, perpendicular to the rotation axis. Part of the infalling material shocks with the disk and is ejected almost perpendicular to the disk, in both directions. The models that best explain this ejection consider the existence of magnetic fields close to the rotational direction, which together with the centrifugal force launches the mass along the rotational axis. The magnetic field makes the system lose angular momentum, helping the formation of the star (otherwise it will be destroyed by the centrifugal forces at a fast rotating speed). Therefore the presence of outflows over various evolutionary stages is a key component for the star formation process to stay alive.

Infall and outflow processes are connected, where a stronger outflow is a result of a larger infall rate. Magnetic fields can only have an impact if there is ionised material, even for a small (1 to 10 %, Anglada et al. 1998) ionisation fraction. The magnetic fields sweep the ions along and these, by friction, move the rest of the material away.

There are different ways of detecting YSO outflows. They can be detected by detailed images or by their spectroscopy signature at optical or radio wavelengths, each regime tracing different physical conditions, densities and temperatures along the outflow. Outflows originating at the disk or close to the star eject material which has a neutral component (atomic and molecular gas) and an ionised component, and is also called *jet* that moves at very high velocity ($\geq$ 100 km/s) and is highly collimated.

The outflow sweeps up the ambient molecular cloud which moves much slowly ($\sim$ 10 km/s) than the jet. This material is also much colder ($\sim$ 10 K) that the outflow close to the disk and could be traced by low CO transitions CO (1-0) and CO (2-1) and other molecules. This material could keep being collimated (but not so strongly as the jet), and it is known as a *molecular outflow*.

In high resolution spectra of lines such as CO, the *molecular outflow* velocities can be detected by the *wings* being shifted to the red or to the blue, with respect to the systemic velocity, depending on the orientation of the outflow, as shown in Fig. 1.9.

If there is not enough angular resolution to identify whether the red or blue emission come from different regions, we could infer that there is an outflow just by checking whether the spectra have *wings*.

The *jet* is the material ejected directly from the disk which needs to be slightly ionised (1-10 %) and could be detected for emitting recombination lines (such as H_α) or forbidden lines ([SII], [OIII], ...).

In radio frequencies, *jets* emit through the free-free emission as a continuum (which is the

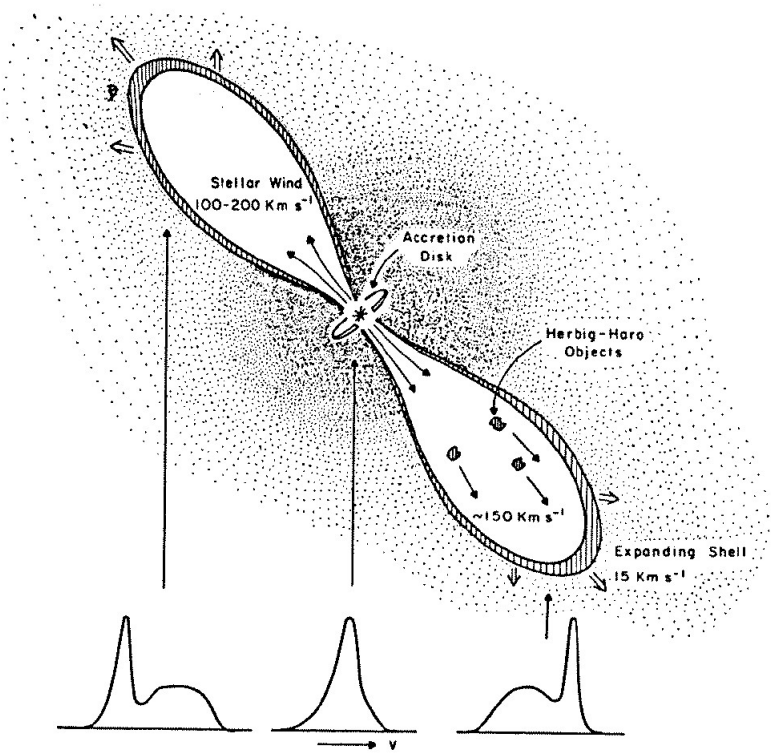

Figure 1.9: Bipolar molecular outflow cartoon from Snell et al. (1980) taken from Guillem Anglada (1996).

dominant emission components at these long wavelengths). This emission is similar to that of HII regions but the ionisation mechanism can not be the same. The photoionisation observed in the HII region is caused by UV photons emitted by a close massive star, but the radio jets are observed originating from protostars of very low luminosity, which are unable to produce sufficient UV photons in the gas. Therefore, it is considered that the shocks associated to the jet, which could be internal shocks in the jet and shocks within the ambient media, produce the ionisation.

When a *jet* is observed at optical ranges, usually only the blue shifted outflow is detected, because the red part travels through the embedded cloud of dust and gas and is obscured by extinction. As radio wavelengths do not suffer from extinction, both parts of the radio jet can be observed and they are collimated and bipolar.

Therefore optical and radio observations from a jet are complementary as they observe different regions from the same jet. Optical observations show farther positions (epochs) from the jet and radio observations the closest (youngest) to the protostar, which are highly affected by extinction due to the high dust density of the envelope or due to its surrounding disk.

Jets also have a neutral atomic component, that can be seen as line emission of HI at 21 cm, which is very difficult to observe and a molecular component detectable through

vibrational excited hydrogen lines at 2μm . These molecular transitions require temperatures higher than 1000 K, which can be found in strong jet shocks.

Jets have also been observed in the CO emission lines and other molecules, from the external region of the gas moving at low velocities (the ambient gas swept up) and an internal region, closer to the axis where the velocities are high and with a higher collimation (the *jet* itself). CO (2-1) maps tends to trace cold gas, and the foreground the ambient gas from the swept-up, but CO (6-5) maps trace both the molecular outflow (at lower velocities) and the jet (at high velocities).

Herbig Haro objects (HH objects) were discovered in molecular outflows in the fifties (Haro & Herbig 1955). They were detected as moving objects, some 0.1-1 pc from the central star, and were detected via forbidden lines (see Fig 1.10). Simulations of those lines suggested these were caused by shocks. Also X-ray detections of HH objects, such as HH 248, have been deeply studied (Bonito et al. 2010; López-Santiago et al. 2015).

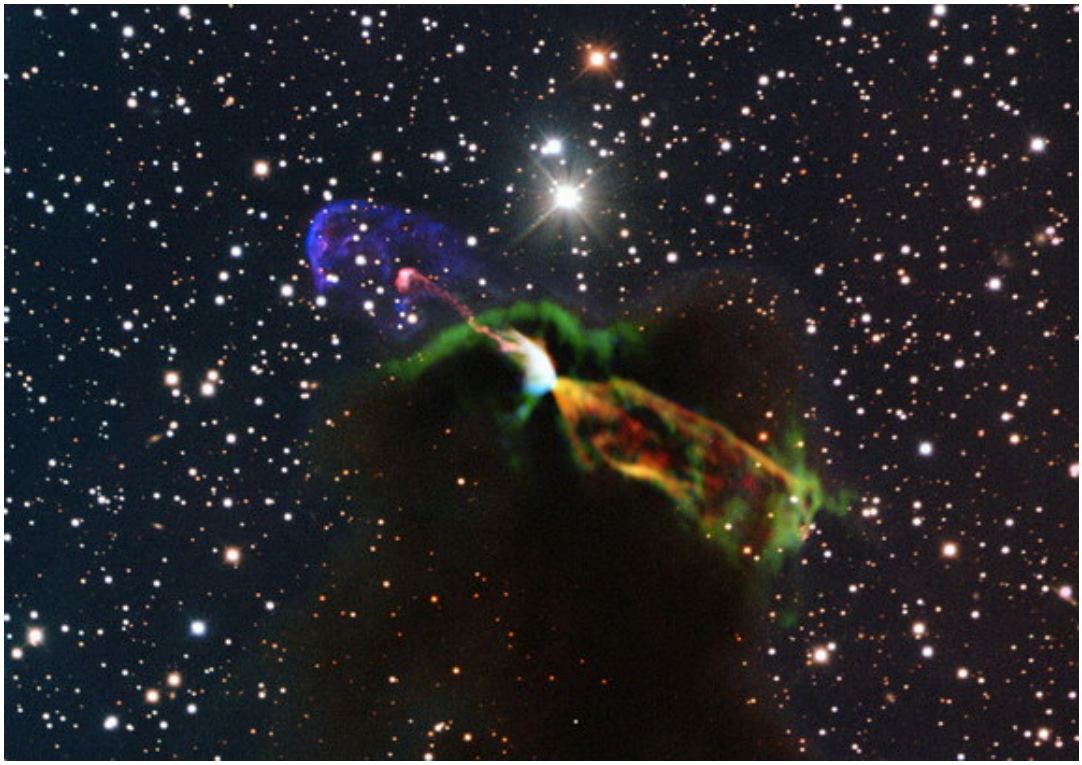

Figure 1.10: This image of the Herbig-Haro Object HH 46/47 is a composition of radio observations (Atacama Large Millimeter/submillimeter Array) combined with visible observations (ESO's New Technology Telescope). The ALMA observations (lower right in orange and green) revealed a large energetic jet, driven by a new born star, moving away from us. This emission is not detected in the visible range as is hidden by the dust and gas in the region. ESO NNT observations (upper left in pink and purple) shows the visible part of the jet, streaming partly toward us .Image adapted from http://www.space.com/22428-amazing-star-birth-photos-alma-telescope.html

Outflow typical velocities are of the order of 5-10 km/s, meanwhile typical jet velocities are of the order of 100 km/s. For collimated emission in the plane of the sky the velocities are higher than the observed.

Most Class 0 protostars drive powerful "jet-like" CO molecular outflows, (Bachiller 1996) with mechanical luminosities of the same order as the bolometric luminosities of the central source (Curiel et al. 1990; Andre et al. 1993). Usually Class I outflows are less powerful and collimated than Class 0 jets.

Outflows from low-mass protostars are generally very supersonic, and low in density, compared to their surroundings. Usually the interaction of the outflow with its surroundings takes the following form: on its first encounter, the outflow is decelerated supersonically to a much lower speed, while the swept-up ambient material is accelerated, also supersonically; energy and momentum are conserved in the process. This produces a *double-shock* structure as seen in Fig. 1.11: the wind shock, essentially always a dissociative *J-type shock* in which the outflow decelerates; the cloud shock, usually a non-dissociative, magnetic *C-type shock* in which the ambient material accelerates; and the two post-shock cooling regions in-between. The whole structure moves away from the outflow source, at a speed slow compared to the outflow speed (momentum conservation again). This is described in many papers by Draine (1980); Hollenbach & McKee (1989); Neufeld & Dalgarno (1989); Flower & Pineau des Forets (1995); Kaufman & Neufeld (1996); Neufeld et al. (2006). We detect as part of this thesis work a jet in [O I], which trace the post-wind-shock gas.

The far end of an outflow is not the only place where the outflow interacts with the ambient material. The sides of a not-perfectly-collimated outflow also lead to shocks: although there the outflow is incident obliquely on the ambient for some angle close to 90 degrees, is often still highly supersonic (Hartigan et al. 1995; Cohen et al. 1988). This is why one can see the jets as well as the Mach disks at their ends: the jet surfaces are lit up by oblique shocks.

Reflection of shocks from the jet-ambient density jump, or from an unsteady speed of ejection of the outflow, also leads to internal shocks within the outflow. These usually produce a small fraction of the cooling emission which could be neglected to the first order (Hartigan et al. 1995; Cohen et al. 1988) . The more famous parsec-long jets (e.g: HH 111) with multiple HH objects along their length provide some obvious exceptions, but most jets and shocks are as HH 30.

The outflow from a protostar decelerates as it encounters more and more ambient material. The deceleration is generally supersonic and takes the form of a J-type shock (hydrodynamic, dissociative, non-magnetic): one in which there is a discontinuity in the fluid parameters, and for which the fluid parameters on each side of the discontinuity are related by the Rankine-Hugoniot *jump conditions* (Hollenbach 1985; Hollenbach & McKee 1989). The peak temperatures in post-shock gas can be greater than 5000 K (any outflow speed > 17 km/s will do), and [O I] 63.2 μm heavily dominates the cooling below 5000 K. So the intensity of [O I] is related to the flux of atoms crossing the shock front: each of them brings its thermal energy to the T = 5000 K point in the postshock column, and all of this energy is radiated as [O I] photons (see Appendix A for more information on the mass-loss rates calculations from the [O I] luminosity).

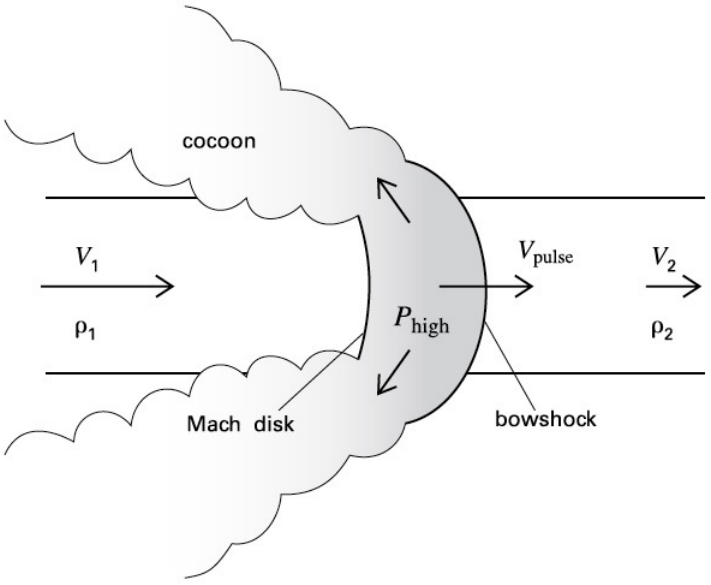

Figure 1.11: Structure of the working surface in a variable jet (schematic). Gas of density ρ_1 and speed V_1, emitted by a star on the left, encounters a flow with density ρ_2 and lower speed V_2. The large value of pressure P_{high} in the intershock region expels material into the cocoon. Both the Mach disk and the bowshock travel at the speed V_{pulse}, intermediate between V_1 and V_2. Image from Stahler & Palla (2005).

1.3 Tracers of star formation regions

In this work we detect for the OMC-2 region emission lines of hyperfine structures ([O I], [O III], and [C II]) and in the CO, H_2O and OH molecular lines, which act as the main coolants in the accretion shocks. For this reason here we add what can be useful information for the reader.

As of today, more than 180 molecules have been detected in the interstellar medium or circumstellar shells (http://www.astro.uni-koeln.de/cdms/molecules).

The star-formation environments are a mix of gas and dust clouds where molecules, atoms and ionised material coexists with magnetic fields, turbulences and gravity. External impact from cosmic rays, external radiation fields from close bright stars and shocks add even more complexity to these regions, where the newly born stars eject outflows and radiation to the environment (Schulz 2005).

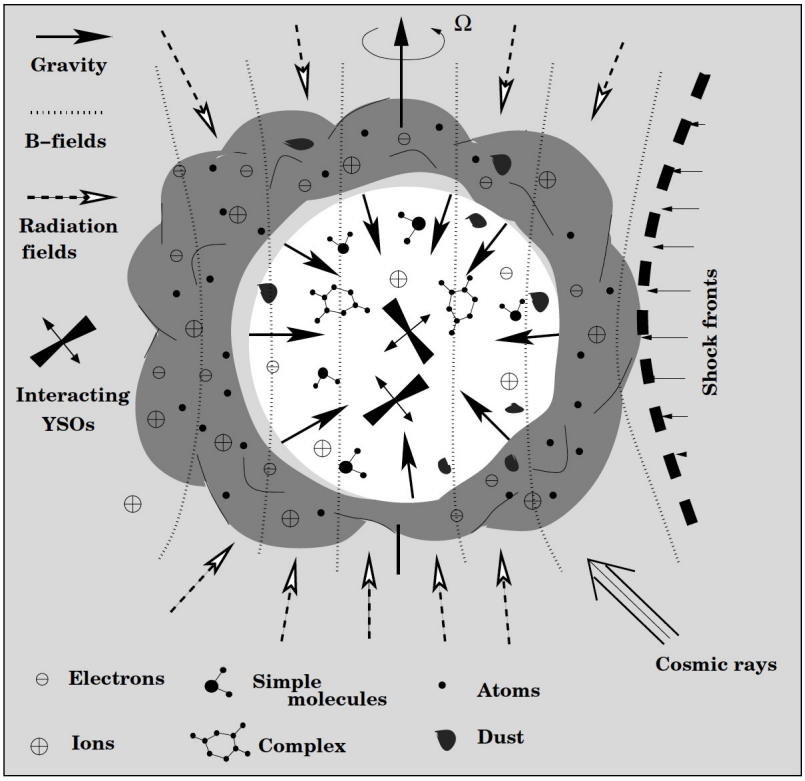

Figure 1.12: Star-forming regions tracers. Image adapted from the Schulz (2005).

Molecules, such as H_2, CO, H_2O , can be excited rotationally, vibrationally, or electronically by collisions with other H_2 molecules, or radiatively by the high temperatures that occur in shocks. These molecules tend to achieve a lower energetic level for which radiative transitions occur, cooling the material in the process by releasing photons. At the low temperatures of the molecular clouds only rotational transitions (the ones that require less energy to be excited) occur. The rotational transitions are characterised by a quantum momentum (*J*), which is the quantum number of the upper state in the transition. These rotational transitions are radiative transitions (emit a photon), and are only permitted between a level *J* and a level *J - 1* (Krumholz 2011).

Hydrogen is a the most abundant element. In the atomic state, the hydrogen has a transition at 21 cm (1.4 GHz) with an associated energy lower than 1 K, therefore it can be excited in cold regions (such as molecular clouds). This transition is detected in the Milky Way and nearby galaxies (Krumholz 2011). However, at high densities, similar to those where stars form, hydrogen should be found in molecular state (H_2). The lowest energetic rotational transition for H_2 requires an excitation of the molecule involving an energy of the upper level of 510 K (*J*= 2-0). The reason for this high energy value is because H_2 is a light species and the energy is related with the mass by $E \sim m^{-1/2}$. In the ISM, where the temperatures are of the order of ~10 K, the rate of molecules in state J = 2 is given by $\sim e^{-10/500} \approx 10^{-22}$. In order words, in molecular clouds there are no H_2 molecules capable of emitting (Krumholz 2011) and we can not observe them via H_2 molecules, so we have to resort to other species.

CO is the most abundant molecule in space after H_2. The CO molecule is more massive than H_2 and its lowest rotational transition at an energy of ~ 5.5 K above its ground state, therefore low enough to be excited at the low temperatures of molecular clouds. The molecule ^{12}CO is optically thin at densities lower than 10^3 cm^{-3} and when it becomes optically thick, ^{13}CO can be used to derive the physical conditions of the cloud.

CO, in the molecular clouds, are optically thick at infrared wavelengths at low J, where the levels are most populated, and optically thin at high J levels, less populated. The reason is that for a rotational transition (e.g., $J = 1 \rightarrow 0$), the photon emitted is more likely to be absorbed by a particle from the $J = 0$ level to populate again the J =1 than escaping the cloud and be detected. Therefore this transition ($J = 1 \rightarrow 0$) is optically thick. Therefore the cooling is dominated by the lowest J level which is not optically thick (Krumholz 2011). CO J =1-0 is used to trace molecular clouds at radio wavelengths, being one of the main components of the molecular clouds in the Milky Way.

Fine-structure lines are generated by magnetic dipole transitions within multiplets (Watson 1985). They have very low probability to occur compared to other species (CO, H_2O) but from a very low density medium ($n \leq 10^5$ cm^{-3}) they can be detected. The detection of these fine-structure lines became possible recently, since the development of high-altitude telescopes such as the Kuiper Airbone Observatory (Storey et al. 1979) or spacecraft telescopes. In neutral regions, such as molecular clouds, the most important lines detected in the far-infrared are [C II] at 157 μm, [C I] at 609 and 370 μm, [Si I] at 129 and 68 μm, [O I] at 63 and 145 μm. In ionised regions, the fine-structure fine infrared-lines detectable are [N II] at 203 at 121 μm and [O III] at 88 μm (Watson 1985).

An example of their detection in the Galactic Center region is shown in Fig. 1.13.

Dinerstein (1995) determined that the infrared lines are relatively insensitive to changes of electron temperature (T_e, see Appendix C for explanation). T_e diagnostics can be computed by comparison of low-energy levels to high-energy levels. In regions where there are no optical or ultraviolet lines detected, such as in molecular clouds, one can use infrared line ratios in certain regimes, i.e: [O I] 63 to 145 μm at T$\leq$ 500 K. Given that infrared lines are strongly affected by collisions at low densities, their dependence with density (n) and temperature (T) is often difficult to separate. It is necessary therefore to compare at least two line ratios from one ion to derive reliable temperature constrains (Keenan et al. 1991) or from several species, assuming a value of their relative abundances, as explained in (Watson 1985; Tielens & Hollenbach 1985). Watson and Tielens constrained the density (n) and the temperature (T) in photodissociation regions (PDRs) by measuring the line ratios of [O I] 63 to 145 μm and [O I] 63 to [C II] 157 μm .

As already mentioned previously, accretion shocks in protostars occur due to the supersonicaly free-falling material from the envelope onto the disk and due to bipolar jets injecting material into the ambient cloud at supersonic speed. In the first case the shocks are *J, for jump, type* (Neufeld & Dalgarno 1989) and in the second case *C, for continuum, type* (Kaufman & Neufeld 1996) shocks. The heating of the cavity walls by the UV-radiation from the protostar can also produce molecular lines (Spaans et al. 1995). The FUV field produced in regions behind the J- shocks can induce photodissociation regions (PDRs) in

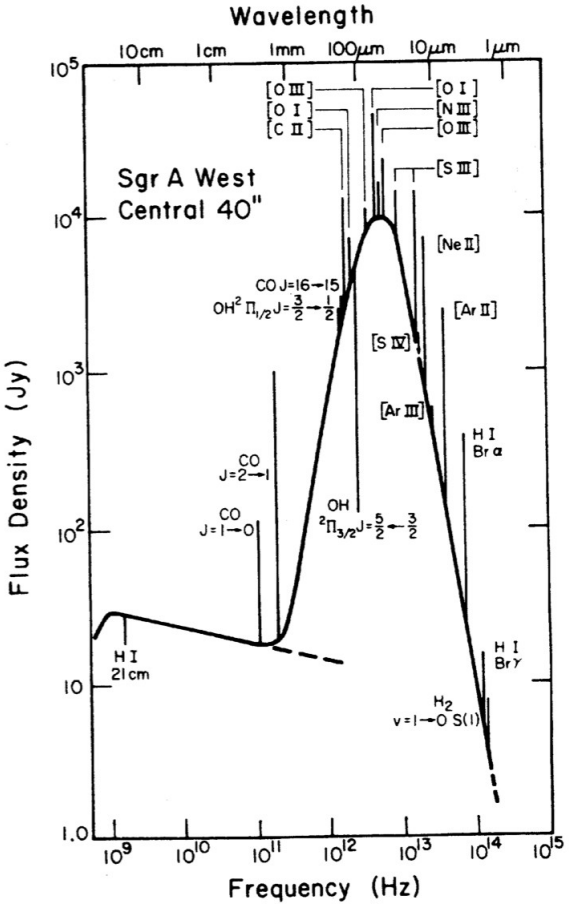

Figure 1.13: The spectrum of the Galactic Center region, Sgr A West. Image adapted from Watson (1985)

the flow cavity walls, e.g. (Molinari & Noriega-Crespo 2002).

The primary coolants of the post-shocked gas are atomic fine structure lines and molecular lines in the far infrared ($\lambda \geq 50\mu$m), such as [O I] at 63.18 μm and 145.57 μm for the *J-type* shocks and CO and H_2O for the *C-type* shocks (Hollenbach & McKee 1989; Kaufman & Neufeld 1996). These ionic and atomic fine structure lines and the molecular lines in the mid- and far-IR wavelengths are powerful diagnostics of the density, temperature, velocity fields and elemental abundance and extent of the emitting region (Watson 1985).

Molecular lines provide information of the density and temperature of the medium (Evans 1999) and kinematics (Ohashi et al. 1999). These results help to refine the continuum measurements, which trace the dust and are affected by uncertainties due to poorly understood properties (coagulation degree, thickness of ice mantles); Ossenkopf & Henning (1994); Bianchi et al. (2003); Evans et al. (2001). As shown in Fig. 1.14, different molecules are identified in different locations of a protostar, as different phenomena take place there. Jets can be traced by [OI] at 63 and 145 microns (Hollenbach & McKee 1989). The shocks between the outflows and the surrounded quiescent material can be studied in emission lines (gas) of H_2 in the near- and mid-infrared (Beckwith et al. 1983)

and CO and OH lines in the far-infrared wavelengths(Watson et al. 1985; Storey et al. 1981). As the CO far-infrared lines are density sensitive, from their analysis one can be extract shock's compression ratio information.

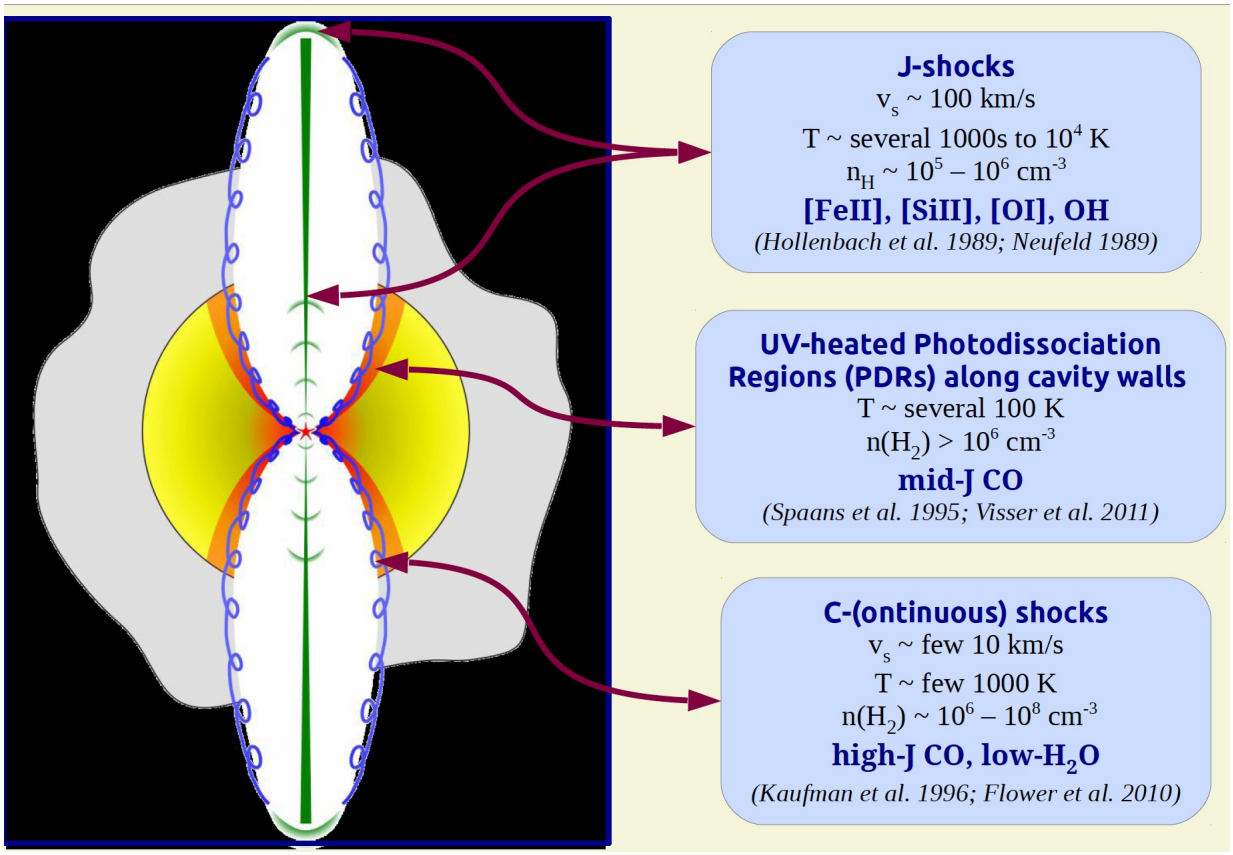

Figure 1.14: Detection of molecules in the different positions of the protostar. Image taken from van Dishoeck et al. (2011)

Stars are formed in pre-stellar cores with very low temperatures (~ 10 K) and high central densities (~ 10^5 cm^{-3}) (Stahler & Palla 2005; Hartmann 2009). At this temperature most of the gas species freeze-out onto dust grains, and so a depletion of CO from the gas phase has been observed (Caselli et al. 1999; Bergin et al. 2001; Tafalla et al. 2004).

In the protostar phase, the infalling material from the envelope falls onto the disk with supersonic velocities where a disk shock decelerates its speed to 2-3 km/s. This jump in conditions is traced by the called *J-type* shocks, (Neufeld & Hollenbach 1994) which compres the material and heat the envelope material before falling onto the disk. The cooling processes that release this hot postshock gas at the disk surface will emit the ro-vibrational H_2O and OH lines (Neufeld & Hollenbach 1994; Watson et al. 1985, 2007). Watson et al. (2007) detected for the first time H_2O in this "envelope-disk" accretion shock in the Class 0 NGC 1333-IRAS 4B from data obtained with IRS on board the Spitzer satellite.

Jets and outflows inject mass into the molecular cloud during the star-formation process (Bachiller 1996). The hot (T≥ 2000 K) shocked molecular matter associated with them is

detected by the H_2 molecules at near-infrared transitions (Gautier et al. 1976; Beckwith et al. 1983). The width of the molecular lines detected from outflows are of the order of $\sim$ 100 km/s (Zuckerman et al. 1976; Nadeau et al. 1982), and with very high resolution instruments different velocity components were spatially resolved (in the molecular cloud L1551, by Snell et al 1980, and in Orion and IRC +10°216 by Bally et al. 1983). As reported by Watson (1985), during the outflow lifetime, large amounts of energy and momentum may be feed into the surrounding molecular clouds, playing a role in their support against self-gravity (Bally & Lada 1983).

Far ultraviolet radiation originates from supersonic shocks and may generate photo-dissociation regions (PDR) in the flow cavity walls. In *C-type* shocks, the dissociation of molecules (e.g. specially of H_2) does not take place and for that reason the temperatures of the gas is greater than $\sim$ 200 K, most of the oxygen is converted to water by fast endothermic reactions:

$$O + H_2 \rightarrow OH + H$$

$$OH + H_2 \rightarrow H_2O$$

In *C-type* shocks other process have been discovered, e.g. *sputtering* (Flower & Pineau des Forets 1995; Schilke et al. 1997). This process consists of the return of some species to the gas phase as a result of the collisions of ionised particles (dust has negative charge) accelerated by magnetic fields with other molecules (especially H_2 molecules) and among dust grains. This is considered to be the reason for the detection of SiO, H_2O, NH_3 and CH_3OH in protostellar outflows (Bachiller & Pérez Gutiérrez 1997; Jørgensen et al. 2004; Caselli et al. 1997). The cooling of the gas after these species are released tends to be fast (few hundred years) and it is led mainly by H_2, H_2O and CO (Kaufman & Neufeld 1996). These repeated mechanisms of shock plus freeze-out was proposed by Bergin et al. (1999), to explain the high abundance of water in solid form in molecular clouds ($\sim 10^{-4}$ H_2O molecules per H_2 molecule).

1.4 The Orion star-forming region

The OMC-2 region studied at this work is located at the north side of an externes Orion Cloud cluster embedded in a narrow filament of 2 pc long with is leaving the Orion Nebulae Cloud (ONC). For this reason we introduce here the area.

To understand star formation across the different spatial scales and evolutionary stages, it is necessary to understand star formation of protostars, because it is at this phase that the stellar mass is determined and protoplanetary disks are formed.

To build a generally accepted theory about the different processes of star formation, from a protostar deeply embedded in a cloud core to its transition to a pre-main sequence star/disk

system, we need a large sample of young stellar objects. The Spitzer Space telescope has systematically identified a vast number of protostars in molecular clouds in Orion, Perseus, Ophiuchus, Serpens, Chamaleon II and Lupus clouds.

The Orion Molecular cloud is the richest nursery of protostars within 500 pc of the Sun (488 candidates identified by Megeath et al. 2012). They contains protostars for all stages (from Class 0 to Class II), form in all types of environments (from embedded to isolated), and with a large range of luminosities (from 0.1 to 100000 $L_{\odot}$). Fig. 1.15 shows the Orion region observed by the Herschel satellite (PACS and SPIRE), where the dust from the dense clouds is well traced by combining data from XMM-Newton (EPIC), where the brightest targets extinted by these clouds are detected.

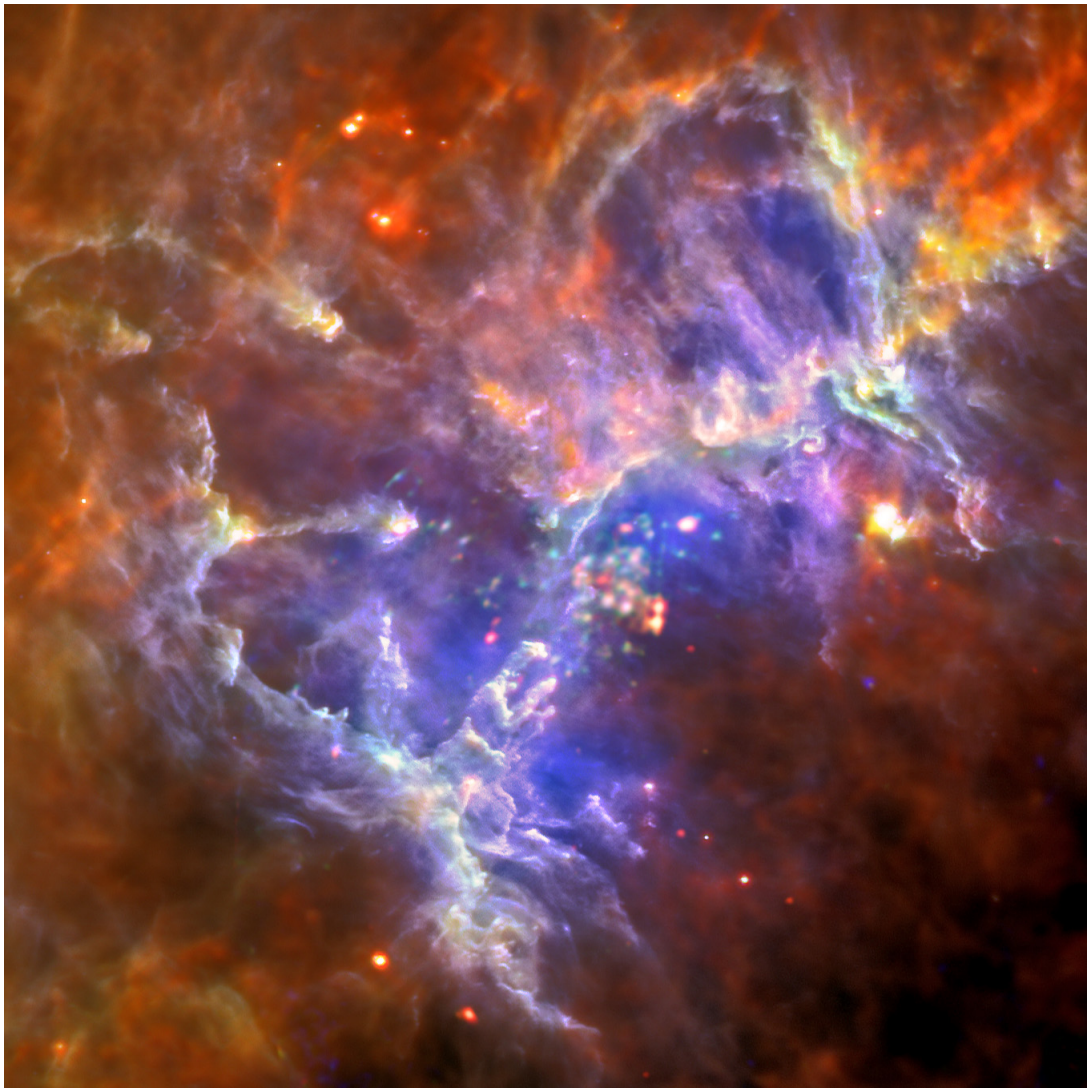

Figure 1.15: The Orion region. Credits: far-infrared: ESA/Herschel/PACS/SPIRE/Hill, Motte, HOBYS Key Programme Consortium; X-ray: ESA/XMM-Newton EPIC/XMM-Newton-SOC/Boulanger.

The Orion complex region is the closest star-forming region where both low and high-

mass star formation is taking place (Bally 2008). In this star-forming region within 12 Myr at least ten thousand of stars belonging to six subgroups and short-life clusters have been generated. Some of the most massive stars died as supernovas generating a super-bubble, and inside are several star-forming regions (Ochsendorf et al. 2015). As shown in Fig. 1.16, the Orion region contains two main regions: Orion A (in the south-west) and Orion B (in the north-east).

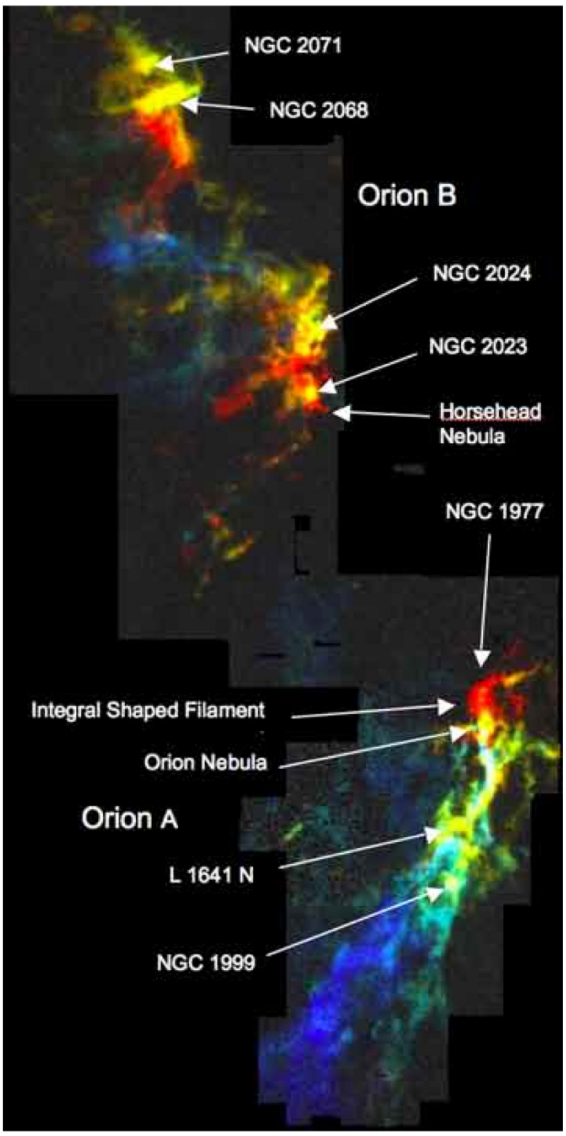

Figure 1.16: CO J=1-0 image showing the Orion A and B clouds using colours to represent Doppler shifts (blue for V_{LSR} = 0 to 5 km/s, green for V_{LSR} = 5 to 10 km/s, and blue for V_{LSR} = 10 to 15 km/s). Data collected with the 7-m radio telescope on Crawford Hill in Holmdel, NJ. (Bally 1989; Bally et al. 2000).

1.4.1 The OMC-2 region

In the OMC-2 region we focused on the intermediate-mass protostars FIR 3 and FIR 4.

The OMC-2 region was detected for the first time by Gatley et al. (1974) as a new ∼1′ region associated with a ∼6′ cloud on the north of an external Orion Cloud cluster embedded in a narrow filament 2 pc long leaving the Orion Nebulae Cloud (ONC). Within this he detected five new infrared sources (∼ 500 $L_{\odot}$) emitting strongly in CO. The OMC-2 region was later widely studied by Johnson et al. (1990); Chini et al. (1997); Reipurth et al. (1999); Carpenter (2000); Peterson & Megeath (2008a); Adams et al. (2012); Manoj et al. (2013); Kama et al. (2013); Furlan et al. (2014); Megeath (2014) as a very active star-forming region of low- and intermediate-mass stars, which contains some of the most luminous far-infrared and submilimeter sources in the Orion A complex region outside from ONC.

FIR 3 was identified by Gatley et al. (1974), and FIR 4 was not identified until Chini et al. (1997) (see Fig. 1.17). They are separated by 20″, corresponding to 8400 AU at the Orion distance (Mezger et al. 1990).

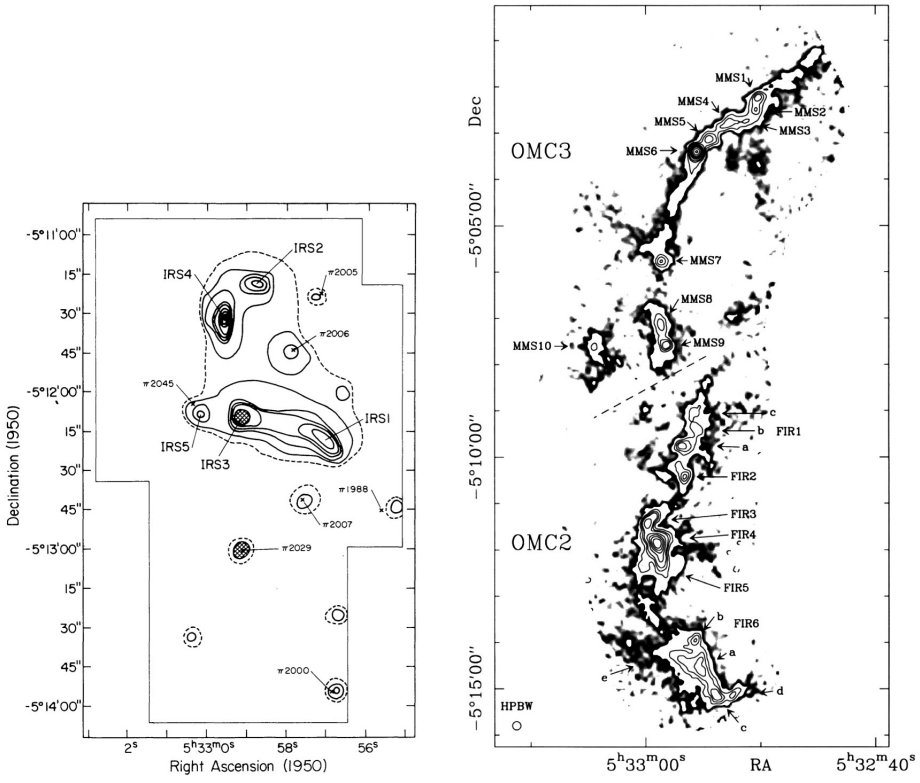

Figure 1.17: (*left*) OMC-2 region observed by Gatley et al. (1974) and (*right*) by Chini et al. (1997).

FIR 3 (also called HOPS370 in this work) was identified as a two-component object by Cohen & Frogel (1977), but could not the resolved until Nielbock et al. (2003). FIR 4 (called HOPS108 in this work) has a large envelope of mass 2.5 to 10 $M_{\odot}$ and dominates

the submillimeter emission in this field.

Furlan et al. (2014) and Furlan et al (2015) analysed the 1.2 to 870 μm spectral energy distribution of FIR 3 and FIR 4 (see chapter 3) by combining near-infrared data from 2MASS, mid- and far-infrared data from Spitzer, Herschel space telescopes and submilimeter photometry from the APEX telescope. Looking at the SEDs of protostellar objects, we can see how the peak of emission in protostars, formed by central protostar, disk and envelope, is at far-infrared wavelengths. The reason behind is that the radiation emitted at short wavelengths by the central protostar and by the the accretion shocks from envelope material that falls onto the disk and is accreted by the central object, are absorbed and re-emitted by the dust in the disk and envelope. Younger objects (HOPS108) are more embedded, showing only a single and strong peak at 100 μm which provide high submilimeter luminosities (Enoch et al. 2009; Stutz et al. 2013). The SED also show at absorption features at 10 and 18 μm and some at other wavelengths, caused by the material along the line of sight, mainly sub-μm -sized silicate grains and ices (Boogert et al. 2008; Pontoppidan et al. 2008), which are stronger for more embedded objects (HOPS 108).

From Furlan et al. (2014), HOPS 108 (FIR 4) was classified as a Class 0 object with bolometric luminosity $L_{bol} \sim 38\ L_{\odot}$ and bolometric temperature $T_{bol} \sim 38$ K. The total luminosity is considered to be $\sim 400\ L_{\odot}$ and the envelope material 0.8 $M_{\odot}$. This object is considered to be very embedded with an extinction $A_v \sim 19$ mag.

However HOPS 370 (FIR 3) was classified as a Class I object with bolometric luminosity $L_{bol} \sim 360\ L_{\odot}$ and bolometric temperature $T_{bol} \sim 72$ K. The total luminosity is considered to be $\sim 550\ L_{\odot}$ and the envelope material 0.1 $M_{\odot}$ .This object is considered to be less embedded, with $A_v \sim 2$ mag. For both, the inclinations are close to face-on.

Furlan et al. (2014), shows the OMC-2 region imaged with Spitzer, Herschel and APEX with FIR 3 and FIR 4 marked with green crosses (see Fig 1.18. The position of FIR 3 (top) corresponds to the position of SOF 2N in Adams et al. (2012), and the position of FIR 4 has its peak over 8 to 70 μm. In this figure we see how for FIR 4, the peak emission at 160 μm and longer wavelengths is shifted to the south-west, most probably tracing the original cold dust and gas cloud from where this source is forming.

Observations in the far-infrared (Manoj et al. 2013; Kama et al. 2013) and centimetre wavelengths, (Reipurth et al.1999 and Osorio et al, in preparation) show that FIR4 exhibits a radio jet signature. Whether it is generated by OMC-2 FIR 4 or FIR 3 is one of our major subjects of investigation in this work.

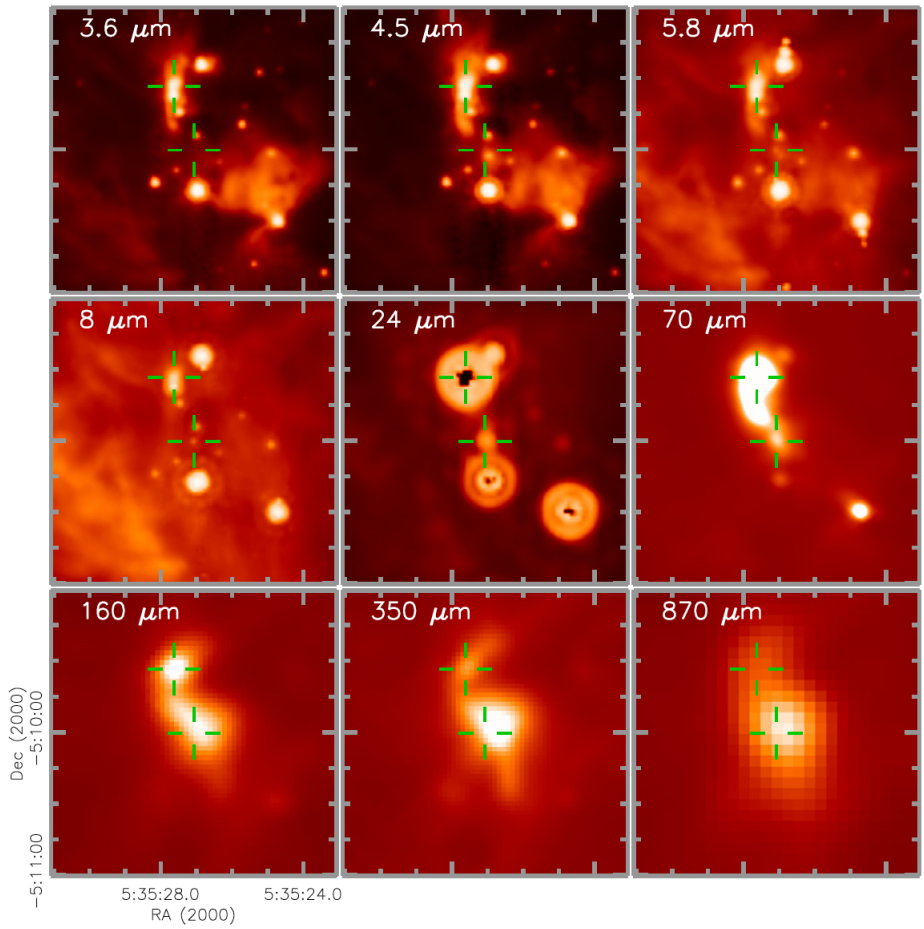

Figure 1.18: Combination of Spitzer and Herschel images of the OMC-2 region taken from Furlan et al. (2014). IRAC 3.6, 4.5, 5.8, and 8.0 μm, MIPS 24 μm, PACS 70 and 160 ,μm SABOCA 350 μm, and LABOCA 870 μm images of the region around OMC-2 FIR 4 (SOF 3, HOPS 108). At 24 μm the saturated sources to the north, south, and southwest are OMC-2 FIR 3 (SOF 2N, HOPS 370), OMC-2 FIR 5 (SOF 4, HOPS 369), and SOF 5 (HOPS 368), respectively. The crosshairs show the position of FIR 3 and FIR 4.

1.5 Motivation and Objectives of this PhD thesis

I faced this PhD work after 10 years of scientific and instrumental work.

My first contact with scientific research was thanks to Dr. Enrique Solano. He taught me how to access to archival data and exploit it. We developed in MIDAS a semiautomatic method able to identify Lambda-Bootis candidates in the INES catalogue. This work was presented at the SEA conference in 2000.

After this, we started a bigger project which allowed me to obtain the DEA degree in 2003 by the Universidad Complutense de Madrid. This work consisted on the identification of stars which could harbour planets. For that purpose we developed a semiautomatic method to identify methalic lines in absorption at a sample of Echelle spectra from the EXPORT sample, lead by Dr. Carlos Eiroa (Gonzalez-Garcia & Solano 2003). I had the great opportunity to attend to specialised courses during this period such as NEON school in 2002 at the Asiago Observatory, were I learnt the basics for observing and data processing, as well as to the IAC Winter-school on the topic of payload for space missions.

I started to feel fascination about the Brown Dwarf objects and I had the great opportunity to be able to work with Dra. María Rosa Zapatero-Osorio. With her I had access to maps from 3.5-m telescopes from Calar Alto and Monte Palomar. Using near-infrared filters we identified new brown dwarf candidates in Orion, Perseus and Pleiades Clusters. I had the amazing luck to access to observe with the 1.5-m Carlos Sánchez and the 2.5-m Nordic Optic telescopes with a very successful experience. With Maria Rosa I learnt the huge work behind a publication and with her support, I made my first author publication González-García et al. (2006).

Research has always being my passion. I looked for jobs and I was very lucky to start working at ESAC, a wonderful research environment, initially for the XMM-Newton project (2001-2008) and later in the Herschel project (2008-2015). Free time permitting, I kept collaborating to publications for the XMM-Newton project: (Rodriguez Pascual et al. 2002; Schartel et al. 2003; Ehle et al. 2004); and in the Herschel project: (O'Rourke et al. 2014; Eiroa et al. 2013b,a; Müller et al. 2012; Popesso et al. 2012; O'Rourke et al. 2012a,c,b; Küppers et al. 2012; O'Rourke et al. 2012b; Kueppers et al. 2012; Müller et al. 2012; O'Rourke et al. 2012e,d; Eiroa et al. 2011; O'Rourke et al. 2011; Marshall et al. 2011; Eiroa et al. 2010).

At the XMM-Newton project I started as Computer Operator and, a year later, as Instrument Controller. In the first position (during 2001) I learnt how to maintain Operational machines (VMS, Linux, Windows) and the SCOS-b platform used by ESA for real time operations, apart of sanity checks to the machines and perform backups. As XMM-Newton Instrument Controller (2002-2008) I learnt the real-time operations and how to take the appropriate decision at any time of the day when alerts related to the instrument voltages, temperatures and radiation affected a running observation; to perform an initial assess to the real time data which could be later use to understood under what circumstances the observations were carried out; to compare the X-ray Universe with the well known optical Universe with the XMM-Newton instrumental eyes; to analyse

how eclipses and derivation on the orbit could be controlled and to appreciate the amazing net between User support group, Mission Planing, Flight Dynamic teams, Spacecraft controller, Instrument controller, Network team, Computer Operator, Pipeline processing team and Archive teams. Being always curious,it was amazing to learn from different involved agents and their dedicated work generating an opportunity from any potential problem.

In 2008 I joined the Herschel Data Processing team as scientist analyst of the data. My tasks, apart of contributing to design the automatic processing of the data, was to perform a first, and later a deep, quality control of the data, focused on the PACS data. The complexity of the PACS spectrometer data gave me more than one troubleshooting but all was easier with the incredible knowledge from the scientist in charge (who was later my supervisor: Dr. Roland Vavrek) and the PACS ICC. The difficulty of the data processing, its analysis and the desire to make the best of my position made me to learn more and more their details and even to attempt to add my/our own contribution to it, as we show in this PhD work.

Two main goals drove this PhD work:

- **Technical goal:** To create optimally processed spectroscopy data products for the OMC-2 region by the Herschel/PACS unprecedented spatial resolution (8 ″-13 ″) and line sensitivity (8.01×10^{-18} Watts/m^2 - 1.75×10^{-16} Watts/m^2) in the 55-200 microns range of the far-infrared.

  Design a semi-automatic pipeline customised for the optimal reconstruction of spectral mapping data obtained on the OMC-2 region. By this process we create hyperspectral cubes, line flux maps, continuum maps, line ratio maps, signal-to-noise maps and quality assessment to these products. These products are ready to feed back to the Herschel Science Archive as User Provided data Products (UPDPs) providing a long-standing added value to Herschel's legacy science.

  Generic purpose components of our processing tasks have been feed back to HIPE and the PACS standard spectroscopy product generation pipeline, such as optimal settings for spectral drizzling (applicable to oversampled maps) and the multi resolution baseline estimator algorithm.

- **Scientific goal:** The modelling of the star formation processes that take place in the OMC-2 region between FIR 3 and FIR 4 targets. Our objective was to obtain high spatial resolution PACS spectrometer line maps for :

  – the fine structure [O I] 63 and 145 μm lines: to spatially resolve the jet in this region, already suggested by Williams et al. (2003); Shimajiri et al. (2008). We will study the [O I] luminosity at the position of FIR 3 and FIR 4 along the jet. Electron densities could also be calculated to better constrain the physical properties of this jet.

  – the CO lines in the PACS range (J_{up} = 14 - 46): to generate rotational diagrams from where to identify the rotational temperature (or temperatures) to obtain the gas density and temperature by comparing the measure CO line ratios to a

grid of model of rotational diagrams generated for large range of values of T (100-5000 K), and densities n(H_2)~ (10^2-10^{12} cm^{-3}), and a column density (or optical depth) (Neufeld & Kaufman 1993; Neufeld 2012; Manoj et al. 2013).

- Measure the relation of abundance between CO and H_2O.
- Contribute to the better understanding of the OMC-2 region combining the Herschel data to other data from the HOPS team (*Spitzer*, APEX,VLA).

2

The Herschel Space Observatory

This chapter briefly describes the Herschel satellite, its mission level components, and its scientific instruments.

2.1 Herschel mission overview

The Herschel satellite (Pilbratt et al. 2010), Fig. 2.1, was a cornerstone mission of the ESA. It was launched on 14th May 2009, together with the Planck satellite by an Ariane 5 rocket into a transfer orbit (see Fig. 2.2). After six months Herschel achieved its operational orbit, a Lissajous type at 700000 km around the second Earth-Sun Lagrange Point, which is at 1.5 million kilometres from the Earth. This orbit was selected for its stable radiation and thermal environmental conditions required for collecting high sensitivity observations in the far infrared and sub-millimiter domains.

The Herschel satellite was the largest space telescope ever launched, with a 3.5-m diameter mirror. A sunshield protected the satellite from the Sun, and its instruments were cooled by superfluid liquid helium to their operating temperature. The three instruments, located at the focal plane (Fig.2.3), performed imaging photometry and spectroscopy in the wavelength range 55-671 μm. They are the Photodetector Array Camera and Spectrometer, PACS, (Poglitsch et al. 2010), the Spectral and Photometric Imaging REceiver, SPIRE (Griffin et al. 2010), and the Heterodyne Instrument for the Far Infrared, HIFI (de Graauw et al. 2010). The first two instruments were operated as a camera or a medium-resolution spectrometer and HIFI is a high resolution spectrometer. Their location at the

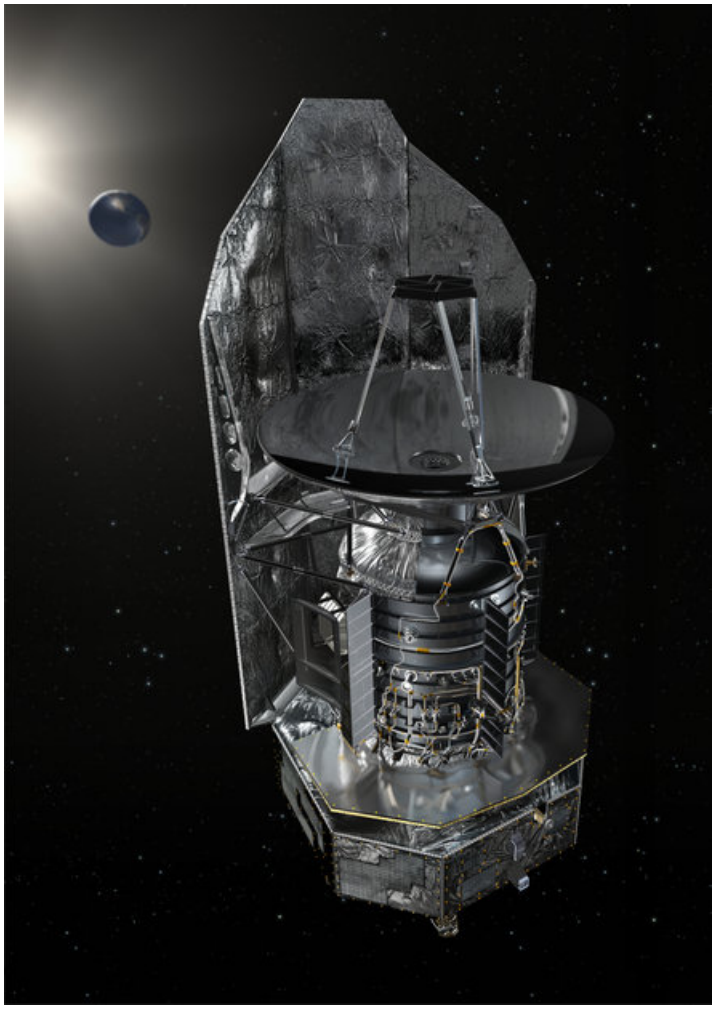

Figure 2.1: The Herschel satellite

focal plane can be seen in Fig. 2.3 and their capabilities are listed at Table 2.1.

Herschel revolutionised the observing capabilities in the poorly-explorer wavelength window covered previously by far-infrared satellites (IRAS/ISO) and ground-based radio antennas and the Kuiper Airbone Observatory. Herschel data provided new light on the earliest epoch of proto-galaxies, the cosmologically-evolving AGN-starburst symbiosis, the mechanisms involved in star and galaxy formation and the connection between them, the physics of the interstellar medium, astrochemistry and solar system studies, among others.

We briefly describe the three instruments but most of the data used in this thesis are from PACS and SPIRE.

SPIRE	3-band imaging photometer
wavelength bands	250, 350, and 500 μm
FOV	$4' \times 8'$
detectors	139, 88 and 43 pixel bolometer arrays
spectral resolution	~ 3
SPIRE	Fourier Transform spectrometer
wavelength bands	194-313 μm & 303-671μm
FOV	circular (ϕ : 2.6′)
detectors	37 and 19 pixel bolometer arrays
spectral resolution	370-1300 (high) / 20-60 (low)
HIFI	heterodyne spectrometer
wavelength coverage	157-213 μm &240-625μm
FOV	single pixel on the sky
detectors	5×2 SIS & 2 ×2 HEB mixers
spectrometers	auto-correlator and acousto-optical
spectral resolution	typical 10^6
PACS	2-band imaging photometer
wavelength coverage	60-85 μm / 85-130 μm &130-210μm
FOV	$1.75' \times 3.5'$
detectors	64×32 and 32 ×16 pixel bolometer arrays
PACS	integral field spectrometer
wavelength coverage	55-210 μm
FOV	$47'' \times 47''$
detectors	2 25×16 Ge:Ga arrays
spectral resolution	1000-4000

Table 2.1: Detail of the Herschel instruments at the focal plane

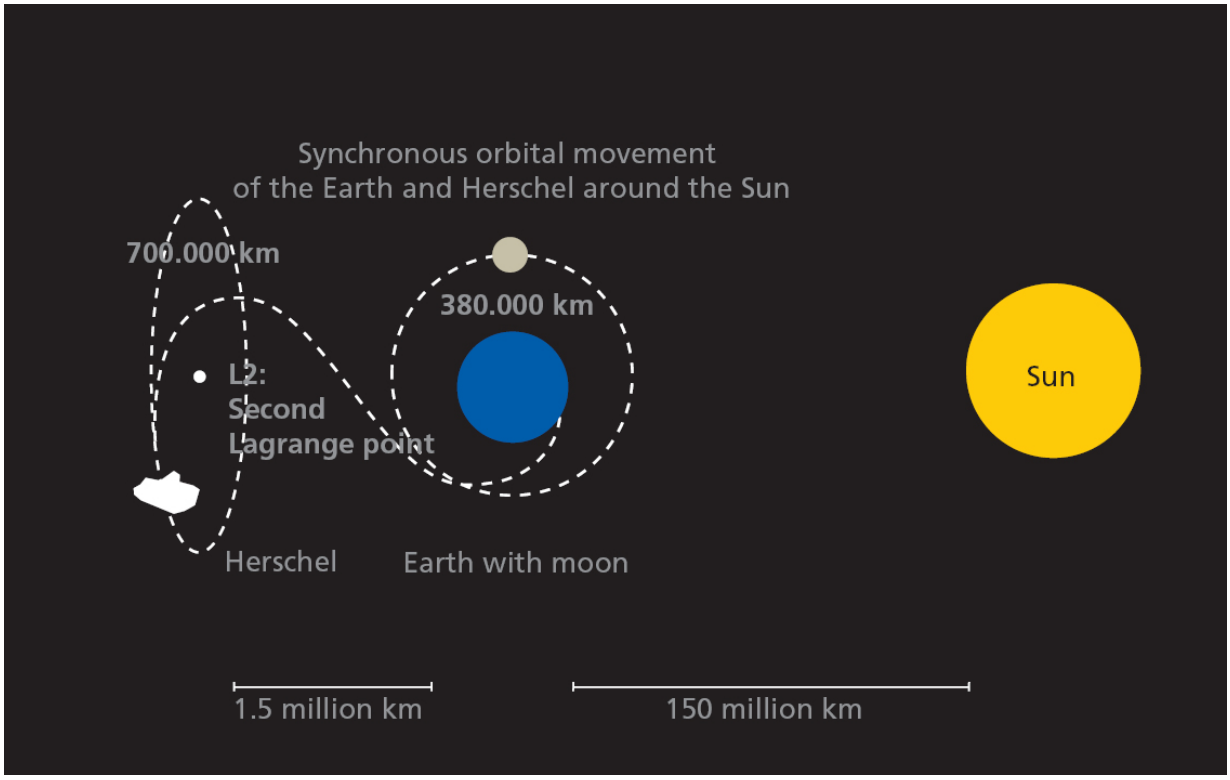

Figure 2.2: The Herschel transitional and operational orbits

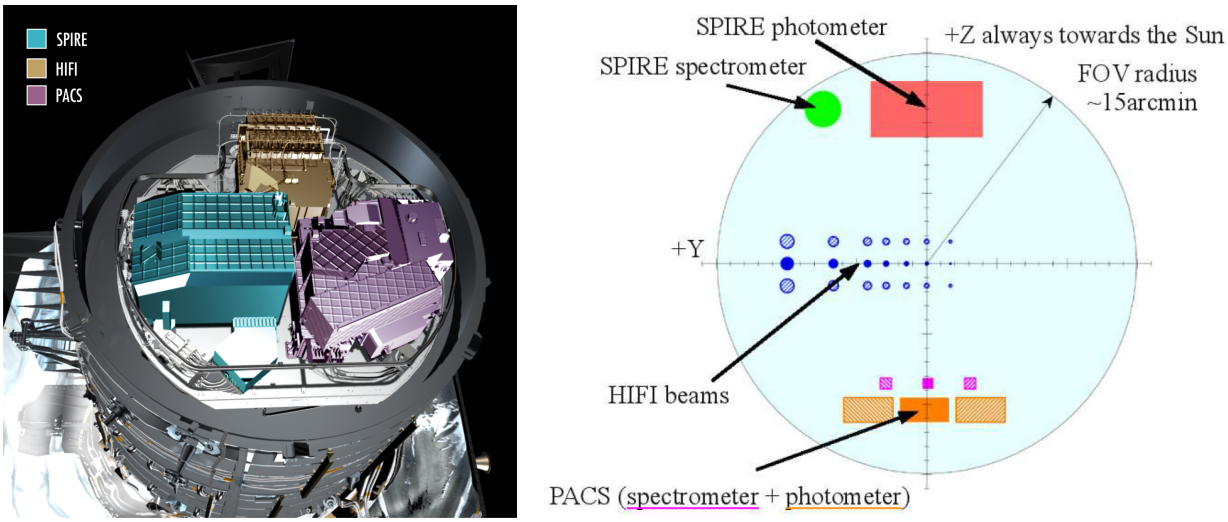

Figure 2.3: The Herschel instruments at the focal plane

2.2 The PACS instrument

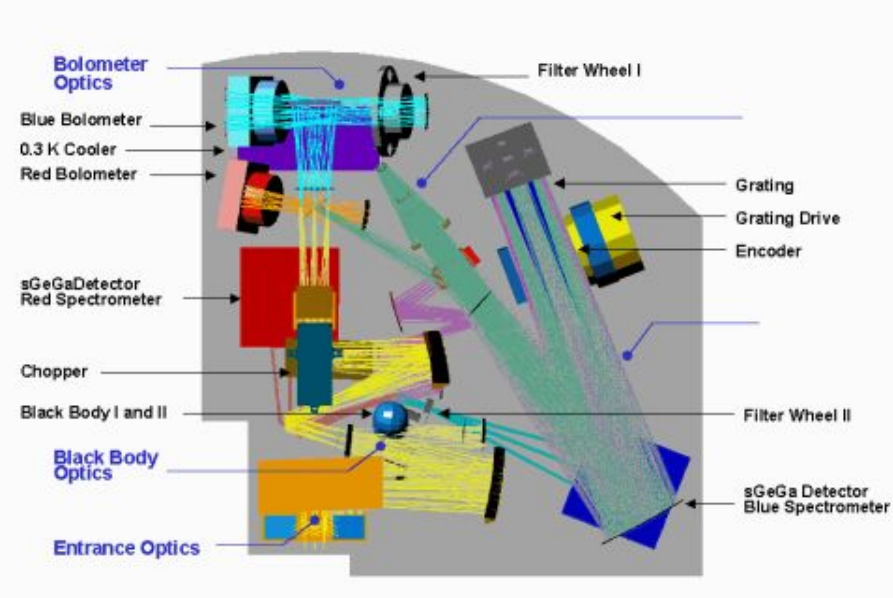

Figure 2.4: The PACS optical path (figure collected from the PACS Observer's Manual)

The PACS instrument operated as a camera or as a spectrometer, depending on the optical path followed by the light, as shown in Fig. 2.5.

The **PACS photometer** took always two images from two filters (blue and red). At the definition of the observation it was possible to select between two blue filters (centred at 70 μm or at 100 μm) and a single red filter (centered at 160 μm). The blue channel has a 32×64 pixel detector array and the red channel 16×32 pixels array. Both cameras have a field-of-view of 1.75′×3.5′. Most of the scientific observations were carried out in scanning mode, which allowed efficient use of observatory time by optimising between coverage and depth.

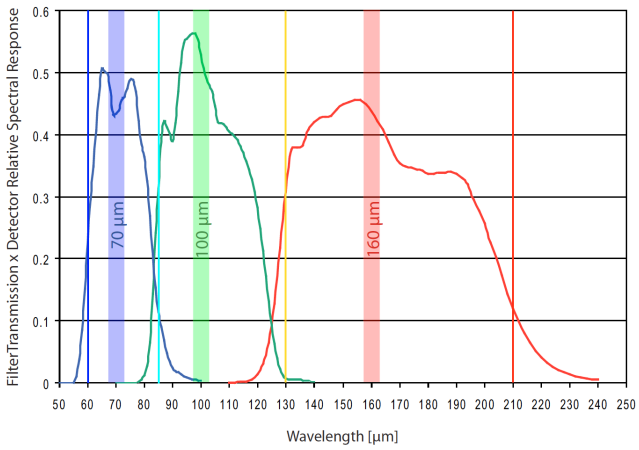

Figure 2.5: The PACS photometer filters. Figure collected from Poglitsch et al. (2010).

The **PACS spectrometer** is an Integral-Field spectrograph (IFS) designed to gather data simultaneously both along the spatial- and spectral domains. Integral field spectrographs are instruments that allow you to gather spectra of the sky over a two-dimensional field-of-view. Regardless of the technique used to obtain the data, the final product is a data-cube, with axes of x, y (or RA, Dec; the two spatial axes) and wavelength (velocity). See Fig. 2.6.

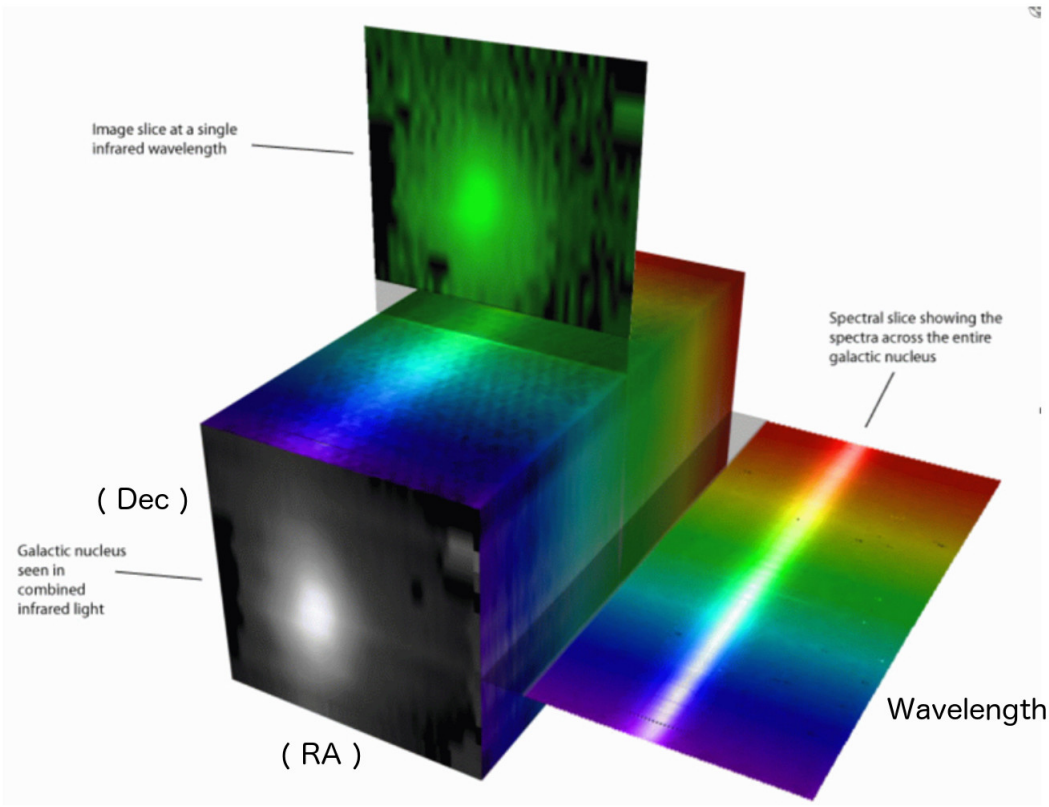

Figure 2.6: The IFU concept. Image adapted from http://ifs.wikidot.com/what-is-ifs

The PACS instrument design enables imaging spectroscopy in a time-efficient way without compromising science performance. Its unprecedented spatial resolution and sensitivity to lines and continuum makes the instrument a pioneering milestone with a proven science legacy for the next decades in far-infrared molecular astronomy.

The spectrometer array is composed of 5×5 spatial pixels (spaxels) of 9.4″ each, covering an instantaneous field-of-view of 47″×47″. An image slicer divides and rearranges the 5×5 field-of-view into a 1×25 long slit and feeds onto the two (red and blue) 25×16 pixel detectors (cryogenically cooled Ge:Ga photoconductors arrays at a 1.65 K operating temperature), see Fig. 2.7. A reflective diffraction grating in a Lyttrow mount diffracts the optical path into three orders that together cover the spectral range 52-220 μm. The diffracted light is spread over the 16 spectral pixels of the detector.

Despite the spectrometer technical complexity, the highly redundant nature of the raw data

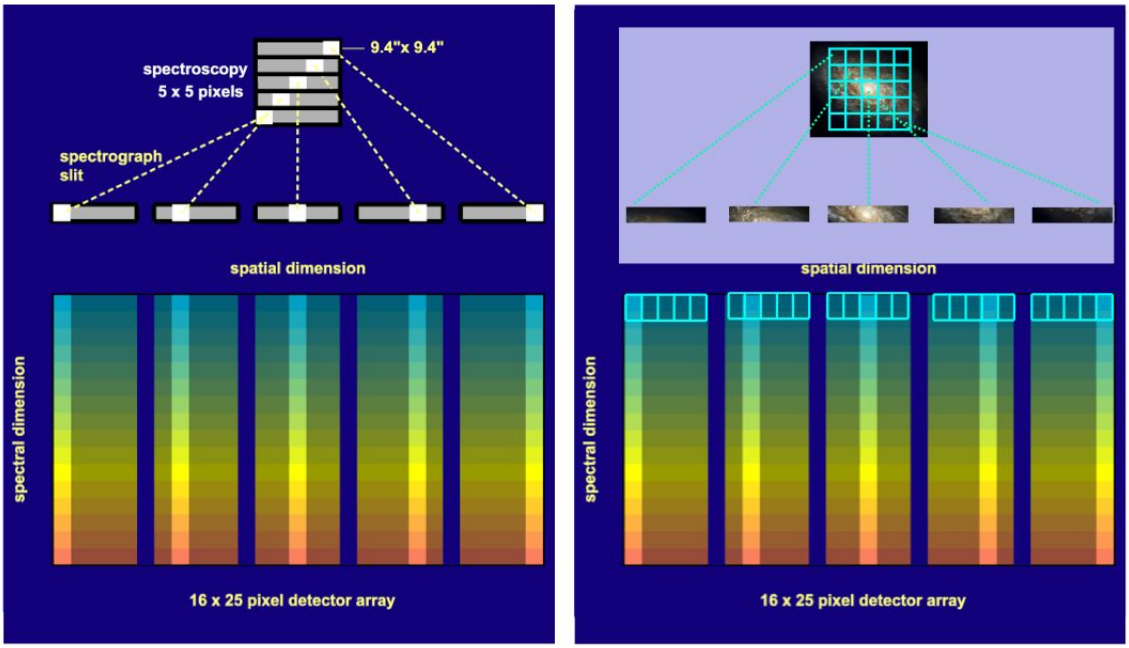

Figure 2.7: PACS spectrometer slicing concept. Image collected from the PACS Observer's Manual.

acquisition mitigates the impact of cosmic ray irradiation effects and increases the signal-to-noise ratio. This instantaneous coverage is rather limited, therefore to access the full spectral range the grating had to be rotated within a wide range of angles. Single grating steps correspond to only a fraction of the wavelength coverage, therefore consecutive steps were taken to cover the requested spectral range. As a result raw data in the spectral domain are highly redundant. Diffracted orders were separated by order-sorting filters and by selecting the range of grating angle. The light beam falling onto the red channel (high-stressed detector) is separated by a dichroic mirror and let the 1st order selected light through a filter. The light beam from the dichroic in the blue channel passed through a filter wheel where either the second or the third grating orders are selected and imaged onto the array (low-stressed detector). Data were obtained simultaneously in the blue- and red channels. Only a small fraction of pixels suffer from excess noise. Median NEP values are (8.9 -10)$\times 10^{-18}$W$Hz^{-1/2}$ for the stressed and (2.1- 10)$^{-17}$W$Hz^{-1/2}$ for the unstressed detectors, respectively.

2.3 Observing with PACS photometer

Astronomical Observing Templates (AOT) were provided to parametrise Herschel observations and to let the astronomer select the observing modes most suitable for the target of interest:

- PACS Photometer AOT

- SPIRE/PACS Parallel Mode AOT

In SPIRE/PACS parallel mode the two instruments were operated simultaneously, covering slightly distinct field of views. The beam is fully sampled for the short and long wavelengths covered.

The PACS photometer AOT offered three kinds of observing techniques:

- Point source photometry, using chopping-nodding beam modulation.
- Scan map mode to cover a small or a larger map.

The Parallel Mode AOT offered only scanning mode with settings primarily optimised for the SPIRE instrument.

Pointed observations, using the chopping-nodding technique were replaced with the 'mini-scan' map technique after discovering that the second technique performed better in terms of point source sensitivity and area coverage efficiency. Therefore here we will only describe the scan map mode.

The scanning technique was used for all type of targets observed by the PACS photometer. It consists of scanning the sky (as its name stands for) in parallel lines at a constant speed by slewing the satellite (see Fig 2.8). The observer defines the scanning speed and the length of the scan leg, separation between legs, repetition number and the orientation angles of scan legs projected on the sky.

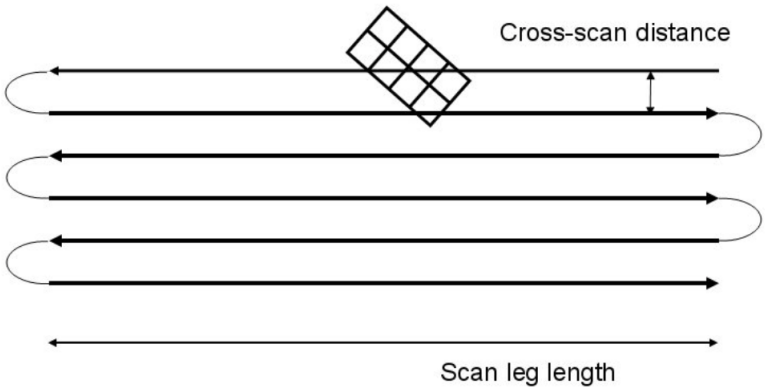

Figure 2.8: Representation of the scan map technique. Figure collected from the PACS Observers Manual

The scan map mode - especially for minimaps - provided a non-homogeneous sampling of the covered area. The regions in PACS photometer maps which have a higher coverage have a higher sensitivity. Coverage maps are also provided as part of the pipeline products for inspection.

Tables 2.2 summarises properties of the PACS photometer applicable to the thee bands in scan-mapping and parallel mode AOTs.

Wavelength (μm)	Scan speed ($''$/s)	FWHM ($''$)	Pixel size ($''$)	Flux units	Sensitivity for point source (5σ, 1h)
70	20	5.46×5.76	1.6	Jy/pixel	5 mJy
	60	5.75×9.0			
100	20	6.69×6.89	1.6		5 mJy
	60	6.89×9.74			
160	20	10.65×12.14	3.2		10mJy
	60	11.31×13.32			

Table 2.2: Essential properties of the PACS photometer AOTs

2.4 Observing with the PACS spectrometer

The PACS spectrometer observing logic required rotation of the diffraction grating to modulate the angle of incident and refracted light, to extend the wavelength coverage beyond the very limited instantaneous coverage of the grating. The choice of grating angles together with the choice of diffraction order determines the covered wavelength range in the blue and red channels, as shown on Fig. 2.9.

PACS spectrometer observations can cover the spectral range 52-210 μm. Depending whether the scientific goal was the detection of single lines, a forest of lines, or the continuum, one could chose the Astronomical Observing Templates (AOTs) :

- **Line Spectroscopy:** A maximum of ten lines could be observed per observation for a fixed diffraction order. The range of the grating scans allowed each of the 16 spectral pixels to cover the profile of a particular line. The grating was operated at high sampling mode, covering more than three times a resolution element. This way a small but highly redundant wavelength range is optimised for full profile coverage of the line with the line at the centre and with sufficient continuum on both sides to facilitate reliable flux extraction (profile fitting).
- **Range Spectroscopy:** Considering several short ranges (up to ten) or a single SED range (a very large range which covers a complete order). The short ranges, which could cover a broad line (with wings) or several close lines, were observed with high spectral sampling. For SED observations, the grating sampling was lower (Nyquist sampling the instantaneous coverage). The full PACS spectral range could be covered by the concatenation of two SED observations: one with filters B2A or B3A and R1 [(51-71) μm and (102-210) μm] and with filters B2B and R1 [(71-105) μm and (140 -210) μm]. B3A and B2A bands cover the same wavelength but in different orders (3 and 2).

2.4.1 Beam-modulation techniques

The flux gathered by PACS observations is ultimately dominated by the high telescope background. To eliminate this telescope background (as well as sky background) and

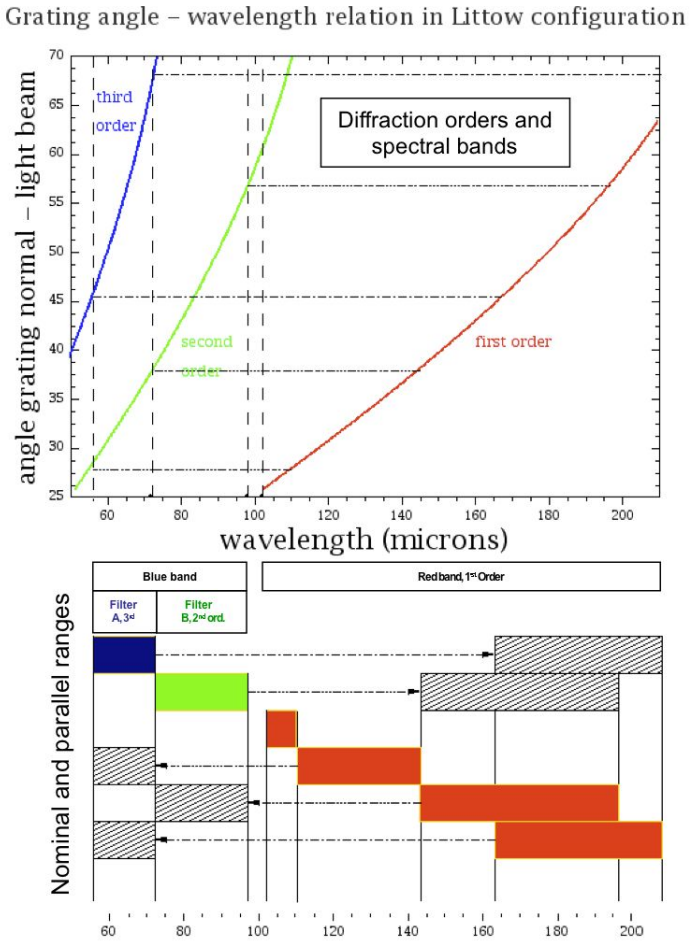

Figure 2.9: *Up:* relation between grating angle and the wavelength at the PACS spectrometer instrument. *bottom:* nominal and parallel ranges between the blue and red channels. Image from the PACS Observer's Manual.

estimate the very small signal of the astronomical source, a differential measurement technique was required in which the incident beam was modulated between on-source and off-source positions. The beam-modulation techniques the PACS spectrometer AOTs provided were :

- **Chop/Nod mode :** This technique is the combination of the deflectable mirror chopping (on- and off-source) and the telescope nodding (on- and off-source). This was the standard observing mode recommended, especially for faint lines (peak-to-continuum below 4-5 Jy) with faint or bright continuum. The off-position could be selected at chopper throws of: 6′(large), 3′(medium) or 1.5′(small).

  For PACS spectroscopy observations the grating stepped forward one step at a time, at each grating position, the light path was modulated between on-source and off-source following a chopping pattern achieving a deeper observation the more the nodding cycle was repeated. Each line was observed at least two times per nod position and could be made deeper by repeating the number of grating cycles, as shown by the top image in Fig. 2.10.

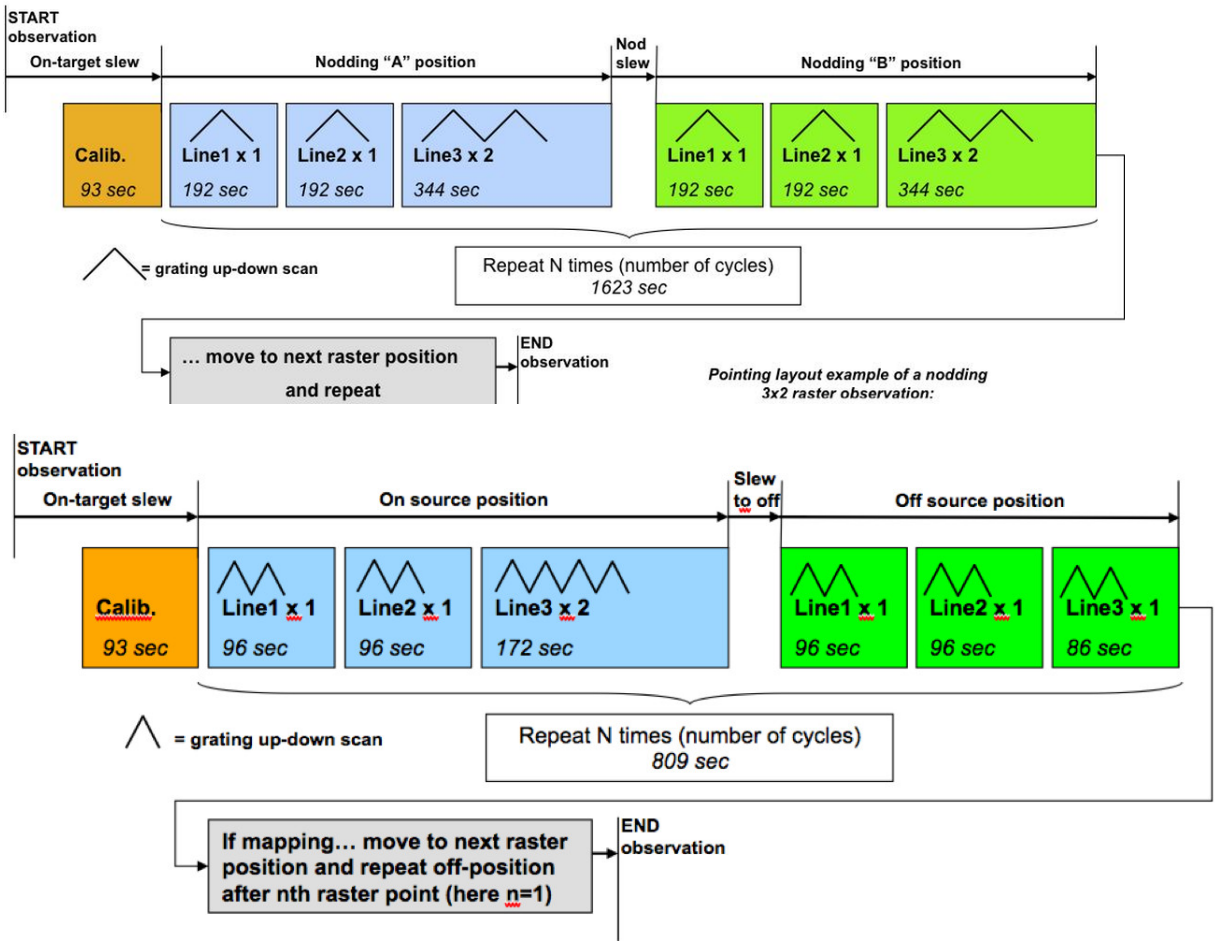

Figure 2.10: Setup of a typical PACS spectrometer (*top*) for chop/nod mode observations, (*bottom*) for unchopped mode observations. Figures from the PACS Observer's Manual.

- **Unchopped mode :** Designed for crowded fields were no nearby off-source was available within the largest chopper throw (6′). Instead of modulating on-off source at a high frequency (on every grating position), in this observing mode the source was observed over the full wavelength range, followed by an off-source observation (see bottom image in Fig. 2.10). The off-source position had to be placed within 2 degrees on a (sky) emission-free area to avoid contamination of the spectra obtained on the target of interest.

  For sources fainter than ~20 Jy continuum this technique provides an uncertain estimate of the continuum level, as advertised to users in the PACS Observers manual. Line fluxes, however, are equally reliable for bright emitters (typical at least 1 Jy per spaxel peak-to-continuum) as on spectra obtained with chop/nod mode.

  To minimise for instantaneous changes of the detector response due to cosmic rays, the grating scanned 4 times faster than during the Chop/Nod mode, duplicating the number of repetitions with respect to the chopped mode. As the read-out-time is half time than of the chopped mode, overall times were comparable.

To prevent too much time between pointing on and off-source, for **pointed** observations, different lines were collected in different observations. However, for **raster** observations, the first and the last position were always off-positions, and repeated off-positions were every 30-60 minutes during the observation. To perform a proper removal of the telescope background, the off-position should be observed at the same high signal-to-noise as the on-source observations. This was achieved by spending the same time at the off-position as at the on-position (or that at a raster position).

Observations with the Line Spectroscopy AOT provided the off-position as a block built-in within the AOT. The Range Spectroscopy AOT for the unchopped mode did not included such an off-position block. This mode collected the off-positions as a separate (second) observation which could be separated on the sky up to a maximum of 2 °. The same wavelength ranges were covered by the on-target and the off-target observations, and a single pointed off position could be shared by a group of on-target observations, observed as pointed or raster modes. This way the observer had the full flexibility to adjust the observing strategy to the number of targets the programme was aiming for.

The spectrometer performance in terms of line- and continuum sensitivities and the spectral resolution is summarised in Table 2.3 and Fig. 2.11.

Band	Wave range (μm)	Beam size	FoV	$\triangle\lambda/\lambda$	Point source (line, continuum) RMS at 5 σ, 1h ($W/m^2, mJy$)
B3A(B2A) B2B R1	51-73 71-105 103-220	9″up to 100μm with 10″at 120μm , 14″at 180μm	47″× 47″ 9.4 ″spaxel for rasters	2600-5400 1800-3000 900-2100	($1e^{-17}$, 250) ($4e^{-18}$, 310) ($2e^{-18}$, 150)

Table 2.3: Essential science performance properties of the PACS spectrometer

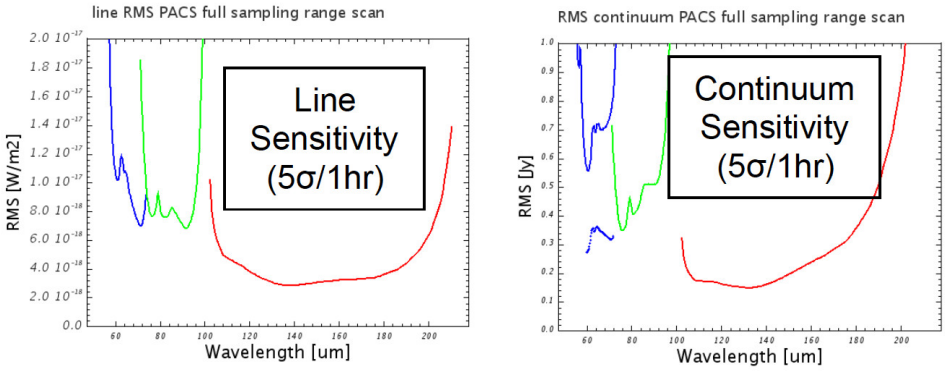

Figure 2.11: *Left:* PACS line sensitivity and *Right:* PACS continuum sensitivity. Images from the PACS Observer's Manual.

2.4.2 Spatial sampling

By spatial sampling the PACS spectrometer AOTs were divided in:

- Pointed observations
- Mapping or raster observations

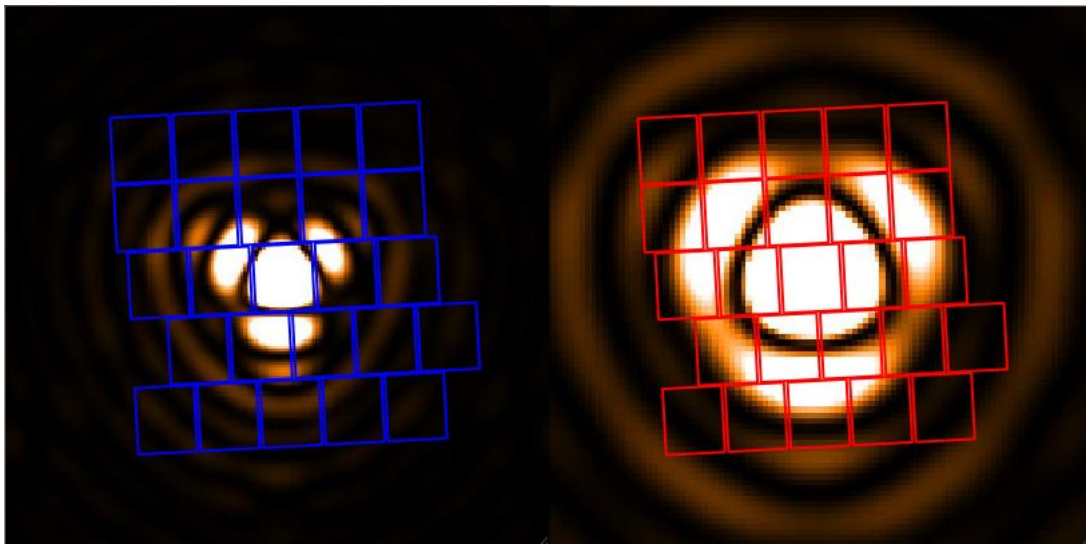

Figure 2.12: Spatial distribution of the PACS beam at 62 μm and 150 μm with the footprint of the IFU over plotted. Figure from the PACS Observer's Manual.

Figure 2.12 shows the beam at two image slices: at 62 μm and at 150 μm with the footprint of the IFU overlaid. The uneven distribution of the spaxels can be seen. The PSF has a flux distribution that contains three faint lobes due to the secondary mirror support strategy. The spaxels are as large as the PSF FWHM in the blue and not much smaller in the red. The PSF/beam is undersampled at all wavelengths. Only by collecting raster maps could the beam be well sampled. Oversampled mapping observations sample the beam more finely over an area only marginally larger the the spectrometer field-of-view. These very time-consuming observations were recommended to create full-power spectral maps of regions limited in area. The recommended raster settings were the following:

- blue camera: raster step sizes of $\leq$ 3 $''$with at least 3×3 steps in the raster.
- red camera: raster step sizes of $\leq$ 4.5 $''$with at least 2×2 steps in the raster.

For large-area coverage rasters the sampling density had to be traded-off against area covered. Applying the following raster settings the beam was sampled by 2-3 spaxels and at the same time maximised the mapping efficiency:

- blue camera: raster step sizes of $\leq$ 16 $''$with at least 3 steps in the raster (in both directions).
- red camera: raster step sizes of $\leq$ 24" with at least 2 steps in the raster (in both directions).

Mapping observations combined with unchopped range observing mode provided a highly efficient use of instrument resources as the on-time/off-time source time could be significantly larger than unity. The off-position observation was a pointed observation covering the same wavelength range as the raster, but the time such off observation requires was equal to the time spent on a single raster position for the on-source observation.

In the technical part of this thesis a large effort is devoted to finding the optimal methods for reconstruction of spectral cubes from oversampled raster maps.

2.5 The SPIRE instrument

The SPIRE instrument (Griffin et al. 2010) is the Herschel sub-millimeter camera and spectrometer. The camera and spectrometer are considered sub-intruments and only one operates at the time, as shown at Fig. 2.13.

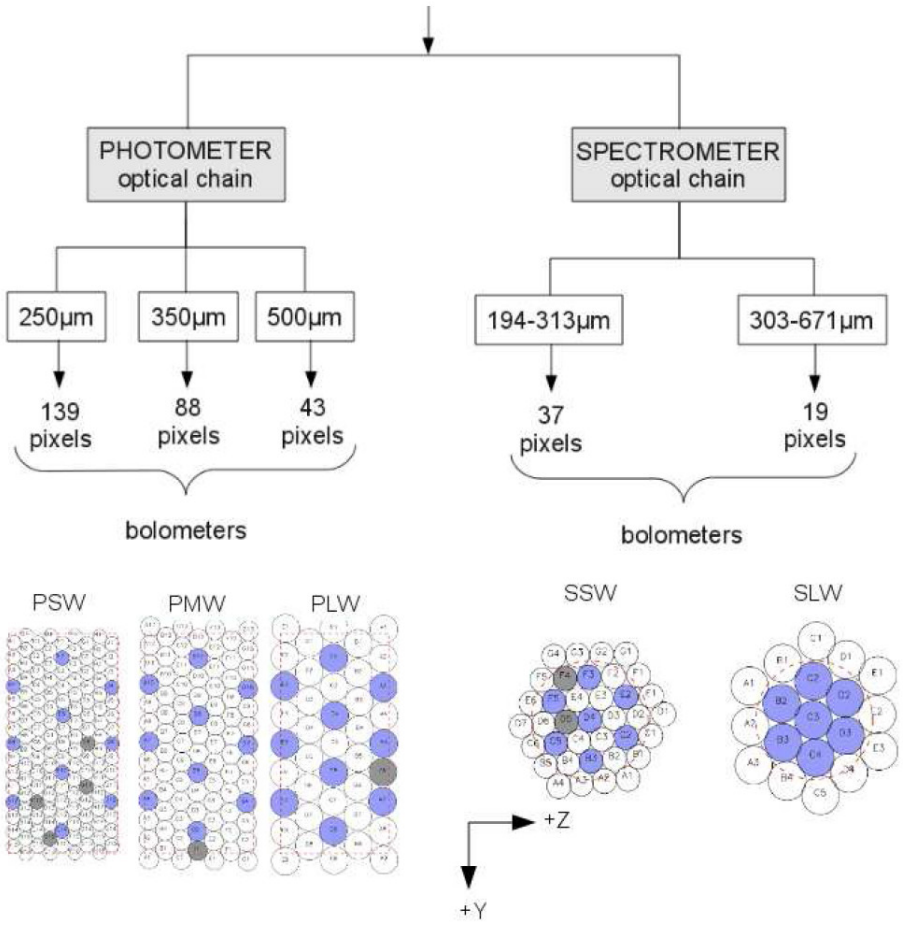

Figure 2.13: The SPIRE optical path. Figure adopted from *The Spectral and Photometric Imaging Receiver (SPIRE) Handbook*, HERSCHEL-DOC-0798

The **SPIRE photometer**, Fig. 2.14 divided the input light using dichroics into three bands, with reference wavelengths at 250μm (PSW), 350μm (PMW) and 500μm (PLW), all collected simultaneously. The camera field-of-view covers 4′×8′. The photometer detector arrays are bolometers, with different number of pixels per band: 139 pixels (at 250μm), 88 pixels (at 350μm) and 43 pixels (at 500μm). These bolometer arrays are hexagonally packed and are coupled via feed horns.

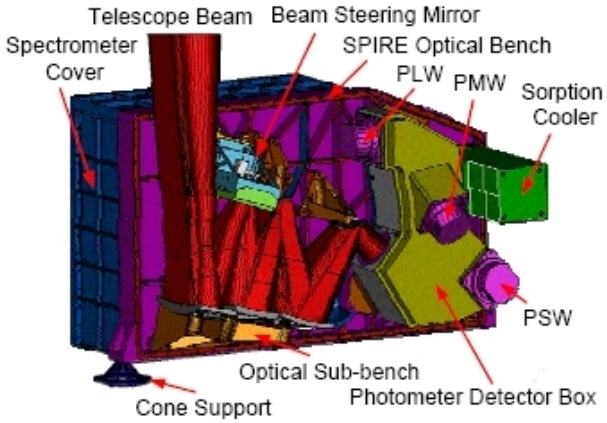

Figure 2.14: The SPIRE photometer instrument. Figure from the SPIRE Handbook.

The **SPIRE spectrometer**, an imaging Fourier-Transform (FTS) in Mach-Zender configuration. Fourier Transform spectroscopy is a spectroscopic technique based on the coherence of the signal emitted by a radiative source using time-domain or space-domain measurement. For measuring the temporal coherence there are also other technique such as the continuous wave Michelson. Naylor et al. (2003) describes the concept of FTS spectroscopy, and this is shown in Fig. 2.15.

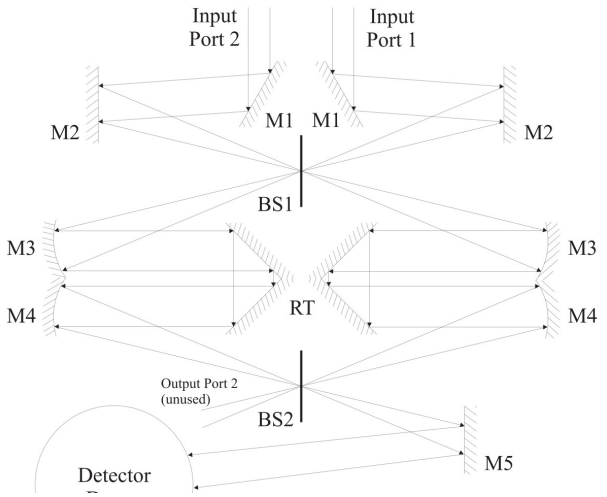

Figure 2.15: A schematic of the Mach-Zehnder Fourier transform spectrometer. Figure adopted from the SPIRE Observers's Manual

SPIRE covers the range 194-671 μm or 447-1150 GHz, also simultaneously in two bands. A dichroic beamsplitter separates the first spectral order from the second, and sent the signal to the detectors, which are feedhorn-coupled bolometers. The spectrometer field-of-view is a 2.6′ diameter circular area and its detector arrays are 37 pixels (for the short wavelength range) and 19 pixels (for the long wavelength range).

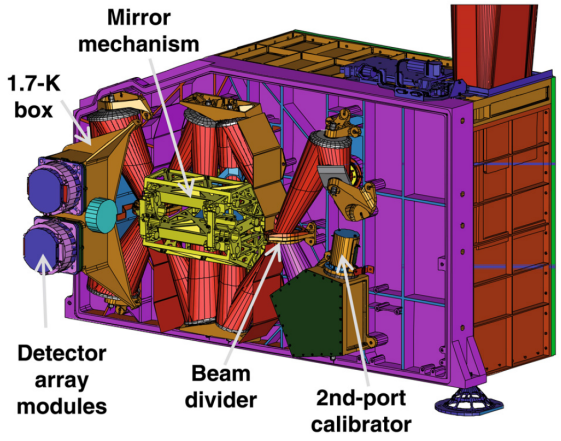

Figure 2.16: The SPIRE spectrometer instrument. Figure from the SPIRE Handbook.

General details of the SPIRE spectrometer, spectral ranges and sensitivities are given in Table 2.4 and 2.5.

Band	Lambda	FOV (units)	Flux	Line flux sensitivity RMS at 5 σ/1h (W m^{-2})
SSW SLW	194-313 μm 303-671 μm	2.6 ′	Jy or W m^{-2}/sr	SSW= 1.56-2.15 SLW= 0.94-2.94

Table 2.4: Capabilities of the SPIRE spectrometer for sparse sampling

The spectral resolution element for a Fourier transform spectrometer is given by $\Delta\,\sigma = 1/(2 \times \mathrm{OPD}_{max})$, where OPD_{max} is the maximum optical path difference achieved by the mirror mechanism. The line FWHM of the Sinc function, the natural line profile of SPIRE spectra, is given by $1.207 \times \Delta\sigma$.

The SPIRE spectrometer observations always provide information at the full wavelength range. Depending on the target observed (point or extended), different spatial sampling techniques could be used by a single or multiple spacecraft pointings and by multiple position offsets of the internal beam steering mirror.

2.5.1 Observing with SPIRE spectrometer

Observations executed by the Herschel instruments were designed by the astronomers following Astronomical Observing Templates (AOT). The SPIRE spectrometer AOTs were

defined by:

- spectral sampling:
  - high resolution (HR)
  - medium resolution (MR)
  - low resolution (LR)
  - high and low resolution (H+LR)
- pointing modes:
  - single pointing
  - raste pointing
- spatial sampling:
  - sparse
  - intermediate
  - full sampling

2.5.1.1 Spectral resolution

The SMEC (Spectrometer Mirror Mechanism) scanned at a constant speed over different distances to give different spectral resolutions. To increase the redundancy of the data, the scans were done in pairs (per repetition) along the forward and backwards direction (i.e, the wavelength range was covered twice). The SPIRE spectral resolution for each of the scanning modes are reported in Table 2.5.

In detail:

- **High resolution:** This mode was recommended for observations where the whole SPIRE range 194-671 μm was used, e.g: for line identification (e.g: CO ladder). This produced spectra at high resolution $\Delta\lambda$ = 1.2 GHz or $\lambda/\Delta\lambda$ = 1000 at λ = 250 μm .
- **Medium resolution:** was never use for scientific observations. Its resolution was $\Delta\lambda$ = 7.2 GHz or $\lambda/\Delta\lambda$ = 160 at λ = 250 μm .
- **Low resolution:** This mode was recommended for studies of the continuum. Its resolution was $\Delta\lambda$ = 25 GHz or $\lambda/\Delta\lambda$ = 48 at λ = 250 μm .
- **High and Low resolution:** This mode allowed for a high resolution (to study spectral lines) and a low resolution (to study the continuum). The number of repetitions for the low and the high resolution scans could be different, depending on the SNR required, and the continuum would benefit from both repetitions.

Mode	Spectral resolution element cm^{-1}	FOV	Line FWHM cm^{-1}	Sensitivity
High	0.0398 ± 0.0002	2.6 ′	0.0480 ± 0.0002	1.0-2.2×10^{-17} W/m^2
Medium	0.240 ± 0.010		0.290 ± 0.012	
Low	0.83 ± 0.04		1.00 ± 0.05	40-88 mJy

Table 2.5: Spectral resolution for SPIRE sparse sampling, from SPIRE Spectrometer PointSource ReleaseNote

2.5.2 Pointing mode

The different positions of the spacecraft during an observation are called pointings. They could be a :

- **Single point source mode:** This mode was recommended for point sources, as the instrument stared at a fixed position in the sky, and the field of view is a 2 ′diameter circle.
- **Raster pointing mode:** This mode was recommended for studies of regions more extended than 2 ′. The telescope pointed to different positions on the sky, taking spectra at each, and following an hexagonal pattern of pointings. See Fig. 2.17.

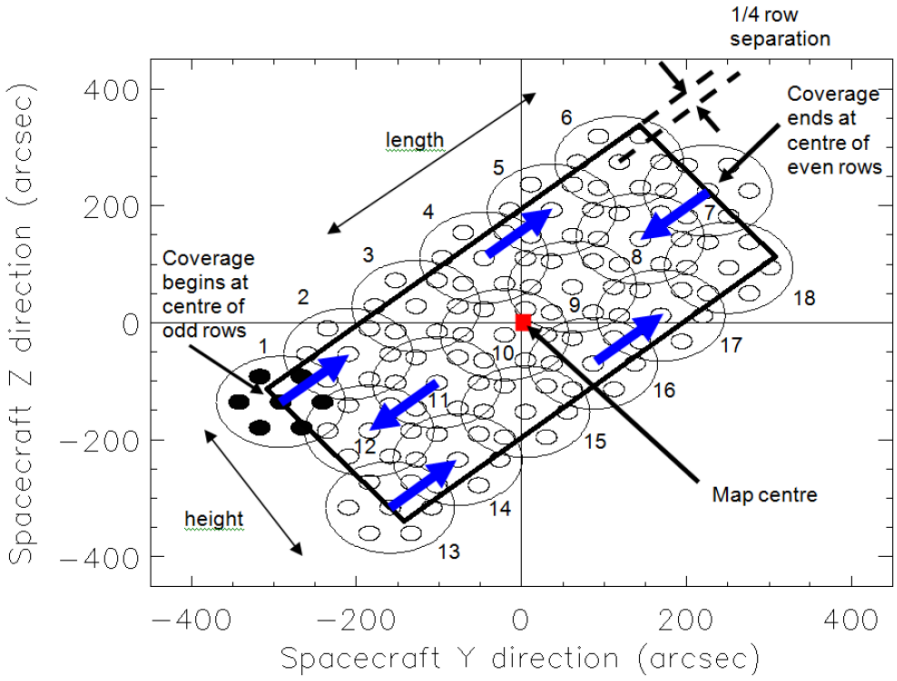

Figure 2.17: Explanation of raster pointing technique

2.5.3 Spatial sampling

The spatial sampling of the SPIRE spectrometer in its raster mode could be configured as:

- **Sparse Image Sampling:** Observations collected with this mode usually had the source at the centre and a sparse of the surroundings, adapting a hexagonal-pointing raster pattern.
- **Intermediate Image Sampling:** Observations collected with this sampling mode provide a good sampling but not the Nyquist sampling. The Beam Splitter Mirror (BSM) moved following a 4-position low frequency *jiggle* pointing pattern.
- **Full Image Sampling:** Observations collected with this mode provide a Nyquist sampling. The BSM followed a 16-position low frequency *jiggle* pointing pattern.

Fig. 2.18 showed how the beam size changes with sampling:

- **Sparse Image Sampling:** The beam increases from ~ 32.5 ″ for SSW spectra to ~ 50.5 ″ for SLW spectra.
- **Intermediate Image Sampling:** The beam increases from ~ 16.3 ″ for SSW spectra to ~ 25.3 ″ for SLW spectra.
- The beam increases from ~ 8.1 ″ for SSW spectra to ~ 12.7 ″ for SLW spectra.

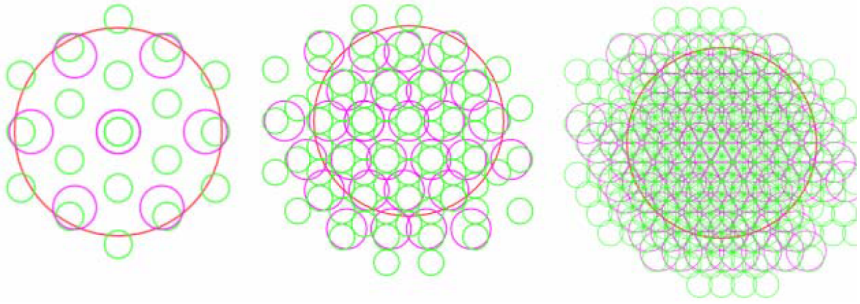

Figure 2.18: Footprint of the SPIRE detector arrays for sparse (left image), intermediate (centered image) and full spatial sampling (right image) modes. Figure taken from SPIRE Handbook.

2.5.4 Flux calibration accuracy

The calibration of the SPIRE spectrometer was based on Uranus. Cross checking with observations from Mars, asteroids and stars have been done and also with HIFI and PACS and other facilities. The flux accuracy is presented at Table 2.6.

Band	Flux density accuracy
SSW 194 -313 μm	10 - 20 %
SLW 303 -671 μm	30 %

Table 2.6: Calibration accuracy for the SPIRE intermediate and full sampling, from SPIRE Spectrometer Mapping ReleaseNote

An addition uncertainty in the flux measured at the continuum of a 10-15 % due to imperfections of the flat fielding across the array.

Pointed observations cover a field-of-view of 2.6′, while raster will cover a wider area. The pointing accuracy is within expectations from the spacecraft Absolute Pointing Error of approximately 2.0″.

2.6 The HIFI instrument

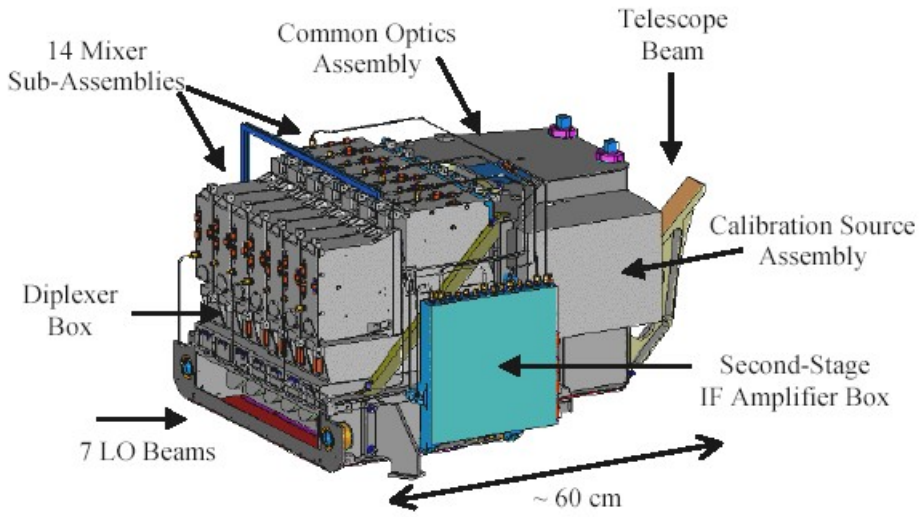

Figure 2.19: The HIFI optical path

HIFI is the Heterodyne instrument in the far-infrarred which contains two spectrometers, with high and very high resolution in the range 157-213 μm and 240-625 μm (1490 -1910 GHz and 480-1250 GHz).

The heterodyne technique requires mixing the source signal with another signal ("local oscillator") in order to bring the input signal down to a detectable frequency, without

losing information. This detected signal is called *Intermediate Signal* (IF) and is given as ($|f_s - f_{LO}|$). As the *IF* is an absolute value, it is sometimes difficult to know wether the line corresponds to an upper or lower restwavelength, unless the line is well known. HIFI behaves as a *dual-side-band* type as the detected signal is repeated at the lower and upper side bands. Its data is Double Sideband Data (DSB) data (see Fig. 2.20). To identify the real wavelength at which an specific line is detected a deconvolution is needed.

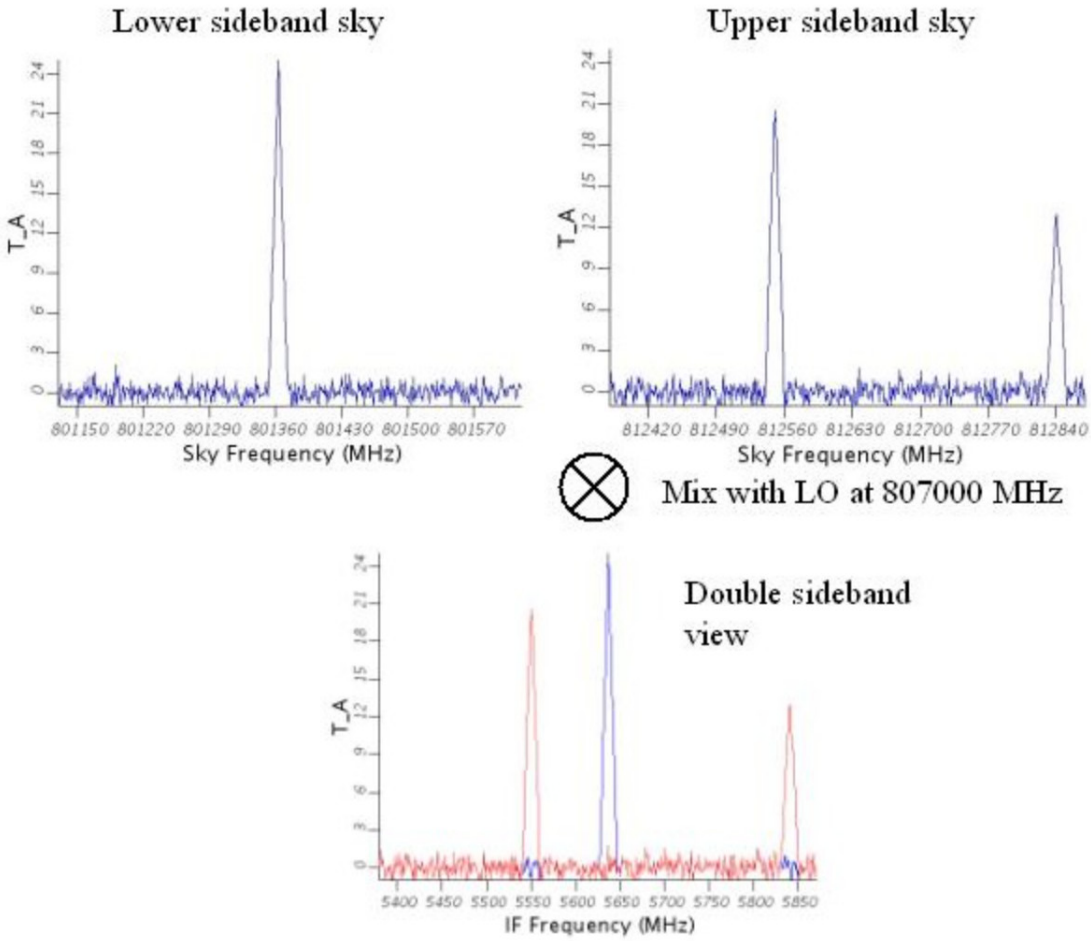

Figure 2.20: Superposition of upper (red) and lower (blue) sideband spectra for DBS spectra for the Orion cloud at 807.0 GHz. Image adopted from the HIFI Observer's manual

For HIFI, bands 1 to 5 use SIS- type mixers (superconductor-insulator-superconductor), and bands 6 and 7, use Hot-Electron Bolometers (HEBs). See Table 2.7.

The HIFI IF is detected by two types of spectrometers: a wide-band spectrometer (WBS) and high-resolution spectrometer. The bandwidth covered for the WBSs is of 4 GHz for bands 1 to 5 and is 2.4 GHz for bands 6 and 7, with a resolution element of 1.1MHz. The bandwidth covered for the HRSs varies up to 2GHz, with an adjustable resolution element between 0.125 and 1.00MHz.

HIFI has two WBS spectrometers and two HRS spectrometers, to be able to detect the

Band	Mixer type	LO Lower frequency GHz	LO Upper frequency GHz	Beam Size $''$	IF Bandwidth GHz
1	SIS	488.1	628.4	39	4.0
2	SIS	642.1	739.9	30	4.0
3	SIS	807.1	952.9	25	4.0
4	SIS	957.2	1113.8	21	4.0
5	SIS	1116.2	1271.8	19	4.0
6 + 7	HEB	1430.2	1901.8	13	2.4

Table 2.7: HIFI frequency coverage and band allocation. Table adopted from HIFI Observer's Manual

horizontal and vertical polarisation of the light.

The flux units for the HIFI data are given in antenna temperatures (T_A).

3

The Herschel Orion Protostar Survey (HOPS)

Figure 3.1: HOPSTeam logo

This chapter describes the scientific goal of the HOPS survey and the implementation of its observing program.

3.1 Scientific motivation

The *Herschel* Orion Protostar Survey (HOPS) Open Time Key Program lead by Dr. Tom S. Megeath, focuses on the study of star-formation processes and on characterising the physical properties of low- and intermediate protostars in the Orion Nebulae (Orion A & Orion B).

Herschel data were complemented by *Spitzer* 3-24 μm photometry and 5-40 μm spectroscopy, *Hubble* high angular resolution near-IR imaging and millimetre observations of the surrounding gas. APEX (SABOCA at 350 μm and LABOCA at 870 μm) data were used to constrain the protostar envelope masses and sizes, and with the 160 μm Herschel maps also the ambient dense gas temperatures and column densities.

ISO and *Spitzer* observations were used to detect the infalling material, the inner regions and the outflow cavities of the protostars. Therefore, the main result from *Spitzer* helped to characterise the geometry of the protostars. *Herschel* observations were used to determine the envelope properties (warm inner and outer part) and their infall rates could be well contained. Therefore, the main result from Herschel was to obtain the luminosity of the protostars. *APEX*, for which the emission is optically thin, provides as main result the total mass and size of the protostars. HOPS observed a large sample of protostars (see

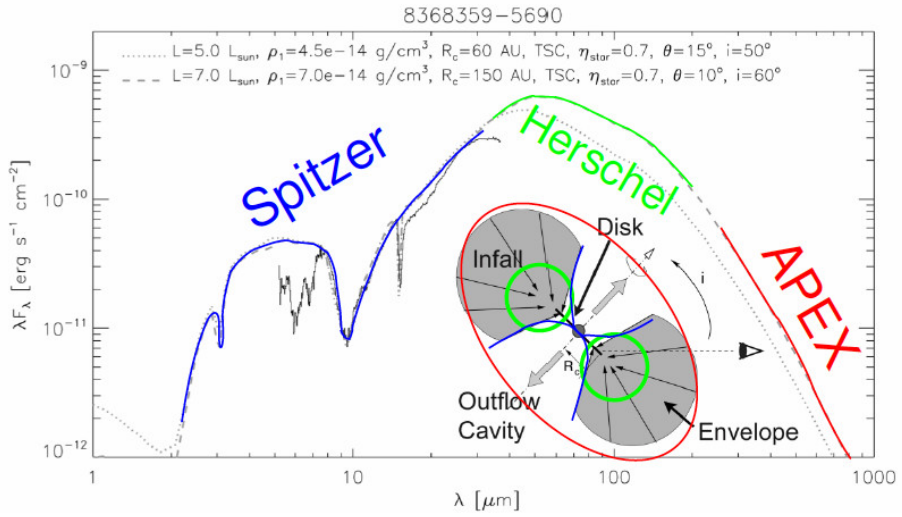

Figure 3.2: Spectral Energy Distribution of a typical YSO overlaid with the range of sensitivity exhibited by different experiments from the near-infrared to submillimetric wavelengths.

Fig. 3.3) covering a wide range of initial conditions and environments, which is needed to completely understand the impact of environment conditions (magnetic fields, close outflows) on star-formation.

The high angular resolution, wavelength coverage, and sensitivity was essential to isolate individual protostars in complex environments to resolve the far-IR emission around individual protostars, and study both the spectra and the broad-band SEDs in the far-IR. The PACS photometer bands (70 and 160 μm) are where most of the protostar luminosity is radiated (Fig 3.2).

For this purpose PACS, as a camera and spectrometer, collected a total of 200 hours on the Orion molecular cloud. 298 protostars were imaged with the PACS camera at 70 and at 160μm using the scan map mode at medium speed (20″/s). In total, 114 fields of 5′ to 8′ were imaged during an observing time of $\sim$ 140 hours.

A total of 36 protostars were observed with PACS range spectroscopy for $\sim$ 60 hours: 7

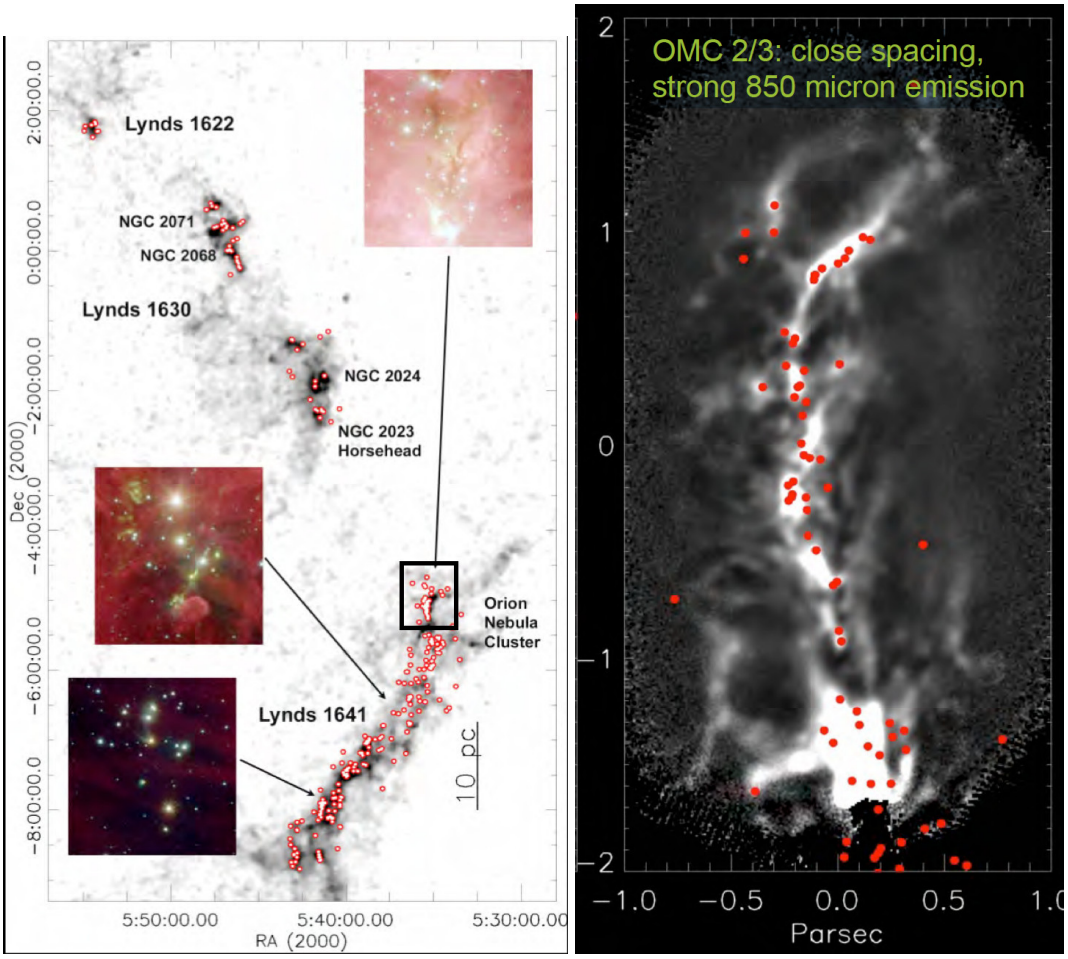

Figure 3.3: (*left*) YSO targets observed by HOPS and (*right*) zoom on the region marked as a box in the *left* image, which contains the OMC-2 region. Both figures were collected from a talk given by T. S. Megeath, the HOPS team P.I.

hours in chop/nod pointed mode and the rest in unchopped mode, 33 hours of them in mapping mode and 20 hours in pointed mode.

All these data are expected to be a legacy of information on the accretion physics of protostars.

3.2 Results from the Herschel Orion Protostar Survey

Here we present the results from the HOPS study so far, and how this lead to the subject of this thesis.

3.2.1 PACS Bright Red sources

The HOPS Team performed a census of protostars in Orion from 24 - 870 μm imaging obtained with Spitzer, Herschel, and APEX as part of the HOPS programme. Stutz et al. (2013) identified **15 new protostars** from the Herschel data, which were not previously part of the 300 *Spitzer*-identified protostars in Orion from the HOPS programme. From these two samples, Stutz et al identified 18 extremely red protostars (i.e., log [λ F$_\lambda$70 / λ F$_\lambda$ 24] $\geq$ 1.65), and being the reddest known in Orion were given the name **PACS Bright Red sources** or PBR. Their identification at only long wavelengths in Fig. 3.4 and their distribution across the HOPS sample is shown in Fig. 3.5.

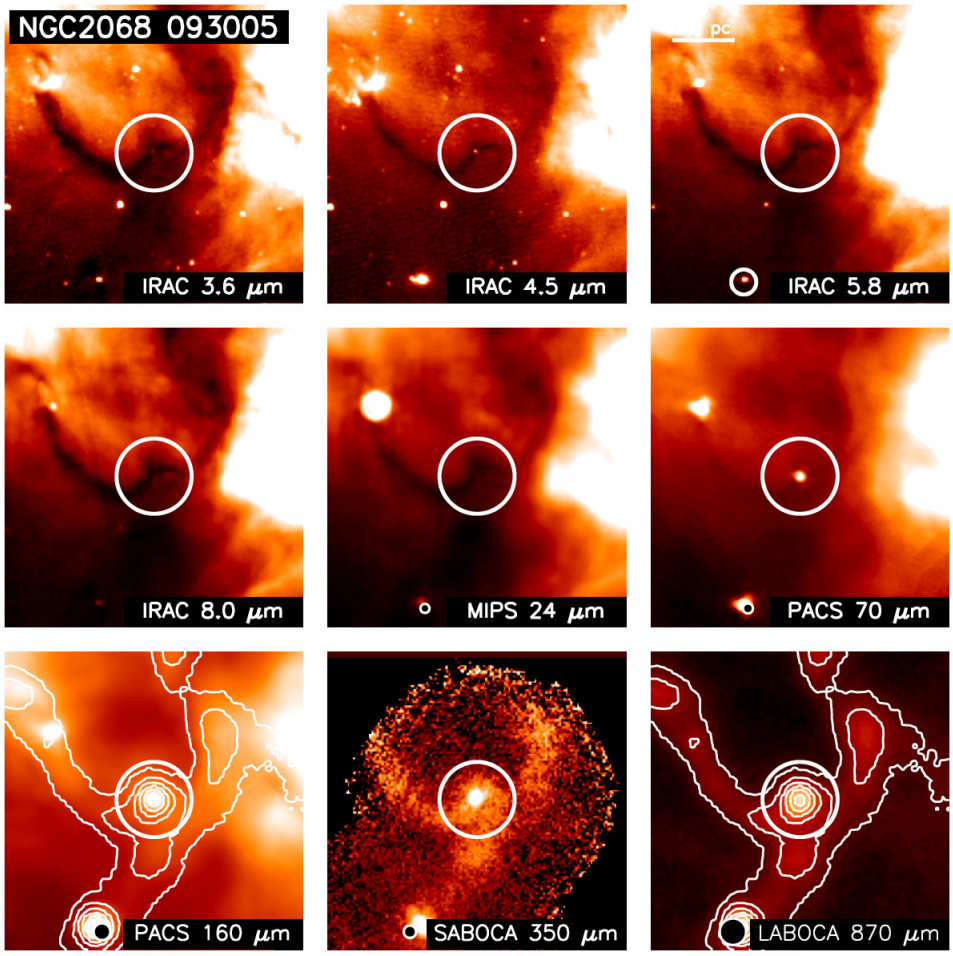

Figure 3.4: *Top* shows a composition of images collected by the HOPS programme at the position of the PBR object NGC2068 093005. This object is detectable only from 70 μm onwards. Therefore is one of the new protostars identified by Herschel. *Bottom*) image show the spectral energy distribution of this target peaking at 160 μm (Herschel range). Image adopted from Stutz et al. (2013)

Their analysis of these PBRs revealed that they have very red SEDs, with T$_{bol}$ < 45 K, and large sub-millimeter fluxes (L$_{smm}$/L$_{bol}$ > 0.6 %). From comparison of the SEDs with the radiative transfer models of protostars, Stutz et al. (2013) concluded that PBRs are

most likely extreme Class 0 objects with a higher than typical envelope masses (0.2$M_{\odot}$-2$M_{\odot}$), possibly high mass-infall rates, and luminosities of 0.7 $L_{\odot}$- 10 $L_{\odot}$. The age of these PBRs is estimated to be 0.005-0.025 Myr and the fraction of them identified in the Orion B cloud is 5 times higher than in the Orion A cloud, most probably due to their differences in star formation histories.

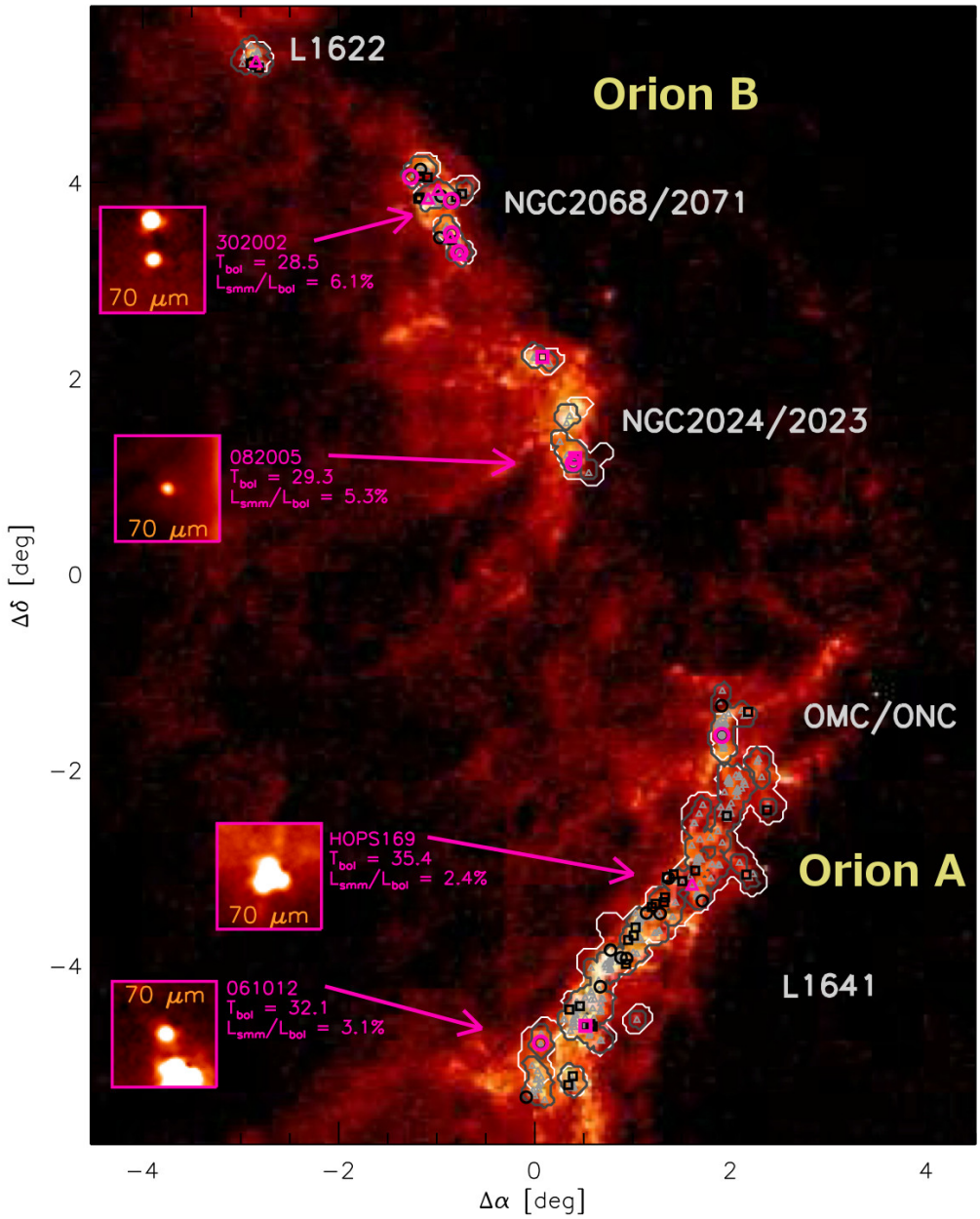

Figure 3.5: Identification of the new PBRs objects in the Orion Molecular Cloud. Image adopted from Stutz et al. (2013)

3.2.2 The modelling of CO emission from protostellar cores

Manoj et al. (2013) detected, using PACS spectrometer data, typical emission lines of outflows CO, OH, [O I] and H_2O as shown in Fig. 3.6 at the protostars stage when the protostar and the disk obtain their definitive mass and form.

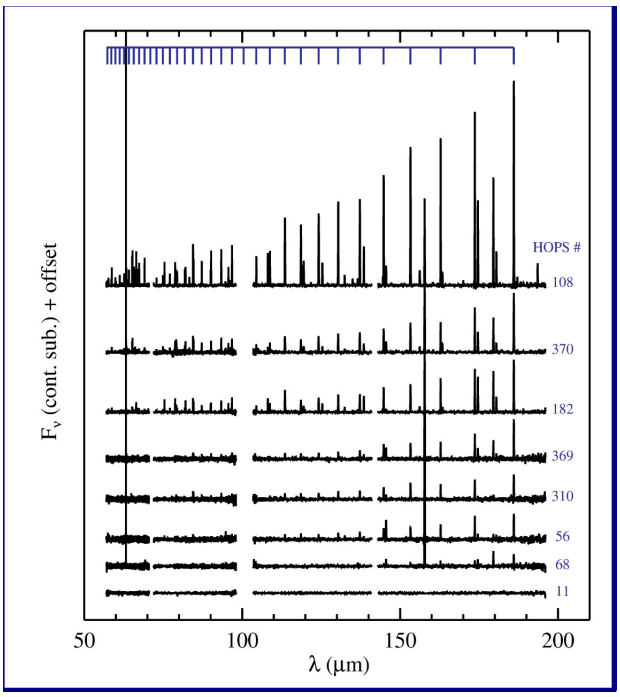

Figure 3.6: Identification of the lines in the PACS range for a set of protostars from the Herschel Orion Protostar Survey. Image taken from Manoj et al. (2013).

Manoj generated CO rotational diagrams from the CO lines (J_{up} = 14 - 46) detected within ≤ 2000 AU from each of the 21 protostars detected by PACS from the HOPS sample (see Fig. 3.6). The rotational diagrams of all protostars are very similar, with 3-4 rotational temperature components identified. The CO transitions with higher J_{up} presented the highest rotational temperatures.

Manoj compared the observed CO line to a grid of Neufeld (2012) models rotational diagrams, generated for large range of temperature values 200-2000 K and densities in the range 10^2 -10^{12} cm^{-3}. χ^2 minimisation was used to find the best-fitting model. The results find that the gas is *sub-thermal*, with n(H_2) ≤ 10^6 cm^{-3} at T ≥ 2000 K, as seen in right image in Fig. 3.7. These conditions most probably occur in post-shock regions in molecular outflows and the cavity walls, at 100-1000 AU distance from the protostar, rather than at the photodissociation regions (PDRs) from the UV-heating along the envelope cavity walls.

Manoj et al. (2013) studied the CO ladder spectra of 21 protostars in Orion molecular clouds within a projected distance of ≤ 2000 AU from the centre of the protostar (the Orion Molecular Cloud distance ~ 420 pc (Sandstrom et al. 2007; Menten et al. 2007).

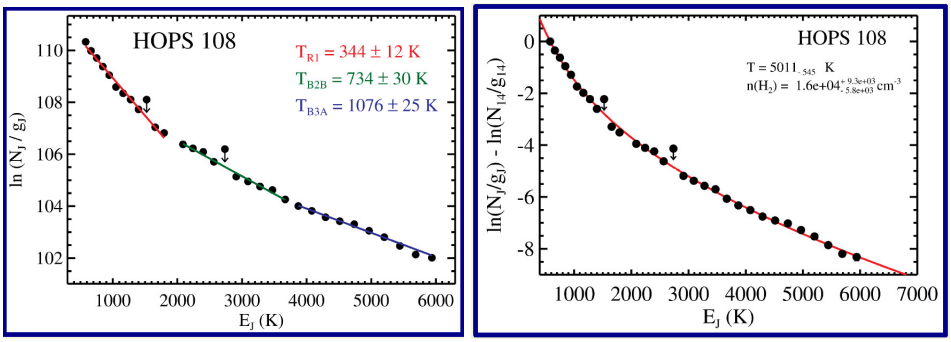

Figure 3.7: (*Left*) rotation diagram for the HOPS 108 (FIR 4) target , where at least three components can be derived and *right* the estimated gas temperature and densities comparing observed results to Neufeld (2012) grid of model. Images adopted from Manoj et al. (2013).

Manoj found that the sum of the CO luminosities (L_{CO}) increases with the protostar luminosity (L_{bol}) and that CO luminosities (L_{CO}) did not have any connection to evolutionary indicators, such as T_{bol} or envelope properties, such as envelope density, as shown in Fig. 3.8.

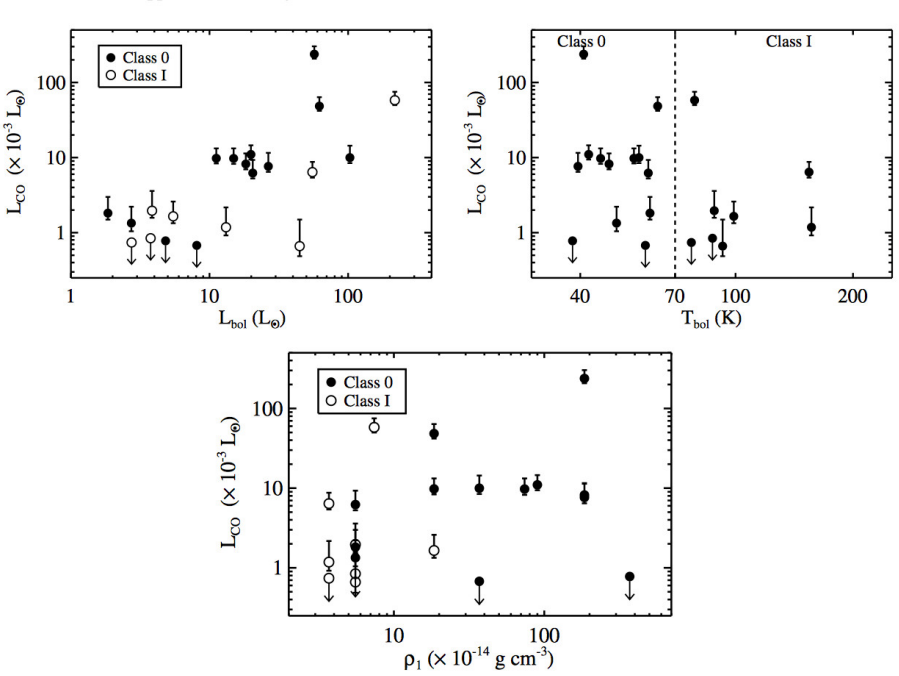

Figure 3.8: Total luminosity of the CO lines detected within the PACS wavelength range with S/N > 3σ as a function of L_{bol}, T_{bol}, and envelope density (ρ_1). Image adopted from Manoj et al. (2013).

3.2.3 Modelling SEDs of the protostars in the OMC-2 region

Several studies have been done by the HOPS team of the OMC-2 region (Adams et al. 2012, Furlan et al. 2014, Osorio et al, in preparation) including our contribution (González-García, in preparation).

The spectral energy distribution of the OMC-2 FIR 4 source (identified in the HOPS sample as HOPS 108) was studied, comparing to models that considered a protostar and disk, and combining near-infrared data from *2MASS* (Skrutskie et al. 2006), *SOFIA* data from Adams et al. (2010), *Spitzer* Orion Molecular Cloud Survey from Megeath et al. (2005), *Herschel* Orion Protostar Survey (HOPS; Megeath et al. (2010), and submillimeter *APEX* data with other near-infrared and millimetre data from the literature. Contrary to previous studies, which gave FIR 4 more than 2000 $L_{\odot}$, Adams et al. (2012) estimates for this object a luminosity in the range of 30-50 $L_{\odot}$ and infall rates $\sim 1\times10^{-4}$ $M_{\odot}$ yr^{-1}. FIR 4 is the most embedded source Class 0 protostar in the HOPS sample.

The study from Furlan et al. (2014) expanded the study from Adams et al. (2012) for HOPS 108 (or OMC-2 FIR4), to resolve the mystery of the protostar luminosity being measured as 1000 $L_{\odot}$ by Crimier et al. (2009) but 30 $L_{\odot}$ by Adams et al. (2012), using 3.6-870 μm images from Spitzer, Herschel and APEX. Furlan et al. (2014) found an emission peak in images at 8-70 μm, and a different emission peak at images 160-870 μm, as shown in Fig. 3.9. The first emission peak is considered to be at the protostar and the second, spatially more extended, to the large molecular cloud in which the protostar is forming, as shown in Fig. 1.18 in chapter 1. Furlan et al. (2014) used a more elaborate a grid of models developed for the HOPS program based on R statistic, (Whitney et al. 2003b,a; Terebey et al. 1984), and assigned to FIR 4 a luminosity of 17 $L_{\odot}$ and to the extended emission up to 100 $L_{\odot}$.

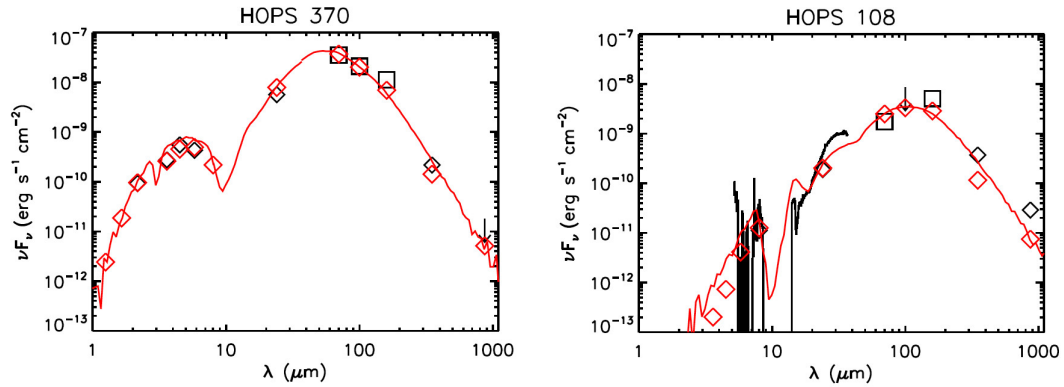

Figure 3.9: (*Left*) SEDs of HOPS 370 and (*right*) of HOPS 108, taken from Furlan et al. 2015.

Furlan et al (2015, ApJ submitted), extended her study of the SEDs to 330 protostars in the Orion star-forming region in the 1.2-870 μm range combining 2MASS, mid- and far-infrared data from Spitzer, Herschel and sub-millimeter photometry from the APEX telescope. The results of best-fitting of the flux distribution to a grid of 30400 protostar model SEDs, calculated using the 2008 version of the Whitney et al. (2003b,a) Monte

Carlo radiative transfer code (Stutz et al. 2013), which considers a protostar with a disk and an envelope with cavity carved in it, have conclude that in the HOPS sample, 92 objects are Class 0, 125 Class I, 102 flat-spectrum and 11 Class II objects. The analysis of the HOPS protostars SEDs by Furlan et al is an ideal sample to derive a better understanding of the early evolution of young stars, when the impact of the outflows and cavities carves are also considered in the study.

3.3 Data processing and analysis of the HOPS spectroscopic sample

Our role in the HOPS team is to provide a dedicate pipeline processing fine-tuned for the HOPS observing strategy. This pipeline can be used to produce the legacy products for the HOPS targets. We focused in particular on HOPS 370 and HOPS 108, both on their individual datasets (See Fig. 3.10) and on combining their observations to better study the interactions between them.

The PACS spectroscopic observations of the OMC-2 region were carried out using range spectroscopy mode to achieve a Nyquist-sampled coverage over 57-196 μm. The region centred on HOPS 370 was observed in the full PACS spatial resolution mapping mode, oversampling the beam by using a 3×3 raster in the blue channel and 2×2 raster in the red channel, with sub-pixel raster point/line step sizes of 3″and 4.5″, respectively. The region centred on HOPS 108 was observed in single-pointing mode. We applied the unchopped beam-modulation technique developed for crowded-field spectroscopy. Off-positions free of cloud emission of 2° from the target were observed to remove the telescope and sky background.

The Nyquist sampled wavelength range of 57-71 μm was observed in the third grating order (B3A), the range 71-98 μm in second order (B2B), and the range 102-196 μm in the first order (R1). The second (B2A) and third (B3A) grating orders were observed with the blue camera, while the first order (R1) spectra was taken with the red camera simultaneously with one of the blue observations. The broad-range spectral scans were repeated 2 times on each raster position for the mapping observations, and 4 times for the pointed observations, in order to achieve at least a 5σ detection for the diagnostic lines across the sampled area and to improve spectral sampling provided by the sub-pixel offsets between grating scans.

The HOPS 370 (FIR 3) mapping observation was composed of a sequence of on-target raster and off-target pointed observations which ensures the continuum signal-to-noise achieved per raster position is identical to the signal-to-noise achieved within the single off-position observation. The off-block is subtracted from every raster position of the corresponding mapping observation. To shorten the timescale between on- and off-blocks, each of the B3A/R1 and B2A/R1 observations were split up into two identical subgroups, resulting in four on- and off observations pairs in total, for the extra cost of $\sim$ 15 min instrument and spacecraft overheads. For the 3×3 blue rasters $\sim$ 89% of time was spent-on

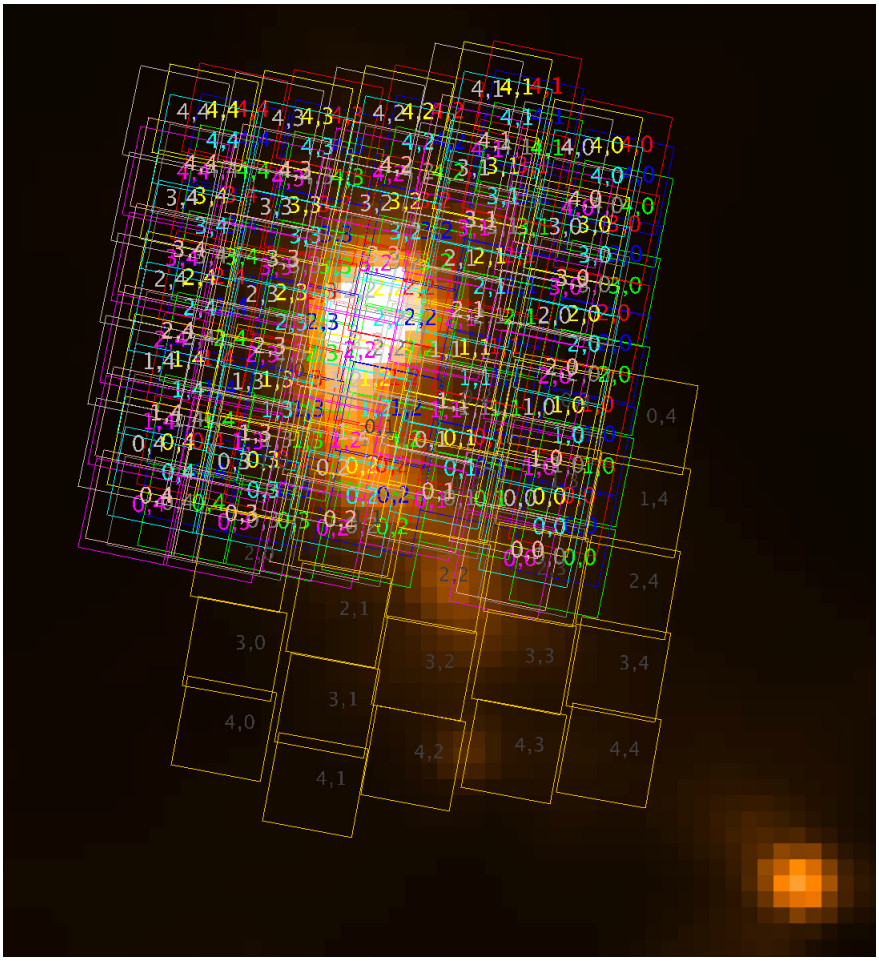

Figure 3.10: PACS 70 μm image of the HOPS sample for the OMC-2 region. Overplotted the footprint of the PACS spectrometer observations for HOPS 370 (top) a 3×3 raster and HOPS 108 (bottom) a staring observation.

source, while for the 2×2 red rasters ~ 75% of the time was used for on-target observations exhibiting an excellent observing efficiency. The HOPS 108 (FIR 4) pointed observations, followed a similar design principle except the choice of wavelength range combinations introduced a slightly improved spectral data redundancy and deeper detection limit. The on-source time consisted of ~ 50% of the total observing time of pointed observations.

HOPS 370 was observed in 2011 August over a total of 10.4 hrs (including overheads), and HOPS 108 was observed on 2012 February over 2.8 hrs. Tables 3.1 and 3.2 are the log of PACS and SPIRE observations of the OMC-2 region.

Table 3.1: Log of PACS photometer observations

HOPS ID	ObsID	Date	Duration (s)	RA (hh mm ss)	DEC (deg)	Observing mode	Spectral range (μm)
370	1342205228	2010-09-28	1645	5 35 24.710	−5 09 06.02	scan 45 °	70/160
370	1342205229	2010-09-28	1645	5 35 24.710	−5 09 06.02	xscan 135 °	70/160
370	1342205230	2010-09-28	397	5 35 24.710	−5 09 06.02	scan 45 °	70/160
370	1342205231	2010-09-28	397	5 35 24.710	−5 09 06.02	xscan 135 °	70/160
108	1342205226	2010-09-28	1229	5 35 26.280	−5 06 35.24	scan 45 °	70/160
108	1342205227	2010-09-28	1229	5 35 26.280	−5 06 35.24	xscan 135 °	70/160

Table 3.2: Log of PACS and SPIRE spectroscopic observations. The rasters observations are reported as $n \times m$, which are step number times step size.

PACS							
HOPS ID	ObsID	Date	Duration (s)	RA (hh mm ss)	DEC (deg)	Observing mode	Spectral range (μm)
$370^{(off)}$	1342227763	2011-08-30	989	5 32 18.750	−6 24 27.50	pointed	57-71&170-213
$370^{(on)}$	1342227764	2011-08-30	8933	5 35 27.670	−5 09 35.10	3×3	57-71&170-213
$370^{(off)}$	1342227765	2011-08-30	989	5 32 18.750	−6 24 27.50	pointed	57-71&170-213
$370^{(on)}$	1342227766	2011-08-30	8933	5 35 27.670	−5 09 35.10	3×3	57-71&170-213
$370^{(off)}$	1342227768	2011-08-30	1520	5 32 18.750	−6 24 27.50	pointed	50-98&102-196
$370^{(on)}$	1342227769	2011-08-30	6083	5 35 27.670	−5 09 35.10	2×2	50-98&102-196
$370^{(off)}$	1342227770	2011-08-30	1520	5 32 18.750	−6 24 27.50	pointed	50-98&102-196
$370^{(on)}$	1342227771	2011-08-30	6083	5 35 27.670	−5 09 35.10	2×2	50-98&102-196
$108^{(on)}$	1342239690	2012-02-27	1930	5 35 27.070	−5 10 00.40	pointed	50-71&102-142 &170-213
$108^{(off)}$	1342239691	2012-02-27	1930	5 32 18.750	−6 24 27.50	pointed	50-71&102-142 &170-213
$108^{(off)}$	1342239692	2012-02-27	3079	5 32 18.750	−6 24 27.50	pointed	71-98&141-196
$108^{(on)}$	1342239693	2012-02-27	3079	5 35 27.070	−5 10 00.40	pointed	71-98&141-196
SPIRE							
108	1342242624	2012-03-12	9203	5 35 27.070	−5 10 0.40	raster	250 − 650

4

Calibration and data processing pipelines

4.1 The Herschel Interactive Processing Environment

The Herschel Interactive Processing Environment HIPE (Ott 2010) is the software application for the processing and analysis of Herschel data. This application provides many interactive analysis tools for examining the various intermediate and end data products, together with a scripting environment based on Jython. By using scripts, users can run standard processing procedures or write their own specific analysis procedures.

Every year there is an update of the pipeline and calibration trees which creates a new version of HIPE for the astronomical community and which is used for the bulk reprocessing of the complete Herschel Archive data.

HIPE provides code from the Herschel Common Science System (HCSS) framework, instrument specific code (respectively PACS, SPIRE and HIFI code), and documentation. Data processing and data analysis can both be done within HIPE.

The standard processing of an observation is done with scripts called **pipelines**. A pipeline is a combination of tasks, applied in a sequential order to the raw instrument data, which at the end generates a calibrated map/cube/spectrum, being science-calibrated in products with physical units. The different flavours of pipelines, per instrument and observing mode, are available via a HIPE menu.

Each of the observations collected by the Herschel satellite are automatically processed

in the SPG (Standard Product Generation) environment at the Herschel Science Centre (HSC) in a bulk processing mode. The raw and intermediate levels are wrapped in a container called Observation Context and ingested into the Herschel Science Archive (HSA). Each Observation Context (and all the levels inside: auxiliary context, calibration context, level 0 context, level n context, quality context) have an associated SPG version and calibration tree version. Scientific product analysts at the HSC perform manual quality control for each scientific observation. The most interesting checks for the astronomer, to assess whether the observation retrieved from the Herschel Science Archive should or should not be reprocessed for his/her science are:

- The SPG (Standard Product Generation) version which with this observation was last processed at the HSA.
- The latest HIPE version. Any updates between the HIPE version and the SPG version?
- Calibration version tree used for the SPG processing.
- Calibration version tree available in HIPE and any updates between the two versions.
- Whether the best possible pointing reconstruction was applied.
- How well the pipeline used by the SPG environment deals with the type of data (AOT, type of source) of their observation.

4.2 The PACS photometer pipeline for the OMC-2 region

PACS raw photometer data are distributed in 32×64 detector pixels arrays (for the blue and green bands) and 16×32 detector pixel arrays (for the red bands).

PACS photometer Observation Contexts contain a red and a blue camera data at each reduction level. For the different PACS processing levels, the data are organised in different formats:

- **Frames:** are the class of product at Level 0 (raw), 0.5 and 1 (partially-reduced). The data are organised along the timeline, in the order they were collected. A separate data stream is provided from each detector pixel. Each data point corresponds to a different time (1/40 sec readout) and, because the telescope is continuously scanning the sky, to also different points on the sky.
- **Maps or Single Images:** are Frames cleaned of instrument effects and turned into 2D maps, i.e, each pixel in a map is the flux of that part in the sky, created from a reorganisation and merging of the data time-line streams in the frames. The units are Jy/pixel (Level 2, Level 2.5 and Level 3 contexts).

In the pipeline (Wieprecht et al. 2009) options are :

- Scan map and mini map (this also includes SPIRE-PACS parallel mode).
- Chopped pointed source (only used for calibration)

The PACS photometer observations we analysed for this work used the scan map mode. The log of the observations can be found in Table 3.1.

The PACS photometer observations were processed by the HOPS team (Ali et al, in preparation) following the standard PACS photometer pipeline up to Level 1 but with customised map construction method/task.

4.2.1 Standard Herschel PACS data reduction for scan map observations

The tasks applied to the raw data (Frames) are common to all the PACS photometer pipelines. Here we list Level 0 data to Level 1 steps. At the end of the Level 1 the PACS data are calibrated in Jy/detector pixel.

(1) Data retrieval from the HSA, with *getObservation*.

(2) Propagate the meta data from the observation context to the level-0, with *pacsPropagateMetaKeywords*.

(3) Construction of the calibration tree, where latest calibration files are stored, with *getCalTree*.

(4) Add the pointing information to the Status table.

(5) Separate science from non-science data (i.e, internal calibrator measurements), by *detectCalibrationBlock* and *removeCalBlocks*.

(6) Identify bad data and generate a mask (BADPIXELS masks) by *photFlagBadPixels*, the cross-talk effect, by *photMaskCrosstalk*, and the saturated pixels by *photFlagSaturation* generating the masks SATURATIONHIGH and SATURATIONLOW.

(7) Convert digital units to Volts, by *photConvDigit2Volts*.

(8) Translate the time assigned to the data from spacecraft counter to UTC, by *addUtc*.

(9) Calculate the chopper positions respect to the optical axis and record in the Status table, by *convertChopper2Angle*.

(10) Converts Volt to Jansky and apply flatfield correction, by *photRespFlatfieldCorrection*

(11) Apply non-linear flux corrections by *photOffsetCorr* and *photNonLinearityCorrection*.

(12) For Solar System objects, correct the data to a fixed position in the sky, by *correctRaDec4Sso*.

(13) Apply the temperature evaporation correction by *photTevCorrection*.

From Level 1 to the end Level we can select between different pipelines depending on our scientific case:

- Point sources: Apply the high-pass filtering and specProject tasks.
- Extended sources: Apply GLS a mapmaker (Unimap or MadMap) or a destriper mapmaker (JScanMap).

As our scientific case is an extended source, we used a GLS mapper: MadMap. This method is based on MadMap IDL code translated into HIPE by the PACS team. The MADmap algorithm, which stands for Microwave Anisotropy Dataset mapper (Cantalupo et al. 2010) can remove the uncorrelated one-over-frequency noise (1/f) from bolometer Time Ordered Data (TOD), preserving the large scale spatial signal distribution. The steps are:

(1) Build the TOD

- Define the astrometry of the output map
- Remove the bad detector pixels
- Compute the indices of the sky pixels, which are the projection of each input detector pixel into the output sky grid.
- Remove glitches from timeline data
- Divide the data by the scan legs
- Divide the data per detector pixel

(2) Run MadMap task

4.2.2 Evolution of data processing pipelines from HIPE 8.0 data to HIPE 12.1 data

New algorithms for processing extended sources were developed after we had reduced our data, and these show a better result than MadMap in some cases. One of these tasks is also based on GLS mapmaker, called *Unimap* (Palmeirim et al. 2013; Piazzo et al. 2015) and the other is based on a destripper mapmaker, *JScanMap* which is a conversion of the well known idl Scanamorphous (Roussel 2013) in Java code by the PACS team.

4.3 The PACS spectrometer pipeline

PACS spectrometer Observation Contexts are organised into several data processing levels. At each level a data container is created which contains data at that particular processing level. Each container has a number of data chunks, the so called slices. A **slice**

contains the data from a unique logic block, e.g, for the same spectral band or line, for a single nod, for the same repetition cycle and for a single pointing in the sky. See de Jong et al. (2012) for more details about this slicing framework.

At the different PACS processing levels the data are organised in different formats:

- **Frames:** name given to the class of products generated with the PACS raw data. Data are arranged following the 25 × 18 detector layout, although only a 25 × 16 subarray is used for science. The 16 in the array are from the 16 spectral pixels, and the 25 are the 25 spaxels of the PACS IFU. (Level 0 and Level 0.5 context).

- **PacsCubes** : Frames cleared, calibrated and reorganised into cubes of λ, RA,Dec with several individual spectra within each spaxel - one for each repetition and each of the 16 spectral pixels. (Level 1 context).

- **RebinnedCubes:** The individual spectra in each spaxel of the PacsCubes have been spectrally merged into one spectrum. (Level 2 context).

- **Spectral Cubes:** Drizzle, interpolated or projected cubes, spatially resampled and mosaicked. (Level 2 context). The three types of cube result from three different algorithms offered.

The PACS spectrometer pipeline (Schreiber et al. 2009) choices are for :

- Chop/Nod line and short range observations

- Chop/Nod range and SEDs observations

- Unchopped line observations

- Unchopped range, for single or combined observations

The HOPS 370 (FIR 3) mapping observation was composed of a sequence of on-target raster and off-target pointed observations, such that the continuum signal-to-noise achieved per raster position is identical to the signal-to-noise achieved within the single off-position observation.

The HOPS108 (FIR 4) pointed observations followed a similar design principle except the choice of wavelength range combinations introduces a slightly improved spectral sampling (a higher data redundancy and a deeper detection limit). The on-source time consists $\sim$ 50% of the total observing time of pointed observations. Details from these observations (on- and off-target) are listed in Table 3.2 in Chapterchap:HOPS.

Therefore we describe here the standard processing steps applied for these observations. Comparison to other modes and the evolution of the pipeline along the different HIPE versions will be mentioned briefly at the end of this section.

4.3.1 Standard Herschel PACS data reduction for unchopped range observations

The tasks applied to the raw data (Frames) **from Level 0 data to Level 0.5** are common to all the PACS pipelines.

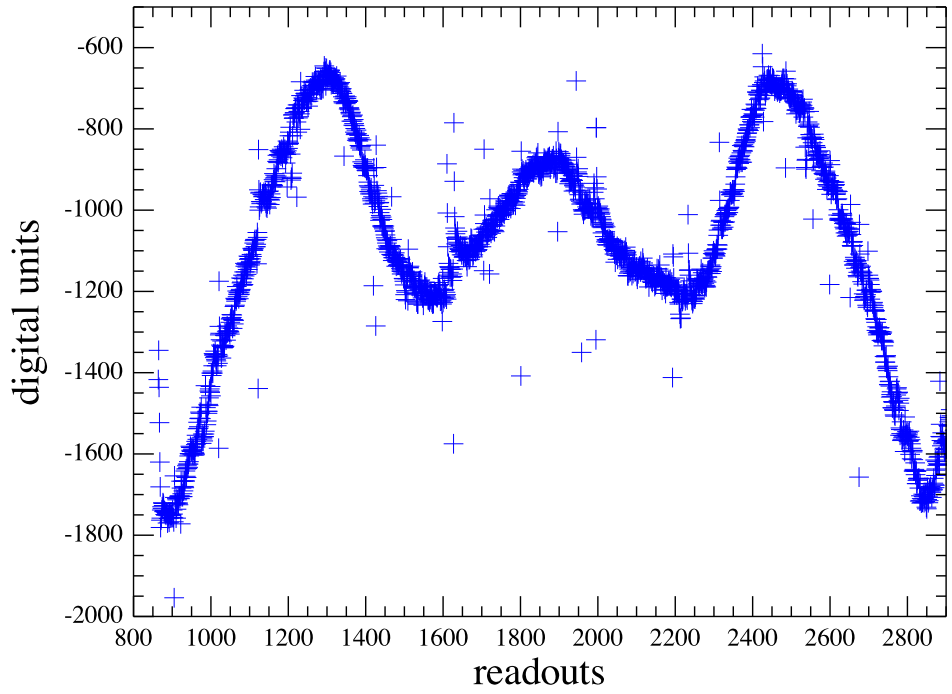

Figure 4.1: Level 0 for one of the HOPS observations from this thesis (1342227764). Step (4) in the process. Y axis is digital units (i.e, instrumental) and x axis is readouts, i.e: a simple counter of data points.

(1) Data retrieval from the HSA, with *getObservation*.

(2) Propagate the Meta data from the observation context to the level-0 products, with *pacsPropagateMetaKeywords*.

(3) Construction of the calibration tree, where latest calibration files are stored, by *getCalTree*.

(4) The data at the point are in instrumental units and are unprocessed. Fig 4.1 show an example of such a raw dataset. The wavelength range covered by this observation is 145-210 μm . The grating scans successively with time, so each readout is a different wavelength. The grating scanned first from low to high wavelength and then scanned a second time from high to low wavelength - here the symmetry in the plot.

(5) Identify saturated data and generate a mask (SATURATION), by *specFlagSaturationFrames*.

(6) Convert raw data into units of V/s by *specConvDigit2VoltsPerSecFrames*.

(7) Separate science from non-science data (i.e, internal calibrator measurements), by *detectCalibrationBlock*.

(8) Translate the time assigned to the data from spacecraft counter to UTC, by *addUtc*.

(9) Assign coordinates (RA,Dec) to the central spaxel, by *specAddInstantPointing*.

(10) For Solar System objects, correct the data to a fixed position in the sky, by *correctRaDec4Sso*.

(11) Identify the chopper or nodding position where the data were collected and insert this information in the *Status* table, by *specExtendStatus*. The *Status* table is a collection of *status* values of the instrument at each point in time during an observation. See Fig. 4.2.

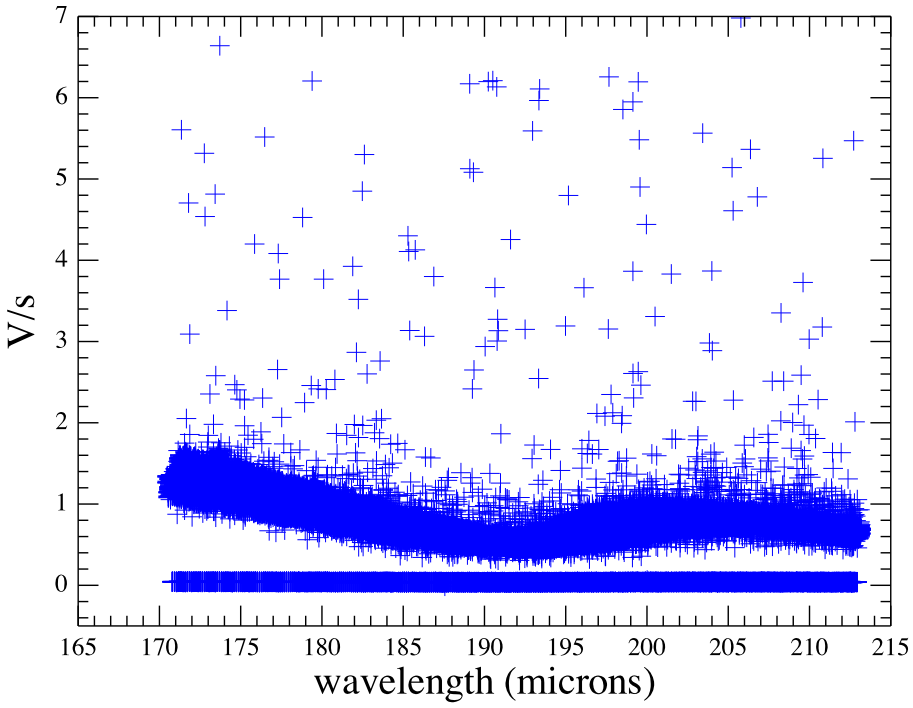

Figure 4.2: Data structure at step (11) of the pipeline applied from Level 0 to Level 0.5. The data units are in Volts per second. The data at value zero are bad data, which will are masked by the pipeline.

(12) Convert chopper positions to sky coordinates, by *convertChopper2Angle*.

(13) Assign to every pixel its (RA,Dec) position and store them in the BlockTable of the slicedFrames.

(14) Translate index array to wavelength array and identify data collected outside the filter bands to generate a mask (OUTOFBAND), by *waveCalc*.

(15) Correct wavelengths for the Herschel velocity, by *specCorrectHerschelVelocity*

(16) Identify logical blocks, which will allow a logic data-slicing, by *findBlocks*

(17) Identify bad and noisy pixels and store them in the BADPIXELS and NOISYPIXELS masks, by *specFlagBadPixelsFrames*.

(18) Slice the data according to slicing rules (i.e: wavelength block, pointings, nod, on to off-source) by *pacsSliceContext*.

(19) Identify data collected during movements between chopper and grating positions and generate masks (GRATMOVE and UNCLEANCHOP), by *flagGratMoveFrames, flagChopMoveFrames*. Fig. 4.2 is the same data as in Fig. 4.1, but now in V/s versus μm . The bad data, masked in previous tasks, are shown.

(20) *only for Unchopped observations* Flag that data were not following a correct chopper pattern, by *specAddGratingCycleStatus*.

From Level 0.5 to Level 2, the pipeline suitable for the observing mode is selected. For our scientific goal we used the standard unchopped range pipeline *Combine On-Off obs* in HIPE 12.1 and calibration version 65, with some extra tasks that we will explain in chapter 7.

The standard pipeline for the unchopped range mode processes the on- and the off-source observations separately and then combines them at the end. Here we provide a brief description of the tasks applied.

(1) Identify glitches in the data (i.e, cosmic rays) and generate a mask (GLITCHES), by *specFlagGlitchFramesQTest*.

(2) Activate existing masks and translate capacitance settings to the lowest detector, by *convertSignal2StandardCap*.

(3) Calculate the **detector response** and the **dark current** by comparing data collected from the internal calibration source during the observation and the existing calibration information (from the astronomical calibrators). The result is stored in the product **csResponseAndDark**. The task responsible for this is called *specDiffCs* and the calibration files used are *ObservedResponse*, which contains the information for calibration observations (stars, asteroids, Neptune and Uranus) and *calSourceFlux*, where the absolute fluxes from the calibration block are recorded.

(4) Subtract the dark current, by *specSubtractDark*.

(5) Apply the relative spectral response function, taken from the calibration tree with *rsrfCal*.

(6) Apply this correction to the absolute response stored at CsDarkAndResponse, by *specRespCal*.

(7) Apply the spectral flat-fielding to normalise the spectra from the 16 pixels for each spaxel independently. Each pixel has data from at least 2 grating scans (2 spectral segments), and hence each spaxel has at least 16×2 spectral segments, which need

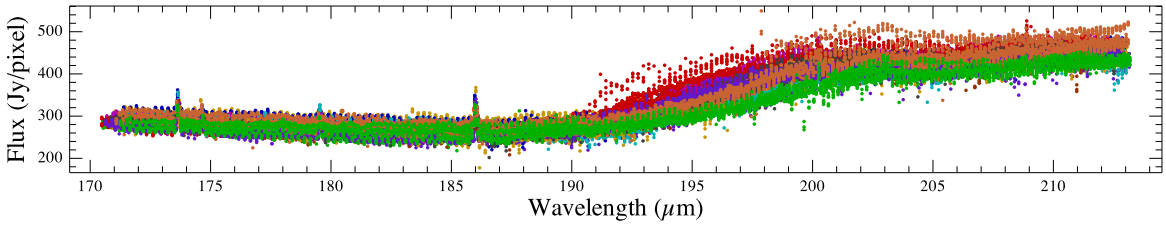

Figure 4.3: Data structure at state (6) of the pipeline applied from Level 0.5 to Level 2, just before the FlatFielding task. Each color is the spectrum from a different spatial pixel of the central spaxel (module 12). It is clear that the different pixel-spectra have offsets with respect to each other correct for this.

to be normalised to the average response before a subsequent spectral averaging is done. This is to improve the signal-to-noise of the final spectra. This is done with *specFlatFieldRange*. This requires computing a reference spectrum per spaxel (using only the non-masked data) and computing a fit to the continuum for all the spaxel populations, shifting these fits to the reference spectrum fit. This normalises each separate spectrum (of the different scans and different pixel) to the mean spectrum in the spaxel . The red leak spectral range, ($\lambda \geq$ 200 μm) are removed, as the standard calibration is invalid at these wavelengths. The fit consist of a polynomial, usually of order 3 to 5. Compare Fig. 4.3 to Fig. 4.4 to see the effect of flat-fielding.

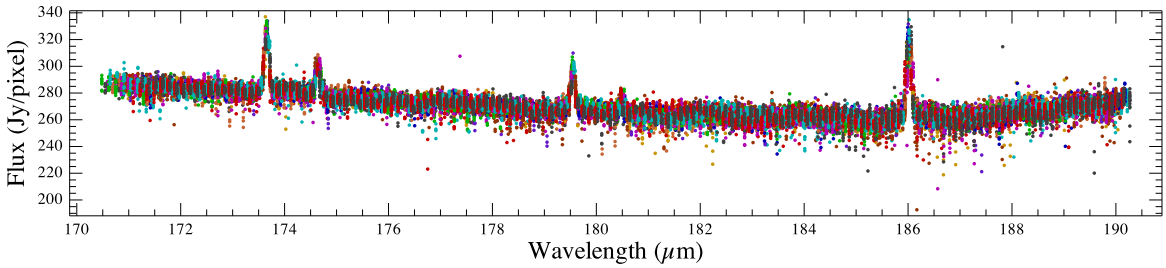

Figure 4.4: Data after flat-fielding now.The different coloured spectra now lie on top of each other: compare to Fig. 4.3. The red part of the spectrum has been cut as these data could not be calibrated at the time of our data reduction.

(8) Transform slicedFrames to slicedCubes create the first cube of the pipeline, with *specFrames2PacsCube*

(9) Set the metadata of the cubes to indicate whether the observation is at the On- or Off-target position, to be able later to identify the cubes to be subtracted.

Already the Level 1 products have been generated here and these are the slicedCubes. To complete the processing up to the Level 2, we execute the following steps:

(1) With *waveGrid* from the on-target data a spectral grid is calculated.

(2) Identification of outliers is done and stored in a mask (OUTLIERS), by *specFlagOut-*

liers.

(3) The slicedCubes spectra in each spaxel are averaged, to create slicedRebinned-Cubes, by *specWaveRebin*, along the spectral grid previously created.

(4) The off-source data are subtracted from the on-source data. See Fig. 4.5.

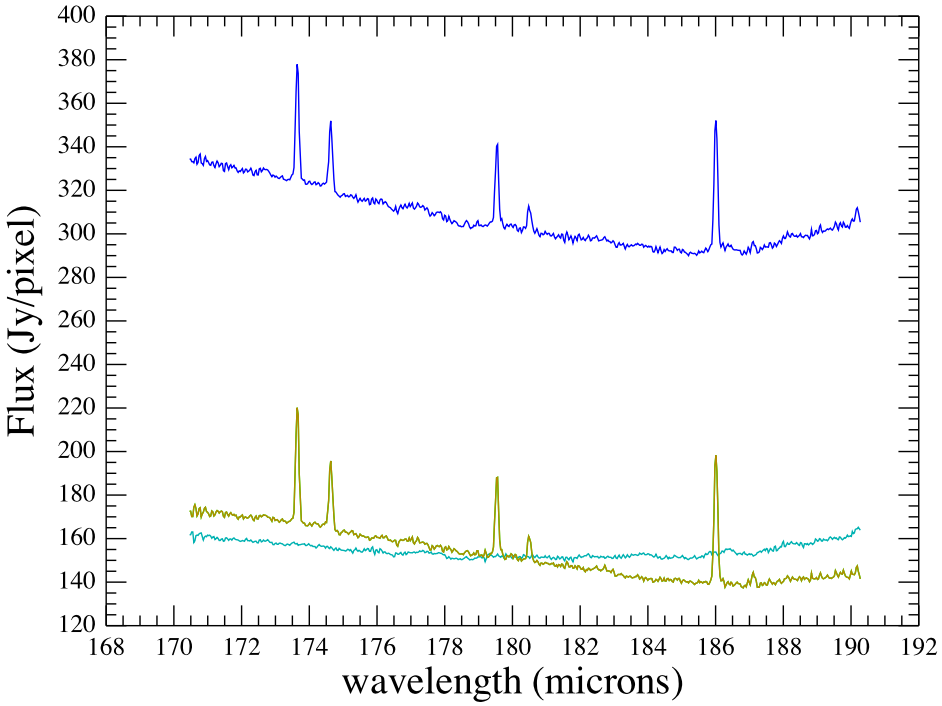

Figure 4.5: A spectrum from one spaxel of one raster position for the same observation shown in the previous plots. Blue curve are the on-source data and green are the off-source data. The brown spectrum is the on-off. This is the result of running the standard pipeline script for unchopped raster observations.

(5) The cubes are mosaicked, i.e: spatially-regridded onto a regular grid. Depending on the method we used we obtained:

- ProjectedCubes, by *specProject*,
- SpecInterpolatedCubes, by *specInterpolate*, and/or
- DrizzleCubes, by *drizzle*

4.3.2 Evolution of data processing pipelines from HIPE 8.0 to HIPE 12.1

For all pipelines :

- There is a ~10% continuum flux difference between cubes created by HIPE 12.1 and HIPE 8.0. This is due to the different methods used to calculate the absolute response. At the beginning, the ground-based pre-flight *nominal response* was used. Later in the mission (HIPE 12) the measurement per observation from the PACS internal calibration sources was used.

- An improvement of the absolute flux calibration, as the spectra from the astronomical calibration sources were extracted from the cubes in such a way as to compensate for pointing jitter. This produced a cleaner calibration with less scatter. The improved results are used by the *specDiffCs* task which fills the the variable *csResponseAndDark*, that is used at the task *specRespCal*.

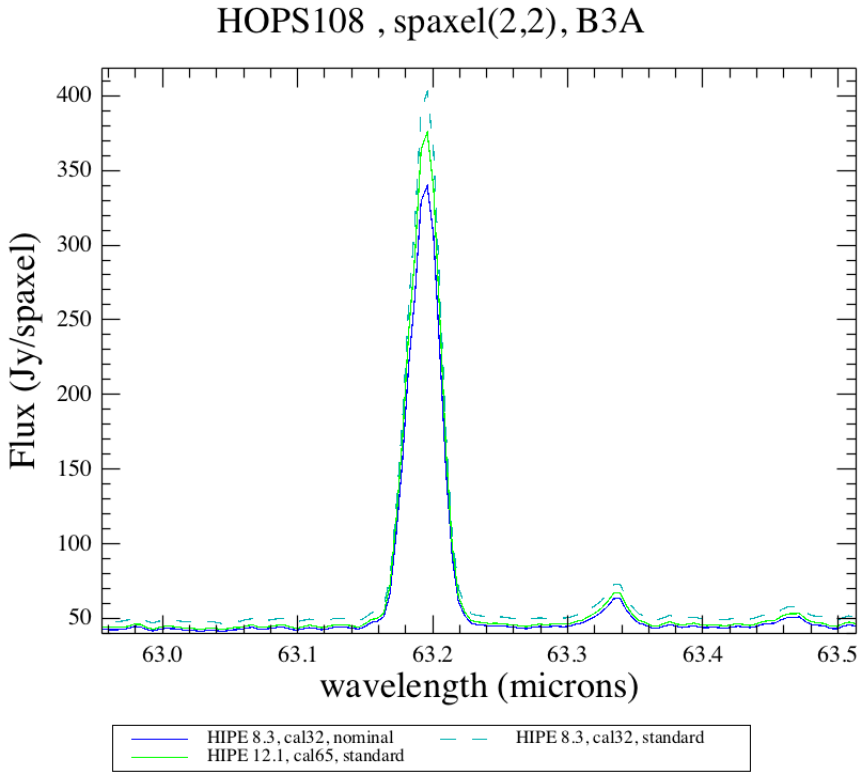

Figure 4.6: Comparison of the spectrum for the PACS central spaxel, from a PACS rebinned cube, between HIPE 8 and HIPE 12.

For the Unchopped range pipeline:

- Different methods were developed to subtract the off-position for unchopped range observations. However, as can be seen at Fig. 4.7, all provide a similar result for one of our observations when used in the same HIPE processing version.

- The transients correction task for unchopped observation was not available until HIPE 13 and so we could not use it for our work. This task corrects from transients which may occur at a point in time in the observation.

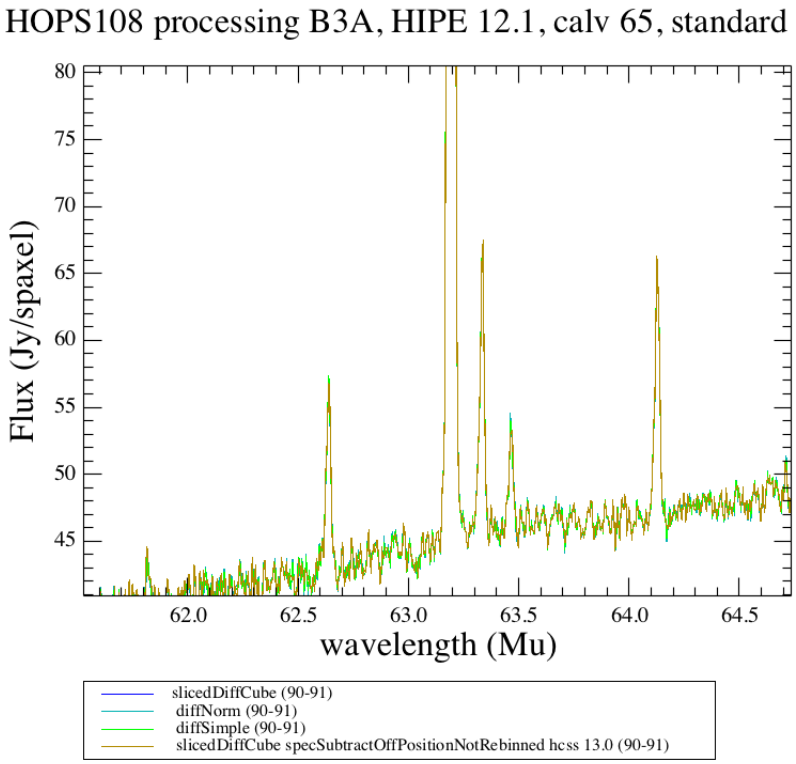

Figure 4.7: Comparison of the spectrum for the central module from a PACS Level 1 cube, when applying different off subtraction methods in HIPE 12.1 (calibration version 65).

A transient is an event that changes the response of the detector, creating effects similar cosmic ray hits: a sudden increase in the flux in the spectrum followed by a slower decay back to the correct level. The effect of not correcting transients is a lower signal-to-noise in the final cubes. The specific *baseline subtraction* task we used for our processing in chapter 7 reduce the transients effect. Therefore we are sure that our cubes have a high signal-to-noise.

We discussed how we modified the pipeline to improve these standard results in chapter 7.

4.4 The SPIRE spectrometer pipeline for the OMC-2 region

The data of SPIRE spectrometer are provided as Observation Contexts, which are all the raw and reduces data of all bands and all pointings.

At the different SPIRE processing levels the data are organised in different formats:

- **Raw SPIRE Timeline (RST)**: Contains many separate datasets (one per telemetry packet produced by the satellite). Level 0 context.

- **Timeline**: Timelines converted into physical units. Level 0.5 context .
- **Interferogram** : one per scan. Level 1 context. The units are Volts.
- **2D spectra**: A 2D spectrum from each sky position. The units are W/m^2/Hz/sr. Level 2 context .
- **Cube**: Spectral cubes generated from all the detectors and pointings reorganised on a rectangular equidistant spatial grid. The units are W/m^2/Hz/sr. Level 2 context.

The pipeline paths altered when reducing spire spectrometer data are:

- SOF1: for "sparse" observations
- SOF2: for "intermediate" and "full" observations

The SPIRE observation we analysed for this work, as part of the HOPS data collected for the OMC-2 region, has the obsid 1342242624. It is a full raster and we followed the standard processing steps for SOF2 SPIRE spectral mapping observation in HIPE 12.0, which we describe below.

Here we describe the SPIRE spectrometer pipeline from Level 0 to Level 1. This consists of 8 main steps:

(1) Data retrieval from the HSA, with *getObservation*.

(2) Construction of the calibration tree, where latest calibration files are stored, by *spireCal*.

(3) Retrieval of auxiliary products required during the processing.

(4) Modification of data timelines: by time-domain operations on detector samples. In detail the tasks applied here are:

- Computation of Beam Steering Movement (BSM) Angles Timeline (BAT), which contains the position of the BSM as a function of time in spacecraft coordinates. This value is not a direct measurement but obtained from the comparison of the sensor signals from the housekeeping data (1Hz rate) and the BSM position table in the calibration tree, where all spacecraft (Y,Z) angles for a given chop and jiggle BSM sensor are given.
- Removal of glitches (first level deglitching) caused by cosmic ray hits and/or impulse-like events in the detectors using wavelet-based methods.
- Identification and removal of electrical crosstalk.
- Correction for non-linearity in the response of the detectors.
- Correction of missed data samples (clipped samples) identified by the Engineering conversion pipeline (up to Level 0.5).
- Correction of the signal time-shift between thermal response of the detectors and the combination of the electronics read-outs.

- Removal of correlated noise due to temperature fluctuations.

(5) Creation of interferograms to obtain the source spectrum from the measured data. The detector samples must be linked with the position of the spectrometer mechanism (SMEC) in the form of interferograms. A proper transformation of the interferogram with the Discrete Fourier Tranform is the goal. As their samples are decoupled in rate and time, the following actions are required.

- Interpolation of the the spectrometer mechanism (SMEC) timeline from non-uniform to uniform in position, in terms of optical path difference (OPD).
- Merging the spectrometer detector and the mapped SMEC timelines.

(6) Modification of Interferograms,

- by the subtraction of the background signal, arising from Herschel mirror, internal calibration sources, and from beamsplitter emission.
- by a baseline removal of the detector signal. The interferometer spectra are composed of two components: one constant and one modulated as a function of optical path difference (OPD). The first does not contain spectral information, but has a signal offset. The evaluation and removal of this offset is done on the measured interferogram, on a detector-by-detector and scan-by-scan basis, by fitting with a fourth order polynomial.
- by identification and removal of glitches (second level deglitching). This is done by comparing, on a OPD-position-by-OPD-position basis, the samples from one scan to this from all other scans in the same observation.
- by phase correction.
- by multiplication with a apodizing function.

(7) Transformation of interferograms into spectra via Fourier Transform process.

(8) Modification of the spectra

- by flux conversion.
- by optical crosstalk removal.
- by spectral intensity averaging, across all wavenumber scans.

The final step, required to transform the SPIRE Level 1 Spectrometer Detector Spectrum (SDS) products to the SPIRE Level 2 Spectral Cube products, is the spatial regridding.

The result from the spectrometer pipeline is a single spectrum per detector. Our SPIRE full mapping observations followed a honeycomb pointing pattern and for the Level 1 SDS product is an interpolated cube with equidistant sampling in the two spatial dimensions. The spatial grid is equidistant in frequency.

5

Spectral cube reconstruction techniques

The PACS spectrometer pipelines generate three types of hyper-spectral cube as Level 2 products. They are the result of applying the *drizzle*, *specProject* or *specInterpolate* tasks. These tasks reorganise the *PacsCube* or the *PacsRebinnedCube* into regular spectral and spatial grids, mosaicking the different pointing positions from an observation onto a single mosaic cube with an user-defined spaxel size.

5.1 Construction of the spectral grid

The **spectral grid** is constructed within a task called *wavelengthGrid*. We explain what this task does and also take the chance to explain the *upsample* and *oversample* concepts, which are also used in the construction of the spatial grid.

The "PacsCube" contains a dot-cloud of calibrated data, where each dot corresponds to a spectrum from a single spaxel: each spaxel contains 16 data points per grating position - for the 16 spectral pixels - and these are repeated for each grating position sampled during the observation. Note that the grating was always scanned twice, so the entire wavelength range is sampled twice. This dot cloud has to be resampled and binned both in the spatial and spectral domain in order to create a mosaic spectral cube with an equidistant wavelength grid.

The wavelength grid is set by the parameters: oversample, upsample and a starting wavelength point. Considering the whole spectral range from the observations $[\lambda_{min}, \lambda_{max}]$, and

λ_i the central wavelength of the resolution elements, increasing i along the spectral range as λ_0 , λ_1, λ_2,...,λ_n, we have,

$$\lambda_0 = \lambda_{min} \tag{5.1}$$
$$\lambda_{i+1} = \lambda_i + \frac{\Delta\lambda_i}{oversample}$$

The *upsample* value will increase the redundancy. The shift from one spectral bin to the next is of 1/*upsample* times its width. Therefore, instead of having a list of central wavelengths as λ_0 , λ_1,..,λ_n we have each bin divided into smaller ranges by λ_{00} , λ_{01},...,λ_{0n}, ...to λ_{n0} for bin 0, λ_{n1} for bin 1,...,λ_{nn}, taking index j values between 0 and *upsample* -1.

$$\mathrm{d}w_i = \frac{\lambda_{i+1} - \lambda_i}{upsample} \tag{5.2}$$

$$\lambda_{ij} = \lambda_i + j \times \mathrm{d}w_i \tag{5.3}$$

The width of a bin k can be obtained as:

$$\Delta\lambda_k = (\lambda_{k+1} - \lambda_k) \times upsample \tag{5.4}$$

To generate the spectral grid in our processing, we selected the values of *oversample*=2 and *upsample*=1 (each bin is independent of the next, therefore is no dependence in the data points of the bins). This allows us to measure the true *rms* noise from the spectral continuum, as the standard deviation of the continuum is that depending only on the individual measured data-points.

Now we will briefly describe the different algorithms which make use of the waveGrid method to reorganise the data on new spectral grid and spatial grids (detailed information is available from the Pacs Data Reduction Guide (*PDRG*)).

5.2 Naive reconstruction (specProject) algorithm

The specProject algorithm was developed for the PACS integral field unit (IFU) spectral data and is available in HIPE since HCSS 2.0 as a Java task developed by the PACS ICC. This task converts a spatially irregularly gridded collection of spectra (from PacsRebinnedCube) onto a spatial grid of regular, small, square spaxels. For that, SpecProject determines the flux from the input spaxels that affect each output spaxels and its neighbours. Weights are applied to ensure flux conservation in this overlap. The output spaxels are smaller than the input spaxels: the recommended output spaxel size is 3″. The user may decide to set this value (or a different one) or provide as input a full WCS to grid onto.

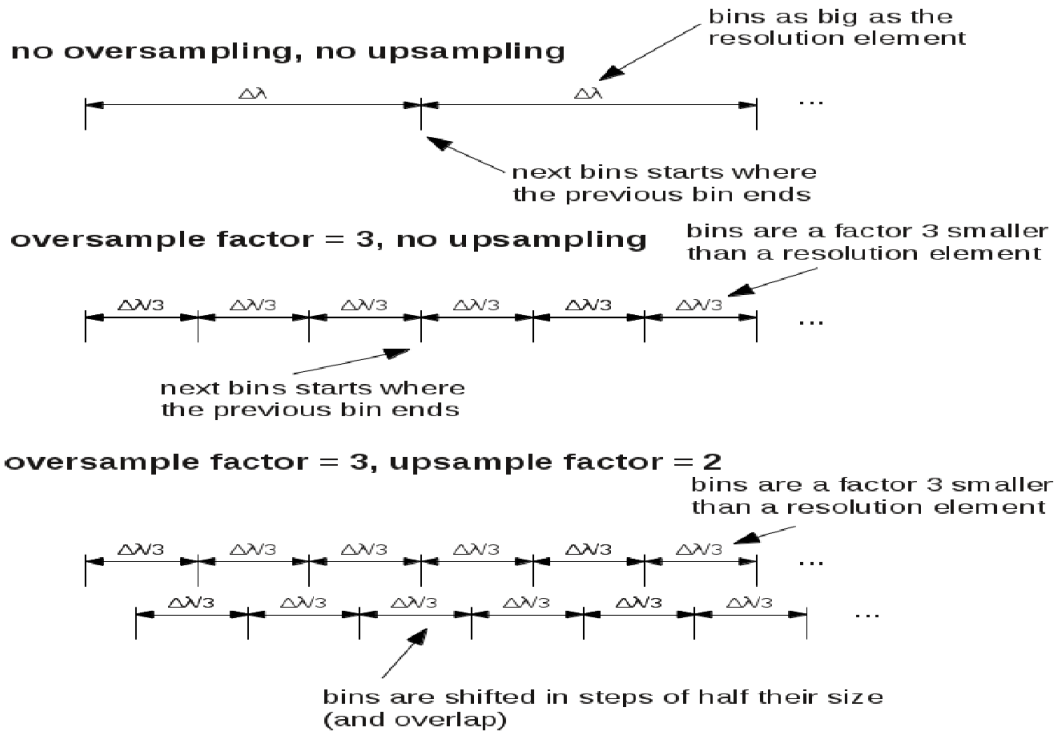

Figure 5.1: Explanation of *oversample* and *upsample* concepts, applied for the generation of the spatial and spectral grids (figure from S.Regibo, 2014)

The specProject task performs very efficiently (in time and memory requirements) for all types of observations (range and line scans, chop/nod and unchopped, pointed and raster) irrespective to the length of the spectral range.

5.3 Drizzling algorithm

The drizzle algorithm was developed for the HST images (Fruchter & Hook 2002) and adapted for the PACS integral field unit (IFU) spectral data (Regibo 2012) since HIPE 11.0. The goal of this algorithm is the recovery of the spatial information for Nyquist or over-sampled maps, by taking advantage the redundant information from a position in the sky (ra,dec) of dithered observations (mapping observations).

The quality of spectral cubes, the 2d image slices at each wavelength in a cube, can be greatly improved by combining all sub-spaxel dithered 2d slice images. This what drizzle and specProject do when working on mapping observations. Each of the spaxels from the different pointings can be thought of as sampling a final, higher-resolution spectral-image, which is the *true image* of the sky convolved with the beam and the spaxel shape. However, the simple projection of specProject generally introduces additional blurring due to convolution with the spaxel shape. It is to overcome this that the drizzle task was

created for PACS mapping observations.

The drizzle algorithm is conceptually straightforward. Spaxels in the input cubes, for each pointing in the raster, are mapped into spaxels in the output grid - this taking place at each wavelength of the spectral range , i.e. spectral image by spectral image - taking into account shifts and rotations between each image, (the RA, Dec in a cube in fact changes slightly with wavelength). To avoid convolving the image with the large spaxel *footprint* of the PACS IFU, drizzle allows the user to shrink the pixel before it is averaged into the output image, through the *pixfrac* parameter. The new shrunken pixels, or *drops*, are rained down (or *drizzled*) upon the spectral images of the output grid.

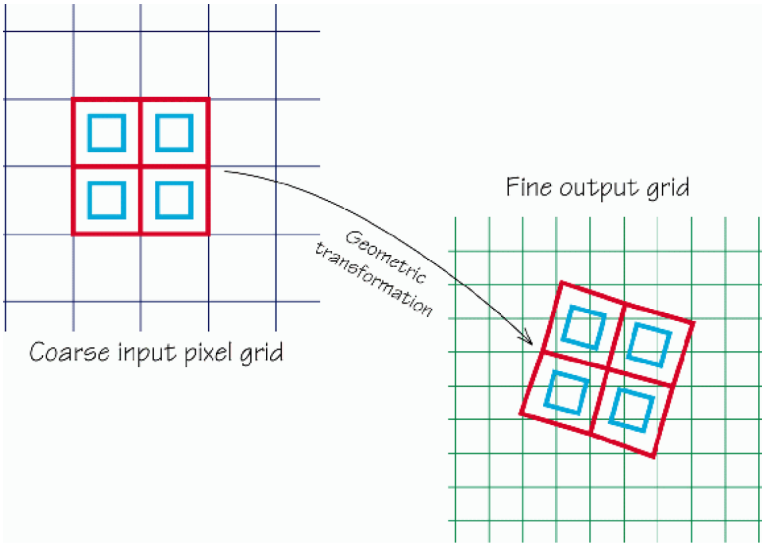

Figure 5.2: Description of the drizzle algorithm(Regibo 2012)

The shrinking factor is a value given as a percentage of the input pixel size and is defined by the user. The input pixels contribute to the output pixel with weights that are proportional to the overlap between drop size and output pixel size.

Each input pixel (x_i, y_i) from an input image slice i (i.e, a wavelength slice) with a flux density of $d_{x_i y_i}$, user-defined weight of $w_{x_i y_i}$, and a fractional overlap of $0 < a_{x_i y_i x_o y_o} \leq 1$, are adapted onto an output pixel (x_o, y_o) with weight $W_{x_o y_o}$ and intensity $I_{x_o y_o}$. The equations are the following:

$$W'_{x_o y_o} = a_{x_i y_i x_o y_o} w_{x_i y_i} + W_{x_o y_o} \tag{5.5}$$

$$I'_{x_o y_o} = \frac{d_{x_i y_i} a_{x_i y_i x_o y_o} w_{x_i y_i} s^2 + I_{x_o y_o} W_{x_o y_o}}{W'_{x_o y_o}} \tag{5.6}$$

where s^2 (the pixel area) the flux conservation factor.

The drizzle algorithm starts by creating an empty flux (*I*) and weight (*W*) maps, and then looping over all pixels in all the input cubes, generating output weights and intensity maps, which for each output pixel (x_o, y_o) have these values :

$$W_{x_o y_o} = \sum_i \sum_{xi} \sum_{y_i} a_{x_i y_i x_o y_o} w_{x_i y_i} \tag{5.7}$$

$$I_{x_o y_o} = \frac{\sum_i \sum_{x_i} \sum_{y_i} \mathrm{d_{x_i y_i}} a_{x_i y_i x_o y_o} w_{x_i y_i} s^2}{W_{x_o y_o}} \tag{5.8}$$

The selection of the drop size should balance between removing the detector footprint and having a quasi-uniform coverage of the output pixels.

The output spaxel size at the final spatial grid is optimised for the central wavelength:

$$cdelta = \frac{FWHM_{beam}}{\frac{oversample}{upsample}} \tag{5.9}$$

Before applying the algorithm, a regular output spatial grid is created where the output spaxel size depends on the values selected for the parameters *oversample* and *upsample*.

5.3.1 Application to PACS spectrometer data

PACS spectrometer pointed observations are undersampled. The Nyquist-Shannon sampling theorem states that at least 2-3 pixels should fit next to each other in the FWHM of the telescope PSF, but the PACS detectors, as shown in Fig. 5.3, with a $9.4'' \times 9.4''$size, are not able to fullfill this requirements as the PSFs are $\sim 8.2\ ''$(at shortest wavelengths) to $14''$(at longer wavelengths).

The input PACS spectrometer data for the drizzle algorithm are PacsCubes. For chop/nod observations the nods have not yet been combined, as they are treated as separate pointings by Drizzle. The same spectral and spatial grid is applied to both nod positions separately and their flux combined afterwards on the new spatial grid. For unchopped observations the input data are already off-subtracted before applying drizzle.

A thorough analysis of the recommended output pixel size was done for highly sampled observations (Regibo 2012) and for oversampled maps by us, for this PhD thesis. (For details please see next chapter). The conclusion was that the recommended values for drizzle are:

- **for highly sampled observations:**
  - *oversample*=3
  - *upsample*=2
  - *pixfrac*=0.6

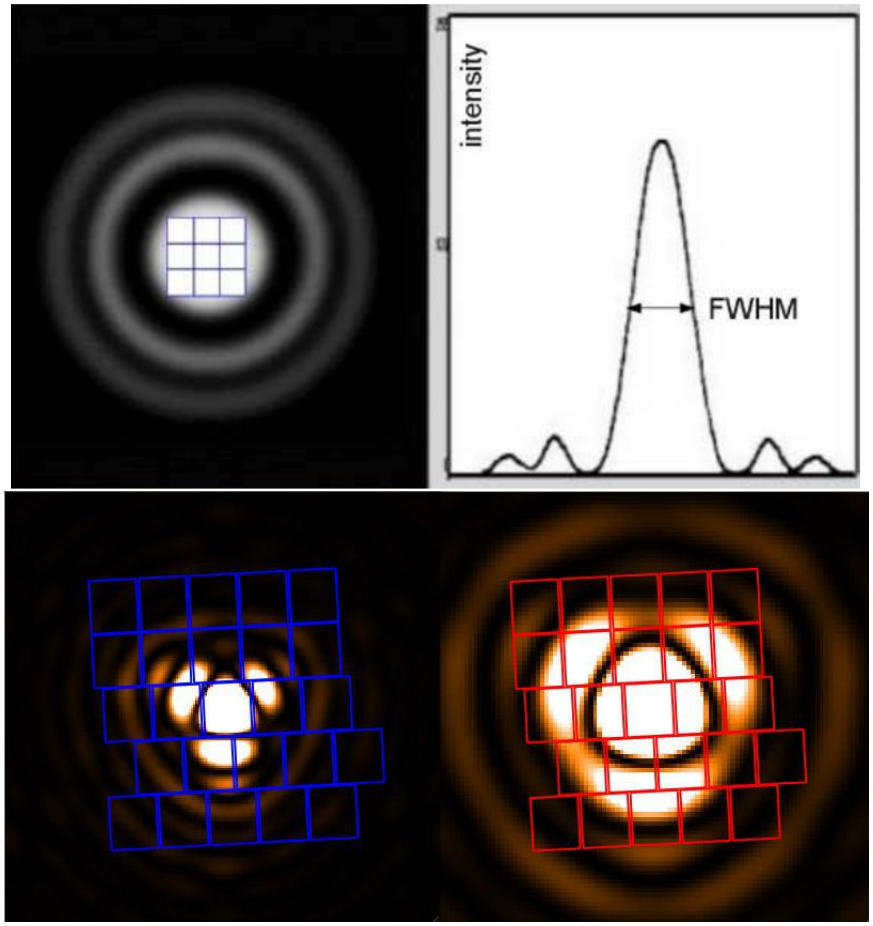

Figure 5.3: Nyquist sampling definition wavelengths.

- **for oversampled maps:**
  - *oversample*=3
  - *upsample*=2
  - *pixfrac*=0.3-0.4

5.4 Interpolation with the Delaunay triangulation algorithm

This is the most recent mapping task created for PACS undersampled and Nyquist sampled rasters and for single pointings. It uses Delaunay triangulation to map the the input spatial grids to a regular, combined, and better-sampled output spatial grid, and the fluxes are interpolated onto the new grid points from the old grid points. There is no extrapolation done at the edges of the FoV, so the cubes from specInterpolate are slightly smaller than those from specProject and drizzle. The interpolation happens for every wavelength

bin in the observation.

The task *SpecInterpolate* was developed for this purpose in collaboration with HSC and the PACS ICC for HIPE 13.0.

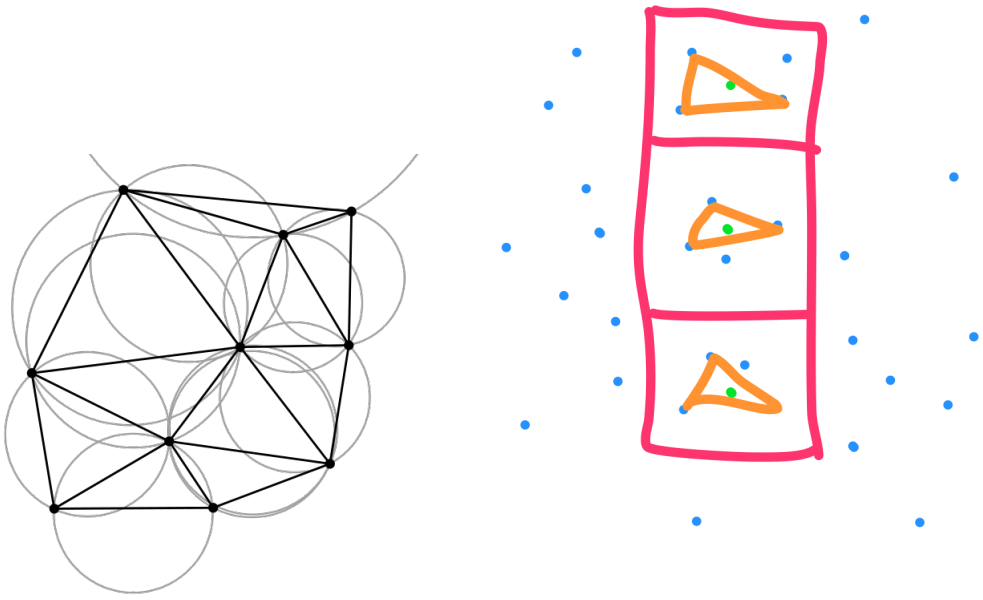

Figure 5.4: (*let*) The concept of applying the Delaunay triangulation. Figure from the PACS Data Reduction Guide for spectrometer data.(*right*) This drawing illustrates that specInterpolate can not be used for observations with dense spatial sampling. Blue dots are the central spaxels for a raster observation. If the output spaxels are set too large (red squares) then the 3 input positions (orange triangles), chosen by the Delaunay algorithm, all inside a single spaxel (red square). This means not all the FoV covered by a single spaxel is included in the interpolation. The SNR of the result will hence suffer.

Delaunay triangulation is a technique to interpolate irregularly sampled data onto a regular grid, as shown in Fig. 5.4. The input grid corresponds to the central positions of the 5×5 spatial grid of spaxels for each cube, and the output grid corresponds to the centres of the projected spaxels of size chosen by the user.

The technique is useful mainly for undersampled maps (such as a single pointing observation) to allow the user to create small pixelised representation of the area observed. Strictly speaking, the method does not provide a "map" because the input data undersamples the beam. Instead, it provides a set of approximated images at each wavelength in the cube.

The choice of output pixel size has to be carefully chosen based on the wavelength range (beam size) of the cubes and the spatial sampling required. Too large output pixels may sample only noise peaks in the data, therefore the signal-to-noise might be compromised (see Fig. 5.4). This is typically the case for oversampled data, therefore specInterpolate is only recommended for undersampled datasets.

The PACS ICC recommends an output spaxel size between 4.7 ″and 3 ″to produce nice spectral images without "artificial" shapes arising from over-interpolation. As there is no extrapolation in the outside part of the irregular Delaunay triangles, the footprint of the spatial grid generated by *specInterpolate* is always smaller than for the other two gridding methods, which do on extrapolation at the edge of the field-of-view.

5.5 Comparison of the three methods

Each method has its best case where to be applied. For example, specInterpolate is recommend for undersampled and Nyquist sampled maps, drizzle is recommended for well-sampled maps (oversampled maps and Nyquist sample) of short wavelength, and specProject can be applied to any case.

Flux conservation is ensured in the three methods. Detailed comparison of the data generated by the different methods is done in section 7.2.

6

The optimization of the drizzle algorithm for oversampled maps

Drizzle was originally developed for chop/nod observations by the PACS ICC (S.Regibo, 2014). For unchopped observations, an additional complication is the need to subtract off-source pointing from on-source pointing, these coming from separate observations. This subtraction is done on the PacsRebinnedCubes in the standard pipeline, but to work with drizzle, it had to be done on the PacsCubes. The task to subtract the off- cube from the on- source cube at the Level of the PacsCubes were designed by the PACS ICC and made part of the interactive pipeline. The optimal use of the drizzle algorithm for unchopped oversampled maps is described in this chapter.

The astrometric accuracy and flux conservation of the drizzle algorithm was tested by the PACS ICC, and in our work we focus on finding the optimal spatial grid parameter values.

The optimal parameters for drizzle will not immediately depend on whether it is applied to chop/nod or unchopped observations. However, with unchopped observations a slightly better spatial resolution is possible for the resulting maps. This is because for chop/nod observations, the two nod positions, which are combined in drizzle, do not overlay exactly on the sky (see Fig. 6.1): the combination therefore is slightly "blurred". Hence the optimal drizzle parameters could be different for chop/nod and unchopped observations.

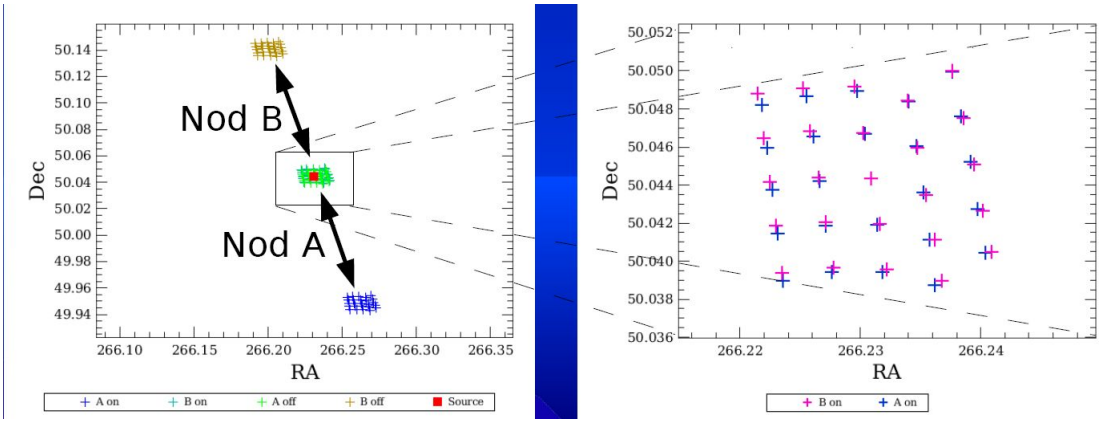

Figure 6.1: The overlap of two nod positions for chop/nod observations it is not exact. This could cause a "blurring" effect in the drizzle cubes.

6.1 Input parameters for the drizzle algorithm

The drizzle algorithm requires the generation of a regular spatial grid and spectral grid. The first spatial grid is an intermediate grid where the flux from each input physical spaxel is distributed over an area of smaller shrunk pixels (drops), before their final projection onto a second regular spatial grid applies.

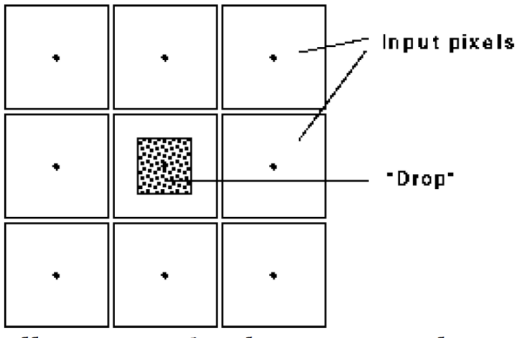

Figure 6.2: Explanation of drop size and shrinking factor at the drizzle algorithm (figure from Regibo (2012).

- The parameter that defines how much a spaxel is shrunk for the intermediate grid is the *pixfrac*. This value is a percentage of the initial spaxel size. See Fig. 6.2.
- The two parameters responsible for determining the final **spectral grid** are *oversample* and the *upsample*. The *oversample* determines the size of the spectral bins as (1/ oversample), and the *upsample* the shift between the input bins of the grid. Note, if *upsample* > 1, then subsequent bins in the output grid may sample the same data points, therefore the data in the bins are correlated.
- The two parameters responsible for determining the final **spatial grid** are *spatialOversample* and *spatialUpsample*. The concept is the same as *oversample* and *upsample* for the spectral grid.

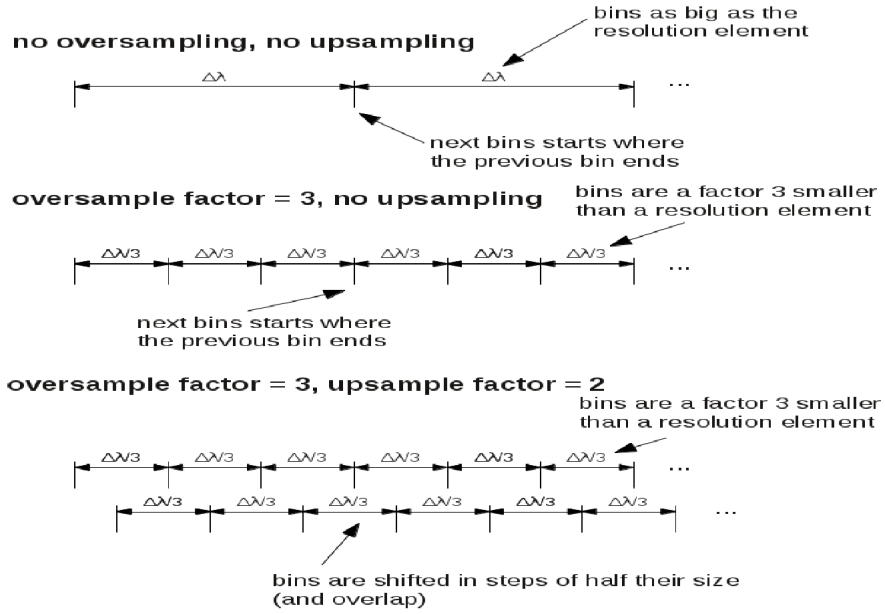

Figure 6.3: Explanation of *oversample* and *upsample* concepts, applied at the generation of the spectral grids. Figure from Regibo (2012)

- The output pixel size for the final spatial grid is optimised for the central wavelength, following equation 6.1.

$$cdelta = (beam)/oversample/upsample$$

We focused on optimising the parameters **spatialOversample**, **spatialUpsample** and **pixfrac**, to obtain a tradeoff between highest achievable spatial resolution and the map quality for our unchopped oversampled maps.

The optimisation was done using hybrid simulations, where a real raster observation served a placeholder for a simulated flux distribution of a point source with Gaussian beam profile. We compared the expected (input) flux distribution of the modelled Gaussian, with the result from running drizzle with different parameters at a particular wavelength. The result which reconstructs the beam width closest to the input width was searched for. In addition, we searched for maps without any undesired spatial structure and artefacts. We also compared with the results for the same simulation data but using *specProject* to create the cubes. The reason was that *specProject* was the most used task and the only alternative for drizzle for our observations.

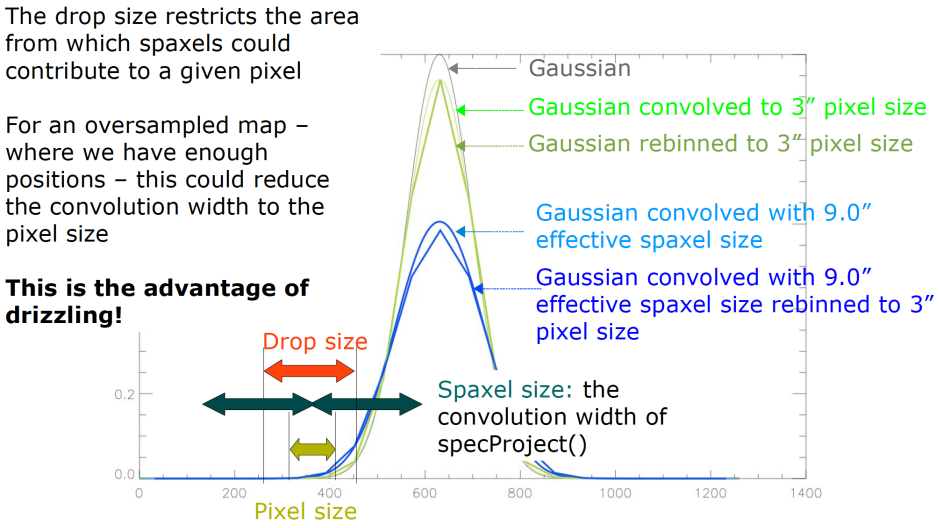

Figure 6.4: Illustration of the effect of drizzling on the cross-section of a Gaussian beam profile. We plot the input Gaussian and those which are convolved with the spaxel size rebinned to the output pixel size.

6.2 Drizzle parameter optimization baseline

First we tried optimising drizzle using real unchopped range oversample mapping observations. The observation used was 1342215657, HOP85 target, a 3×3 oversampled raster with step size of 3″. This target is not a point source and did not result in spectra which varied enough to find optimal drizzle parameters, as is shown in Fig. B.1 in the Appendix B. Hence we continued our tests on simulated data. Such hybrid simulations have the advantage that we eliminate the impact of any artefacts in the input data and the effects of any pointing errors from the spacecraft. A parametric Gaussian beam profile was evaluated for each frame precisely at the spatial position the frame was assigned to. This way, we assume the pointing reconstruction has infinite accuracy and any blurring effect due to residual errors in the pointing product will not affect our optimisation goal. This would never be the case using real data.

We expect that an ideal mapping reconstruction of such hybrid cubes from a raster observations shall reproduce the flux distribution of the input source, i.e. the Gaussian beam profile. Any degradation (broadening) of the reconstructed Gaussian is a result of imperfections in the projection process.

We tested with a single source and with a double-peak simulated source (both having Gaussian profiles but different peak intensities).

The placeholder of hybrid simulations used for drizzle optimisation were:

- ~ 0.5 μm around 62 μm from obsid 1342215657, which is an oversampled map optimized in the blue range (3×3 raster with step size of 3″).
- ~ 1 μm at 168 μm from obsid 1342215662, which is an oversampled map optimized

in the red range (2×2 raster with step size of 4.5″).

We processed these with HIPE 8.0. The flux from the Pacs Level 1 cube was replaced with a Gaussian flux distribution with a FWHM of 8.17 ″in the blue range and 12 ″in the red. These widths are those of the the beam at those wavelengths.

For both short ranges we generated drizzle cubes varying three parameters of the spatial grid: upsample, oversample and pixfrac. More detail on the parameters used is seen in Table 6.1.

As the output spaxel size depends on oversample, upsample and the wavelength, the spaxels of the drizzle cubes have different sizes. The parameters applied for the generation of the spectral grid were fixed (oversample =2, upsample=1) in order to avoid correlated noise between spectral bins, and to allow a direct estimation of the continuum noise.

Table 6.1 detail the 7×9 tests applied per band.

λ_0 (μm)	oversample	upsample	input beam	pixel size	pixfrac (″)
68	3.0	3	8.29	0.9210	0.1- 1.0, in steps of 0.1
68	3.0	3	8.29	0.9210	0.1- 1.0, in steps of 0.1
68	3.0	2	8.29	1.3815	0.1- 1.0, in steps of 0.1
68	3.0	1	8.29	2.7630	0.1- 1.0, in steps of 0.1
68	2.0	3	8.29	1.3815	0.1- 1.0, in steps of 0.1
68	2.0	2	8.29	2.0723	0.1- 1.0, in steps of 0.1
68	2.0	1	8.29	4.1446	0.1- 1.0, in steps of 0.1
181	3.0	3	11.71	1.3012	0.1- 1.0, in steps of 0.1
181	3.0	1	11.71	3.9036	0.1- 1.0, in steps of 0.1
181	2.0	3	11.71	1.9518	0.1- 1.0, in steps of 0.1
181	2.0	2	11.71	2.9277	0.1- 1.0, in steps of 0.1
181	2.0	1	11.71	5.8555	0.1- 1.0, in steps of 0.1

Table 6.1: Set of input parameters used for the drizzle optimisation process at the blue (68 μm) and red (181μm) wavelengths

6.3 Drizzle parameter optimisation results

With the above-described method we quantify the influence of spatial grid parameters on the size of the projected source. We are adopting the best input parameters which preserve spatial resolution but at the same time do not introduce spatial artefacts.

The optimisation of drizzle for oversampled maps is a trade-off between homogeneity in the coverage and spatial resolution. Aggressive shrinking reduces the convolution effect of the detector spaxel size and therefore increases spatial resolution, but at the same time it reduces the chance that all output pixels will have enough data points to project. If

extreme strong shrinking applies, the dot cloud spatial density will be insufficient to fill all pixels and holes (*NaNs*) will appear in the reconstructed map.

The reconstructed maps from all simulations, as well as the measured widths obtained for tested parameter setups, are given in the tables and shown as figures in Appendix B. Our results can be summarised in the following statements:

- As expected, we see a significant difference in the quality with different drizzle parametrisation, in terms of preserving the FWHM of the input beam and at the same time preserving the continuity in the input image. See right panel of Fig. 6.5.
- It may be considered that the spaxel size has some impact, as the best fits agreed with smaller output spaxel sizes.
- We see that oversample =2 , upsample =3 and oversample =3, upsample =2 provide similar values. Both create the same output spaxel size.
- The *closest solution* to the input beam size comes from the parameters oversample = 3.0, upsample = 2-3.
- As expected, strong shrinking provides less of a convolution effect (less rounded flux distribution). Stronger shrinking ($\leq$ 0.3-0.4) results in a gain of 23-29 % in the spatial resolution (see Fig. 6.6) but we then suffer more from discretization effects of the images and also by holes (*NaNs*) in the strongest cases. An example is highlighted in the left panel in Fig. 6.5.
- The measured FWHM increases with *pixfrac* due to the convolution effect of a detector spaxel.
- The best fits agree with smaller output spatial bins ($\leq 2''$). Higher spatial upsampling increases the sampling rate, providing visually a better image from the spectral cube. From Fig. 6.5 we see how the projection algorithm suffers from discretisation effects for the most aggressively shrunken spaxels (typically for pixfrac $\leq$ 0.4).
- Our results are in line with those from Regibo (2012).

Note that flux conservation has been extensively tested in Regibo (2012) and therefore is not required by our study.

6.4 Testing of optimal drizzling on RDor

We applied the optimum oversample and upsample parameters on an observation of R Doradus, which is a point source and a PACS flux calibrator. For that we took from the Herschel Science Archive raster observations R Doradus. Our study consisted of:

- Apply the drizzle algorithm with different shrinking factors (0.4, 0.6, 0.8, 1.0), which values are the percentage of the input PACS spaxel of 9.4″. Results are shown in Fig. 6.7.

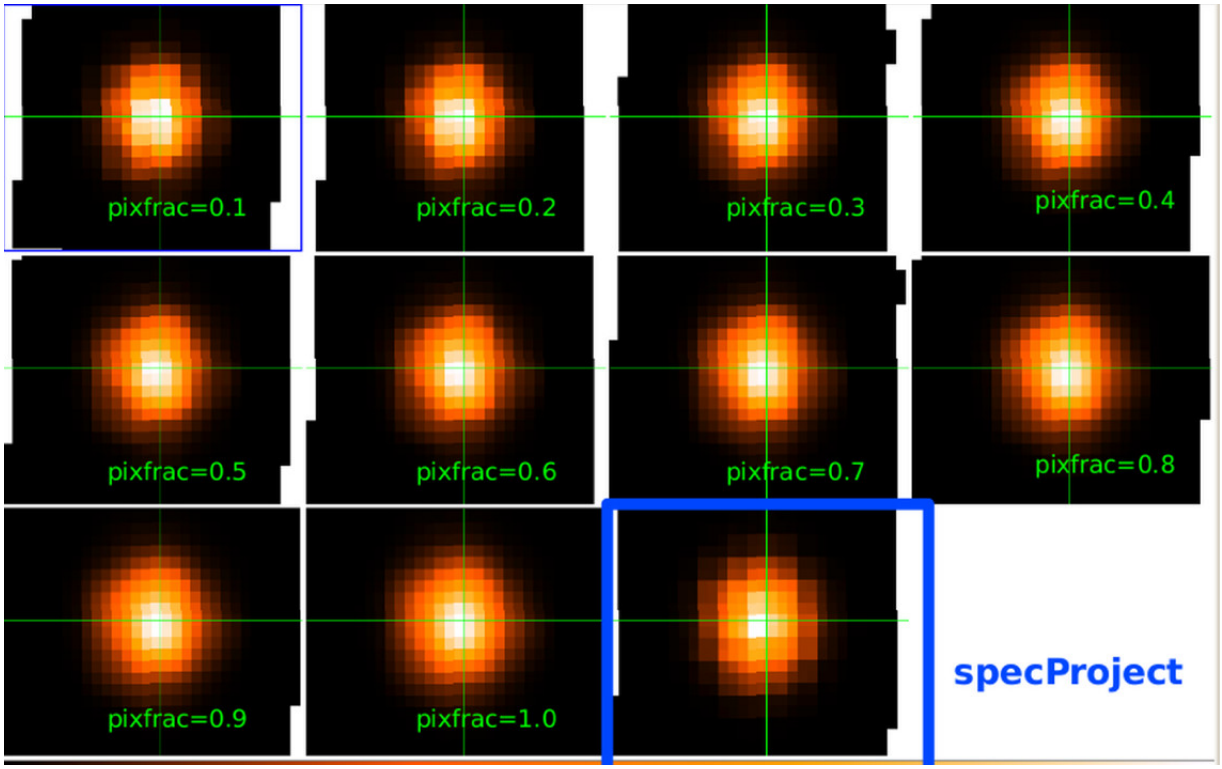

Figure 6.5: (*left*) the impact of a strong shrinking (pixfrac=0.1) in the final map may cause holes, (*right*) spatial distribution for pixfrac from 0.1 to 1 for the selected oversample and upsample values (3,2) and comparison to specProject result on the same data.

- Compare the drizzle algorithm with pixfrac 1.0 to specProject result. Results are shown in Fig. 6.8.

We confirm that the drizzle parameters identified for oversampled maps in the simulated Gaussian sources, are the optimal parameters also for point-like observations such as RDor.

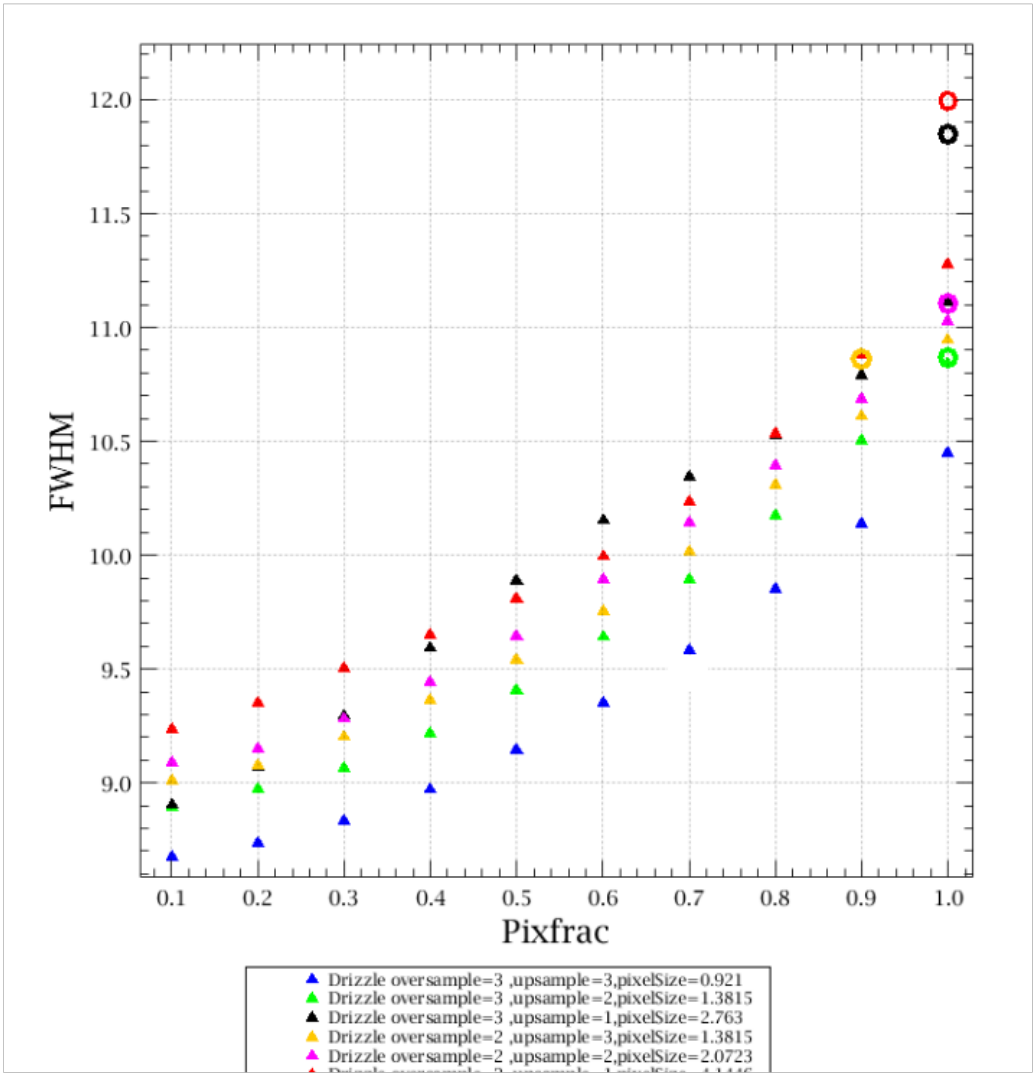

Figure 6.6: FWHM of the projected Gaussian source obtained from drizzle maps versus *pixfrac* for the different set of (oversample, upsample) values selected

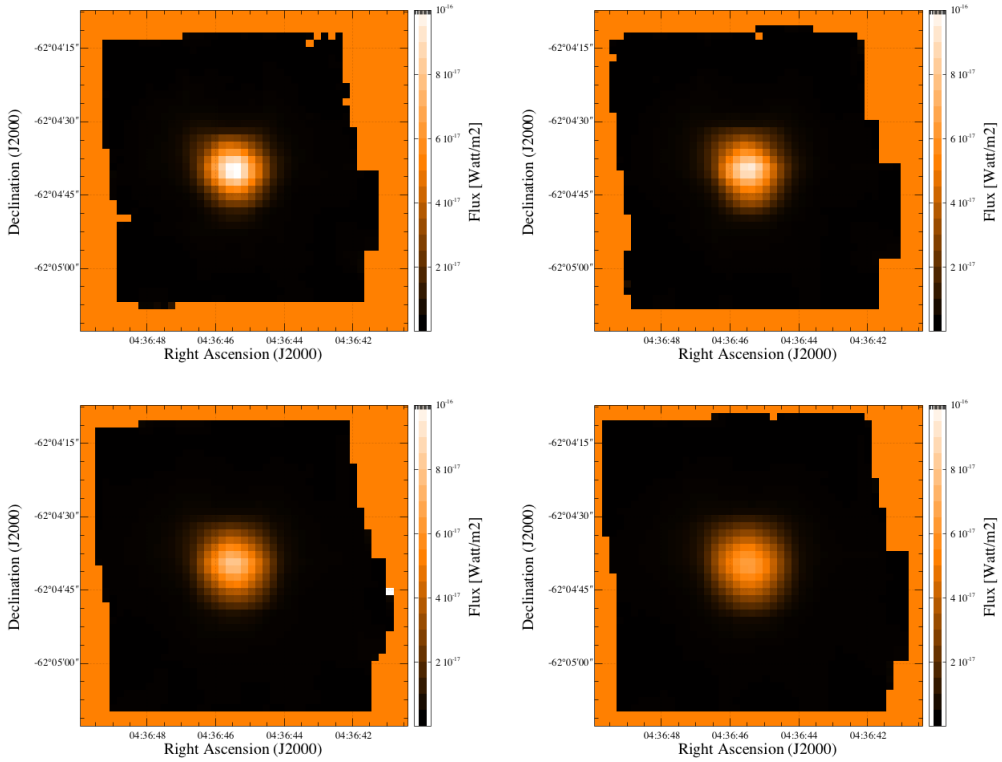

Figure 6.7: Comparison of line maps for a point source (RDor) in a drizzled cube generated with spatial grid parameters (oversample=3, upsample=2) and pixfrac (from left to right) of 0.4, 0.6, 0.8 and 1.0.

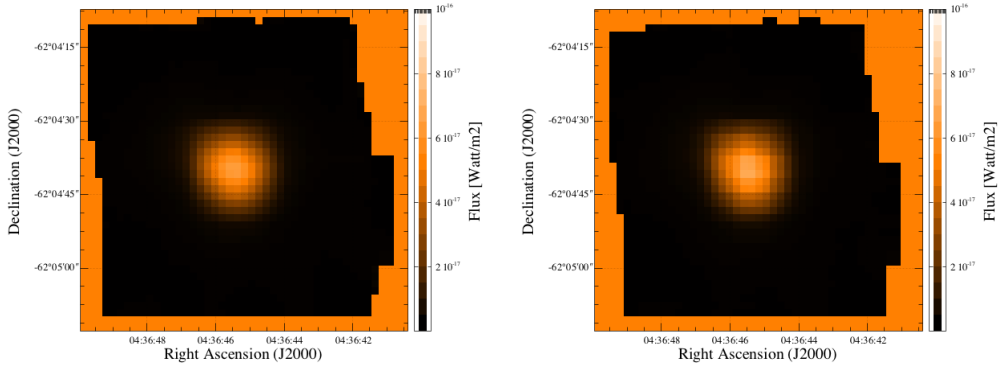

Figure 6.8: Comparison of line maps for a point source (RDor) in a drizzled cube generated with spatial grid parameters (oversample=3, upsample=2) and pixfrac (from left to right) of 1.0 compared to line map generated with specProject (right).

7

Optimisation of standard data processing pipeline for the HOPS OMC-2 data.

In this chapter we present the customised PACS unchopped long-range pipeline we applied to the HOPS spectral data set. Final products from this process are calibrated hyper spectral cubes from which we generate line and continuum maps by fitting each spaxel with a model and turning the fitting results into a 2-dimensional images. The steps of flux extraction are described in Chapter 8.

The standard work-horse observing mode for the PACS spectrometer is line spectroscopy combined with the chop/nod beam modulation technique. This standard observing mode provides the best performance due to optimum spectral data redundancy in the spectral domain, and due to short timescales necessary for the to cover a small spectral range around the line of interest. Because of the short the timescale between on- and off-fields visited by the focal plane chopper, the impact of instantaneous detector response changes is minimised in the differential signal. This mode, therefore, is considered to be the most sensitive and also the most accurately calibrated for continuum flux density as well as emission line flux.

Despite its superior performance, the standard mode does not apply to all science cases, especially when the physical interpretation of the source requires a set of lines spread through the entire range 51-210 μm covered by the PACS spectrometer, and when the sky in the source vicinity does not provide an emission-free area useful to place two symmetric background apertures for the chop/nod positions.

Targets in the HOPS spectroscopy sample are in crowded fields, which inhibits the use of

chopping mode, and the need of efficient coverage of molecular emission lines from CO and H_2O requires long-range coverage.

7.1 Standard pipeline reduction of unchopped range spectroscopy data

Our data were reduced with the *Herschel* interactive processing environment Ott (2010). We used the standard unchopped long-range spectroscopy data processing script to achieve, spectrophotometrically and spatially calibrated cubes for each observed observation. We applied the standard flux calibration scheme, where the system response applicable to an observation is estimated from a calibration block at key wavelengths. The calibration block is executed at the beginning of each on- and off-source observation and the derived system response is adopted for the duration of the observation. The absolute flux level is propagated from the key wavelengths to the covered wavelengths range applying the relative spectral response function (RSRF). The standard pipeline applied to the unchopped range mode observations of the HOPS sample has been described in more detail in Chapter 4.

Unchopped raw data suffer from instantaneous system response drifts due to cosmic-ray impacts on detectors. The typical behaviour of drifting pixel is illustrated in Fig 7.1, where the dots represent the data points from a PacsCube and the straight lines join each group of 16×25 data points. The effect of this drift (as shown by the black dots/line in Fig 7.1) is to change the flux sample at the grating positions sample during the transient events. This often leads to an extra uncertainty in the continuum shape and level, over what is achieved by the chop/nod mode.

Unlike in the case of chop/nod observing mode, where drifts are largely eliminated because of the high frequency in the chop_on-chop_off differential signal, any drifts occurring at timescales shorter than the observation itself remains a property of raw unchopped data. Fortunately, as part of the standard pipeline spectral flat-field task, the continuum sampled by each of the 16 spectral pixels is scaled to the median value and this corrects for residual spectral effects.

Flux calibration accuracies applicable to unchopped range mode have been derived and published by the PACS ICC in the PACS Spectroscopy Performance Document [1]. The unchopped line performance is claimed to be similar based on observations on fiducial flux standards.

We carried out an extensive performance assessment of the HOPS data using our customised pipeline, which confirms that the post-calibration performance is in line with the predicted line- and continuum sensitivities.

[1] [http://herschel.esac.esa.int/twiki/bin/view/Public/PacsCalibrationWeb]

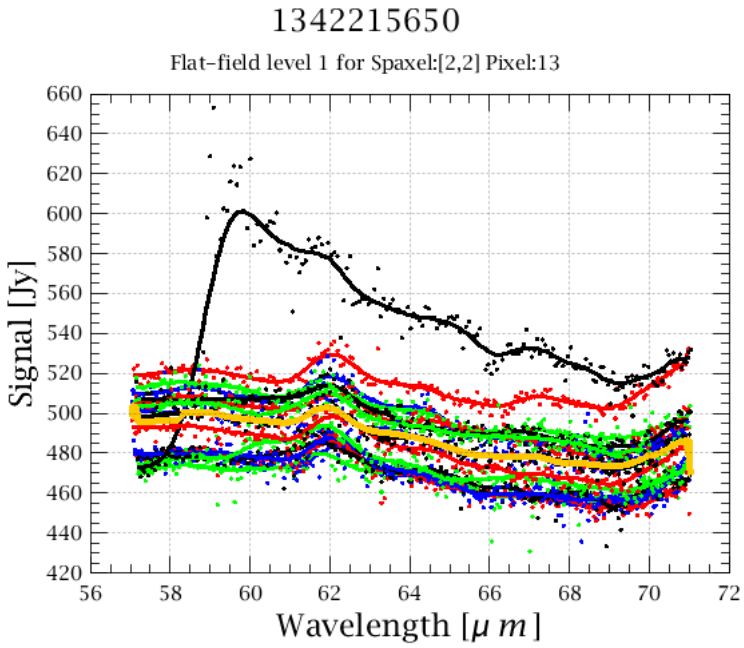

Figure 7.1: Colours represent signal from the subsequent spectral up-down scans obtained from module 12 pixel 3 of the blue spectrometer array. In one up-scan (black curve) the pixel has been hit by a high-energy particle which caused the glitch in signal and the following trend in response.

7.2 Areas of concern for performance improvements

To identify which tasks of the standard data processing pipeline may require improvements, we carried out a number of steps at intermediate processing levels.

- We use the optimal gyro-based pointing reconstruction, which reduces the error on instantaneous positions of each spaxel and provides a more accurate astrometry at the time resolution of individual spectral frames. By "gyro-based pointing reconstruction" we refer to an improved pointing product provided by the HSC, which is based on data provided by the gyroscopes of the satellite. The aim of applying improved a posteriori pointing reconstruction is that the drizzling algorithm (described in the previous chapters) can take full advantage of improved positions and make the reconstructed image sharper.

- We investigated the presence of residual wiggles in the spectra after applying the RSRF to spectra normalis with a fitted continuum, see Fig. 7.2. Any systematic artefacts (i.e. reproducible wiggles on a large set of observations after off-subtraction) decrease both line- and continuum sensitivity. These wiggles are considered residual features which may be due to imperfections in the canonical RSRF, or at least the canonical RSRF may not be perfectly suitable for all flux or signal levels. Possi-

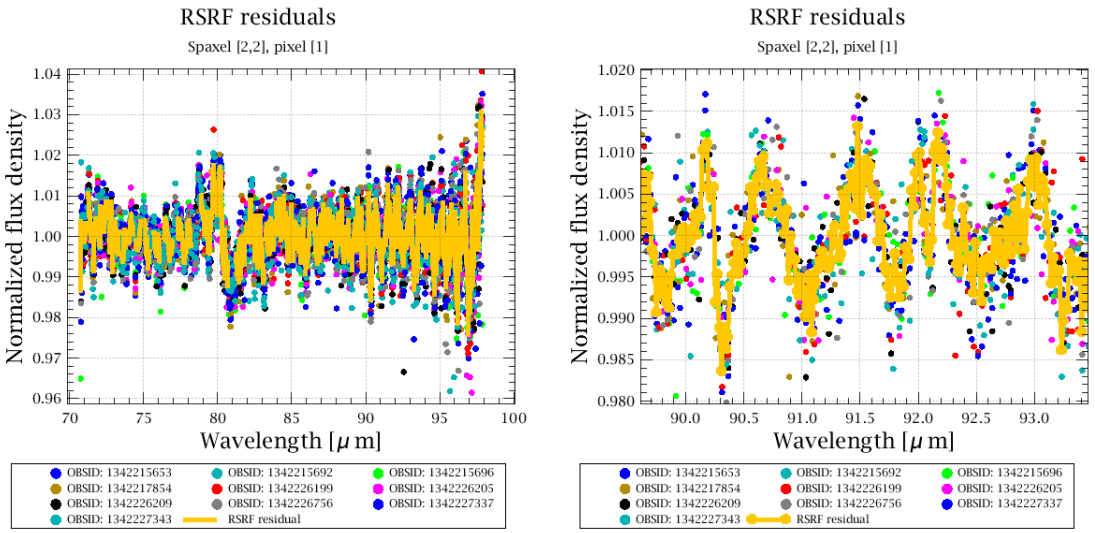

Figure 7.2: (yellow curve) RSRF residuals are reproducible over a large number of observations (the dots). The amplitude of repeating patterns accounts for ∼1.5% of un-calibrated flux modulation in band B2B, and ∼1.0% in band R1.

ble explanations could be uncalibrated non-linearity with flux, or some uncertainty in the lab measured dark current. Therefore, monitoring the presence of residuals and evaluation of their impact on system performance is important. We concluded RSRF residual wiggles contribute less than ∼1.5 % of the continuum noise observed in the entire wavelength range, therefore correction to the first order is not necessary.

- We investigated the post-calibration instrumental noise in the HOPS sample along the PACS wavelength range, see Fig. 7.3. This was done using the central spaxel (9.4″×9.4″) of all the HOPS observations (On- and Off-positions separate). We see that the noise of the On-source observations is slightly higher than that of the Off-sources, due to the presence of strong spectral lines and pointing jitter. Figure 7.3 shows the measured RMS continuum noise as a function of wavelength. Along the PACS range the continuum peak-to-peak noise does not exceed 0.4 Jy, therefore lines with significant detection should have at least 3σ times this flux at their peak at the line central wavelength.

- The last major concern is related to the fact that the system response is adopted from the calibration block executed at the beginning of the observation. Therefore, any system-level drift of detector response (i.e. for the ensemble of the 16 spectral pixels per spaxel, instead of a single pixel outlier) appearing on the timescale of the observation (or longer) will not be calibrated out. This property of unchopped long-range mode clearly appears in the continuum uncertaininty, as for faint continuum sources (below few Jansky per pixel) the continuum level could show a negative value after off subtraction. This indicates a significant uncertainty in the response estimates from the calibration block. We tried to quantify this variability com-

paring the derived response from the calibration block and the response estimated from off-position observations. However, we demonstrate that both methods performs similarly in terms of response level estimates and variability of the estimated response.

To create noise curves separately for the on- and off-observations, we first need to create a so-called "superoff" product from all off-position observations available from the Herschel Science Archive. To all flux calibrated off-spectra we fitted a baseline with the multi resolution baseline estimator, and divided the PacsCubes spectra (dot cloud) with its own smooth baseline. The resulted dot cloud is rebinned and averaged per bin. The result is a very high signal-to-noise shape of the high-resolution residual wiggles introduced before. In the next step, we normalised any given observation (off subtracted) exactly the same way, subtracted the "superoff", added a value 1, and multiplied the resulting spectra with the smooth continuum of the observation itself. The RMS continuum noise is measured in a running boxcar of 3 microns width on these final spectra.

For the superoff product generation we applied our own multi-resolution spectral flat-fielding algorithm, which efficiently estimates the signal from all pixels including those which exhibit a strong response drift.

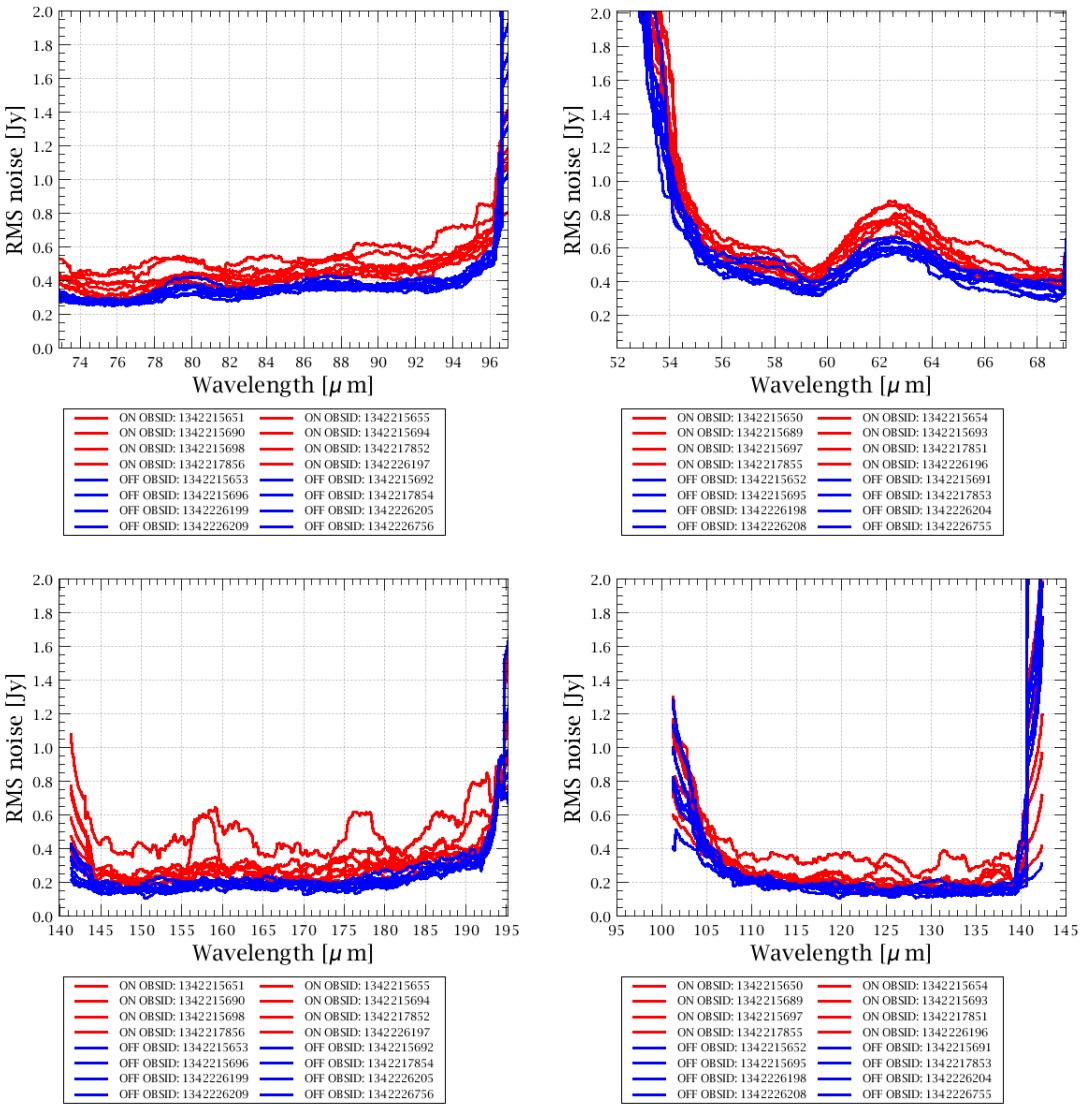

Figure 7.3: Measured noise performance from HOPS spectroscopy data on spaxel 12. Plots of the continuum RMS values versus wavelength. On-source observations (red line) exhibit a significantly higher noise than Off-source observation (blue line), due to the presence of strong spectral lines, pointing jitter, slit illumination effects and probably due to flux-dependent variation in the RSRF residuals. The measured performance, however, exceeds the predicted performance.

7.3 Data processing from Level 0 to Level 1

We started with Level0 products from the archive processed with SPG version HCSS 10.3. We further processed the data in an interactive mode, using HIPE 12.0.1256, calibration version 58 up to Level1 and calibration version 65 from Level1 to Level2.

The HOPS pipeline processing is illustrated in Fig. 7.4, which represents the common processing steps, and in Fig. 7.5, which represents the different processing steps, depending whether the final line maps are generated for the oversampled and undersampled regions together or separately.

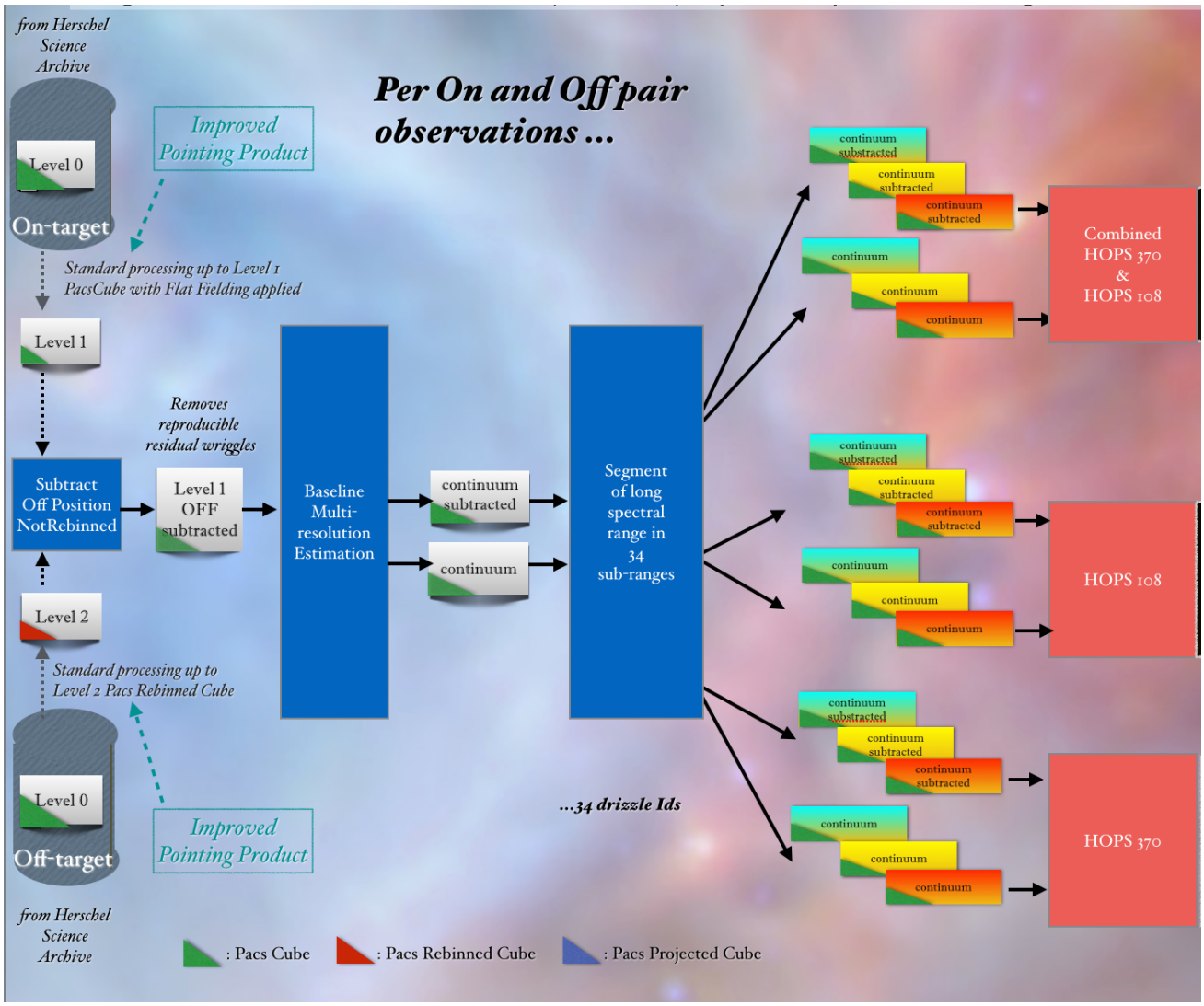

Figure 7.4: Common de processing from Level 0 to Level 1 products.

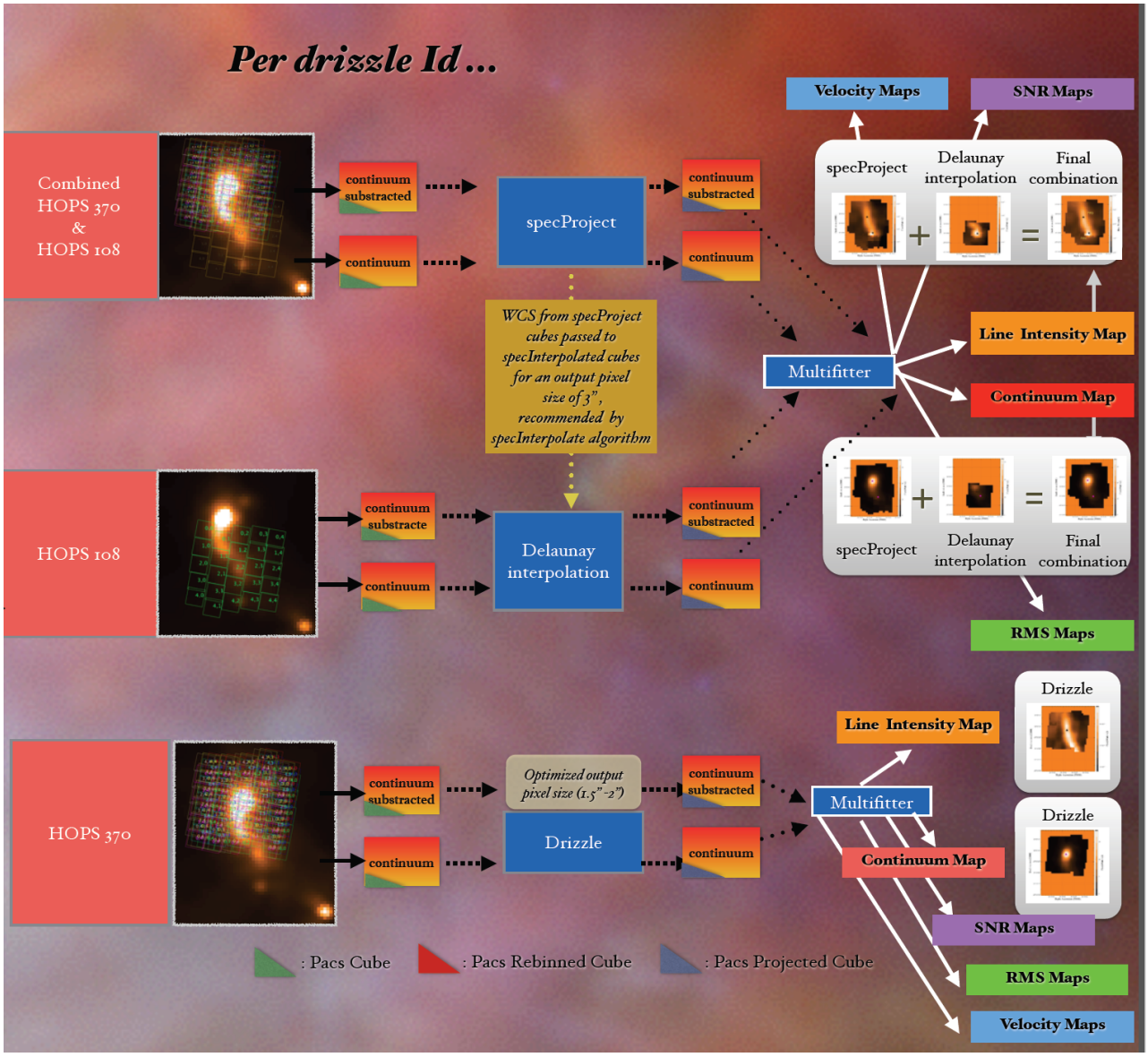

Figure 7.5: Different processing from Level 1 to Level 2 products depending on the observing strategy.

We applied the prototype algorithm that provided an improved pointing product ("gyro-pointing reconstruction" of the spacecraft attitude information). The new pointing product was applied at step (9) of section 4.3 to assign (ra,dec) to the central spaxel.

The improved pointing reconstruction results in a slightly more accurate assignment of data points to positions on the sky (C.Stepheson,2014 and Sanchez-Portal et al. 2014). These improvements go in two directions:

- Improve the error on the determined central sky position of all pointings (APE: Absolute Position Error).
- Improve the residual error on the determination of the pointing (instantaneous position of the spacecraft).

The advantage of an improved pointing reconstruction; smaller residuals down to $\sim 0.1''$ in terms of relative pointing, is important for the drizzling spectral cube reconstruction as discussed earlier.

Another improvement concerns the subtraction of the off-source cubes from the on-source cubes. At the time we processed our data, the off-subtraction was always executed on the rebinned cube of the on and off-target observations. A new task, *specSubtractOffPositionNotRebinned* allows for a subtraction of the off-source Level 1 cubes before drizzle is applied. This task is applied at step (4) in the data processing (sec. 4.3). The wavelength grid applied to the off-positions was adopted from the associated on-target observation.

A third difference with respect to the standard processing is that we applied a **baseline subtraction**. Spectral reconstruction techniques (either drizzle or naive projection) reconstruct the line profiles with higher accuracy if continuum is subtracted beforehand. The reason is because adjacent spaxels may have substantial differences in the continuum levels which are projected together for an oversampled raster. In outputs pixels of the spectral cube, where different continuum levels are co-projected, spectral shapes may become uncertain. Baseline subtraction, therefore, is an essential step before hyper spectral cube reconstruction applies.

On each individual off-subtracted spectral cube we applied for each pointing of our rasters, an iterative multi-resolution wavelet transform algorithm which smoothed the spectra, and this smoothed continuum could be subtracted from the data. A visual explanation of this technique is shown in Fig. 7.6, where the top image is a zoom of a certain range from the bottom image and the the left images shown the effect on a spectrum where the lines were masked and the right images the effect on a spectra with plenty of lines. The resultant products from this task were on one side continuum-subtracted cubes and on the other side continuum-smoothed only cubes. Using this adaptive task, any post-calibration residual continuum wiggles broader than 5-7 $\times$ the width of an unresolved line were efficiently eliminated from the spectra.

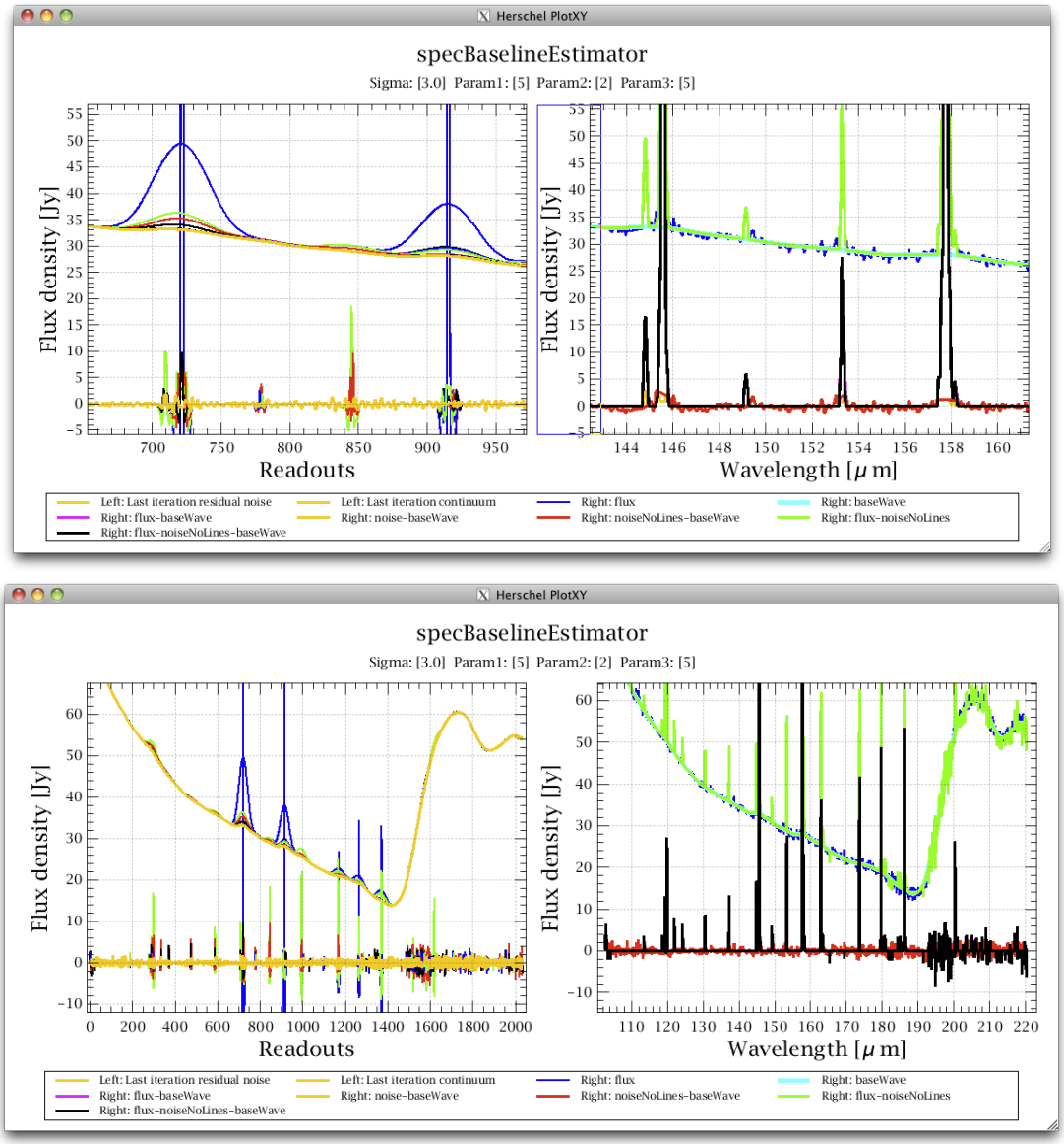

Figure 7.6: Examples of the continuum subtraction. The specBaselineEstimator task applies a multi-resolution wavelet based method which can iteratively estimate the baseline level even in spectra which contain a variety of dominating frequencies. Upper panel, areas of emission lines are zoomed on, Bottom panel, the entire R1 red band spectrum.

The penultimate unique step consisted of combining the Level1 off-subtracted cubes from several observations in a single List Context, as if they were different raster positions from the same observation. We executed this exercise separately per target and combined for the two targets as we need to generate mosaick cubes for the different regions and for the combined region.

The execution of the same steps for a single list context (with all the observations which contribute to an specific range) ensure that the same method is applied for all the (on-off) observations and increase the signal to noise by pushing all the data at the same time into a mosaicking method.

The final unique step was to divide our long spectral ranges into smaller ranges in the Pacs Level 1 cube, producing a suitable input data format for the drizzle algorithm. As has been explained earlier, the drizzle algorithm optimise parameters for the observed wavelength, in particular the output spaxel size. For long wavelength range cubes, therefore the output spaxel size will be too small at the red and too larger at the blue end. The complete PACS wavelength range was divided in short ranges (see Table 7.1) of 3 μm for the blue band and 5 μm for the red band, which we called *drizzleIds*. Drizzle could be then applied to our observations.

7.4 Data processing from Level 1 to Level 2

At this point of the processing we have calibrated and baseline-subtracted oversampled raster maps of the target HOPS 370, some optimised for the blue band and others for the red band, and a single pointing observations of the HOPS 108 target.

At the beginning of our study we focused on HOPS 370 and we put all our efforts on identifying the optimum parameters for reconstruction oversampled maps, as is discussed in Chapter 6. Following the work of Furlan et al. (2014), it was considered very interesting to try to understand the possible interactions between HOPS 370 and HOPS 108. Hence we then turned our efforts to HOPS 108. As HOPS 108 is a pointed observation, the drizzle algorithm used for HOPS 370 could not be used (pointed observations are highly under sampled, drizzle require at least Nyquist sampling).

The first idea was to identify a common cube mosaicking method for the processing of the two targets. We compared the PACS level 2 cubes obtained for the combination of over-sampled observations and under sampled observations with the three methods (specProject, drizzle and specInterpolate) applying the recommended output spaxel size of 3″ for specInterpolate and the 1.4″ taken from our simulations, for a particular wavelength, (63 μm) for drizzle, see Fig. 7.7. The oversampled observations from HOPS 370 overlap with the undersampled observations of HOPS 108.

The following conclusions can be drawn:

- *drizzle* is suboptimal because shrinking of spaxels generate holes in the region of the under-sampled (pointed) observation.

drizzleId	λ_{blue}	λ_{red}	CO (J_{up} - J_{low})	$CO_{restwavelength}$	band
1	56.9	59.6	45-44	58.54	B3A
2	59.0	62.5	44-43, 43-42	59.84, 61.20	B3A
3	62.0	65.0	42-41, 41-40	62.62 , 63.32	B3A
4	64.5	67.0	40-39	65.68	B3A
5	66.0	68.8	39-38	67.33	B3A
6	68.0	70.5	38-37	69.07	B3A
7	70.0	71.1	37-36	70.90	B3A
8	70.7	74.0	36-35	72.84	B2B
9	73.3	76.6	35-34	74.89	B2B
10	76.0	78.5	34-33	77.05	B2B
11	77.5	81.0	33-32	79.35	B2B
12	81.0	84.0	32-31	81.80	B2B
13	83.5	86.5	31-30	84.41	B2B
14	86.0	89.5	30-29	87.19	B2B
15	89.3	92.5	29-28	90.16	B2B
16	92.0	95.5	28-27	93.34	B2B
17	94.0	98.2	27-26	96.77	B2B
18	100.6	106.5	25-24	104.44	R1
19	106.0	111.0	24-23	108.76	R1
20	110.0	116.0	23-22	113.45	R1
21	115.5	121.5	22-21	118.58	R1
22	121.0	127.5	21-20	124.19	R1
23	126.5	131.7	20-19	130.36	R1
25	136.0	143.5	19-18	137.19	R1
26	142.5	150.0	18-17	144.78	R1
27	149.5	155.0	17-16	153.26	R1
28	154.0	160.0	n/a	n/a	R1
29	159.0	167.0	16-15	163.39	R1
31	172.0	177.0	15-14	173.63	R1
32	176.0	183.5	n/a	n/a	R1
33	183.0	189.0	14-13	185.99	R1

Table 7.1: Drizzle Ids in which the complete PACS long-range was divided from Level 1 onwards

- *specProject* does not create holes, but it does not provide a good sampling of data in the under-sampled region. For that reason it seems not to be the best option for the complete region.
- *specInterpolate* does not create holes at the resampled cube either and it provides a better apparent spatial sampling in the under-sampled region. When the spaxel size is small it can create triangle shapes, which will lead to misinterpretation of the results. The 3″ spaxel size provides a good overall map in both regions because specInterpolate deals with spatial gradients in a smoothed way. However we note that specInterpolate is not recommended for the creation of cubes in oversampled regions, such as HOPS 370 target (ICC internal communication; see also Fig. **??**).
- Drizzle keep the highest spatial resolution reconstruction for the HOPS 370 and specInterpolate is suitable for the under sampled OMC-2 region.

Therefore, our conclusion was that to study the OMC-2 region as a common region, we should choose the same pixel size across it, but not the same reconstruction method. For the oversampled region (HOPS 370 observations) drizzle seemed to be the optimum reconstruction method and for the undersampled region (HOPS 108 observations), specInterpolate. Therefore we generated the drizzle cubes for the combined region and later replaced the spaxels of the undersampled region (which did not overlap to the oversampled region) by the specInterpolated results.

7.5 Optimal reconstruction of the spectral cubes for the OMC2 region

The optimal reconstruction for our combined field of view is a combination of undersampled and oversampled maps, done in a way to preserve the spatial resolution as much as possible but at the same time not introducing sharp transitions in the intersection of the zones between the HOPS 370 mapping field and the HOPS 108 pointed field. Drizzle introduces a sharp transition at the edge of the oversampled area due to the strong shrinking factor we applied in this method (top image in Fig. 7.9). The trade-off method requires that spatial resolution for both the oversampled and undersampled areas are similar (bottom image in Fig. 7.9). Despite the fact that drizzle gives the best spatial resolution for the oversampled map, a trade-off solution was adopted for which we used specProject for the north and specInterpolate for the south.

SpecProject cubes were generated for the complete OMC-2 region and specInterpolate cube for the under sampled cube.

We wanted to be sure that the flux per pixel was comparable from specProject and for the set of parameters we determined for our drizzle oversample cubes in the OMC-2 region. For that reason, we generated line maps by integrating the flux under the line (detail explanation in Chapter 8) from the specProject and drizzle cubes at 63μm and 145μm (for the different pixfrac 0.4 and 1.0, and for output pixel sizes 2 ″and 3 ″) and compared

the flux per pixels. As shown in Fig. 7.8, the flux of most of the pixels at the blue and red line maps generated by using specProject and drizzle cubes are comparable, therefore we could safely used specProject.

We concluded that our recommended drizzle shrinking factor (0.4 or 60 %) provides a most similar flux to specProject, which is known to be flux conservative.

The drizzle cubes and line maps derived will be delivered to the Herschel Science Archive for their scientific exploitation.

The flux at the location of the undersampled region from the specProject line map were replaced from the values of the line map from the specInterpolated line map.

The spectra were spectrally re-binned to a Nyquist-sampling (see Fig. 5.3) at the resolution element for unresolved lines. We have chosen not to upsample the data, so that each bin is independent, and so yielding reliable estimates of the noise properties in the spectra.

Note, a proper resolution match of the over- to undersampled areas would require a convolution of the area reduced with specProject. We have decided that this step is not necessary because integrated fluxes around positions of interest are extracted from circular apertures. The total flux within these apertures is very little affected by resolution mismatch. If analysis of these data is to be extended to pixel-by-pixel modelling of the sampled region, then resolution matched mapping would be required.

The SPIRE standard processing is the optimum method for our raster observation. Therefore not special optimisation was required.

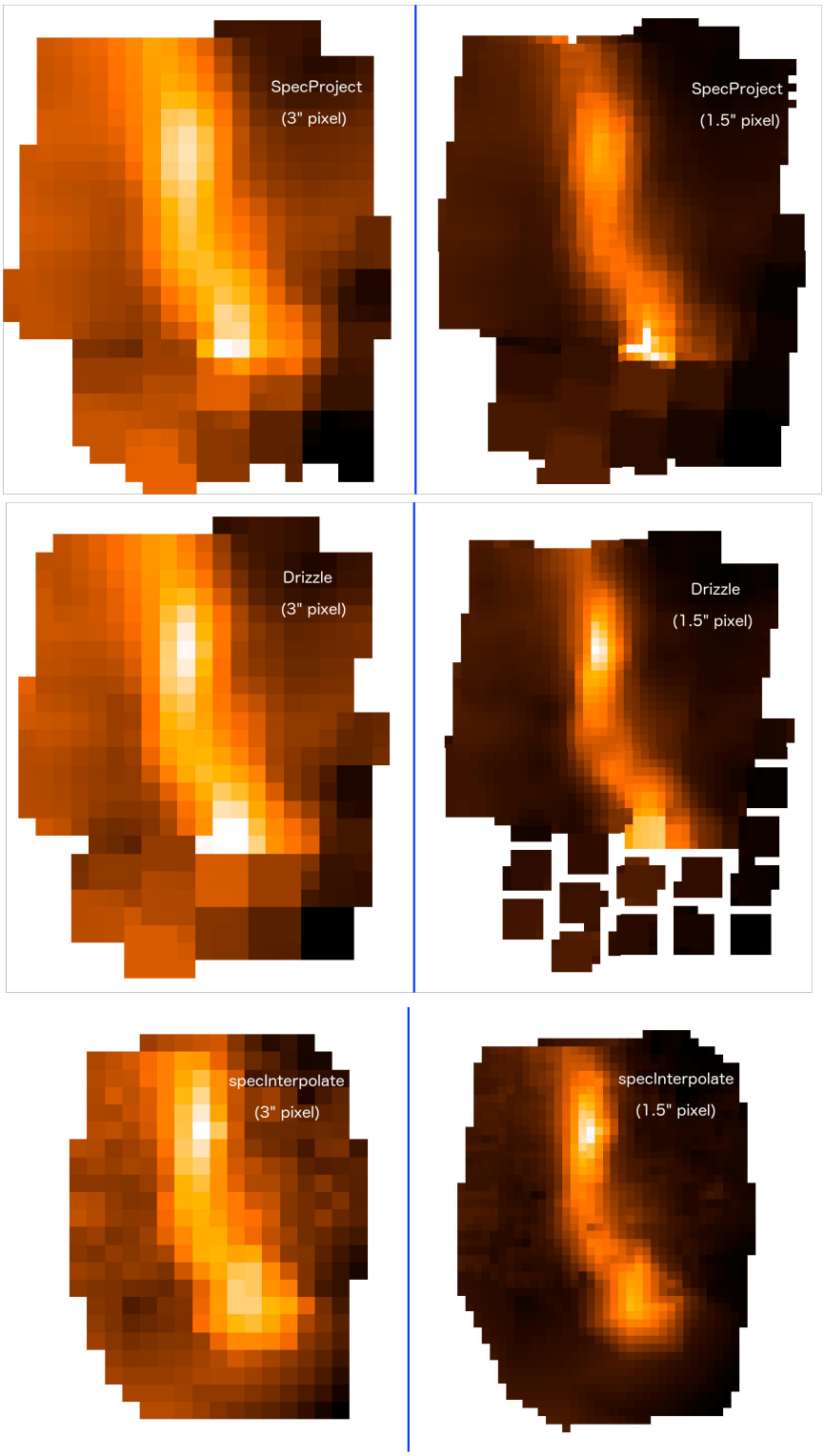

Figure 7.7: Comparison, for a single slice of the Pacs Level2 cubes at 63 μm , of the spatial distribution for (top) specProject cubes, (middle) drizzled cubes and (bottom) specInterpolated cubes. At each one of these images, (left images) show the reconstruction for an output pixel size of 3 $''$and (right images) for 1.4 $''$. Upper part of the data is oversampled and lower part is under-sampled.

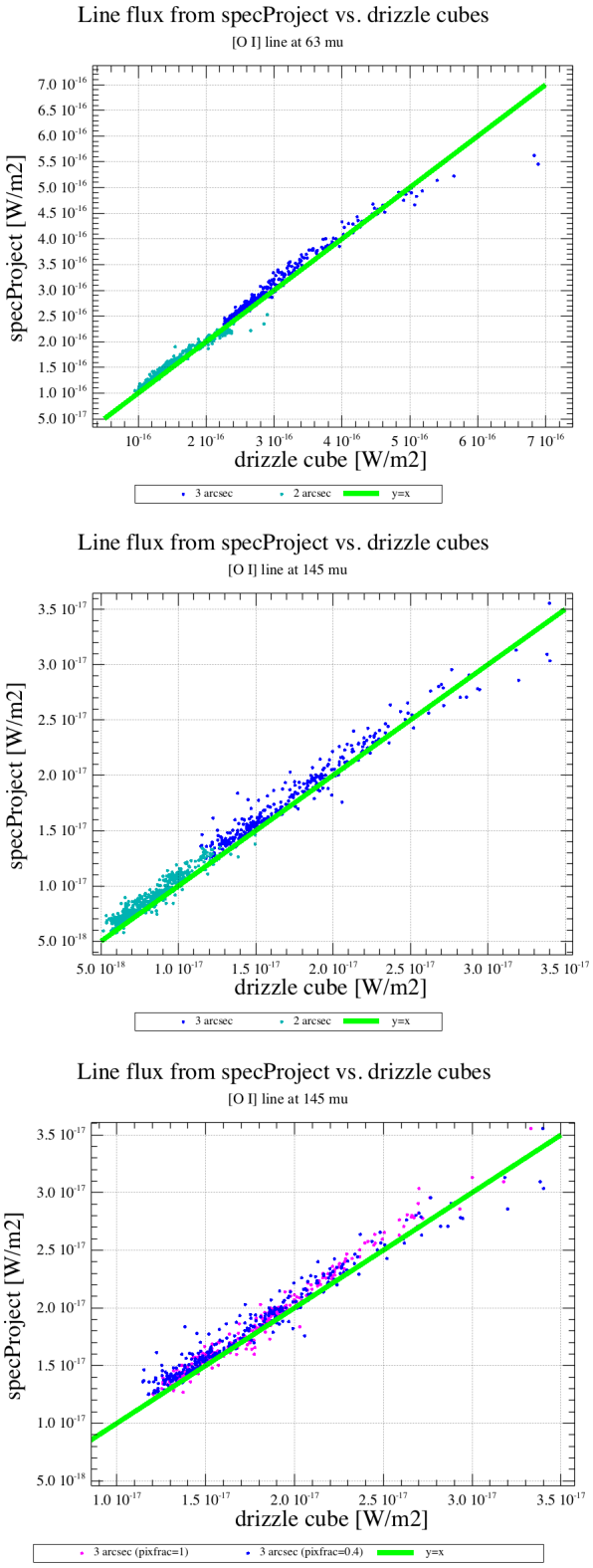

Figure 7.8: Flux comparison per pixel at the line maps generated from specProject cube and for the drizzle cubes at this work. (*Top*) image for [OI] 63 μm line map and (*middle*) image for the [OI] 145 μm line map. The comparison at the line maps with output pixel size of 3″is represented with blue dots and for those of 2″pixel size with green dots. (*Bottom*) image perform a similar comparison between specProject and drizzle for shrinking factors of 60 % (blue dots) and 100 % (pink dots)

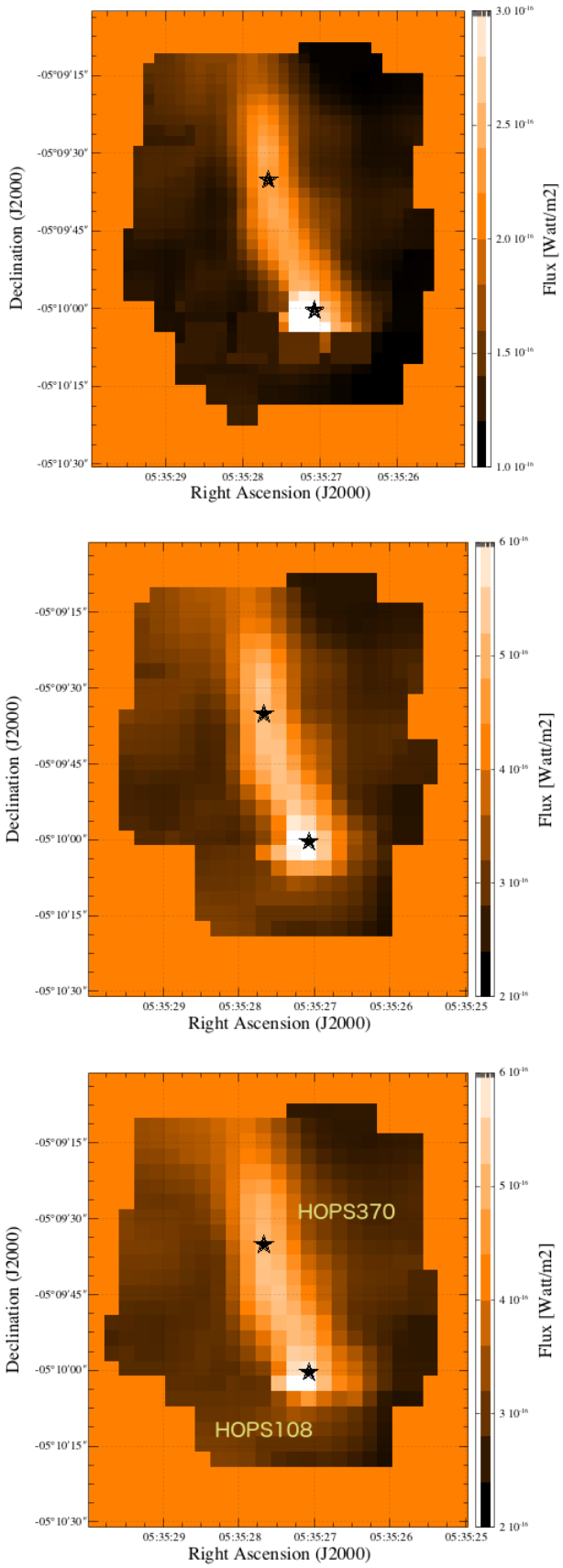

Figure 7.9: *(Top)* The [O I] 63 μm line map generated with Drizzle and specInterpolate for 2″. *(Middle)* The [O I] 63 μm line map generated with Drizzle and specInterpolate for 3″. *(Bottom)* The [O I] 63 μm line map generated with specProject and specInterpolate for 3″.

8

HOPS spectroscopy legacy products

In this chapter we discuss the flux extraction; the creation of the PACS continuum and the continuum subtracted line maps and SPIRE line-plus-continuum line maps, by fitting each spaxel of the hyper spectral cubes, and the fitting results used to create two dimensional line flux and continuum maps.

8.1 Fitting of emission lines and continuum

At this step we identified all significant detections of CO, H_2O and fine structured lines and provided estimated fluxes for all these detections.

8.1.1 Line fitting

For each spaxel of the reconstructed cubes a Gaussian profile was fitted to the emission line and a zero order polynomial to the continuum. Since not all pixels in the spectral cube detect significant line emission, the fitting method needs to distinguish between cases when continuum only or continuum plus line is detected. The most robust solution was to fit first the zero order polynomial to the continuum where the spectral segment corresponding to the expected line profile was masked out. The spectral range of a masked segment around the expected line profile was chosen 3-5 $\times$ the local spectral resolution. Line central wavelengths are adopted from a database of CO, water, OH and fine structure lines rest wavelengths. The continuum subtraction step was applied to all spatial pixels,

irrespective of whether line emission was detected or not. This way, any small residual continuum left over from the multi-resolution baseline fitting were eliminated.

In the second step we fit Gaussian line profiles on the continuum-subtracted spectra. We apply the previously identified line mask, in this case, to identify the wavelength range on which we fit the line profile. This is important, because a single drizzle ID may contain several lines close to each other in wavelength.

The fitting used a Levenberg-Marquardt algorithm to find the best fit, and it returns the model values (peak, λ, sigma, with) and their errors. The fitting was tested in four ways. In the first case the algorithm started in the corner of the hyper spectral cube and fit each spaxel individually. In the second case, the fitting started from a reference spaxel and the fitting results were passed to the neighbouring spaxel and the fitting done with this priors; these fitting results were in turn passed to its neighbour as priors, and this process was repeated until the whole cube was completed. The third method is similar to the second, but the fitting results from a single reference were adopted for all spaxel in the cube. The reference spaxel was identified as the brightest spaxel from a smoothed map that was derived by integrating intensities over the profile of the line. The fourth method is similar to the third method but using the GUI version of the task.

As our purpose was to perform this fitting in an automatic mode, we spent some time analysing which was the best method to fit bright and faint lines. The results of the different fitting methods when applied to a bright line and faint line are shown in Fig. 8.1. The results from method 3 and method 1 are similar; but for faint lines the line maps generated with the multi-fitter provide a more realistic reconstruction of fluxes compared to other methods, as is visible at Fig. 8.2.

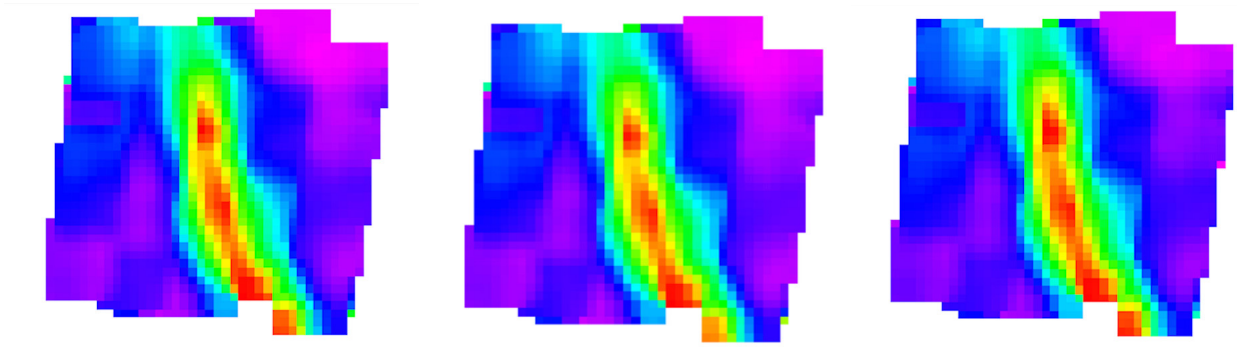

Figure 8.1: Comparison of line maps generated for the different fitting methods for a bright line: (*left*) method 1: fitting spaxel by spaxel in a loop obtaining the model (Gaussian + zero order polynomial) for a spaxel and passing it as input for the fitting of the neighbour pixel, (*middle*) method 3: automatic selection of the reference spaxel and applying to it a model (Gaussian + zero order polynomial) which later will be passed it as input for fitting the rest of the cube with the Multifitter task and (*right*) method 4: same as method 3 using the GUI task.

Manual inspection and in some cases recalculation of the line maps was done for lines contaminated by neighbouring lines, which may vary the parameters from the Gaussian fit or the continuum level.

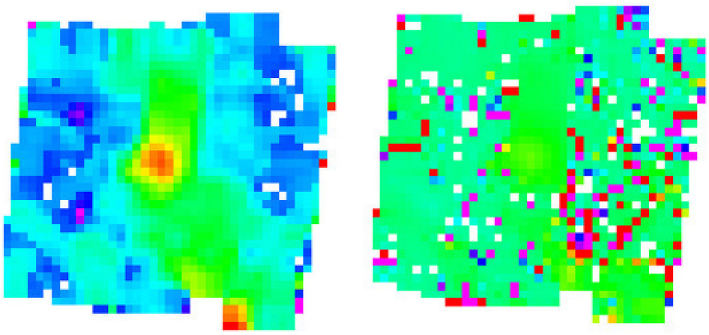

Figure 8.2: Comparison of line maps generated for the different fitting methods for a faint line: (*left*) method 1: fitting spaxel by spaxel in a loop obtaining the model (Gaussian + zero order polynomial) for a spaxel and passing it as input for the fitting of the neighbour pixel and (*right*) method 3: automatic selection of the reference spaxel and applying to it a model (Gaussian + zero order polynomial) which later will be passed it as input for fitting the rest of the cube with the Multifitter task.

After fitting, integrated flux maps were created using the equation of the area under the Gaussian. The result of this process is then a set of line integrated flux maps in units of W/m^2 for each emission line detected.

The bin-to-bin continuum noise was calculated around each line when the line profile was masked out as described above. Measuring the standard deviation of flux per spectral bin, we were able to create **RMS maps**.

We also created **signal-to-noise maps** by subtracting the estimated residual continuum (see next subsection) from the fitted line peak flux divided by the RMS map. From these maps, we identified those positions where the line peak exceeds 5σ confidence level. These positions are stored in a mask product.

Velocity maps were calculated as the multiplication of the shift in peak wavelength with respect to the rest wavelength for each line in our database (CO, H_2O, OH and fine structured lines) times light speed by the rest wave.

Line width maps were generated by calculating the line FWHM from the fit parameters in microns.

8.1.2 Continuum fitting

In this step, on the continuum-only spectral cubes (the multiresolution baseline estimator separated continuum-only cubes from continuum subtracted cubes, being both of them treated separately in the same way) we fit a simple parametric model to obtain continuum estimates applicable at the central wavelength of each spectral line.

A first order polynomial was fitted within the wavelength range of a *drizzleId*. This way, we have segmented the PACS wavelength range to 31 sub-ranges which have been fitted

with the linear continuum model. Priors to the fit were obtained, a reference spaxel was identified from a smooth map where all spectral bins were integrated in wavelengths.

The fitted first-order polynomial was evaluated at the central wavelength of the lines, which was taken from a database of CO, H_2O, OH and fine-structure lines in the PACS spectral range. The WCS associated with the maps were those applied at that specific drizzleId generated by specProject algorithm. The results of this process is a set of continuum maps in units of Jy/pixel for each emission lines detected.

An example of the lines detected within 7 ″ aperture radius around HOPS 370 (red) and HOPS 108 (blue), from which the spectral line maps were generated is shown in Fig 8.3.

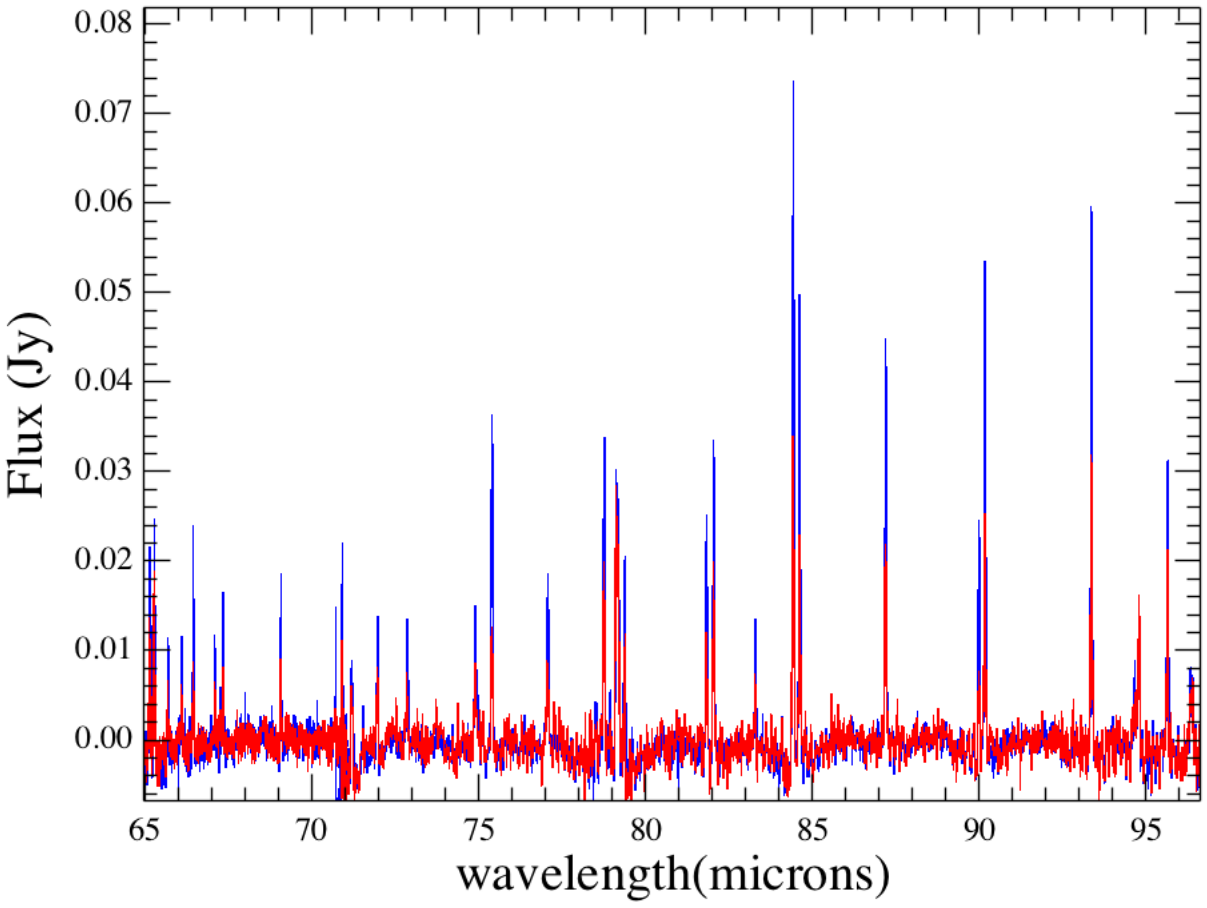

Figure 8.3: Integrating flux extracted for 7″radius around the HOPS 108 (blue) and HOPS370 (red) target.

8.2 Turning fitting results into maps

8.2.1 CO emission line maps

Here we present the line intensity maps of all the CO lines detected in the PACS and SPIRE data of the OMC-2 region.

The maximum flux value displayed at each map is the 85 % of the maximum emission (per line) and the minimum the 15 % of the minimum flux emission. All SNR detections are displayed in the maps. The highest upper quantum momentum (J_{up}) for the CO lines are detected at higher energies and therefore shorter wavelengths, and in some cases they are only an upper limit detection which becomes a NaN pixel value.

The star symbol indicate the position of the two targets at this study: (top) HOPS 370/FIR3 and (bottom) HOPS 108/FIR4. In all cases the brightest emission comes from HOPS 108/FIR4 position. Also visible an extended emission in the line that links the two targets. Scientific analysis of these maps is done in Chapter 11.

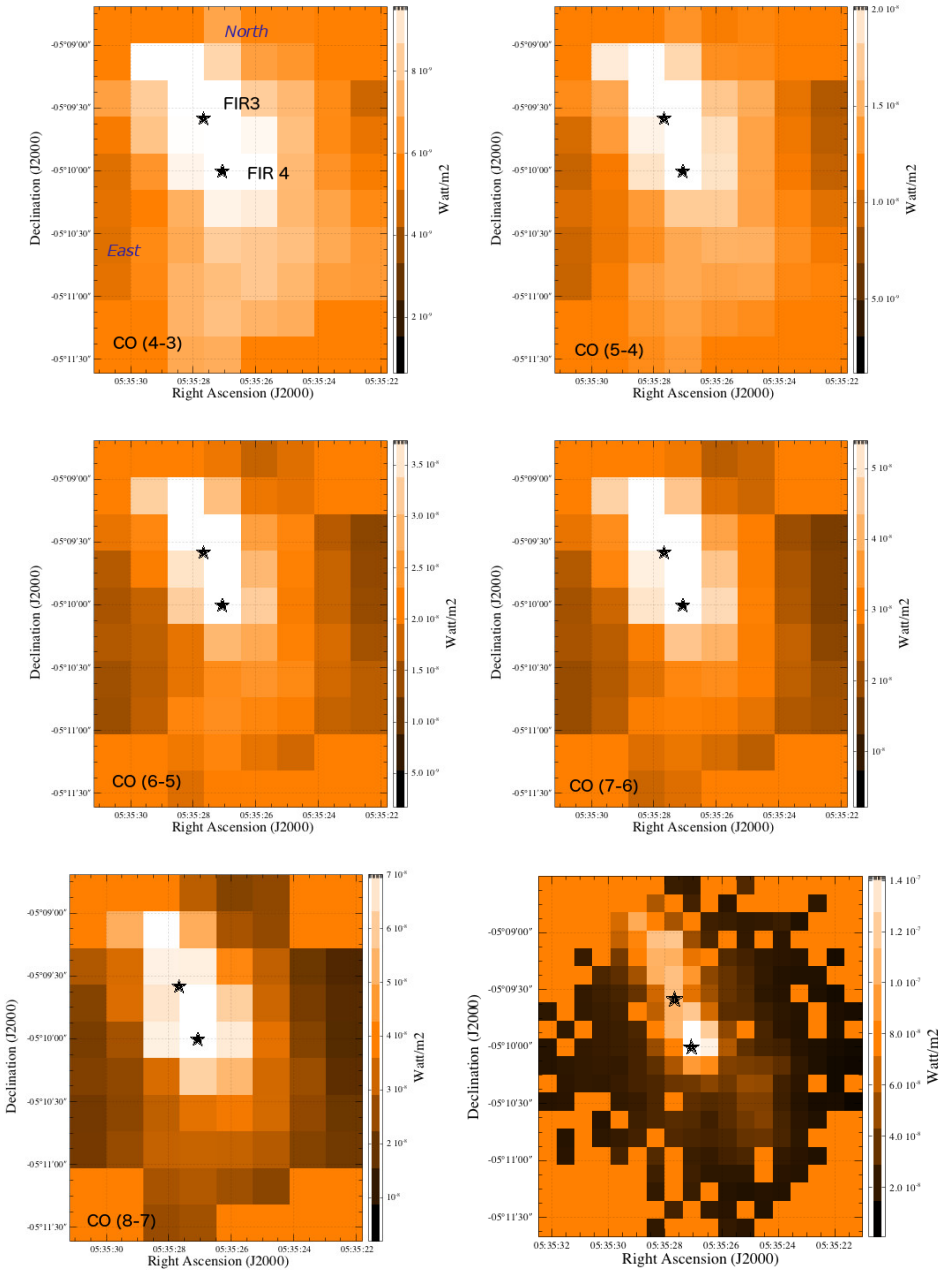

Figure 8.4: Line flux maps of CO transitions detected in the OMC-2 regions for the emission lines CO (4-3), CO (5-4), CO (6-5), CO (7-6), CO (8-7) and CO (9-8). From CO (4-3) to CO (8-7) the lines were detected with the SPIRE SLW detector and CO (9-8) with SSW detector. The star symbols represent the OMC-2 FIR 3 target (top) and OMC-2 FIR 4 target (bottom).

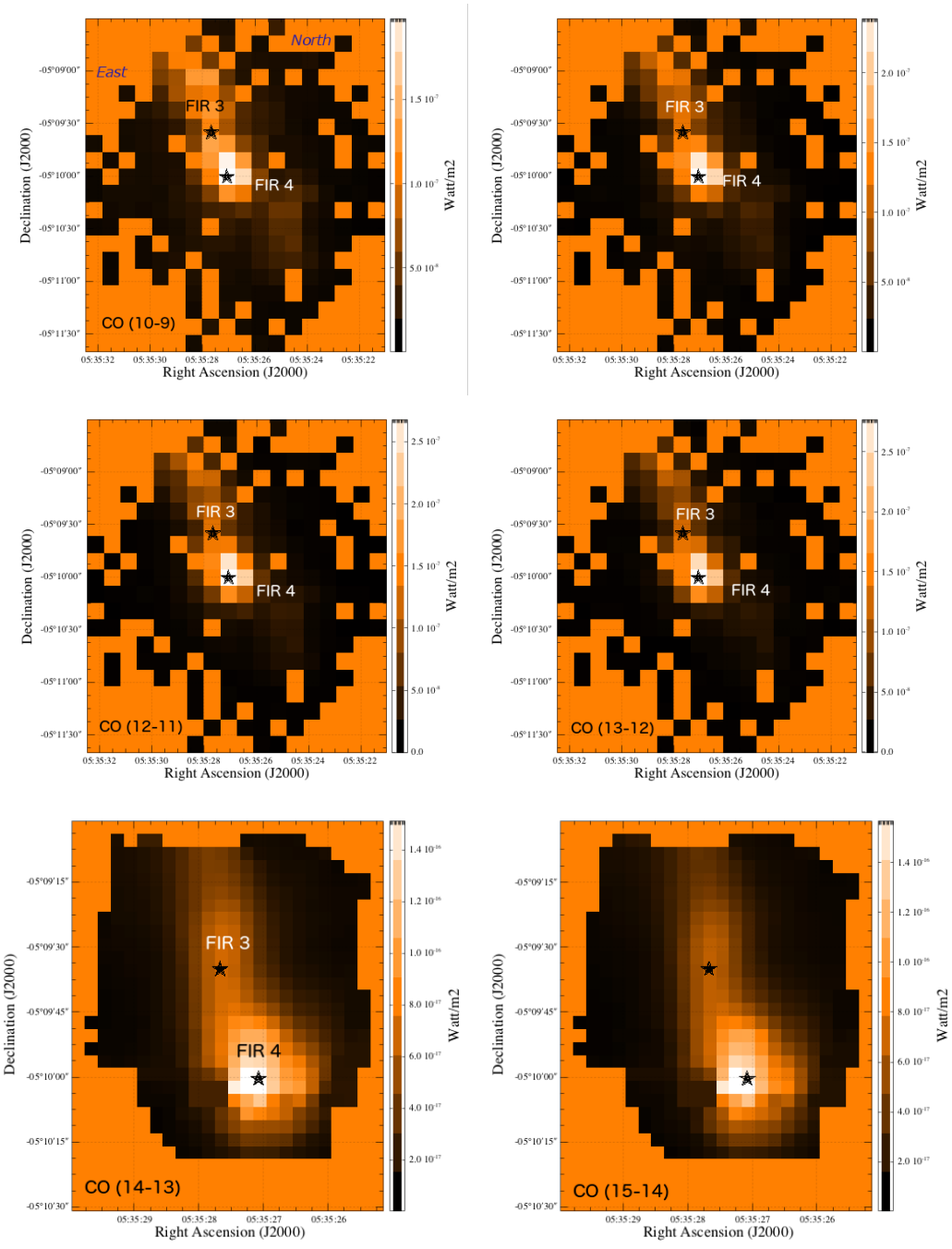

Figure 8.5: Line flux maps of CO transitions detected in the OMC-2 regions for the emission lines from detected from SPIRE SSW from CO (10-9) to CO (13-12) and from PACS from CO (14-13) to CO(15-14). See the difference of field of views between SPIRE and PACS maps. The star symbols represent the OMC-2 FIR 3 target (top) and OMC-2 FIR 4 target (bottom).

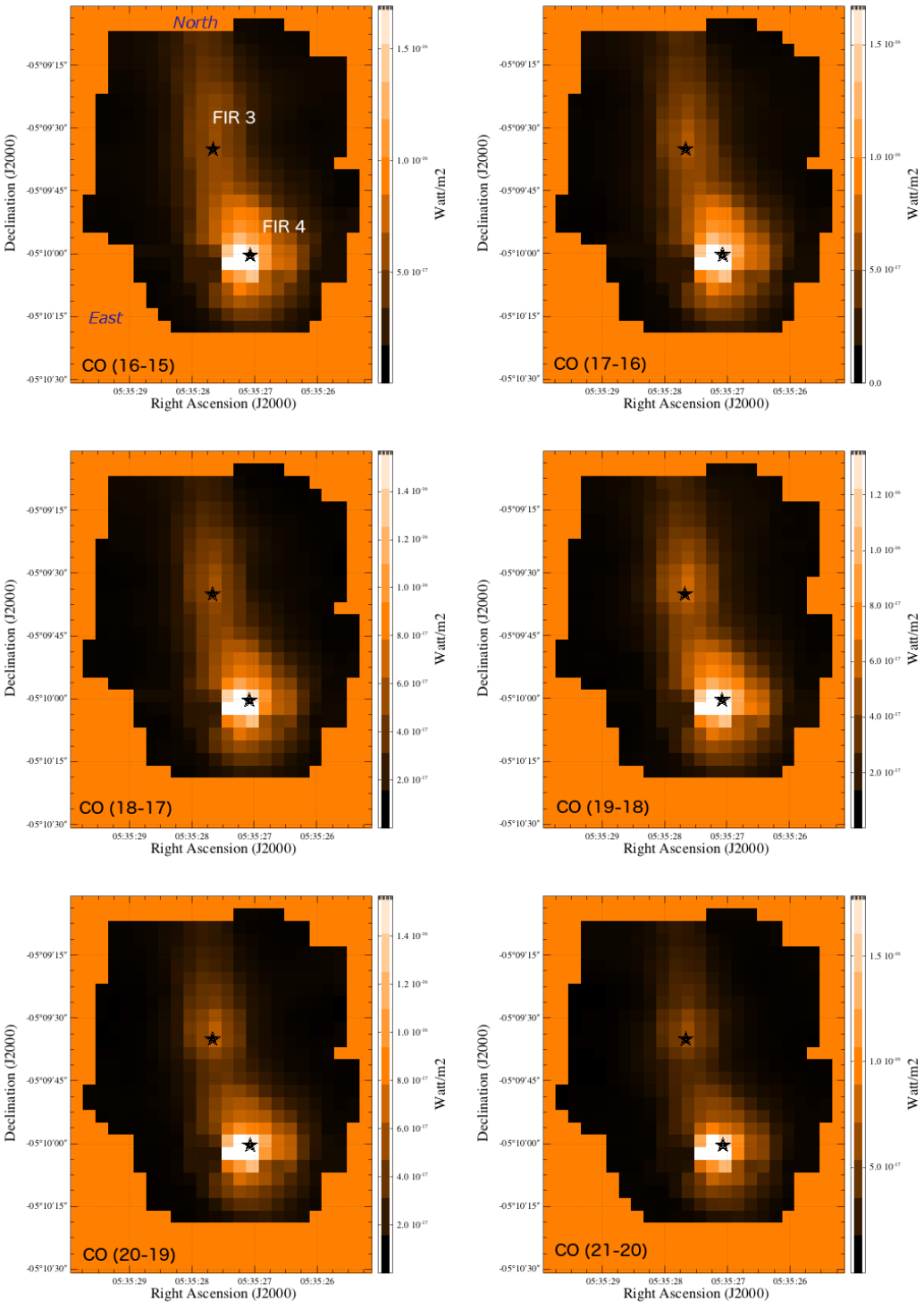

Figure 8.6: Line flux maps of CO transitions detected by PACS in the OMC-2 regions for HOPS 370 (FIR 3) and HOPS 108 (FIR 4) for the emission lines of CO (16-15), CO (17-16), CO (18-17), CO (19-18), CO (20-19) and CO (21-20). The star symbols represent the OMC-2 FIR 3 target (top) and OMC-2 FIR 4 target (bottom).

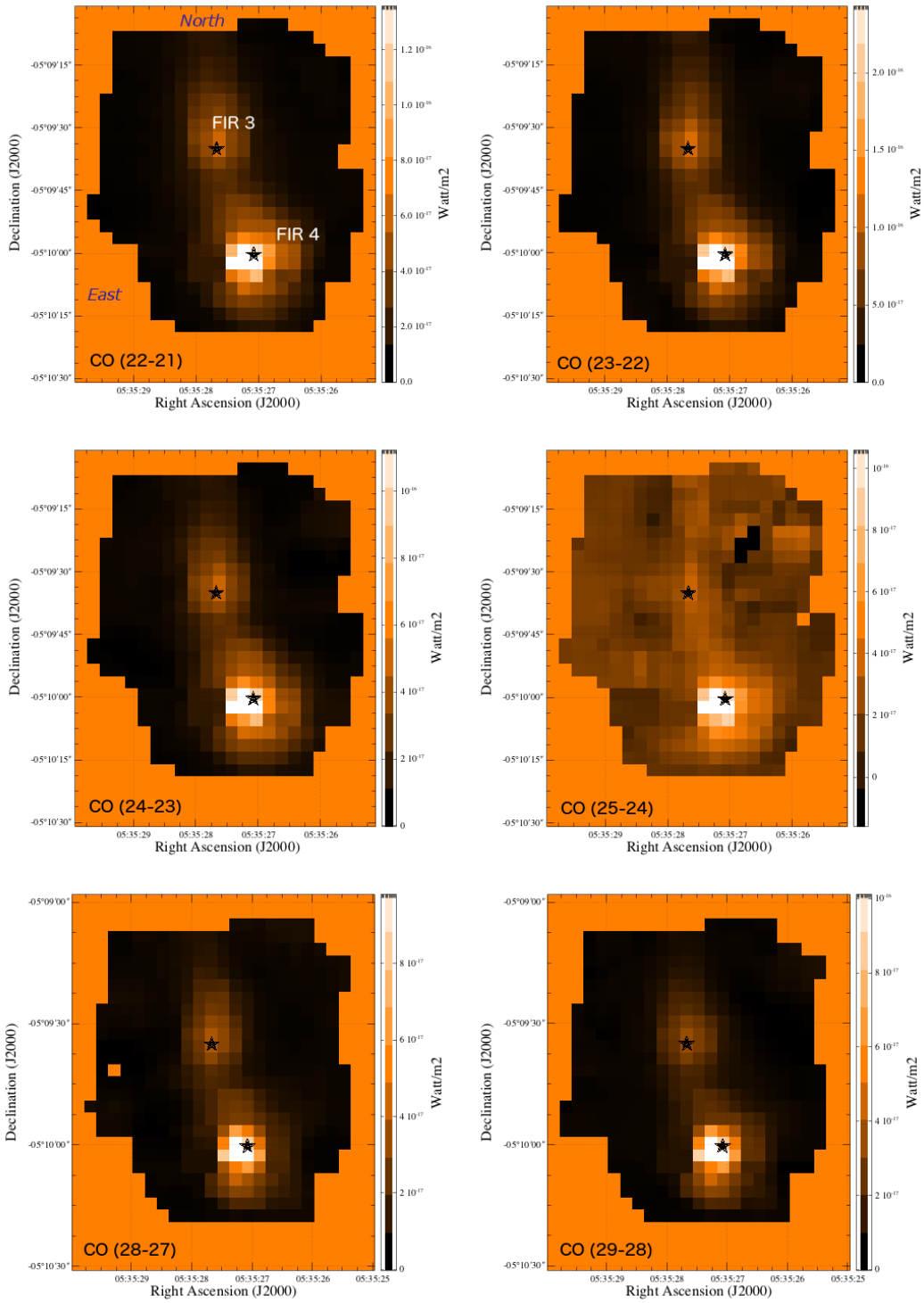

Figure 8.7: Line flux maps of CO transitions detected by PACS in the OMC-2 regions for HOPS 370 (FIR 3) and HOPS 108 (FIR 4) for the emission lines of CO (22-21), CO (23-22), CO (24-23), CO (25-24), CO (28-27) and CO (29-28).

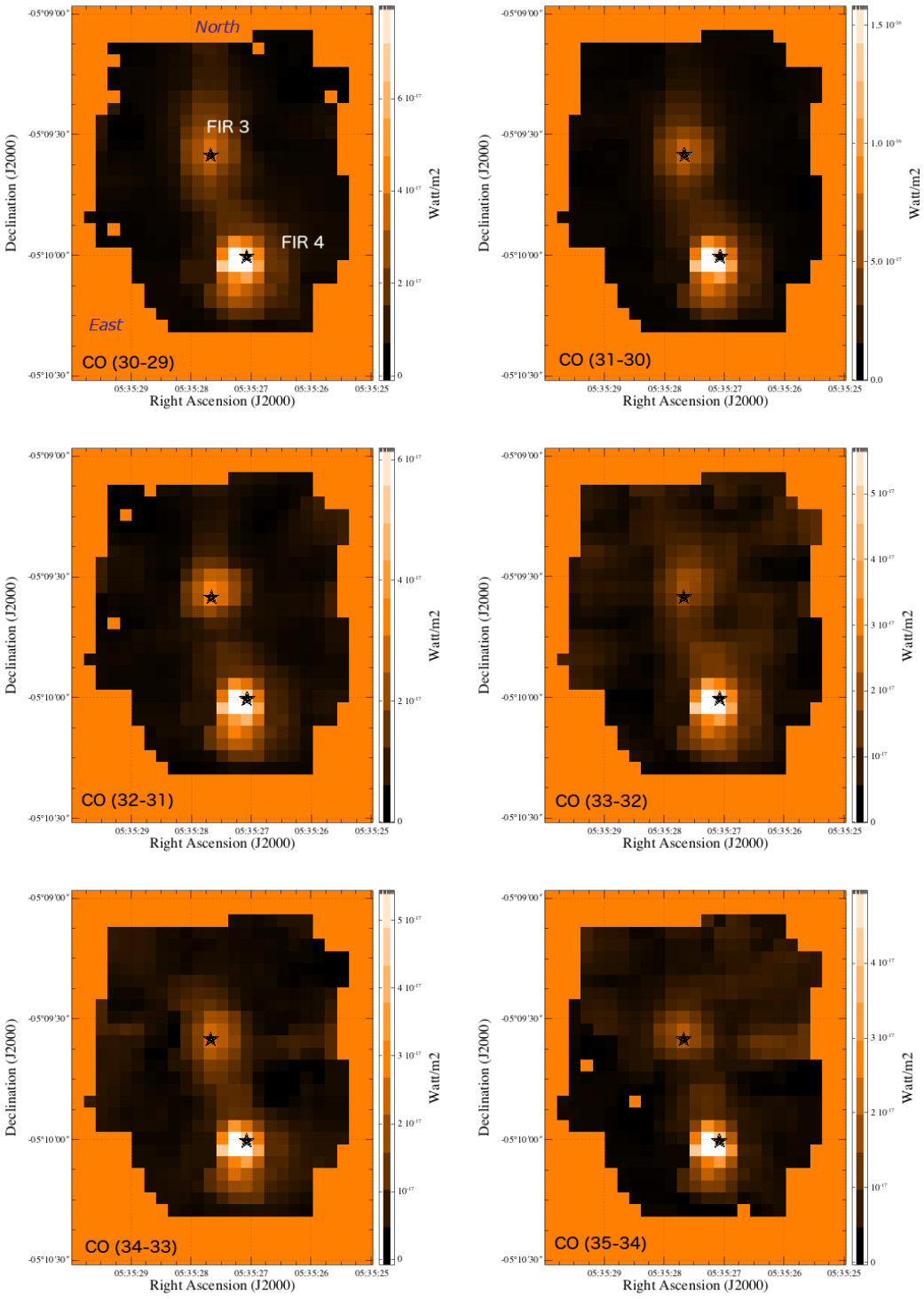

Figure 8.8: Line flux maps of CO transitions detected by PACS in the OMC-2 regions for HOPS370 (FIR3) and HOPS108 (FIR4) for the emission lines of CO (30-29), CO (31-30), CO (32-31), CO (33-32), CO (34-33) and CO (35-34). The star symbols represent the OMC-2 FIR 3 target (top) and OMC-2 FIR 4 target (bottom).

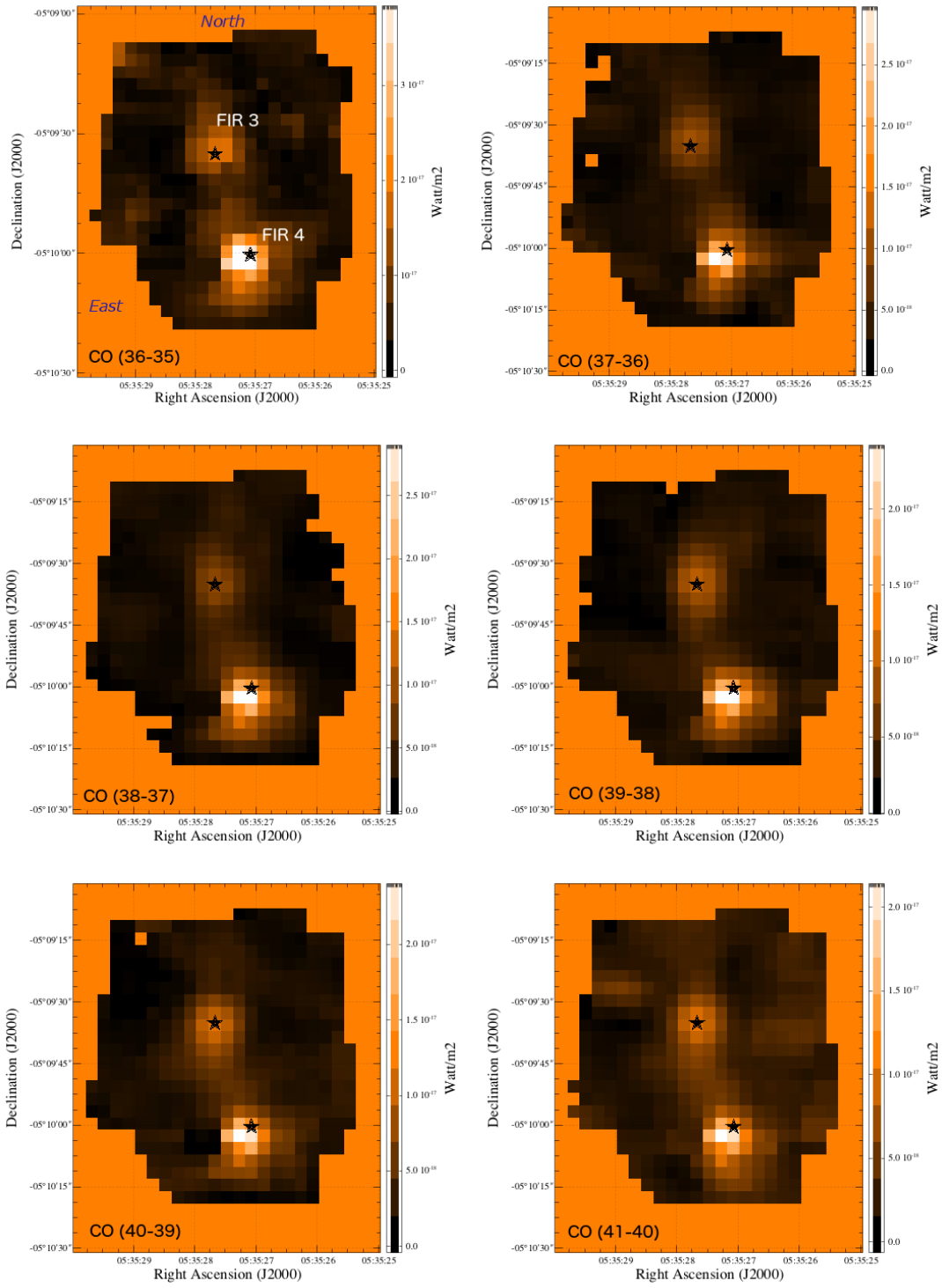

Figure 8.9: Line flux maps of CO transitions detected by PACS in the OMC-2 regions for HOPS370 (FIR3) and HOPS108 (FIR4) for the emission lines of CO (36-35), CO (37-36), CO (38-37), CO (39-38), CO (40-39) and CO (41-40). The star symbols represent the OMC-2 FIR 3 target (top) and OMC-2 FIR 4 target (bottom).

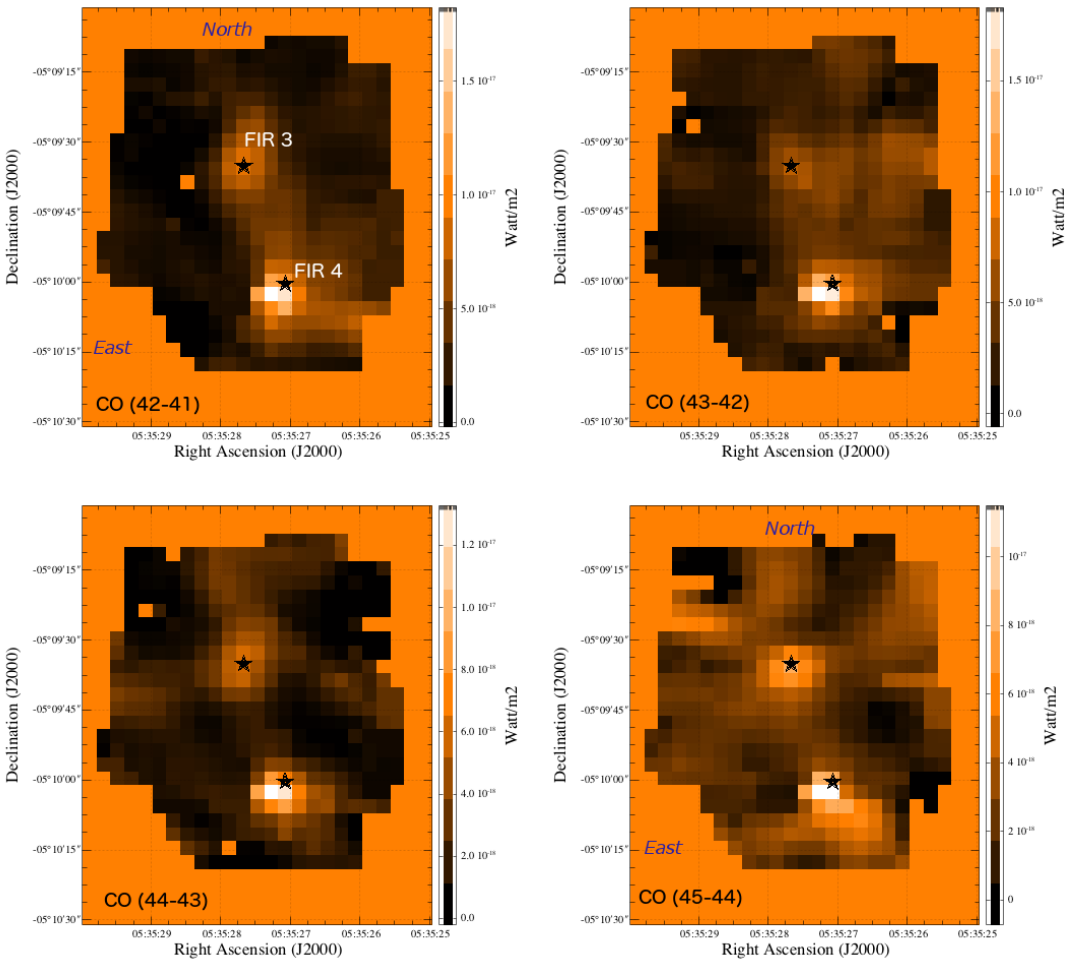

Figure 8.10: Line flux maps of CO transitions detected by PACS in the OMC-2 regions for HOPS370 (FIR3) and HOPS108 (FIR4) for the emission lines of CO (42-41), CO (43-42), CO (44-43) and CO (45-44). The star symbols represent the OMC-2 FIR 3 target (top) and OMC-2 FIR 4 target (bottom).

8.2.2 H_2O emission line maps

Here we present the line maps of all the H_2O lines detected in the PACS data of the OMC-2 region.

The maximum flux value displayed at each map is the 85 % of the maximum emission (per line) and the minimum the 15 % of the minimum flux emission. All SNR detections are displayed in the maps. The highest J_{up} H_2Olines are detected at higher energies and therefore shorter wavelengths, and in some cases they are only an upper limit detection which becomes in a NaN pixel value.

The star symbol indicate the position of the two targets at this study: (top) HOPS 370/FIR 3 and (bottom) HOPS 108/FIR 4. In all cases the brightest emission comes from HOPS 108/FIR 4 position. Also visible is for most maps an extended emission in the line that links the two targets. Scientific analysis of these maps is done in Chapter 11.

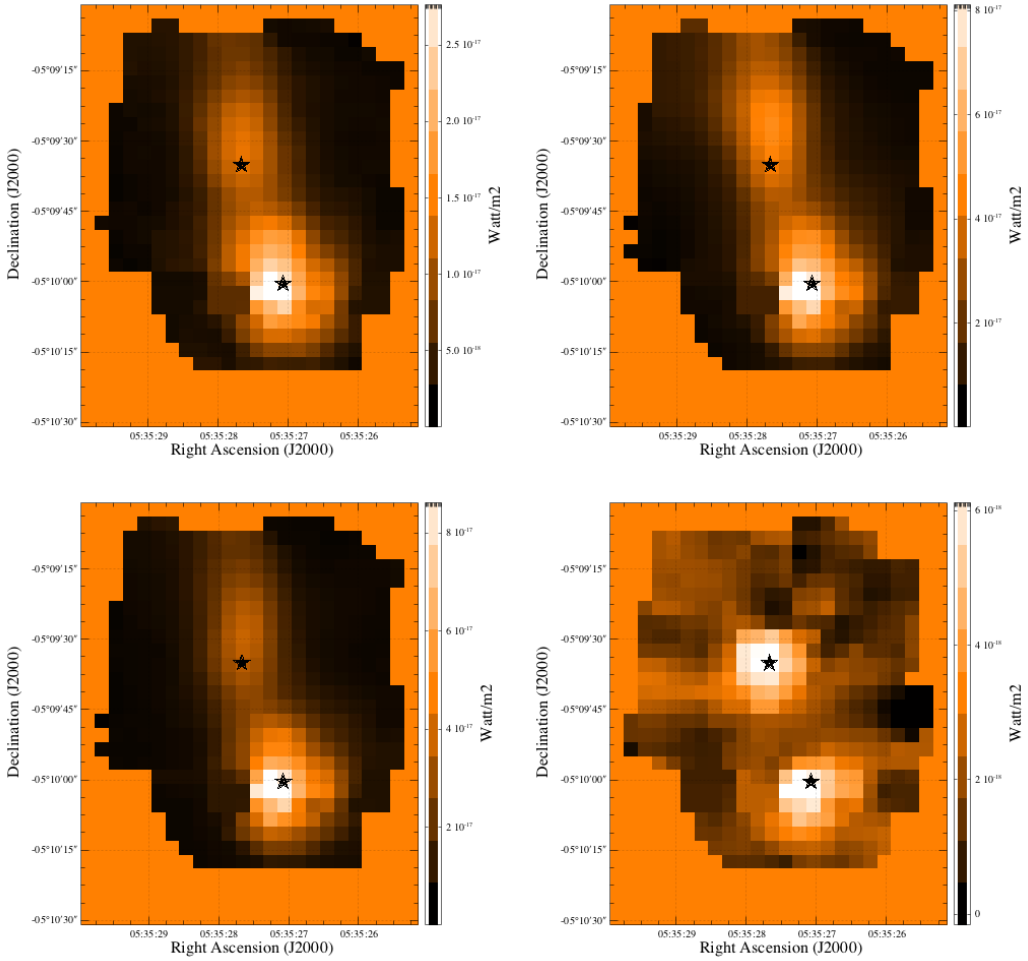

Figure 8.11: Line maps of the *16 ortho-* H_2O detections at the OMC-2 regions. The stars identify OMC-2 FIR3 (top) and OMC-2 FIR4 (bottom). The lines from top left to bottom right are those at the wavelengths: 180 μm , 179.5 μm , 174.6 μm and 160.5 μm .

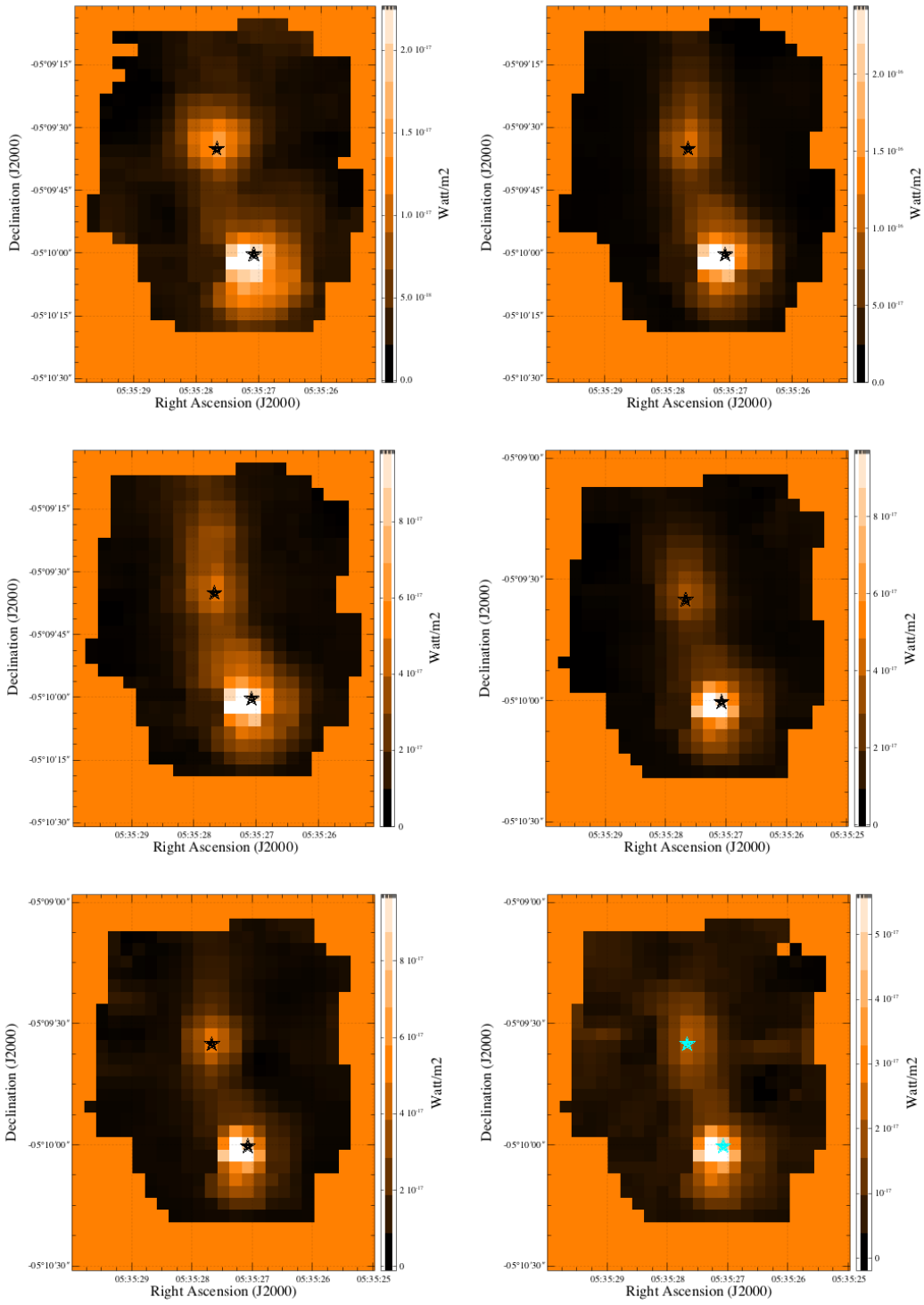

Figure 8.12: Line maps of the *16 ortho-* H_2O detections at the OMC-2 regions. The stars identify OMC-2 FIR3 (top) and OMC-2 FIR4 (bottom). The lines from top left to bottom right are those at the wavelengths: 156.26μm (blended with *para-* H_2O detections at 159.19 μm), 113.53 μm , 108 μm , 96.62 μm , 78.74 μm and 77.08 μm .

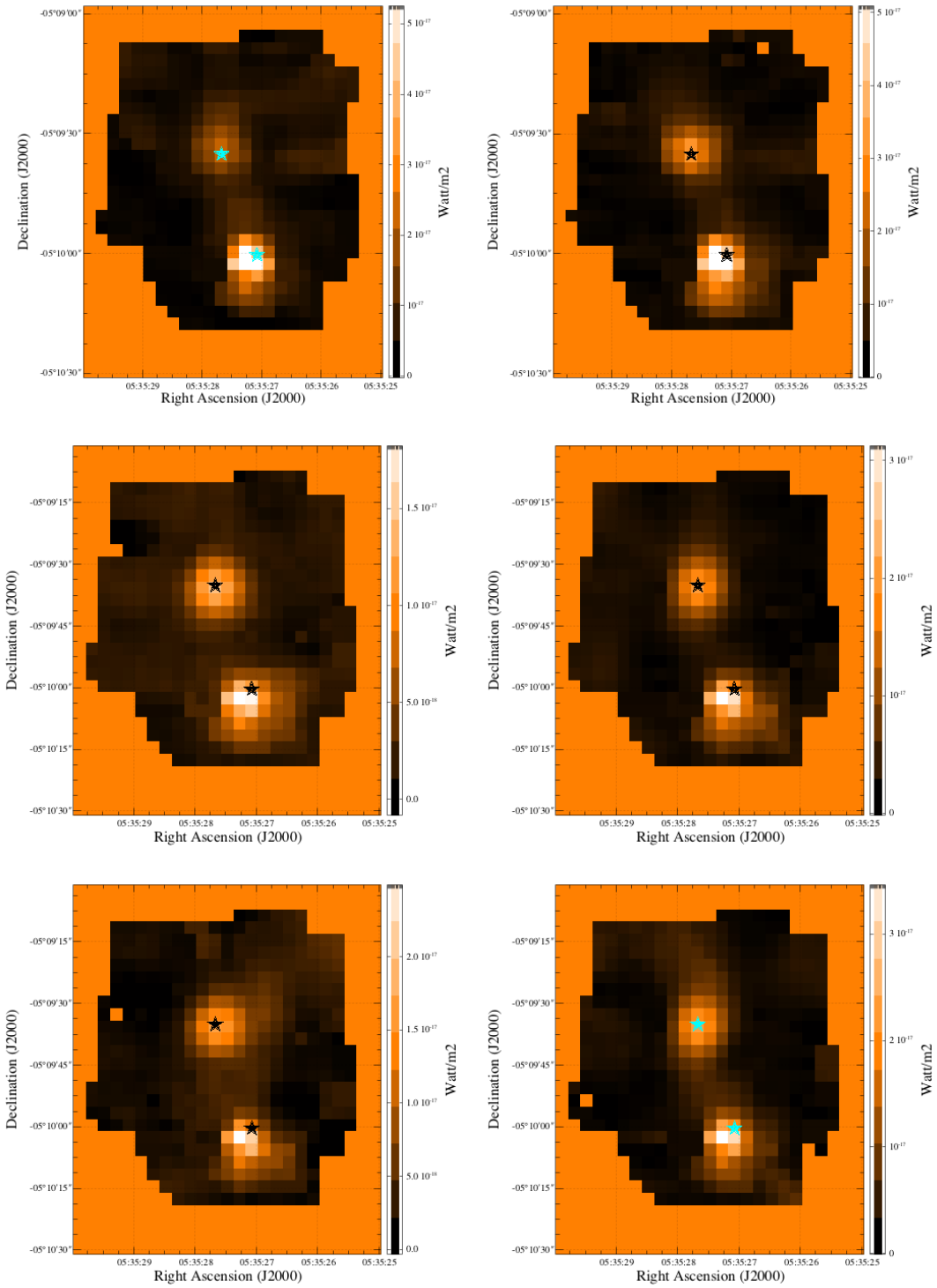

Figure 8.13: Line maps of the *16 ortho-* H_2O detections at the OMC-2 regions. The stars identify OMC-2 FIR3 (top) and OMC-2 FIR4 (bottom). The lines from top left to bottom right are those at the wavelengths: 74.94 μm , 71.94 μm , 66.09 μm , 65.16 μm , 63.32 μm and 58.69 μm .

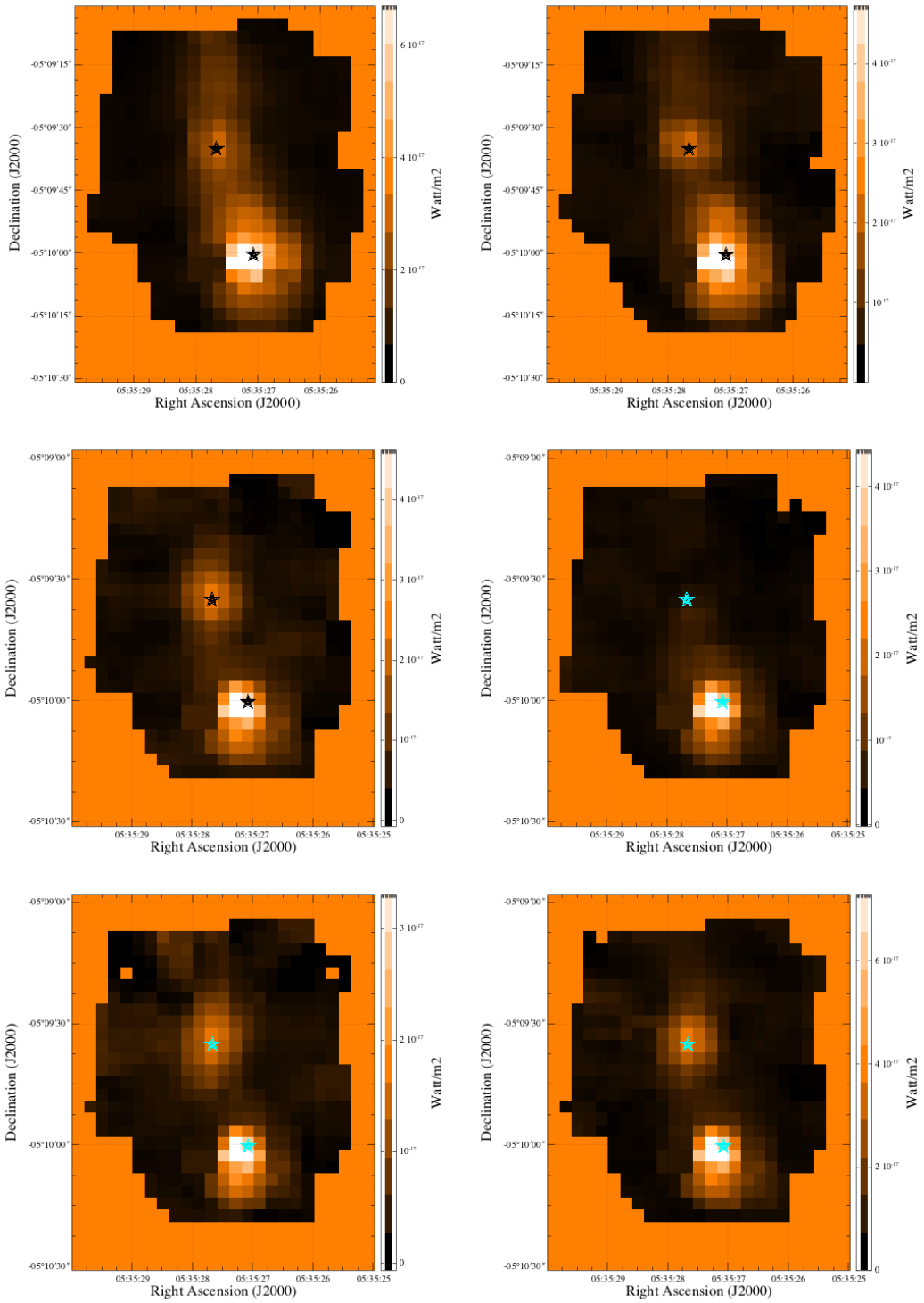

Figure 8.14: Line maps of the *16 para*- H_2O detections at the OMC-2 regions. The stars identify OMC-2 FIR3 (top) and OMC-2 FIR4 (bottom). The lines from top left to bottom right are those at the wavelengths: 138.52 μm , 125.35 μm , 96.62 μm , 89.98 μm , 83.28 μm and 82.03 μm .

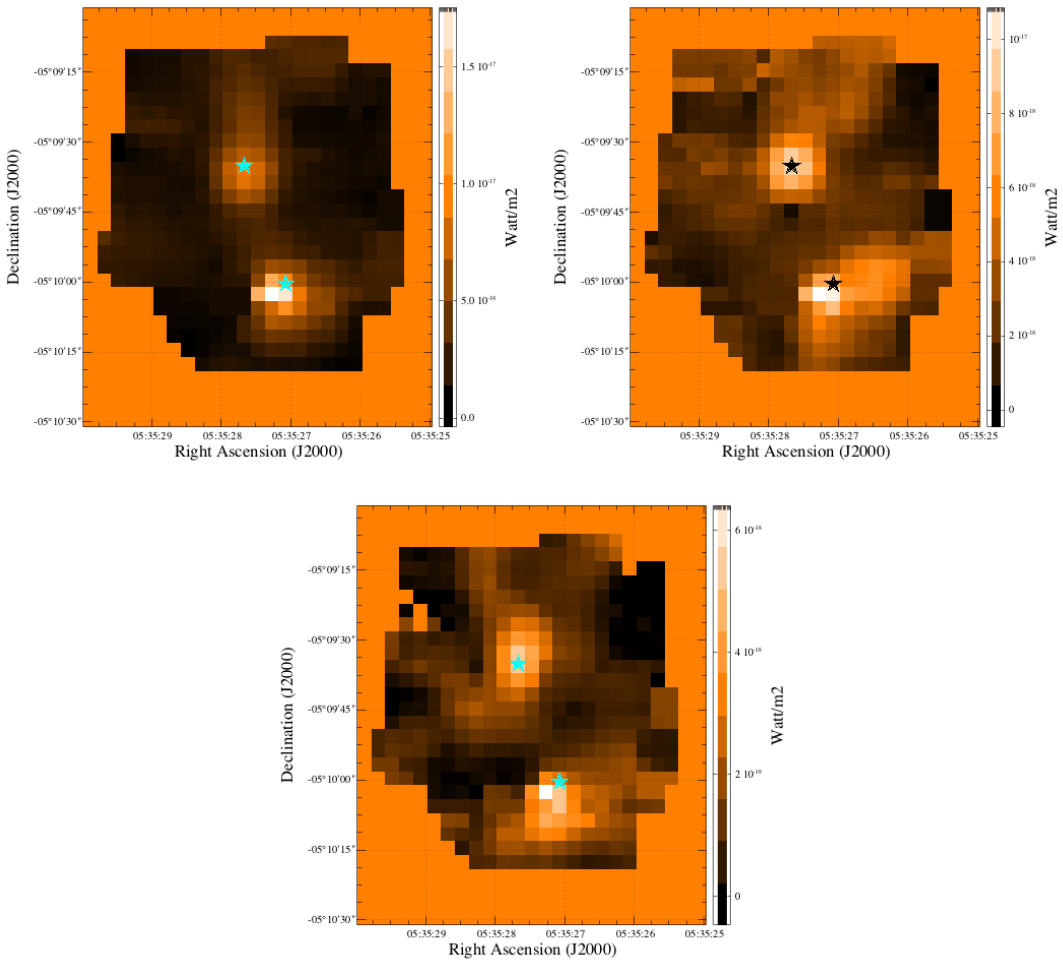

Figure 8.15: Line maps of the (*left*) *16 para-* H_2O at 67.08 μm , 63.45 μm and 59.98μm .

8.2.3 Fine Structure emission line maps

These are the line maps generated for the two [OI] lines and the [CII] line detected in the OMC-2 region. The star symbol indicate the positions of (top) HOPS370/FIR3 and (bottom) HOPS108/FIR4.

The [CII] line map traces the faint, extended emission component while the [OI] lines trace a narrower component, especially the [OI] 63 μm line, as shown in Figure 8.16.

Analysis of the scientific results can be found in Chapter 10.

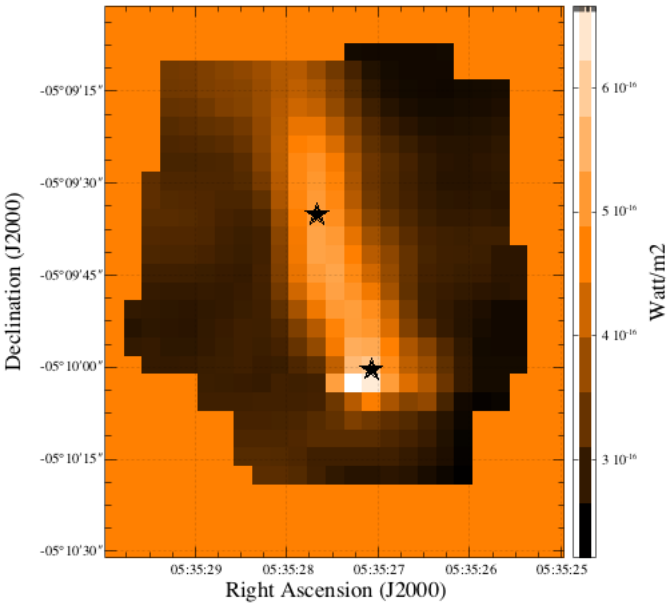
-05°09'15"
-05°09'30"
-05°09'45"
-05°10'00"
-05°10'15"
-05°10'30"
Declination (J2000)
05:35:29
05:35:28
05:35:27
05:35:26
05:35:25
Right Ascension (J2000)
6 10-16
5 10-16
4 10-16
3 10-16
Watt/m2

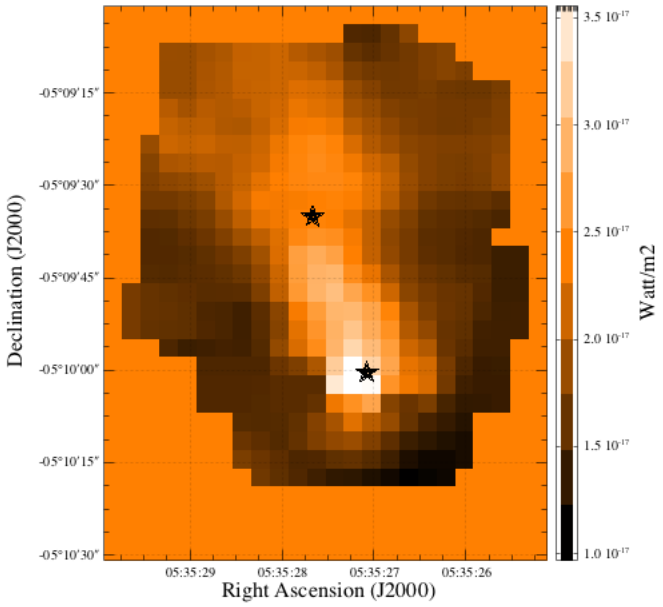
-05°09'15"
-05°09'30"
-05°09'45"
-05°10'00"
-05°10'15"
-05°10'30"
Declination (J2000)
05:35:29
05:35:28
05:35:27
05:35:26
Right Ascension (J2000)
3.5 10-17
3.0 10-17
2.5 10-17
2.0 10-17
1.5 10-17
1.0 10-17
Watt/m2

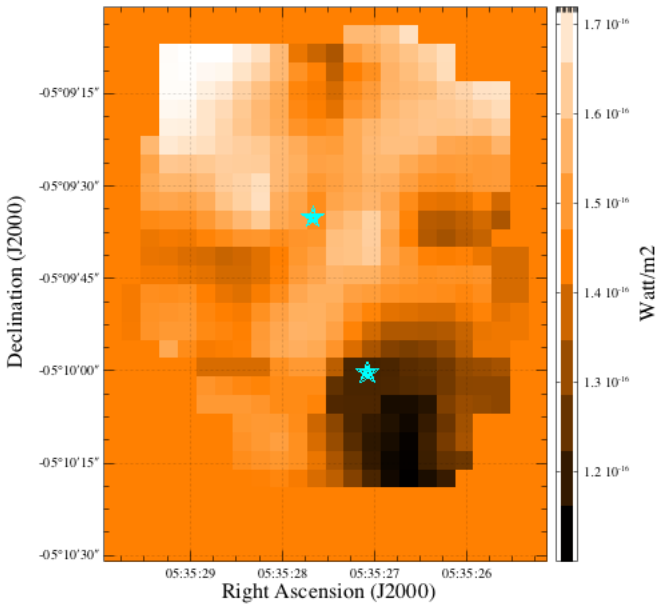
-05°09'15"
-05°09'30"
-05°09'45"
-05°10'00"
-05°10'15"
-05°10'30"
Declination (J2000)
05:35:29
05:35:28
05:35:27
05:35:26
Right Ascension (J2000)
1.7 10-16
1.6 10-16
1.5 10-16
1.4 10-16
1.3 10-16
1.2 10-16
Watt/m2

8.3 Extracting the source fluxes from the maps

To identify an optimal method to extract fluxes from our line maps and to compare to previous fluxes in the literature for HOPS 108, we:

- Analysed the morphology of the source.
- Identified the correct aperture for flux extraction from our line maps.
- Extracted the aperture line fluxes.
- Compared to Manoj et al. (2013).
- Generated of a beam correction factor applicable to point sources extracted from specProjected maps. This was eventually not used in our analysis.

8.3.1 Analysis the morphology of the source

We needed to determine whether HOPS108 was a point source or was slightly extended, as the method of extracting the correct fluxes is different for these two cases.

The first comparison we did was the level 2 "rebinned" cubes, i.e, the 5×5 cubes created before any mosaicking is done, using a task provided by the PACS ICC which extracts the spectrum from the central spaxel (*c1*) and compares it to the flux from the 9 central spaxels (*c9*). The first (*c1*) applies a point source correction to flux measured on the central spaxel only, while the other method (*c9*) applies a correction adequate for flux extracted from the central 3×3 spaxels. This ratio is then compared to that for a perfectly-centred point source. In case the source is extended, we expect the latter method will estimate significantly higher flux values. Deviations when comparing the two methods indicate that the source is not a point source that is well centred in the central spaxel. Visual inspection of the rebinned cubes of the HOPS 108 observations show that the maximum flux is in the central spaxel, so we may discard bad pointing and focus on the compactness or not of the source.

The ratio of *c1 to c9* depends on the continuum, which is not reliable for unchopped mode observations, so strictly speaking we could not use this method for assessing whether our source is point like or not. However, we could use the same method but concentrate on the flux of the emission line rather than the continuum.

Applying both methods to the data we created point source corrected spectrum 1d products and divided the peak line flux values. Our results are recorded in Table 8.1 for some of the CO lines detected in our HOPS 108 spectra. Following a recommendation from the PDRG, one consider c9/c1 a significant indication of extendedness, if the ratio exceeds 1.2 for a dataset where the faintest spaxel among the central 3×3 has a minimum of 5 Jy peak-to-continuum flux.

We did the same exercise on RDor chop/nod calibration observation (1342248689) collected from the HSA which was processed in HIPE 14.0. The result *c9/c1* was less than 1.15 for both blue (∼ 80 μm) and red band (∼ 160 μm). From the it c1/c9 values reported in Table 8.1 we obtained values ≥ 2.0, which means that HOPS108 is not consistent with a point source.

Table 8.1: *c9/c1* comparison from the peak of CO lines detected in the HOPS108 spectra.

CO transition (J_{up} - J_{low})	rest wavelength μm	c9/c1
14-13	185.999	3.33
15-14	173.631	3.57
16-15	162.812	2.86
17-16	153.267	2.44
18-17	144.784	2.44
19-18	137.196	2.50
20-19	130.369	2.20
21-20	124.193	2.05
22-21	118.581	2.10
23-22	113.457	2.09
24-23	108.763	2.20
28-27	93.349	1.75
29-28	90.163	1.82
31-30	84.411	1.65
32-31	81.806	1.63
34-33	77.058	1.66
35-34	74.890	1.79
36-35	72.843	1.83
37-36	70.907	1.47
38-37	69.074	1.67
39-38	67.336	1.67
40-39	65.686	1.59
41-40	64.117	2.15
42-41	62.624	1.85

The second check that we applied was to compare to flux distribution of a point source target (RDor) with the one from HOPS108 at certain wavelengths. For that we:

- Downloaded the HOPS108 image from the HSA processed with SPG version 13.0 (single pointing; with *obsId* of1342239690) and a single pointing image of RDor, (with *obsId* of 1342250905).
- From the HOPS observation the level 2.5 the rebinned cubes products were taken and run through specInterpolate with 3 $''$spaxels (as our line maps have).
- The same was done for the RDor data, using the level 2 (chopNod observations are complete at level 2, unchopped require level 2.5).
- For both we fit the 63 μm line with a Gaussian and a 1st order polynomial to the continuum.
- From the Gaussian integrated flux we created an image with the WCS of HOPS 108 and transposed to to the WCS of RDor.

- We made contours of the RDor image, at the peak flux, 1/4 peak flux, 1/2 peak flux, and 3/4 peak flux.
- We superimposed these contours on the image of HOPS 108.
- The HOPS 63 μm image was scaled to 98 % contour level, allowing so to compare the appearance of a point source from a pointed observation to that for HOPS 108.

The results are shown in Fig. 8.17: while there may be a slight offset in the centring of RDor on our source (< 3″), it is clear that HOPS 108 is close to being a point source but does not have the same flux distribution, since the central bright part is more rectangular and the emission immediately outside the central bright region is relatively bright. Whether this is emission from the HOPS 108 or from the background is not yet established, but in any case it is clear that HOPS 108 cannot be treated as a point source in HIPE, and the PACS task to extract point source corrected spectra cannot be used.

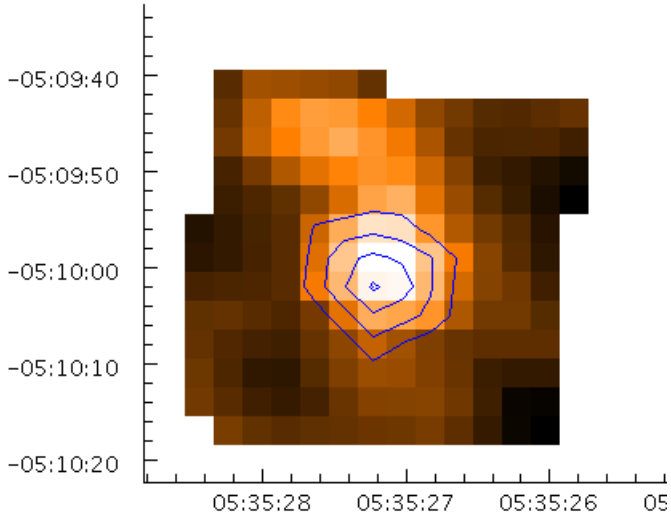

Figure 8.17: The image show the contours levels (75%, 50% and 25% the maximum flux) of the flux distribution line map, generated from specInterpolate cubes with 3 ″spaxel, for a point source (RDor) overlaid with the line map generated with the same technique for HOPS108.

8.3.2 Identification of the proper aperture radius where to measure the flux for the OMC-2 targets

As our targets are extended we will use apertures to measure the emission line fluxes directly from our line maps. For this we need to establish the best aperture radius to use. We compared these flux values for different apertures on our [OI] 63 μm and [OI] 145 μm line maps.

- *an aperture of radius 5.3″*, this radius will generate an aperture equivalent to considering only the central spaxel. From the rebinned cubes, i.e. a single spaxel size (9.4″).
- *within an aperture of radius 15.9″*, this radius will generate an aperture equivalent to central 9 nature spaxels.

- *within an aperture of radius 10″*, this radius will generate an aperture which will contain almost 2 spaxels.

The results are given in Tables 8.2 and 8.3. As the source is not point-like, an aperture with a radius equivalent to the central spaxel will not provide all the flux from the source. However there is line emission over the entire region around the sources, arising particularly from the jet. And aperture of radius 15.9 ″will add much more flux than those from the sources themselves. An aperture of 9-10″is therefore a compromise between including most of the flux from the source without adding much flux from the background emission.

Table 8.2: Fluxes extracted for several aperture radii for HOPS108 and HOPS370 from the line maps of [O I] at 63 μm and [O I] at 145 μm

HOPS ID	line μm	flux(5.3 ″)	flux(10 ″) $\times 10^{-15}$ (Watt m^2)	flux(15.9 ″)	beam radius ″
108	63	4.477	13.402	28.642	4.5
108	145	0.268	0.843	1.799	5.25
370	63	0.390	1.259	2.864	4.5
370	145	0.215	0.770	1.844	5.25

Table 8.3: Fluxes extracted for several aperture radii for HOPS108 and HOPS370 from the line maps of CO (16-15) at 162.8 μm and CO (20-19) at 130.37 μm

HOPS ID	CO transition (J_{up} - J_{low})	rest wavelength μm	flux(5.3 ″)	flux(9 ″) $\times 10^{-15}$ (Watt m^2)	flux(15.9 ″)	beam radius (″)
108	16-15	162.8	1.394	2.865	5.254	5.7
108	20-19	130.3	1.262	2.425	4.063	5.0
370	16-15	162.8	0.522	1.416	3.803	5.7
370	20-19	130.3	0.317	0.896	2.655	5.0

8.3.3 Comparison of the CO fluxes from our line maps with those measured byManoj et al. (2013) for the target HOPS108

Manoj et al. (2013) presented the CO line fluxes for the HOPS spectrometer targets. He processed the pointed observations (among them the same HOPS108 observations that we analyse in our work) with the recommended HIPE at the time (HIPE 8.3 and calibration version 32). The spectra for the different targets were extracted from the central spaxel in the rebinned cube and the line fluxes were calculated as the flux under each of the CO lines. Point source corrections were translated from PACS recommended values to IDL by Manoj and applied to the fluxes. We, instead, extracted aperture line fluxes from the line maps we created for this region. Fig. 8.18 and table 8.4 show how our CO fluxes differ from those of Manoj et al. Where do these differences come from?

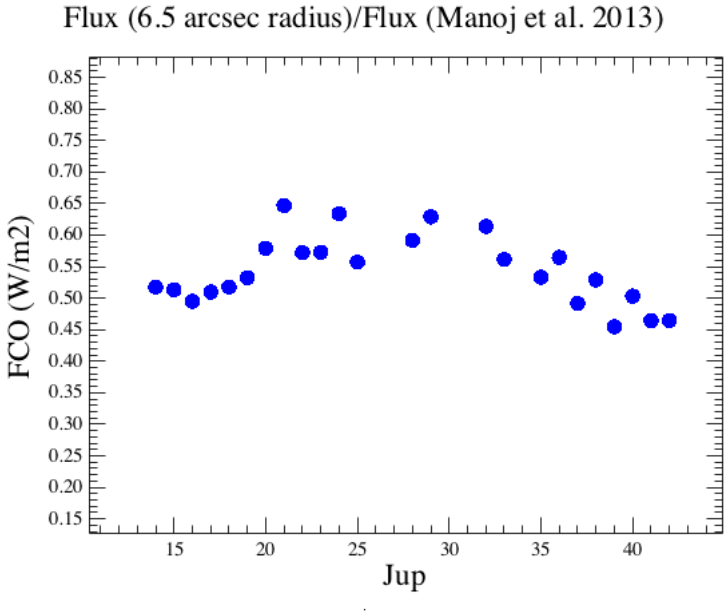

Figure 8.18: Comparison of our flux measurements from the CO line maps detected in the PACS range (J_{up} = 42-14) versus those from Manoj et al. (2013).

Here we enumerate the differences between Manoj et al. (2013) processing and our processing for the same observations of HOPS108, and will explain the different results. Bear in mind that at the beginning we assume that HOPS108 was a point source.

(1) What is the impact on flux values for having processed the data with HIPE 8.0 User Release (Manoj et al. 2013) and HIPE 12.1 User Release (us)?

(2) What is the impact on the flux values of extracting the flux from the central spaxel from the cube (Manoj et al. 2013) and within an aperture from the line map (us)?

(3) Is our source point-like ? What is the impact on flux values when considering our source an extended source rather than a point source?

8.3.3.1 Impact of different HIPE versions on the resulting flux

To compare the results of processing the same data with two versions of HIPE, I retrieved from the archive an obsid from the target HOPS108 and processed it with HIPE 8.0 User Release (associated with calibration version 32) and with HIPE 12.1 User Release (associated with calibration version 65) up to the generation of PACS Rebinned Cubes. These cubes are fully flux calibrated. The older HIPE was that used by Manoj et al. (2013) and the more recent HIPE was used by us. The flux difference of using different HIPE versions is 10 % due to the new calibration scheme. In addition, the absolute response of each observation is measured from the observations themselves in HIPE 12.1 and not from lab simulations as in HIPE 8.0. Detailed plots of this comparison are shown at Section 4.3.2.

The values provided by Manoj et al. (2013) were the fluxes from extracting the spectrum from the central spaxel and applying the correction factors recommended for "point-like" sources provided

in HIPE but coded in IDL. I applied the Point Source Loss correction provided in HIPE 12.1 to the rebinned cubes. The results for the brightest lines are shown in table 8.6, where there is an mean increase of ~ 10 % flux with the new processing.

8.3.3.2 Impact of extracting the flux from the different final products (rebinned cubes vs line maps)

In this section we compare the impact of using different flux extraction methods for a HOPS108 obsid processed in HIPE 12.1. What is presented in Table 8.7 are the fluxes extracted from the same processing at the central spaxel of the rebinned cube without flux loss correction (*flux(2,2)*), with flux loss correction (*flux (PSC)*) and within an aperture of 13 ″ radius at the line map generated at this work by us, explained in Chapter 8.

We see that the flux are larger when extracting from the line maps within an aperture of 13 ″radius. This made us wonder about the compactness of the source and how important to identify a proper aperture radius it is.

8.3.4 Beam correction factors per aperture per band

At the beginning it was thought that HOPS 108 was a point-like source. For that reason the observations were executed in pointing mode and the point source loss correction was applied in Manoj et al. (2013) and the spectra taken from the central spaxel of the rebinned cubes.

As in this work the fluxes were going to be measured from the line maps, instead of the rebinned cubes, and there is no point source loss correction factor delivered by the PACS ICC for such maps, we developed our own correction factor for our measurements. This we present here, as they can be of use for others wishing to do a similar work.

We calculated the ratio between energy encircled within several aperture radii, divided by the energy encircled within a radius of 25 ″(a radius where the complete beams were included at all wavelengths), for the PSF maps taken from the PACS calibration website. The fits files were those in which the source is centered, with a pixel size of 0.5″, at the central spaxel at the wavelengths of 55 μm , 62 μm , 68 μm , 75 μm ,84 μm , 94 μm ,125 μm ,136 μm ,145 μm , 150 μm ,168 μm and 187 μm).

The flux was extracted as in previous cases using the task *annularSkyAperturePhotometry* centred on the beam and subtracting the background from an annulus with internal radius of 25 ″and external radius of 26.5 ″. The variety of radii selected were 5 ″, 5.3 ″, 6.5 ″, 8 ″, 9 ″, 10 ″, 12 ″, 14 ″, 15.9 ″, 18 ″, 20 ″, 22 ″, 24 ″, 25 ″. The position of the centre of the beam was calculated by fitting a 2D Gaussian function to each of the beams. The result of this exercise is presented in Figure 8.19.

Table 8.4: Fluxes extracted from the CO line maps generated by this work for HOPS 108 within an aperture of 6.5″radius versus those reported by Manoj et al. 2013.

CO transition (J_{up} - J_{low})	rest wavelength μm	flux(us) $\times 10^{-15}$ (W m^{-2})	flux (PSC, Manoj) $\times 10^{-15}$ (W m^{-2})
14-13	185.999	1.71	3.31
15-14	173.631	1.68	3.28
16-15	162.812	1.69	3.41
17-16	153.267	1.68	3.30
18-17	144.784	1.62	3.12
19-18	137.196	1.37	2.58
20-19	130.369	1.5	2.60
21-20	124.193	1.66	2.57
22-21	118.581	1.26	2.20
23-22	113.457	2.27	3.96
24-23	108.763	1.06	1.67
25-24	104.445	0.90	1.62
28-27	93.349	0.90	1.52
29-28	90.163	0.90	1.56
31-30	84.411	1.43	2.34
32-31	81.806	0.576	0.94
33-32	79.360	0.502	0.89
34-33	77.058	1.714	0.84
35-34	74.890	0.445	0.83
36-35	72.843	0.369	0.65
37-36	70.907	0.280	0.57
38-37	69.074	0.281	0.53
39-38	67.336	0.210	0.46
40-39	65.686	0.222	0.44
41-40	64.117	0.202	0.43
42-41	62.624	0.1733	0.37

	Manoj et al. (2013) processing	my processing
HIPE version	8.0	12.1
calibration version	32	65
product for flux extraction	rebinned cube	line map
flux extraction method	from central spaxel	within an aperture
point source loss correction	yes	no

Table 8.5: Differences in our processing versus Manoj et al. (2013).

Table 8.6: Fluxes extracted from the rebinned cubes from the pointed observation of HOPS 108 from the central spaxel, with point source correction from us versus those reported by Manoj et al. (2013).

CO transition (J_{up} - J_{low})	rest wavelength μm	flux(PSC,us) $\times 10^{-15}$ (W m^{-2})	flux (PSC, Manoj) $\times 10^{-15}$ (W m^{-2})	diff
16-15	162.812	3.88	3.41	10 %
17-16	153.267	3.57	3.30	8 %
18-17	144.784	3.37	3.12	8 %
20-19	130.369	2.94	2.60	13 %

Table 8.7: Fluxes extracted from the central spaxel of the rebinned cubes of HOPS 108, without and with point source correction compared to the flux from table 8.6 for 13 ″.

CO transition (J_{up} - J_{low})	rest wavelength of transition (microns)	flux(2,2) $\times 10^{-15}$ (Watt m^{-2})	flux (PSC,us) $\times 10^{-15}$ (Watt m^{-2})	flux(13 ″) $\times 10^{-15}$ (Watt m^{2})
16-15	162.812	1.87	3.88	4.19
17-16	153.267	1.86	3.57	4.07
18-17	144.784	1.84	3.37	3.78
20-19	130.369	1.73	2.94	3.46

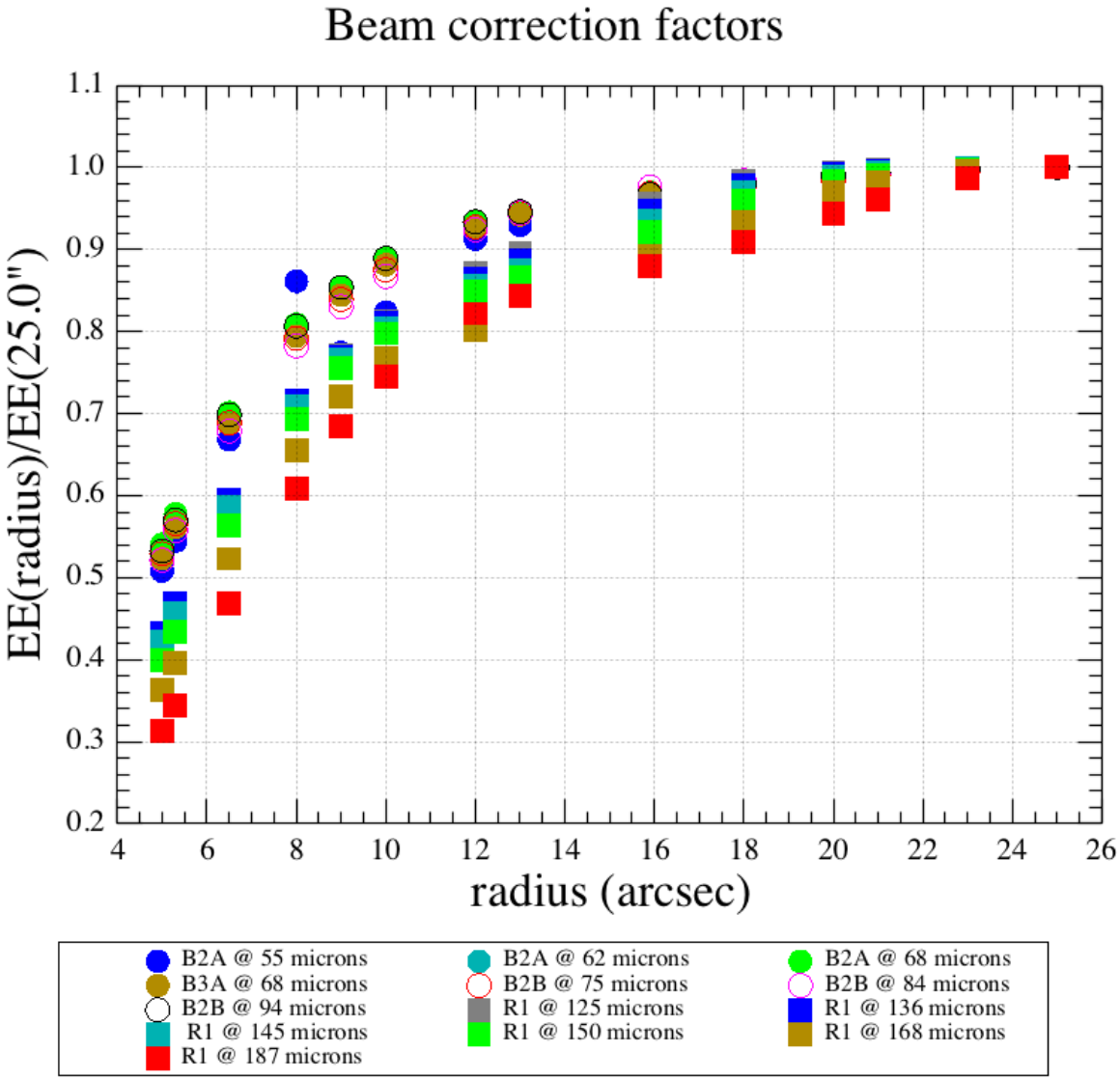

Figure 8.19: Beam correction factors to apply to the aperture photometry values calculated from PACS line maps with pixel size of 0.5″for the set of wavelengths delivered at the PACS calibration website (55μm , 62μm , 68μm , 75μm ,84μm , 94μm ,125μm ,136μm ,145μm , 150μm ,168μm and 187μm).

9

The morphology of protostellar sources in OMC-2

9.1 Methodology to contain possible extended emission

After the generation of our line and continuum maps, we wanted to understand the flux distribution of our [O I] line and continuum maps. Podio et al. (2012) used her method to identify [O I] jets and as our [O I] line seems to have such a flux distribution, we analyse it and some other lines from different species we created.

Flux detected in several spaxels contiguous can be caused by (1) an extended source or (2) a point source very bright or a poorly centred. A method was developed by Podio et al. (2012) which can help to differentiate between these two scenarios.

The method is able to characterise whether the line emission is extended and whether there is an offset between the line and continuum emission peaks by making use of the line-to-continuum flux ratios. When both line and continuum emission come from the same region (for example from an unresolved star+disk system) we expect a constant line-to-continuum flux ratio. However, if the emission come from different regions (or physical phenomena) the line-to-continuum flux ratio will vary from one spaxel to another.

In order to identify whether there is extended emission, Podio et al. (2012) subtracted from the line-plus-continuum image the continuum emission and investigated whether there was residual emission above a statistically reliable level (see equation 9.7).

The line map fluxes (line-plus-continuum fluxes; $F_{line+cont}$) are calculated using equation 9.1, where the flux around the line of interest is integrated (in units of W/m^2).

$$F_{line+cont} = d\nu \Sigma_{i=1}^{n} f_i \tag{9.1}$$

The flux error estimated at each spaxel on the line-plus-continuum image ($\triangle F_{line+cont}$) is obtained as shown at equation 9.2. $d\nu$ is the average spectral element size (in Hz).

$$\triangle F_{line+cont} = d\nu \sqrt{\Sigma_{i=1}^{n} \triangle f_i} \tag{9.2}$$

The continuum fluxes (F_{cont}) were computed using equation 9.4, where the flux densities are co-added (weighted, see equation 9.3) from *n1* spectral elements free of line emission adjacent to the line. The flux error estimated at each spaxel on the continuum image ($\triangle F_{cont}$) was obtained as shown at equation 9.5.

$$w_i = \frac{1}{\triangle f_i^2} \tag{9.3}$$

$$F_{cont} = \Sigma_{i=1}^{n1} \frac{f_i w_i}{\Sigma_{i=1}^{n1} w_j} \tag{9.4}$$

$$\triangle F_{cont} = \frac{1}{\sqrt{\Sigma_{i=1}^{n1} w_i}} = \frac{1}{\sqrt{\Sigma_{i=1}^{n1} \frac{1}{\triangle f_i^2}}} \tag{9.5}$$

The method identifies the *j* spaxel with maximum continuum emission as the one containing the source and calculate the residual flux, $F_{residual}$ and its error $\Delta F_{residual}$, by using equation 9.7.

$$R_j = \left(\frac{F_{cont,j}}{F_{line+cont,j}}\right) \tag{9.6}$$

$$F_{residual} = F_{line+cont} + \frac{F_{cont}}{R_j} \tag{9.7}$$

Considering R_j the residual at the *j* spaxel given by the equation 9.7, it is expected that at the position of the maximum continuum emission the flux at the residual, given by equation 9.9, is zero.

$$\triangle R_j = R_j \sqrt{\left(\frac{\triangle}{F_{line+cont,j}} F_{line+cont,j}\right)^2 + \left(\frac{\triangle F_{cont,j}}{F_{cont,j}}\right)^2} \tag{9.8}$$

$$\triangle F_{residual} = \sqrt{\triangle F_{line+cont,j}^2 + \frac{F_{cont}^2}{R_j^2}\left(\frac{\triangle R_j^2}{R_j^2} + \frac{\triangle F_{cont}^2}{F_{cont}^2}\right)} \tag{9.9}$$

All the positions where the residual flux are non-zero (in units of W/m^2) let us know where there is extended emission.

9.2 Applying the method to OMC-2 data

We applied the method of Podio et al. (2012) to some of the PACS line maps we generated for the OMC-2 region: [OI] 63 μm (Fig. 9.1), OH 84 μm (Fig. 9.2) and OH 119 μm (Fig. 9.4), H_2O 113 μm (Fig. 9.3) and 179.5 μm (Fig. 9.5). As our spectral maps are continuum subtracted, the continuum only maps were added to perform this exercise.

In this section I show 5 figures, each containing 4 images. In all figures (*top left*) image is a smoothed display of the line maps calculated in this work, with a colour scale that allows to better see the different flux levels (in W/m^2 units), (*top right*) shows the continuum maps generated in this work with the same colour scale (*bottom left*) shows the sum of line-plus-continuum map (in W/m^2 units) and (*bottom right*) shows the flux distribution of comparing the line and continuum maps for the same line following Podio et al. (2012) method (i.e. residual maps). These images allow us to see whether line and continuum are or not couple. A deeper analysis of the densities and temperatures derived from our line maps, is done later in Chapters 10 and 11. .

First we will start with a basic interpretation of the data with a visual inspection of the continuum line maps (*top right* image at all figures). We can see that continuum at 63 μm peaks in the north. The emission appears in the south as we go to longer wavelengths and is the dominant peak at 179 μm .

Second, we look at the line emission maps (*top left* image at all figures). The [O I] 63 μm line map shows an elongated shape which cross the map from northeast to southwest, peaking in the southern part. In the 84 μm and 113 μm maps the morphology breaks into two distinct peaks, with the southern being brighter and faint emission joining the peaks. By 119 μm and 179 μm the northern peak itself elongates into two.

Residual maps (*bottom right* image at all figures) show that there is extended emission presented in all maps.

9.3 Interpretation of the results

An initial interpretation of above results tell us that we have two sources, one at the northern part of the map (that we call in our sample HOPS 370) and one at the southwest (called HOPS 108). HOPS 108, as we can also see at our maps, is colder than HOPS 370, because it peaks at longer wavelengths. Furlan et al. (2014) for HOPS 108, estimated a bolometric temperature 30 K and 70 K for HOPS 370. We can also clearly see in the [O I] 63 μm line map, which traces the warm gas, that there is a narrow and extended flux distribution which corresponds to a jet-like structure, and we also find in the literature that jets are trace by this fine structure line at regions of very low density where these transition have the chance to occur (Hollenbach 1985). The H_2O gas detected seems to trace the regions where the ices from the grains are sputtered, released and converted to vapour water due to high energetic shocks, which are known to occur along the outflows (along the envelope cavity and interacting with the molecular cloud to which the protostar belongs).

Figure 9.1: Line and continuum emission for the [O I] 63 μm maps generated at this work. The coordinate axis just indicate the shift in (RA,Dec) respect to the HOPS 370 target (the northern one at these maps). (*Top left*) image is a smoothed display of the line maps calculated in this work, with a colour scale that allows to better see the different flux levels (in W/m^2 units), (*top right*) shows the continuum maps generated in this work with the same colour scale (*bottom left*) shows the sum of line-plus-continuum map (in W/m^2 units) and (*bottom right*) shows the flux distribution of comparing the line and continuum maps for the same line following Podio et al. (2012) method (i.e. residual maps).

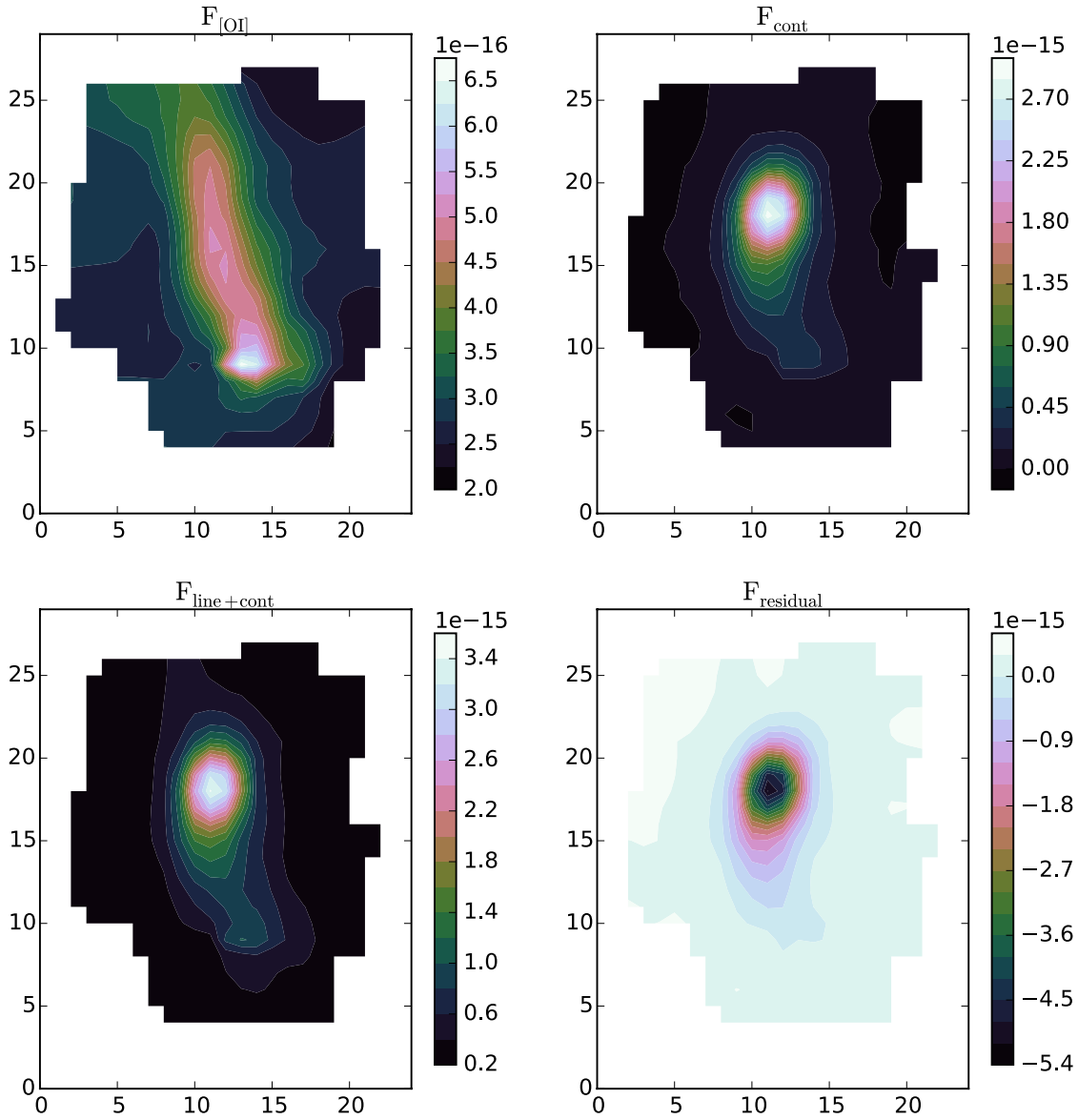

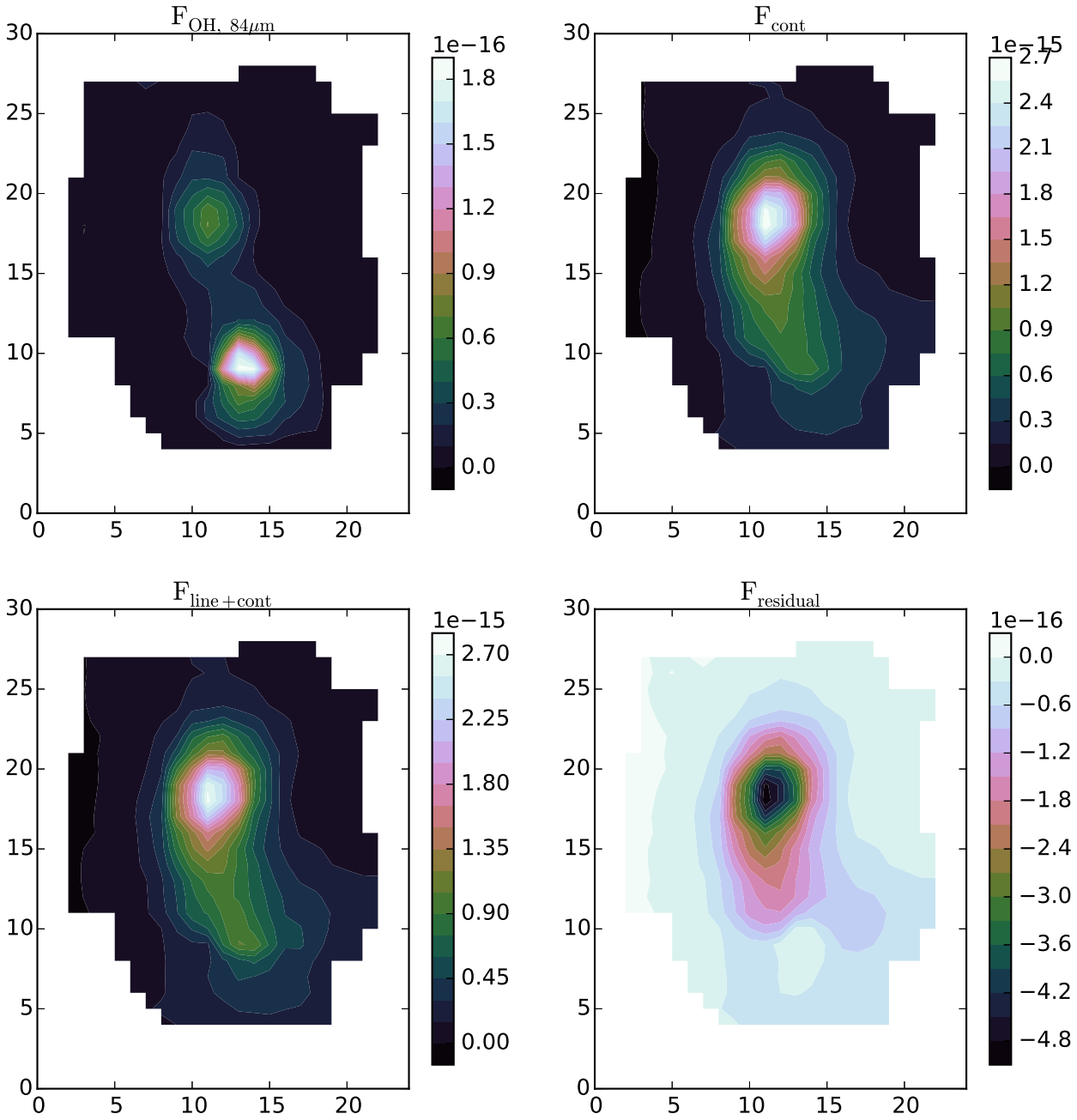

Figure 9.2: Same than Fig. 9.1 but applied to the OH maps at 84 μm

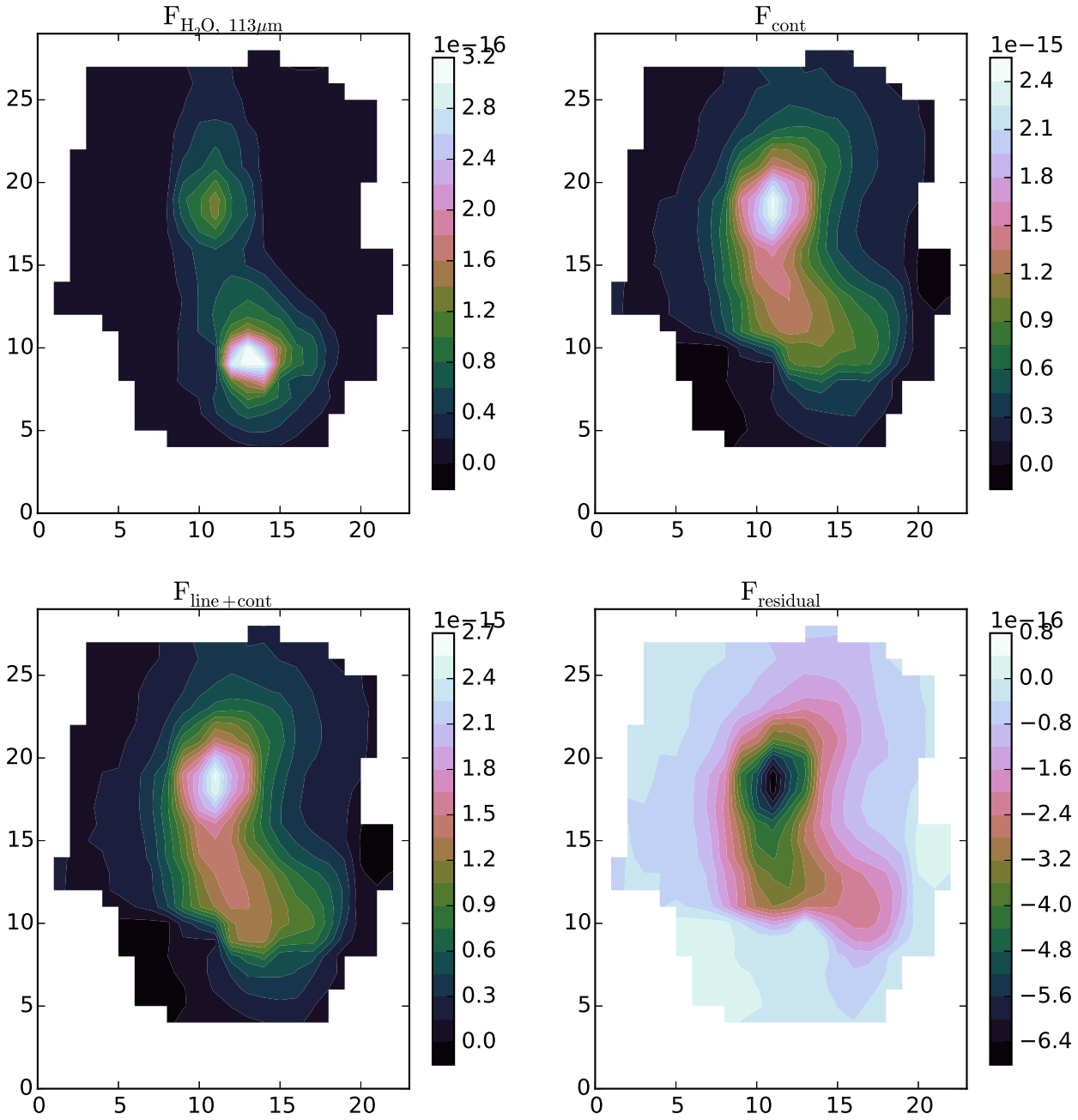

Figure 9.3: Same than Fig. 9.1 but applied to the H_2O maps at 113 μm .

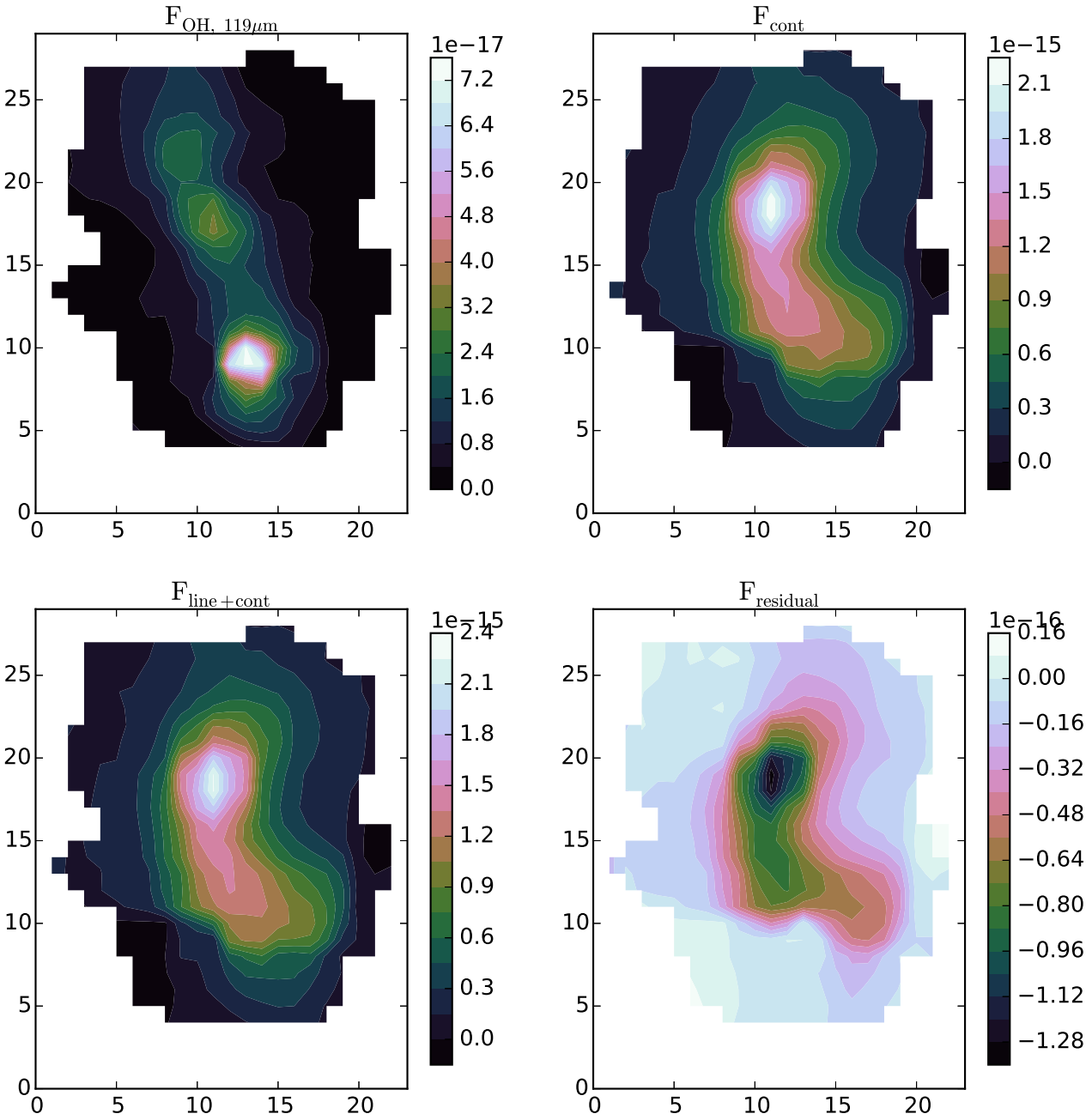

Figure 9.4: Same than Fig. 9.1 but applied to the OH maps at 119 μm .

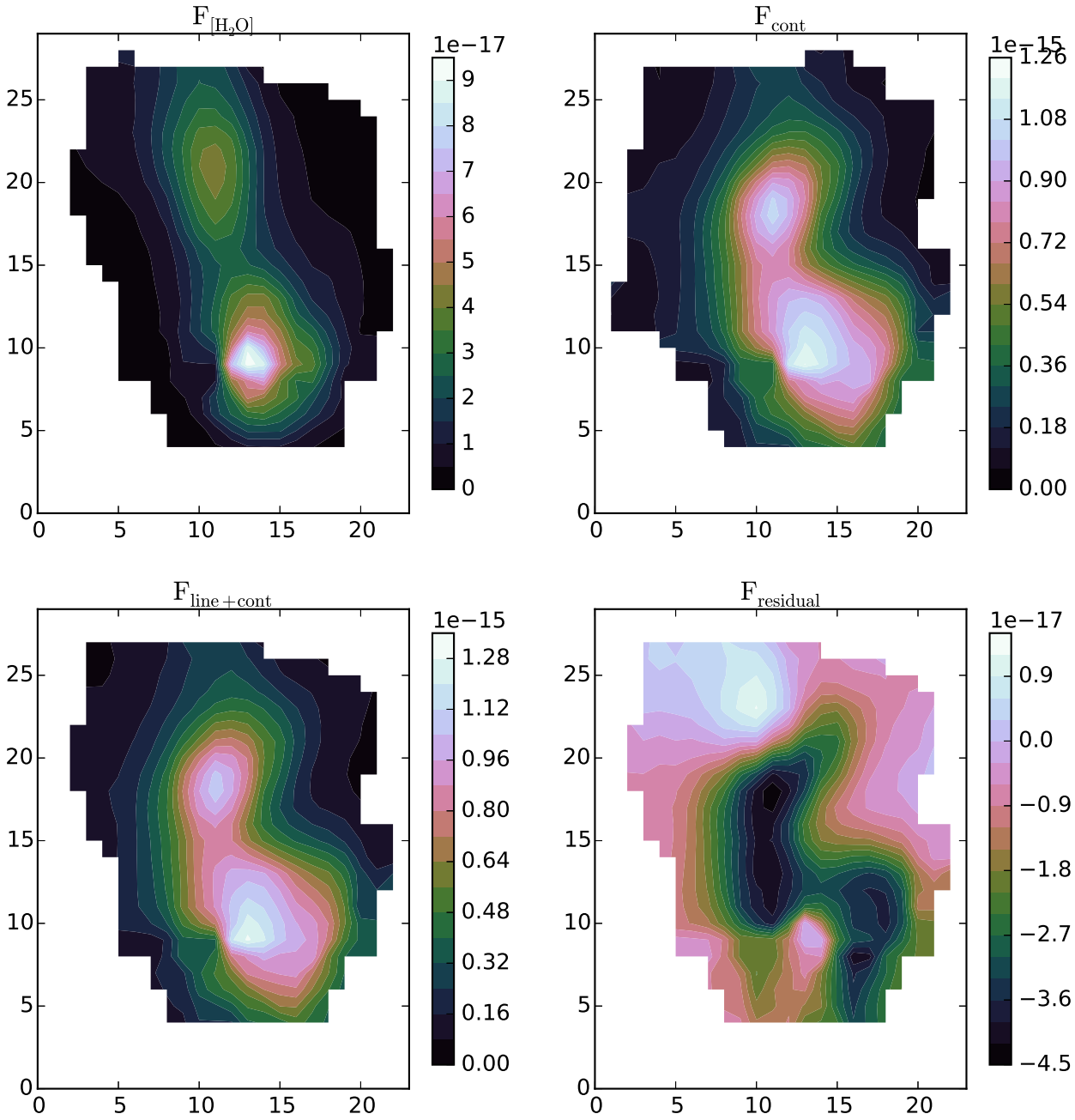

Figure 9.5: Same than Fig. 9.1 but applied to the H_2O maps at 179 μm .

10

Far-IR fine structure line emission from the OMC-2 region

This chapter is focused on the scientific analysis of the fine-structure line maps generated in Chapter 8. We present the first detection of a jet in the far-IR [O I] lines from an intermediate mass protostar. We have carried out a *Herschel*/PACS spectral mapping study in the [O I] lines of OMC-2 FIR 3 (HOPS370) and FIR 4 (HOPS108), two of the most luminous protostars in Orion outside of the Orion Nebula.

The spatial morphology of the fine structure line emission reveals the presence of an extended photodissociation region (PDR) and a narrow, but intense jet emission connecting the two protostars. The jet seen in [O I] emission is spatially aligned with the *Spitzer*/IRAC 4.5 μm jet and the CO (6-5) molecular outflow centered on FIR 3.

The [O I] 63 μm to 145 μm line ratios indicate a density gradient along the jet with density decreasing progressively as one moves away from FIR 3 on either side. The mass loss rate derived from the total [O I] 63 μm line luminosity of the jet is 5.4 $\times 10^{-6}$ $M_\odot$ yr^{-1}, which is an order of magnitude higher than that measured for typical low mass class 0 protostars. The implied accretion luminosity is significantly higher than the observed luminosity of FIR 4, indicating that the [O I] jet is unlikely to be associated with FIR 4. We argue that the peak line emission seen toward FIR 4 originates in the terminal shock produced by the jet driven by FIR 3.

From the observed upper limit of the [O III] 88.4 μm line flux we place a limit on the mass of the ionised gas around FIR 4, thus ruling out the presence of an H II region previously suggested to coincide with FIR 4.

The higher mass loss rate that we find for FIR 3 is consistent with the idea that intermediate mass protostars drive more powerful jets than their low-mass counterparts. Our results also call into

question the nature of FIR 4.

10.1 Relevance of fine structure lines for physical analysis of protostars

The far-infrared lines of [O I] are prominent tracers of jets from young stars and protostars. They provide a straightforward measure of the mass flow through dissociative J-shocks driven by the outflowing jets (Werner et al. 1984; Cohen et al. 1988; Nisini et al. 1996; Hollenbach 1985; Hollenbach & McKee 1989). In regions of high extinction, as those found around young intermediate mass protostars, [OI] lines are a means to trace and characterise jets from outflows, unaffected by extinction or confusion with the ambient molecular cloud.

The OMC-2 region in Orion A is one of the richest targets for [OI] studies of outflows from intermediate mass protostars. It contains a group of eight protostars with luminosities of a 20 to 360 $L_{\odot}$ (Adams2012 et al. 2012, Furlan et al. 2015, ApJS, submitted), much higher than the typical luminosity of 1 $L_{\odot}$ for the peak of the protostellar luminosity function of the Orion protostars (Kryukova et al. (2012), Furlan et al, 2015, ApJS, submitted). OMC-2, part of a 2 pc long, dense filament which extends between the Orion Nebula Cluster (ONC) to the south and NGC 1977 to the north, also hosts a higher than average fraction of young Class 0 protostars (Chini et al. 1997; Peterson & Megeath 2008b; Adams et al. 2012; Megeath et al. 2012; Stutz & Kainulainen 2015).

In this work, we present *Herschel*/PACS fine structure line observations of the OMC-2 protostars FIR 3 (HOPS 370, VLA 11) and FIR 4 (HOPS 108, VLA 12) obtained as part of *Herschel* Orion Protostar Survey (HOPS) open time key program. FIR 3 is the most luminous protostar ($L_{\rm bol}$= 360 $L_{\odot}$) in OMC-2 and drives a bipolar outflow with one lobe extending to FIR 4 (Williams et al. 2003; Shimajiri et al. 2008). While previous observations indicated that FIR 4 has a luminosity of 1000 $L_{\odot}$ (Crimier et al. 2009), the bolometric luminosity has now been revised to 38 $L_{\odot}$ (Furlan et al. 2014). Low-J (J_{up} $\leq$ 3) CO observations do not show a distinct outflow associated with FIR 4. FIR 3 and FIR 4 have the brightest known far-IR line emission in the cloud outside of the Orion nebula (Manoj et al. 2013). While FIR 3 has a far-IR CO luminosity of $\sim$ 0.06 $L_{\odot}$, FIR 4 has a far-IR CO luminosity of $\sim$ 0.2 $L_{\odot}$ and the brightest [OI] and H_2O emission observed among the HOPS sample (Manoj et al. 2013). Moreover, a clear peak in the far-IR line emission is found at the location of FIR 4 (Manoj et al. 2013; Furlan et al. 2014). While our understanding of the nature of FIR 4 is still incomplete (see Osorio et al., in prep.), the detailed physical nature of FIR 3 is now coming into sharper focus.

We detect, for the first time, a jet in the far-IR [OI] lines from an intermediate mass protostar FIR 3. Previous [OI] jets have been detected with Herschel but for low-mass protostars (Podio et al. 2012; Nisini et al. 2015). The jet line luminosity and implied mass-loss rate are a factor of 10 higher than typical values for low-mass class 0 protostars. This jet extends from FIR 3 to FIR 4 and is spatially coincident with CO (6-5) outflow observations, demonstrating a connection between FIR 3 and the bright far-IR line emission at the position of FIR 4. We propose that the bright line emission associated with FIR 4 is produced by the FIR 3 jet.

10.2 Analysis and Results of fine-structure line maps

Our [O I] 63 μm line map of the OMC-2 region is presented in Figure 10.1. Inspection of the line map seems to reveal a jet: a narrow spatially collimated emission feature connecting FIR 3 and FIR 4 which is superposed on uniform extended emission.

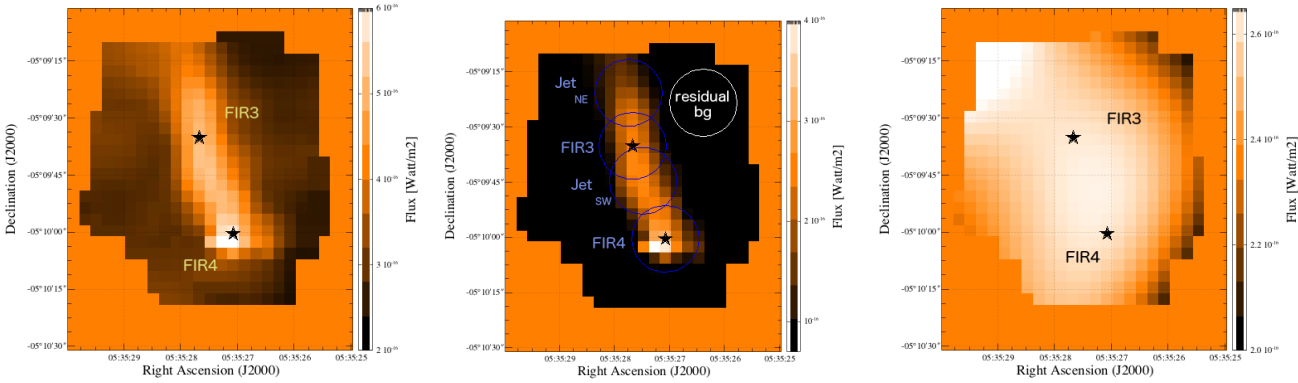

Figure 10.1: *(Left)*: The [O I] 63 μm line map of the OMC-2 region, *(middle)*: the narrow ridge like emission component obtained after subtracting the extended emission background component *(right)*: the extended emission component extracted by fitting a 2D third order polynomial to the line map. The positions, sizes, and names of the line flux aperture measurements listed in Table 10.1 are indicated. The residual background was measured within an aperture of the same radius 9″away from the jet, as shown in the figure.

The central image of Figure 10.2 of the [O I] 63 μm /145 μm line ratio shows that the line ratios of the extended emission are approximately constant and distinct from the narrow jet-like emission, indicating the presence of two different physical origins for the line emission: an extended photodissociation region (PDR) component and a collimated jet.

We isolated the jet component from the PDR for further analysis in the following way. We first masked the flux above a certain threshold where the main emission from the jet at targets were included by visual check (above a certain threshold) and then extracted the extended PDR emission component by fitting the line image with a 2D (surface) third order polynomial. We then subtracted this emission component from the total emission map. The total and separate [O I] 63 μm emission components are shown in Figure 10.1. The procedure was repeated for [O I] 145 μm (Figure 10.2).

The [O I] line maps were smoothed to the same the effective resolution before dividing one by the other. The equation used was **??**.

$$FWHM_{PSF_{63_{NEW}}} = \sqrt{FWHM^2_{PSF_{63}} + FWHM^2_{PSF_{145}}} FWHM_{PSF_{145_{NEW}}} = \sqrt{FWHM^2_{PSF_{145}} + FWHM^2_{PSF_{63}}} \quad (10.1)$$

Since FWHM$_{PSF_{63_{NEW}}}$ is the same as FWHM$_{PSF_{145_{NEW}}}$, we could make a ratio map in which the

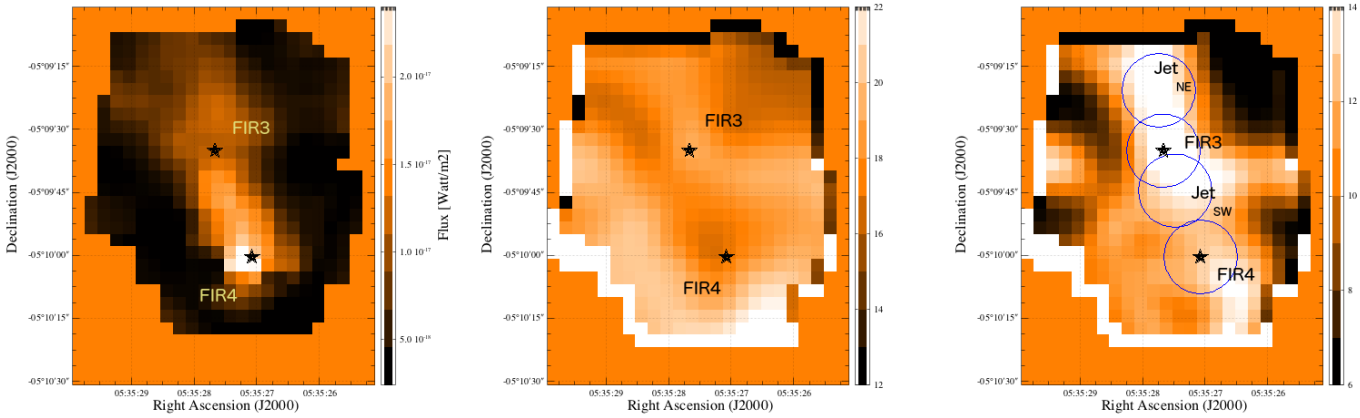

Figure 10.2: [O I] 145 μm map *(left)* and [O I] 63 / [O I] 145 line ratio map before *(middle)* and after PDR subtraction (*right*).

morphology of the emission were real, and not simply caused by the data having radically different native resolutions.

10.2.1 The jet morphology

The [O I] jet has a north-east to south-west orientation. The jet emission extends from the edge of the mapped area in the north-east, through FIR 3, and finally terminates at the location of FIR 4 in the south-west, where the [O I] emission is the brightest. Figure 10.3 shows contours of the [O I] 63 μm jet on a *Spitzer*/IRAC 4.5 μm image (Megeath et al. 2012). The 4.5 μm band contains bright H_2 emission which traces the shocked molecular gas excited by the jet. We observe a prominent extended 4.5 μm jet terminating in a bow shock to the north-east of FIR-3 (extending past the PACS line map coverage). The 4.5 μm jet emission clearly appears to be driven by FIR 3; however, the counter-jet traced by [O I] is not readily seen at 4.5 μm. Figure 10.3 also shows an overlay, with APEX data, of blue- and red-shifted CO (6-5) outflow emission which traces the molecular gas entrained by the jet. The CO emission clearly follows the north-east component of the 4.5 μm jet as well as the [O I] emission extending to the south-west and terminating at FIR 4. Since both CO outflow lobes have high-velocity line wings on both sides of the systemic velocity, the outflow must lie close to the plane of the sky. The combined morphology of all three emission components ([O I], 4.5 μm , and CO) strongly suggests that the jet/outflow is driven by FIR 3.

10.2.2 Excitation conditions in the jet

To investigate the physical conditions along the jet, we measured the [O I] 63 μm /145 μm line ratio at four different locations along the jet (Table 10.1). We compare the observed ratios to predictions for a cloud with uniform density and temperature (Hollenbach & Tielens 1997, 1999). At the high temperatures expected in the dissociative shocks in jets, the line ratio is insensitive to the precise temperature, and indicates electron density (n_e) lies in the range 5-8$\times 10^4$ cm^{-3} (see Figure 10.5).

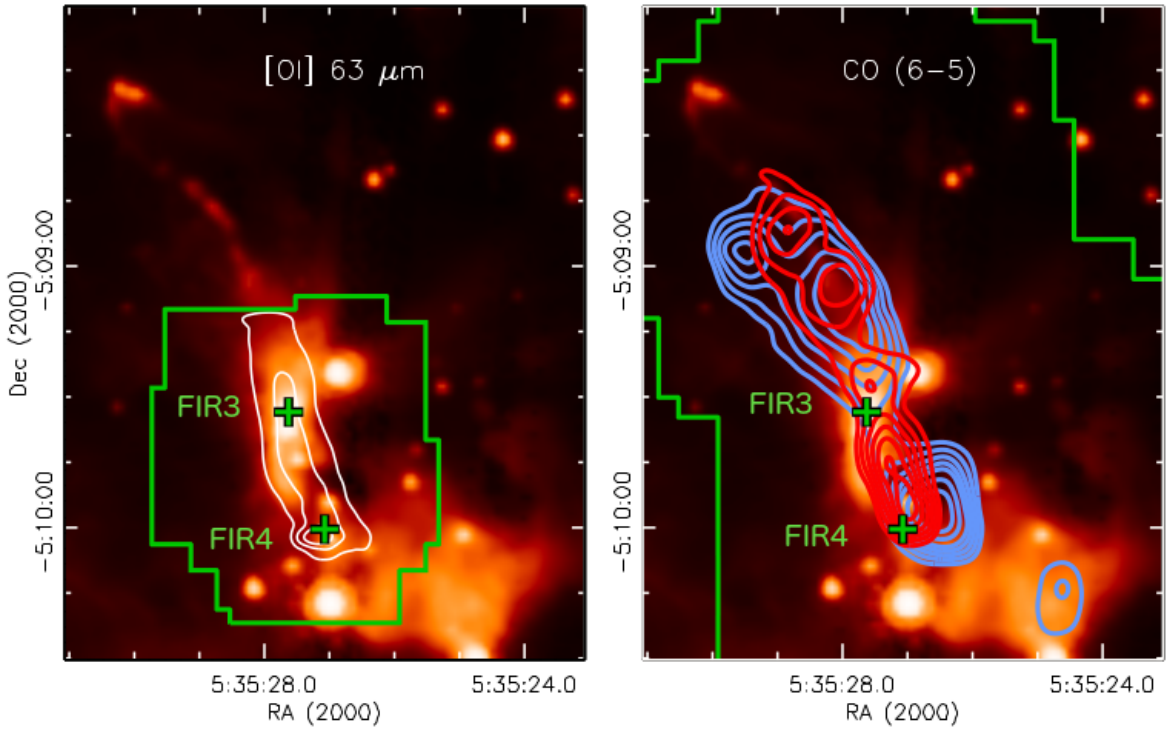

Figure 10.3: [O I] 63 μm line emission from our maps (white contours; levels = 1, 2 & 3 $\times 10^{-16}$ Wm^{-2}/pixel) with the FOV outlined in green *(left panel)*. The blue (−10 to 9 km s^{-1}) and red (14 to 30 km s^{-1}) wings of the CO 6-5 (from the APEX observations) values are the blue and red contours in the *right panel*. Both are overlaid on the 4.5 μm image, which shows the jet extending to the north-east.

The n_e values for the four different sections of the jet were computed for T = 3000 K (see Table 10.1) using the equation given in Appendix C and Figures 10.5. The densities that we derive indicate a gradient along the jet: the density of the jet decreases with increasing distance from FIR 3. The n_e values decreases towards the south-west, reaching a minimum value at the [O I] line emission peak close to FIR 4.

The density also drops on the opposite side, to the north-east of FIR-3. The n_e values suggest that the [O I] jet is driven by FIR 3 with the maximum density of the jet at the location of the driving source, as expected if the [O I] emission originates in the decelerated jet material.

10.2.3 Mass-loss rates from jets

The [O I] 63 μm line luminosity provides a direct measure of the mass-loss rate from protostars (Hollenbach 1985; Hollenbach & McKee 1989). This line is the primary coolant of the predominantly atomic gas in the postshock gas for temperatures in the range of 500-5000 K. The [O I]

Table 10.1: Observed properties of the [O I] jet from FIR 3

	FIR4	Jet_{SW}	FIR3	Jet_{NE}	Entire jet
Flux [O I] 63μm [1] ($\times 10^{-15}$ Wm^{-2})	4.5 ± 0.12	4.6 ± 0.07	4.3 ± 0.10	3.3 ± 0.07	12.6±0.5
Flux [O I] 145 μm ($\times 10^{-15}$ Wm^{-2})	0.28 ± 0.02	0.24 ± 0.03	0.19 ± 0.02	0.14 ± 0.02	12.6±0.5
[O I] 63μm / [O I] 145μm [2]	12.2 ± 0.3	13.5 ± 0.2	14.1 ± 0.2	13.8 ± 0.2	
Luminosity [O I] 63 μm ($\times 10^{-2}$ L$_\odot$)	2.4	2.4	2.3	1.7	6.7
Mass-loss rate [O I] 63 ($\times 10^{-6}$ M$_\odot$yr^{-1})	2.0	2.0	1.8	1.4	5.4
electron density ($\times 10^4$ cm^{-3})	4.8	6.5	7.4	7.0	

line luminosity is proportional to the rate at which jet material flows into the shock front, or the mass-loss rate of the driving source, given by

$$\dot{M}_{out} = 8.1 \times 10^{-5} \quad (L_{[OI]}/L_\odot)\ \mathrm{M}_\odot\ \mathrm{yr}^{-1}$$

The mass-loss rate corresponding to the total [O I] 63 μm luminosity of the jet is 5.4×10^{-6} M$_\odot$ yr^{-1}(Table 10.1). We also computed the shock flow rates at four different locations along the jet from the [O I] luminosities measured within 9″of the positions listed in Table 10.1 (also see Figure 10.1). The flow rates at different sections of the jets lie within a narrow range of 1.4-2.0 ×10^{-6} M$_\odot$ yr^{-1} and differ only by 30% at most, indicating that the mass flow along the jet is relatively smooth and continuous.

Mass-loss rates from protostars are closely connected to mass-accretion rates onto protostars: theoretical models of jet launching predict a proportionality between mass-loss rate and mass-accretion rate:

$$\dot{M}_{out} \ = \ b\, \dot{M}_{acc}$$

where b has a theoretical as well as a mean observed value near 0.1 (Pelletier & Pudritz 1992). The mass flow rate of $\dot{M}_{out}$ = 2.0×10^{-6} M$_\odot$ yr^{-1} at the location of FIR 4 implies a mass-accretion rate, $\dot{M}_{\rm acc}$ = 2×10^{-5} M$_\odot$ yr^{-1}, which corresponds to an accretion luminosity, $L_{\rm acc}$ = 300 $L_\odot$, assuming $R_\star/M_\star = 1\ R_\odot/M_\odot$, appropriate for intermediate mass young stars on the birth line (Palla & Stahler 1993). This value of $L_{\rm acc}$ is close to a factor of 10 higher than the observed $L_{\rm bol}$ for FIR 4, ∼ 38 $L_\odot$(Furlan et al. 2014).

Further, as noted by Furlan et al. (2014), the true luminosity of FIR 4 could be as small as 14 $L_\odot$. On the other hand, the $L_{\rm acc}$ that we derive is consistent with the observed $L_{\rm bol}$ for FIR 3, ∼ 360 $L_\odot$Manoj et al. (2013). Moreover, the $\dot{M}_{\rm acc}$ value indicated by the mass-loss rate derived from [O I] is remarkably close to the envelope infall rate of 1×10^{-5} M$_\odot$ yr^{-1} estimated for FIR 3 from the radiative transfer modelling of the observed broad band spectral energy distribution (Adams et al. (2012), Furlan et al, 2015, ApJS, submitted).

All these different lines of argument strongly suggest that the [O I] jet is driven by FIR 3.

10.2.4 Extended emission from PDRs

As previously pointed out, the spatial morphology of the fine structure line emission seems to indicate the presence of uniform extended emission in the OMC-2 region. The [O I] 63 μm to [CII] at 158 μm and [O I] 63 to 145 μm line ratio maps (see Figure 10.4) show that the line ratios of the extended emission are approximately constant and distinct from the narrow jet-like emission, possibly indicating a different physical origin for the extended emission.

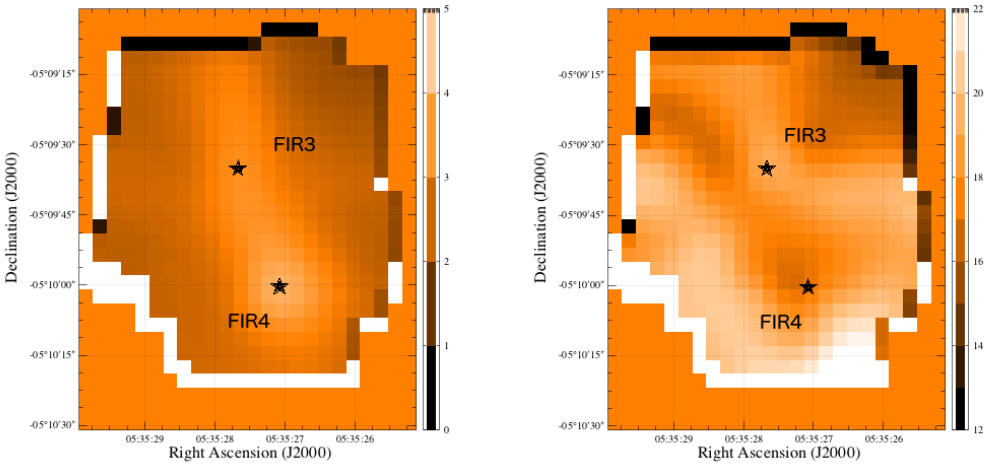

Figure 10.4: The [O I] and [C II] line ratio maps of the OMC-2 region: *left* panel shows the [O I] 63 μm / [C II] 158 μm map and the *right* panel shows he [O I] 63 μm / [O I] 145 μm map. All line ratios are calculated at matched angular resolution.

The OMC-2 region lies between the Orion Nebula Cluster (ONC) to the south and NGC 1977 to the north-east, both of which contain OB stars (Peterson & Megeath 2008b) and the UV radiation from which can produce photodissociation regions (PDRs) on the surface of molecular clouds. Fig 10.4 shows that the line ratios for the extended background emission are more or less constant and very different from that for the narrow jet-like emission, indicating the presence of two different physical components.

The narrow ridge-like emission feature seen in our [O I] 63 μm line map, spatially coincides with the extended molecular outflow driven by FIR 3 reported by Williams et al. (2003) and Shimajiri et al. (2008), and most likely traces hot gas shocked by the jets responsible for the outflow.

In order to confirm the presence of an extended component from the environment, we analysed the ratio maps of [O I] 63 / 145 μm and [O I] 63 μm /[C II] 158 μm , which are shown in Figure 10.4. To quantify the emission from the extended component, we measured the line ratios in six 15″× 15″regions, three on either side of jet. The line ratios are remarkably constant between the boxes:

$$\frac{[\mathrm{OI}]63}{[\mathrm{CII}]158} = 1.9 \pm 0.1 \quad \text{and} \quad \frac{[\mathrm{OI}]63}{[\mathrm{OI}]146} = 17 \pm 1$$

We compared these line ratios to those expected for a cloud with uniform density and temperature to estimate the physical conditions of the extended emission region (Hollenbach & Tielens 1997, 1999). If we imagine each [O I] and [C II] line-emission region to have a uniform density and temperature, we can derive useful characteristic densities and temperatures from the line intensity

ratios, under the common assumptions that the lines are optically thin and unextinguished, the atomic energy levels are collisional excited, and the energy-level populations are in steady state (e.g. Osterbrock & Ferland 2006).

Figure 10.5 contains results of such calculations for the intensity ratios we observe for the FIR 3 jet and for the adjacent cloud emission. We considered only the five lowest-energy levels for neutral oxygen, and the two lowest-energy levels for ionized carbon, to have significant population. We considered only electrons as collision partners, as these rates considerably exceed those from protons and hydrogen even when the ionization fraction is small. We took the relative abundance of C^+ and O to be the solar-system C/O ratio, 0.46 (Lodders & Palme 2009). We used the collision strengths computed by Bell et al. (1998) and Zatsarinny & Tayal (2003) for $e-$O, and by Tayal (2008) for $e-C^+$. Finally, we used the Einstein A-coefficients computed by Froese Fischer & Tachiev (2004) and Wiese et al (2007) for [O I] and [C II] respectively.

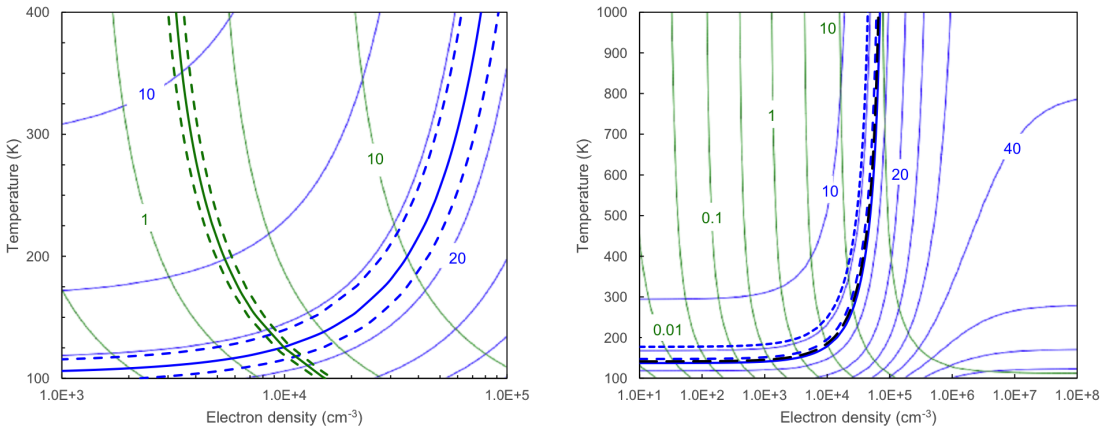

Figure 10.5: *(Left)* Observed [O I] 63.2/145.5 (blue) and [O I] 63.2/[C II] 157.7 line ratio (green) contours compared to expectations for a single-component model. The observed ratios for the regions immediately outside the FIR 3 jet are indicated with heavy solid contours, and the $\pm 1\ \sigma$ band by dashed contours. Thin contours indicate the same line ratios, covering the plotted range of density and temperature, with logarithmically-spaced contours. The families of curves intersect near $n_e = 10^4$ cm^{-3} and T = 130 K, which lie in the ranges common for photodissociation regions in the Orion molecular-cloud complex. *(Right)* [O I] 63.2/145.5 intensity ratios observed along the jet plotted as heavy blue curves: FIR 4 (shortest dashes), FIR 3 (solid), SW/NE of FIR 3 (medium/long dashes). At high temperatures the intensity ratios would indicate electron density in the range $5{\times}10^4$ - $8{\times}10^4$ cm^{-3}.

The observed line ratios give an electron density of $n_e{\sim}10^4$ cm^{-3} and T = 130 K for the extended emission component (see Figure 10.5), appropriate for PDRs with incident FUV field strength of $G_0 \sim 100$ (Kaufman et al. 1999). The values for n_e, T and G_0 that we obtain lie in the ranges commonly observed for PDRs on the surface of molecular clouds (Hollenbach & Tielens 1997, 1999), indicating that the extended emission component seen in the line maps is indeed consistent with PDR emission.

10.2.5 Mass limit on the ionised gas from [OIII] 88.4 μm non-detection

López-Sepulcre et al. (2013) argued the the 3.6 cm continuum emission detected towards FIR 4 (Reipurth et al. 1999) originates in an optically thin H II region produced by a B3-B4 type central star. Such an HII region, however, would produce strong [O III] emission at 88.4 μm, which is the lowest lying line among the ground state multiplet of O^{++}. We do not detect the [O III] line in the PACS spectrum extracted from a 9″ aperture centered on FIR 4 or on FIR 3 (see Fig. 10.6). The 3-σ upper limit for the [O III] line of 4.1×10^{-17} Wm^{-2}. Assuming that all the oxygen is in the form O^{++} (abundance ratio of 6.6×10^{-4}) and a temperature of 8000 K, this gives an upper limit to the mass of the ionised gas around FIR 4 to be 5.5×10^{-6} $M_{\odot}$. For a source size of 9″ in radius (0.02 pc at Orion), this mass translates into electron density, n_e = ~ 9-18 cm^{-3}, which is too low for such compact H II regions, the typical densities of which are in the range of 10^4-10^6 cm^{-3}. Our observations, therefore, rule out the presence of an H II region associated with FIR 4, as suggested by López-Sepulcre et al. (2013).

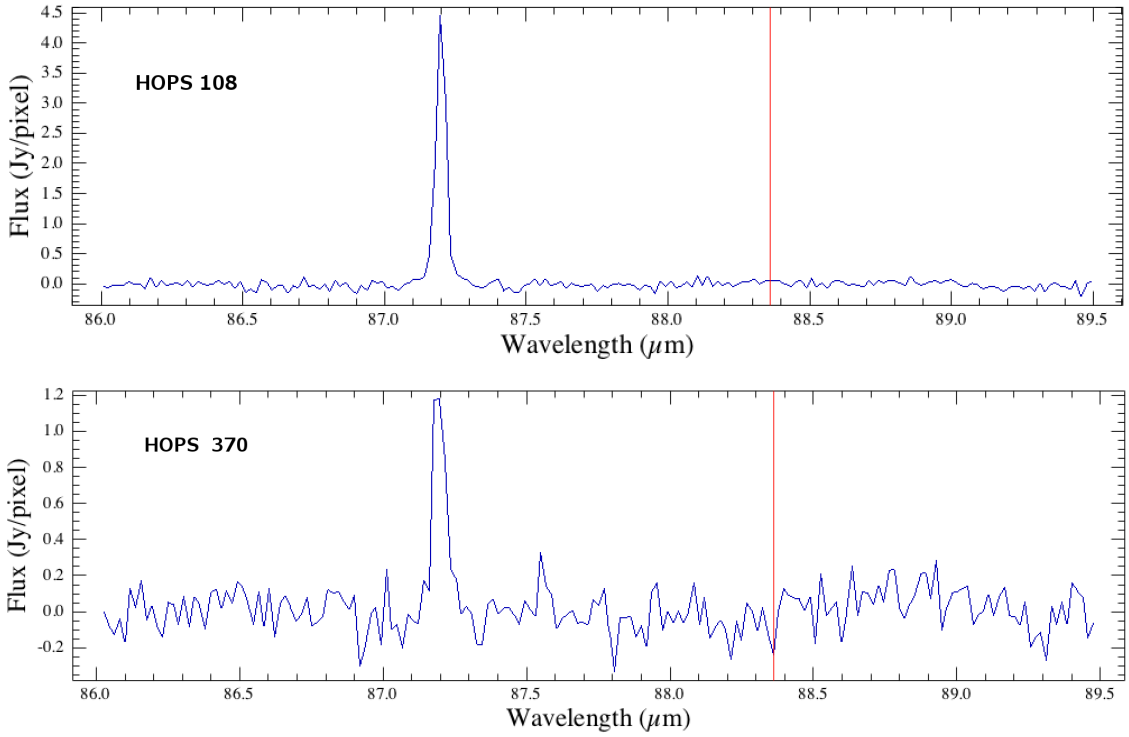

Figure 10.6: PACS spectra centred around FIR 4 at the wavelength of the [O III] line, 88.36 μm , shows no-detection. The strong line that appears in the range is the CO (30-29) emission line, at 87.190 μm.

10.3 Discussion on the analysis of the fine structure lines

Our analysis indicates that the [O I] jet connecting FIR 3 and FIR 4 actually originates from the FIR 3 protostar. Although our *Herschel*/PACS line maps do not cover the full extent of the north-eastern portion of the 4.5 μm shocked emission, the [O I] jet is observed on either side of FIR 3 and terminates at FIR 4. The jet is also spatially aligned with the CO (6-5) outflow, from the CHAMP+ maps, which extends to FIR 4 in the south. The observed [O I] 63 μm / 145 μm line ratios at different parts of the extended jet show the density to be progressively decreasing along the jet on either side of FIR 3. Since the [O I] emission predominantly arises from the shocked jet material, such a density gradient is expected if the jet is driven by FIR 3. The near constant mass-loss rate found along the [O I] jet, indicates a steady and continuous mass flow, also supports this claim. The mass flow rate close to FIR 3 and 20″ (8400 AU) away at the location of FIR 4 are very similar. It is highly unlikely that FIR 4, which is $\sim$ 10 times less luminous than FIR 3 is driving a jet with mass flow rate similar to that of FIR 3. These pieces of evidence strongly suggest that the driving source of the observed [O I] jet is FIR 3.

The peak [O I] emission, nevertheless, is observed close to FIR 4. All the high-excitation molecular cooling lines in the far-IR (H_2O, CO and OH) observed with *Herschel*/PACS also have their peak emission at the location of FIR 4 (Furlan et al. 2014, Gonzalez-Garcia et al. in prep). In fact, FIR 4 is one of the brightest far-IR line emitting source among all the protostars observed by HOPS. The far-IR line luminosities measured within a 9.4″ aperture around FIR 4 is more than 4× higher than that observed for FIR 3 (Manoj et al. 2013). Our analysis and other studies of the region, however, do not show any evidence for FIR 4 driving a powerful outflow/jet which could excite such intense line emission.

We argue, therefore, that the bright line emission seen toward FIR 4 is the terminal shock (Mach disk) of the FIR 3 jet. Such terminal shocks are often the brightest features of YSO jets, and comprise many of the best-known Herbig-Haro objects. FIR 4 may simply lie along the line of sight and may not even be physically associated with the shocked emitting region.

The jet driven by FIR 3 is the first to be imaged in [O I] 63 μm from an intermediate mass protostar. [O I] jets from low mass class 0 protostars observed with *Herschel*/PACS by Nisini et al. (2015) show mass-loss rates in the range of 1-4 $\times 10^{-7}$ $M_\odot$ yr^{-1}. These mass-loss rates are an order of magnitude lower than that of FIR 3. The mass-loss rate for FIR 3 is higher than even the relatively high mass-loss rate of 2-4 $\times 10^{-6}$ $M_\odot$ yr^{-1} found for HH 46 by Nisini et al. (2015). Thus our results indicate that the mass-loss rates in intermediate mass protostars are $\sim$ 10 times higher than that observed for most low mass class 0 protostars, consistent with the idea that they drive more powerful jets than their low-mass counterparts.

11

Far-IR CO and H_2O emission from the OMC-2 region

This chapter focused on the scientific analysis of the CO and H_2O line maps of the OMC-2 region, generated as part of this thesis. We carried out a detailed analysis of CO and H_2O lines extracted from 4 positions along the jet. We first modeled the observed CO line ratios and derived the physical parameters (density & temperature) of the emitting gas. Then, assuming that H_2O emission also arises in this component, we investigated the H_2O abundance in the postshock gas in the outflow. Our analysis indicate that H_2O is under-abundant in shock-heated gas in the jet/outflow from FIR 3.

11.1 Introduction to molecular spectroscopy on the OMC-2 region

In addition to the fine structure lines, our *Herschel*/PACS range spectroscopy observations in the mapping mode of the OMC-2 region also show strong molecular emission lines of CO and H_2O. The atomic jet driven by FIR 3 seen in the [O I] 63 μm and 145 μm lines is also seen in the CO and H_2O lines, indicating the presence of warm and hot molecular material associated with the FIR 3 jet/outflow. In this chapter we analyse the CO and water lines to derive the physical conditions of the molecular jet/outflow from FIR 3. We first model the observed CO line ratios to constrain the density and temperature of the emitting gas and use the the absolute flux to constrain the CO column density. Then, assuming that both CO and H_2O emissions arise from the same molecular gas component at uniform temperature and density, we compare the observed H_2O to CO line ratios

with model predictions to investigate the H_2O to CO abundance ratio, $n(H_2O)/n(CO)$, behind the outflow shocks in the FIR 3 jet.

11.2 Analysis of the CO and H_2O line maps

The jet from FIR 3, seen in [O I] 63 μm emission, is also observed in the rotational transitions of the molecules of CO and H_2O. In Figure 11.1, the map of the OMC-2 region is shown in the CO ($J = 17 \rightarrow 16$) line and H_2O ($7_{0,7} \rightarrow 6_{1,6}$) line. For further analysis we extracted CO and H_2O line fluxes from an aperture of 9″ radius at 4 positions along the jet. The positions and the apertures are the same as those used for the [O I] analysis. The measured CO and H_2O line fluxes along with their uncertainties are listed in Tables 11.1 and 11.3. As in the case of [O I] lines, the peak in CO and H_2O emission is at the location of FIR 4 (HOPS108), which coincides with the terminal shock produced by the jet from FIR 3 (HOPS370).

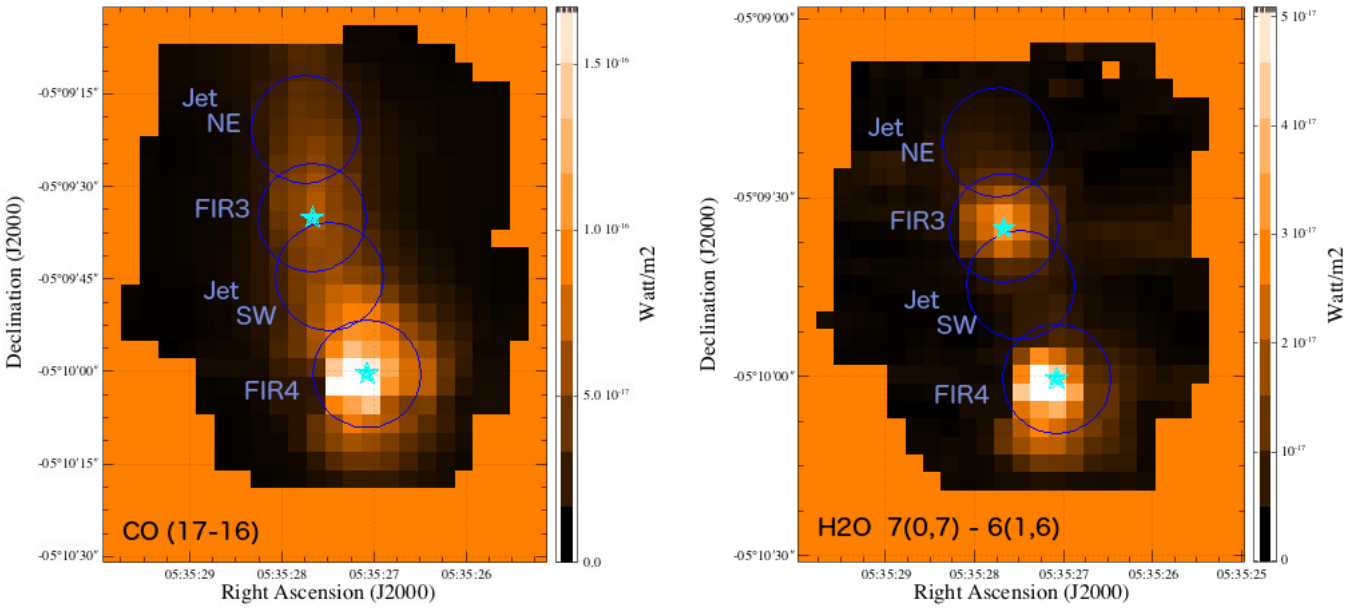

Figure 11.1: CO ($J = 17 \rightarrow 16$) *(left)* and H_2O ($7_{0,7} \rightarrow 6_{1,6}$) *(right)* line maps of the OMC-2 region. The positions, sizes, and names of the line flux aperture measurements listed in Table 11.1 are indicated.

11.2.1 Modelling of the CO emission tracing the jet

In order to determine the physical conditions in the jet, we modelled the observed CO emission as arising from an optically thin medium of uniform temperature and density (Neufeld 2012; Manoj et al. 2013). We computed the synthetic CO rotational diagrams for such a medium for a large range of values of T (100-5000 K), $n(H_2)$ (10^2-10^{12} cm^{-3}), and a column density (or optical depth) parameter $\tilde{N}$(CO) (for details see Neufeld & Kaufman 1993; Neufeld 2012; Manoj et al. 2013). We

then compared the model rotational diagrams with the observed ones to find the best fit solutions by minimizing the reduced-χ^2. The best fit models and physical parameters (corresponding to the minimum in reduced-χ^2) obtained for CO emitting gas for 4 positions along the jet are shown in Figure 11.2 and are listed in Table 11.2. At the location of FIR 4, where we detect 30 CO lines, the density ($n(H_2)$) and temperature (T) of the gas is well constrained. For other three positions, where fewer CO lines are detected, the temperature is well constrained, but the modelling provides only an upper limit to the density, $n(H_2) \leq 10^4$ cm^{-3}. The temperature of the emitting gas appears to be slightly higher at positions FIR 4 and Jet_{SW} compared to that at FIR 3 and Jet_{NE}. We also list the estimated column densities of CO gas, N(CO), at these 4 positions in Table 11.2. The N(CO) values are computed by scaling up the fractional level populations given by the best fit model to the observed flux value of the CO ($J = 14 \rightarrow 13$) line, and for a beam size of 9″ in radius.

Thus, from the best-fit solutions for CO emission, we constrained the density and temperature of the emitting molecular material at 4 locations along the jet. The beam-averaged column density provides a constraint on the optical depth parameter, $\tilde{N}$(CO) = N(CO)/dv cm^{-2}per km s^{-1}, such that log[N(CO)/dv] is in the range of 15.5 to 16.5, for velocities of a few km s^{-1}.

The flux values measured in the same four apertures of the line maps of the final H_2O line maps detected in PACS are given in Table 11.3.

11.2.2 H_2O/CO abundance ratio in the jet

We have detected ~ 24 H_2O lines corresponding to the rotational transitions of H_2O in the ground vibrational state. We carried out a combined analysis of $H_2O$and CO to investigate the H_2O to CO abundance ratio, $n(H_2O)/n(CO)$, in the jet, under the assumption that both H_2O and CO arise in the same gas component. In the following analysis, we fix the density ($n(H_2)$) and temperature (T) of the emitting gas to the values obtained from the CO modelling. We also fix the optical depth parameter for CO, log[N(CO)/dv] in the range of 15.5 to 16.5.

In order to constrain the H_2O/CO abundance ratio, we compared a carefully chosen H_2O to CO line ratio with that predicted by a model for a single gas component at uniform density and temperature. We use the *ortho*-H_2O ($7_{0,7} \rightarrow 6_{1,6}$) line at 71.95 μm, which is one of the highest excitation (E_{up} = 841 K) H_2O line detected in all of the 4 positions along the jet. We then chose the CO (J = 17 $\rightarrow$ 16) line, which has an upper state energy, E_{up} = 846 K, similar to that of the water line. This observed line ratio is compared to the model predictions in Figure 11.3 and 11.4.

It can be seen from Figure 11.3 and 11.4 that for the $n(H_2)$ and T inferred from the fit to the CO emission, the observed o-H_2O ($7_{0,7} \rightarrow 6_{1,6}$) to CO ($J = 17 \rightarrow 16$) line ratios can only be explained by the models if the abundance ratio, $n(o\text{-}H_2O)/n(CO)$ is < 1. Observed line ratios indicate an o-H_2O to CO abundance ratio closer to 0.3. For an H_2O ortho-to-para ratio of 3, this corresponds to a total H_2O to CO abundance ratio $n(H_2O)/n(CO)$ of ~ 0.4. H_2O appears to be under-abundant by more than a factor of 2 compared to CO behind the shocks in the jet driven by FIR 3.

11.3 Discussion on the study of the CO and H_2O lines

11.3.1 Physical conditions in the molecular jet from FIR 3

The densities and temperatures that we obtain from the modelling of CO lines is quite similar to those found for a larger sample to protostars observed with *Herschel* (e.g. Manoj et al. 2013). These high temperatures (T $\geq$ 2500−5000 K) and relatively low densities ($n(H_2) \leq 2.5\times10^4$ cm^{-3}) are typical of gas heated by outflow shocks in protostars (Manoj et al. 2013; Nisini et al. 1999; Giannini et al. 2001). Our modelling indicates that the material in the south-west part of the jet closer to the location of FIR 4 is at a higher temperature (T $\sim$ 4000−5000 K), while at the location of FIR 3 and the north-eastern part of the jet are at lower temperature (T $\sim$ 2500−3600 K). This is consistent with the idea that the location of FIR 4 represents the terminal shock of the FIR 3 jet, where it is decelerated rapidly and most of the kinetic energy of the jet is dissipated, heating the material. Given the best-fit temperatures and densities determined from the CO line ratio modelling, the absolute line fluxes indicate hot (T $\geq$ 2500) CO column densities, N(CO) in the range 0.6 - 2 $\times$ 10^{17} cm^{-2}, averaged over the beam size within which the CO flux was extracted. This corresponds to a H_2 column densities $N(H_2)$ = 2-6 $\times$ 10^{20} cm^{-2} for an assumed CO abundance of n(CO)/$n(H_2)$ = 3.2 $\times$ 10^{-4}. These values are typical of the column densities expected behind molecular shocks (e.g. Neufeld et al. 2006).

11.3.2 Water abundance behind outflow shocks

In the postshock gas behind interstellar shocks, the water vapour abundances are expected to be significantly enhanced compared to those in cold molecular gas. This is because, in fast shocks (shock speed v_s $\geq$ 25 km s^{-1}), the ice mantles on the dust grains can be fully sputtered and the oxygen locked up in ices is released into gas-phase. At high temperatures (T $\geq$ 1300 K) attained in the postshock gas, all the gas-phase oxygen will be converted into water vapour rapidly via a pair of neutral-neutral endothermic reactions. If all the gas-phase oxygen that is not locked up in CO is converted into H_2O, a maximum value of $n(H_2O)/n$(CO) = 1.2 is expected (e.g. Neufeld et al. 2014; van Dishoeck et al. 2013).

The best-fit values of CO line ratios along the FIR 3 jet indicate that the cooling molecular gas behind shocks are at high temperatures (T $\geq$ 2500). Shock speeds significantly higher than 25 km s^{-1} are required to heat up the postshock gas to such temperatures (Kaufman & Neufeld 1996; Neufeld et al. 2014). Such fast shocks would fully sputter the grain mantles and release all the oxygen into gas phase, and all the oxygen would end up as H_2O. Our analysis of the H_2O/CO line ratio, however, indicates that the H_2O to CO abundance ratio $n(H_2O)/n$(CO) in the shock heated gas in the FIR 3 jet is significantly lower than the expected value of 1.2 and is closer to 0.4. Low water abundances in outflow shocks from protostars have also been reported by Karska et al. (2014).

Why, then, are the water abundances low behind the shock fronts in protostellar jets? A few explanations have been suggested in the literatures. One possibility is that faster dissociative shocks are present along with the slower non-dissociative shocks that produce CO and H_2O emission.

The dissociative shocks can produce strong far-UV radiation (Spaans et al. 1995) which can photodissociate H_2O to OH and subsequently to oxygen, resulting in the observed low abundance of H_2O (e.g. van Dishoeck et al. 2013; Karska et al. 2014). The photodissociation of H_2O will result in elevated OH abundances which has been reported in a few cases (Karska et al. 2014). One difficulty with this scenario, however, is that although significant UV radiation field present at the postshock region can diminish water abundance, at the high temperatures (T $\geq$ 2500) that we derive for the emitting molecular gas, neutral-neutral reactions can reform H_2O very efficiently. Another possibility is that a significant fraction of oxygen is locked up in oxygen-bearing molecules other than water ice within the grain mantle and these molecules possibly have a higher sputtering threshold than water ice, so that not all oxygen is released into gas phase to be converted into H_2O.

11.4 Conclusions

We have carried out an analysis of the CO and H_2O lines observed towards the jet/outflow from FIR 3 in the OMC-2 region. Our main results are summarised below.

- CO and H_2O emissions observed towards the jet/outflow from FIR 3 in the OMC-2 regions arise in hot (T $\geq$ 2500−5000 K) and relatively low density ($n(H_2) \leq 2.5\times 10^4$ cm^{-3}) molecular gas heated in jet/outflow shocks.
- Other authors (Herczeg et al. 2012; Goicoechea et al. 2012; Karska et al. 2013, 2014) focused their conclusions on the CO rotation diagrams results, and suggested a solution with 3-4 temperature components that are in LTE with the surrounding gas.
- The best-fit temperatures obtained from the modelling of the CO line ratios suggest a temperature gradient for the molecular gas along the jet. The shock heated molecular gas is progressively hotter going from FIR 3 to FIR 4 along the jet/outflow, indicating that the non-dissociative shocks responsible for heating the molecular gas is stronger towards the south-west part of the jet and strongest at the location of FIR 4. This is consistent with the location close to FIR 4 coinciding with the terminal shock produced by the jet/outflow from FIR 3, where jet/outflow is rapidly decelerated and almost comes to a stop. Most of the bulk kinetic energy of the flow would be converted into random thermal energy, thereby heating the gas to high temperatures, as inferred from observations.
- The observed H_2O to CO line ratios indicate low water abundances in the shock heated molecular gas in FIR 3 jet/outflow. The inferred H_2O to CO abundance ratio, $n(H_2O)/n(CO) = 0.4$, is significantly lower than the expected value of 1.2 in hot ($T \geq 2500$) postshock gas behind the shocks.

Table 11.1: CO line fluxes extracted from the line map within the same four apertures used for the [O I] analysis, with 9″ radius.

CO transition (J_{up} - J_{low})	rest wavelength of transition (microns)	flux_{FIR4} $\times 10^{-16}$ (Watt m^{-2})	flux_{SW} $\times 10^{-16}$ (Watt m^{-2})	flux_{FIR3} $\times 10^{-16}$ (Watt m^{-2})	flux_{NE} $\times 10^{-16}$ (Watt m^{-2})
14-13	185.999	30.14±0.04	14.0±0.12	17.7±0.15	11.3±0.11
15-14	173.631	29.18±0.04	12.7±0.1	16.4±0.14	9.7±0.09
16-15	162.812	28.66±0.07	11.0±0.1	14.2±0.12	9.04±0.08
17-16	153.267	28.18±0.06	11.2±0.1	13.5±0.11	8.09±0.06
18-17	144.784	2.472±0.07	9.5±0.1	10.9±0.1	6.83±0.07
19-18	137.196	22.72±0.1	10.0±0.1	10.5±0.09	6.78±0.07
20-19	130.369	24.25±0.07	9.3±0.1	9.0±0.1	5.97±0.05
21-20	124.193	24.64±0.08	8.7±0.1	8.1±0.1	5.42±0.08
22-21	118.581	19.82±0.09	8.2±0.1	6.6±0.1	5.12±0.07
23-22	113.457	34.08±0.1	15.4±0.12	12.1±0.09	8.96±0.09
24-23	108.763	16.30±0.12	6.7±0.14	5.70±0.11	3.97±0.09
25-24	104.445	15.52±0.6	5.3 ±1.1	5.41±0.8	3.58±0.7
28-27	93.349	11.99±0.05	5.09±0.09	4.00±0.05	2.97±0.06
29-28	90.163	12.50±0.06	4.77±0.08	3.63±0.06	2.39±0.05
30-29	87.190	10.06±0.05	5.3±0.07	3.44±0.06	2.71±0.06
31-30	84.411	18.92±0.07	9.6±0.1	6.43±0.07	3.84±0.07
32-31	81.806	7.67±0.08	4.2±0.1	2.22±0.08	1.43±0.09
33-32	79.360	7.30±0.08	3.0±0.12	2.38±0.09	1.95±0.09
34-33	77.058	6.47±0.08	3.3±0.12	2.37±0.09	1.21±0.1
35-34	74.890	5.46±0.08	2.4±0.12	1.50±0.09	1.05±0.09
36-35	72.843	5.09±0.1	2.4±0.12	1.52±0.09	1.05±0.09
37-36	70.907	2.93±0.1	1.4±0.09	0.94±0.08	0.71±0.09
38-37	69.074	3.10±0.03	1.28±0.03	1.02±0.03	0.65±0.03
39-38	67.336	2.67±0.04	1.43±0.04	0.98±0.03	0.50±0.03
40-39	65.686	2.41±0.05	1.53±0.05	1.22±0.04	0.53±0.04
41-40	64.117	2.16±0.08	1.41±0.06	1.13±0.06	0.58±0.05
42-41	62.624	2.03±0.09	1.29±0.07	1.03±0.07	0.57±0.05
43-42	61.201	1.97±0.06	0.99±0.05	0.95±0.04	0.43±0.04
44-43	59.843	1.23±0.06	0.91±0.05	0.43±0.04	0.62±0.05
45-44	58.547	1.18±0.06	1.01±0.05	0.72±0.05	0.59±0.05

Table 11.2: Physical parameters of the CO emitting gas from modeling

Position along the jet	RA(J2000)	Dec(J2000)	T (K)	$n(H_2)$ (cm^{-3})	N(CO) (cm^{-2})
FIR 4	5 35 27.07	−5 10 0.37	4000 - 5012	$1.0 - 2.5 \times 10^4$	2×10^{17}
Jet_{SW}	5 35 27.48	−5 09 44.64	4000 - 5012	$< 10^4$	6×10^{16}
FIR 3	5 35 27.67	−5 09 35.10	2500 - 3600	$\leq 10^4$	9×10^{16}
Jet_{NE}	5 35 27.74	−5 09 20.70	2500 - 3600	$\leq 10^4$	6×10^{16}

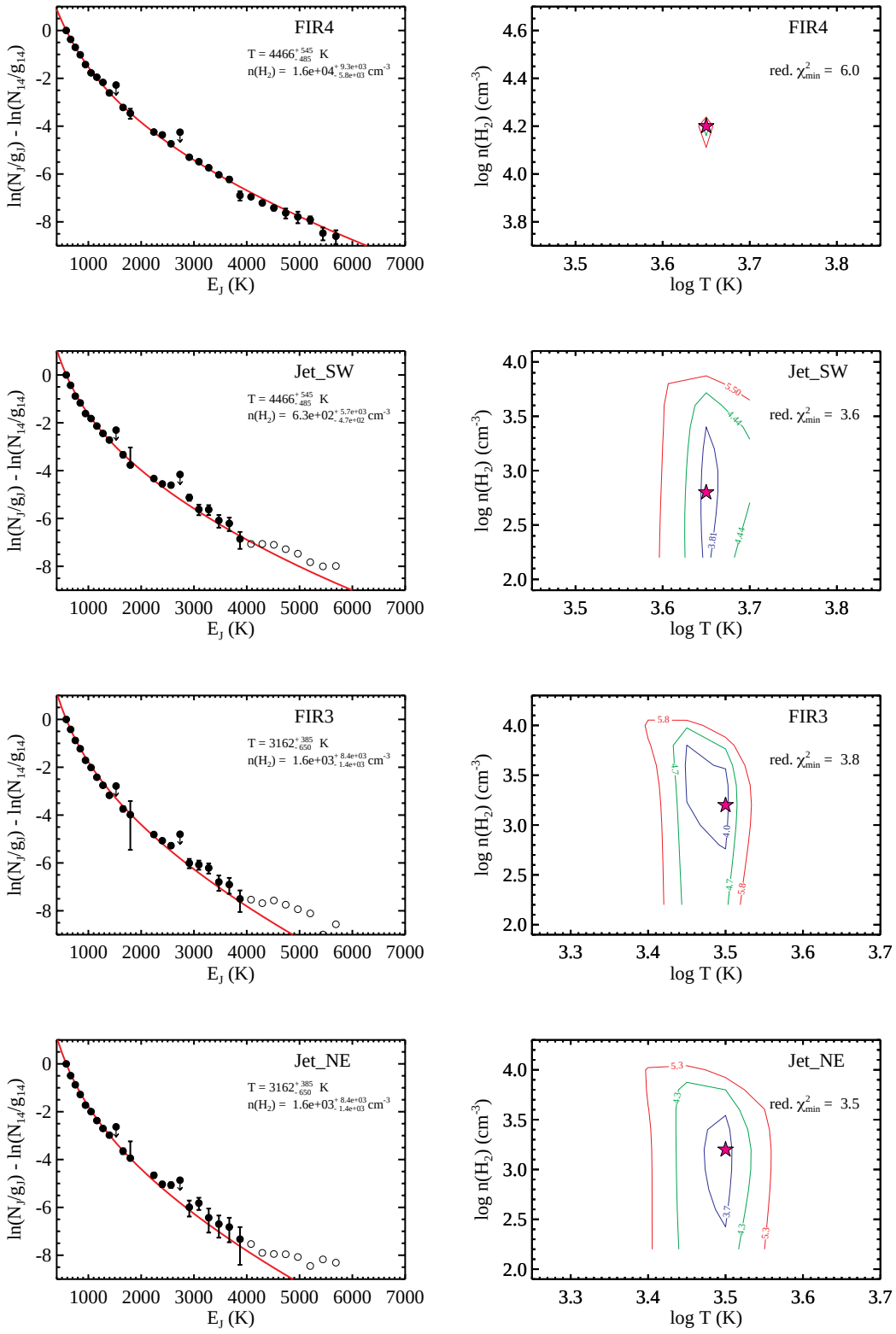

Figure 11.2: *(Left)* Rotational diagrams for CO from an isothermal medium that best fits the observations (solid red line). Downward arrows indicate upper limits to the fluxes of the CO lines which are blended with a nearby line. Open circles correspond to 3 σ upper limits for the non-detections. *(Right)* Reduced-χ^2 contours for T and $n(\mathrm{H_2})$. The star symbol marks the minimum. The contours corresponding to 68.3% (blue), 95.4% (green) and 99.7% (red) confidence levels are shown.

Table 11.3: H_2O line fluxes extracted from the line map within the same four apertures used for [O I], for aperture radius of 9″.

H_2O line (up - low)	rest wavelength of transition (microns)	flux$_{FIR4}$ $\times 10^{-16}$ (Watt m^{-2})	flux$_{SW}$ $\times 10^{-16}$ (Watt m^{-2})	flux$_{FIR3}$ $\times 10^{-16}$ (Watt m^{-2})	flux$_{NE}$ $\times 10^{-16}$ (Watt m^{-2})
2 (2,1) 2 (1,2)	180.488	5.27±0.1	2.7±0.05	2.9±0.03	2.17±0.02
2 (1,2) 1 (0,1)	179.52	15.07±0.14	8.4±0.1	7.9±0.03	8.93±0.02
3 (0,3) 2 (1,2)	174.626	15.10±0.14	6.6±0.03	6.6±0.04	5.89±0.03
3 (1,3) 2 (0,2)	138.528	10.6±0.2	4.4±0.08	4.6±0.07	3.05±0.05
4 (0,4) 3 (1,3)	125.354	7.3±0.1	2.92±0.09	2.6±0.09	1.70±0.07
4 (1,4) 3 (0,3)	113.537	34.5±0.4	15.6 ±0.3	12.3±0.2	9.10±0.09
2 (2,1) 1 (1,0)	108.073	15.0±0.2	7.1±0.15	6.7±0.2	5.77±0.09
4 (4,1) 4 (3,2)	96.757	12.2±0.13	5.0±0.08	3.8±0.07	2.76±0.06
5 (1,5) 4 (0,4)	95.627	5.9±0.1	3.2±0.08	1.9±0.07	1.23±0.06
3 (2,2) 2 (1,1)	89.988	5.4±0.1	0.7±0.07	1.2±0.06	0.49±0.05
6 (0,6) 5 (1,5)	83.284	3.9±0.05	2.4±0.1	1.3±0.08	1.04±0.08
6 (1,6) 5 (0,5)	82.031	8.9±0.1	5.0±0.12	3.0±0.08	2.13±0.09
4 (2,3) 3 (1,2)	78.742	11.6±0.1	6.1±0.13	3.8±0.09	2.55±0.09
8 (5,4) 8 (4,5)	77.082	6.8±0.1	3.1±0.13	2.47±0.1	1.50±0.09
7 (2,5) 6 (3,4)	74.945	5.9±0.1	2.9±0.12	1.79±0.09	1.37±0.09
7 (0,7) 6 (1,6)	71.947	6.3±0.15	3.9±0.13	1.85±0.09	1.3±0.1
3 (3,1) 2 (2,0)	67.089	1.8±0.05	1.3±0.03	0.84±0.04	0.71±0.03
7 (1,6) 6 (2,5)	66.093	2.0±0.05	1.8±0.03	0.96±0.04	0.39±0.04
6 (2,5) 5 (1,4)	65.166	2.99±0.05	2.6±0.03	1.40±0.04	0.76±0.04
8 (1,8) 7 (0,7)	63.323	2.2±0.1	2.2±0.06	1.46±0.07	0.51±0.05
9 (2,8) 9 (1,9)	62.650	2.3±0.1	1.7±0.07	1.36±0.07	0.80±0.05
7 (2,6) 6 (1,5)	59.987	0.6±0.07	0.7±0.05	0.33±0.04	0.33±0.05
4(3,2) 3 (2,1)	58.699	3.2±0.08	3.01±0.03	1.81±0.05	1.36±0.05
4 (2,2) 3 (1,3)	57.636	2.0±0.07	1.40±0.06	0.67±0.05	1.08±0.06

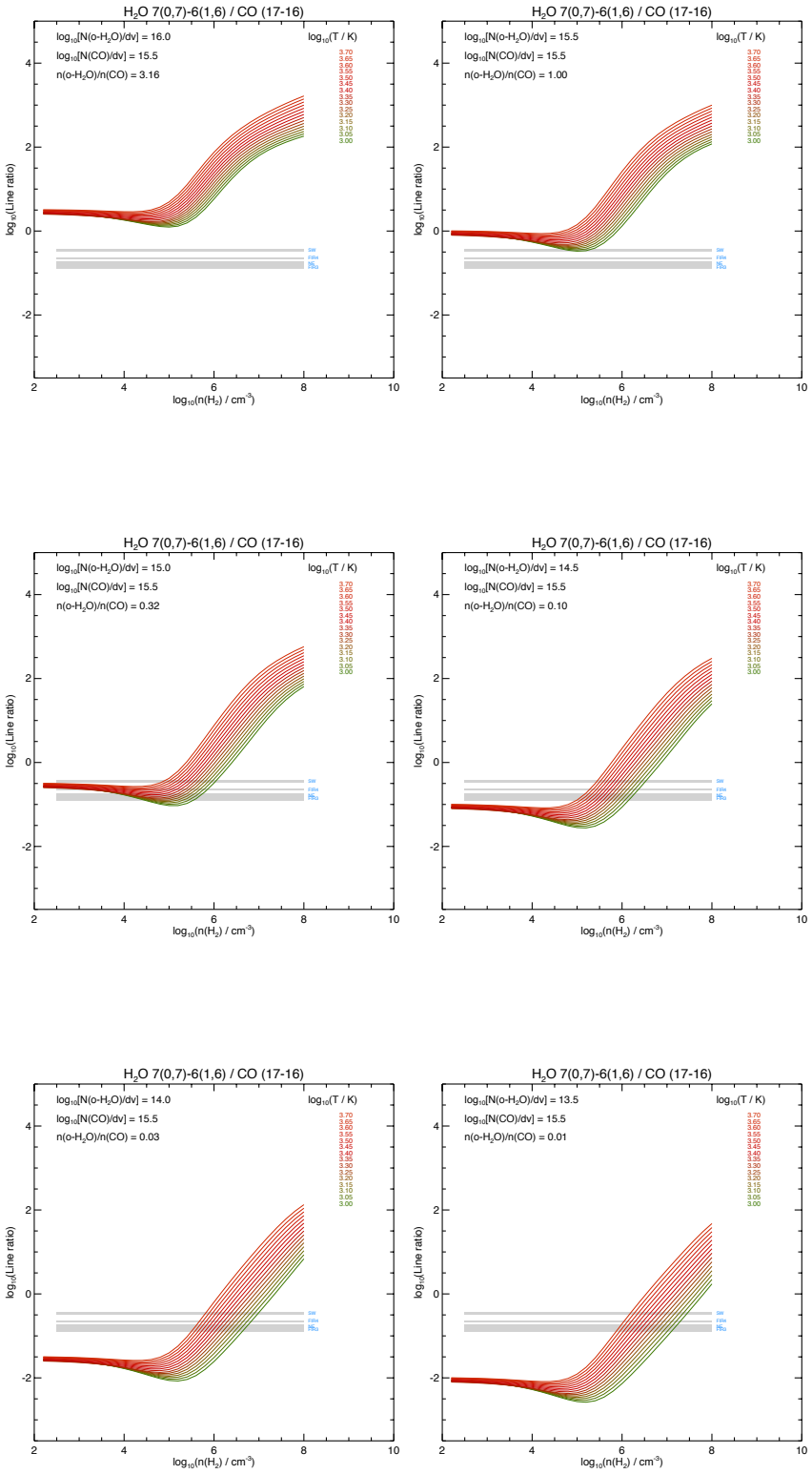

Figure 11.3: The model predictions of o-H_2O ($7_{0,7} \rightarrow 6_{1,6}$) to CO ($J = 17 \rightarrow 16$) line ratio as a function of $n(H_2)$ for various temperatures (color coded) and for a CO optical depth parameter of $log[N(CO)/dv] = 15.5$. Different panels correspond to the abundance ratio, $n(o\text{-}H_2O)/n(CO) =$ 3.16, 1.0, 0.32, 0.1, 003 and 0.01. The observed ratios at the 4 positions along the jet are shown as gray bars, with the spread corresponding to uncertainties. For the $n(H_2)$ and T inferred from the best fit models for CO emission, the observed line ratios indicate $n(o\text{-}H_2O)/n(CO)$ between 1 and 0.32.

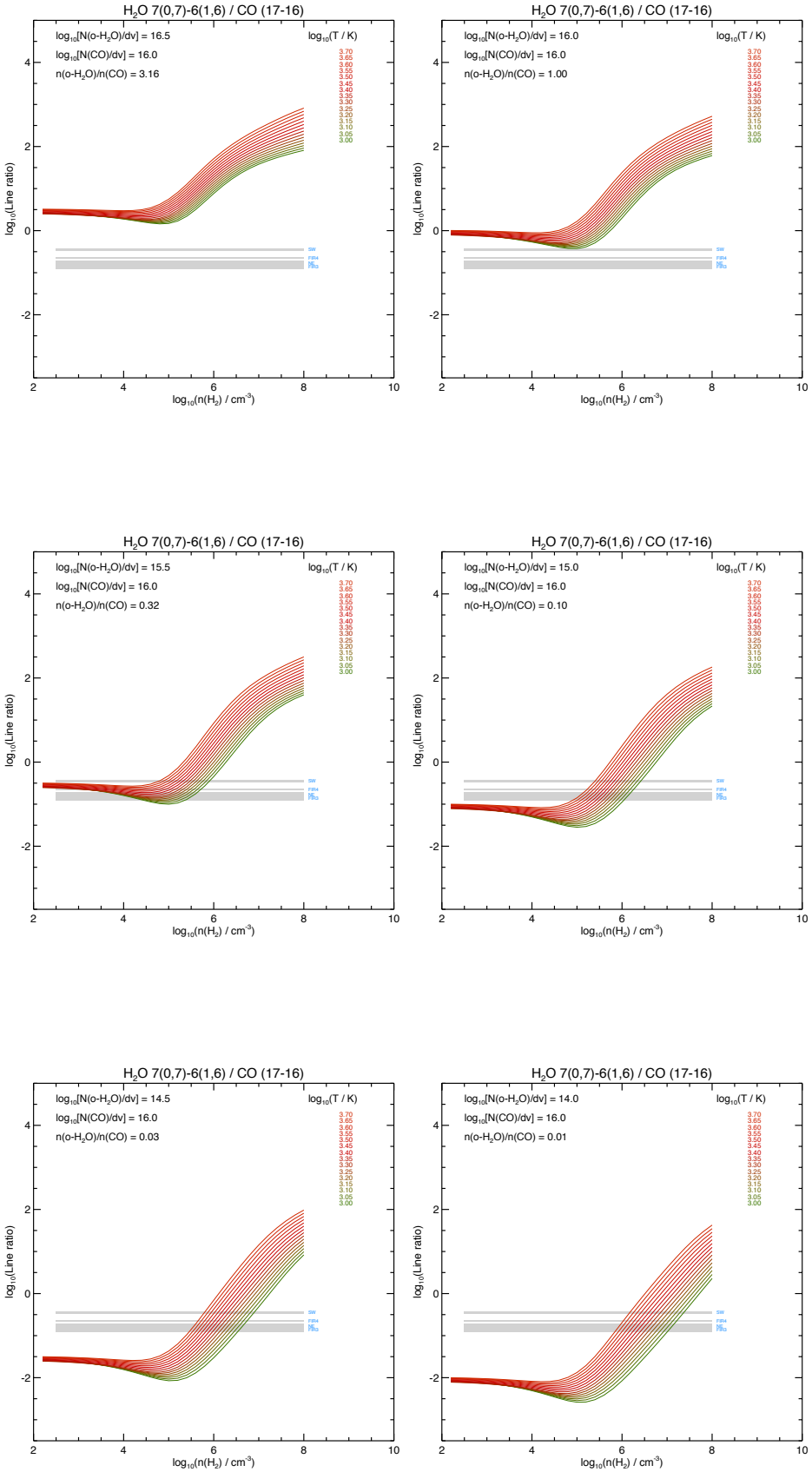

Figure 11.4: Same as in Figure 11.2, but for a CO optical depth parameter of $log[N(\mathrm{CO})/\mathrm{dv}] = 16$.

12

Data synergies and future studies

To extend the analysis of the data obtained with PACS/Herschel for the OMC-2 region, the team (Osorio et al, in preparation) carried out observations at high angular resolution at centimetre wavelengths with the Very Large Array. Here we briefly show them and comparison to the data provided at this PhD work.

12.1 HOPS VLA data from the OMC-2 region

The VLA observations collected were done at very high resolution (~ 5″- 1″) at centimetre wavelengths (6cm, 3cm) and K(1.3cm), Q(0.7cm) bands.

The centimetre emission (6cm and 3cm) mainly traces the free-free emission which could proceed from a radio-jet (Anglada et al. 1996) or indicate the presence of HII regions generated by a high- or intermediate-mass star (López-Sepulcre et al. 2013). In fact, Reipurth et al. (1999) reported the detection of radio continuum at 3.6 cm close to HOPS 108 and HOPS 370 (also named as VLA12 and VLA11, respectively). Unfortunately, the angular resolution of his observations (~8″) was not sufficient to discriminate between these two possibilities.

The new observations obtained by the HOPS consortium (Osorio et al, in preparation) were carried out on October 2014. These observations showed the presence of strong emission at position of HOPS 370, with a slightly elongated morphology in the HOPS 108 direction (see Fig. 12.1) and with a positive spectral index (0.15), such as radio-jets have.

Centimetre emission was also detected at the position of HOPS 108, being less intense than the one reported by Reipurth et al. (1999), but with an interesting filamentary morphology with three emission peaks as shown in Fig. 12.1: the central peak approximately matches with the *Spitzer*

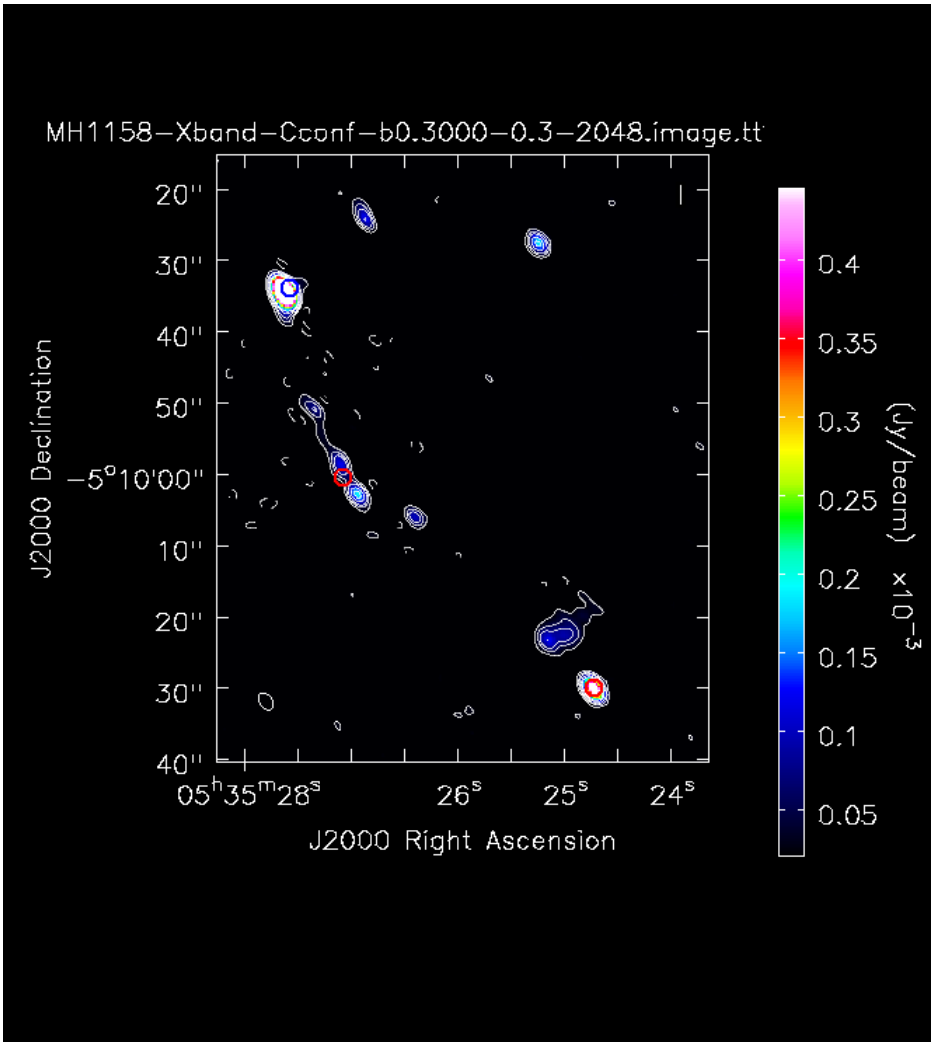

Figure 12.1: VLA map at 3cm at C configuration. Contours presented from [-3,3,6,9,15,21] $\times \sigma$, being σ = 0.008 mJy/Beam. The color scale also corresponds to the 3 cm emission. Beam size represented at the bottom left side of the image.

emission at 4.5 μm (collected by the HOPS team and shown in Fig. 10.3 at Chapter 11) and it is considered to be tracing the position of a young star. Red circles in Fig. 12.1 have been plotted at the position of HOPS 370(*top*), HOPS 108 (*middle*) and HOPS 368 (*bottom*). We can also see in this figure two peaks of emission at either side of the central position (south and north) could be bipolar ejections from the radio jet produced by the protostar.

These detections allowed us to discard the proposal that HOPS 108 was an HII region, and favours the idea that this target has an associated radio-jet. However, the spectral indexes measured for each of these emission peaks, from the observations at 0.7, 1.3 and 5 cm taken at the same epoch from the same HOPS programme seems to be negative.

To have a negative spectral index indicates that the nature of the emission is non-thermal and it could be synchrotron emission. However, this finding is preliminary because the reliability of the measured spectral index (specifically it being <0) is affected by the fact that only upper limits could be measured at 7mm. Also because Fig. 12.1 shows that at the different centimetre wavelengths

the position of the three maximum emission do not overlap: the central peak at 3cm it is slightly shifted respect to the peaks at 1.3 cm and 0.7 cm and the northern peak show emission at 3 cm but not at 1.3 or 0.7 cm.

If the non-thermal nature of HOPS 108 were confirmed at the three peaks observed at 3 cm, it would cast doubt on the idea that HOPS 108 is driving its own radio jet, as at the central position (where the protostar should be for being a radio jet) would not be expected to detect synchrotron due to its high density. One alternative explanation would be that the three detected emission peaks at HOPS 108 are ejections from the material of the radio jet driven by HOPS 370, which central position would then have a positive spectral index, as characteristic of a radio jet. The lobes from this radio jet (driven by HOPS370) could extend up to HOPS 108 and explain the emission of non-thermal radiation, as in the well-known case of Carrasco-González et al. (2010).

One could speculate that HOPS370 is hitting the dense gas at the HOPS 108 position, and inducing star formation there. This idea comes from the fact that the central position, identified by the *Spitzer* 4.5 μm data, the 0.7 cm and 1.3 cm, do not match with the position at 3 cm. This may trigger the idea of having two objects tracing different nature: the first ones could be tracing a protostar and the last one the ejection from HOPS 370 which may be originating the star formation of this new star (Osorio et al, in preparation).

12.2 VLA/PACS data cross-match

In this section we present the overlap of a representative set of PACS line maps generated at this work (background of the images) and on top of them the contours from the VLA 3 cm continuum.

Figures 12.2, 12.3, 12.4 and 12.5 show the positions which were identified by *Spitzer* 4.5 μm are close to the positions (marked with white crosses) from HOPS 370 (northeast) and HOPS 108 (southwest). These positions are the ones identified for the protostars at the *Spitzer* 24 μm and *Herschel* 70 μm images from the HOPS team. We also see how the elongated structure of the contours around HOPS 108 match nicely with the jet traced by the [OI] lines.

The fact the there is $\leq 2\,''$shift in the position of HOPS 108 need to be still clarified whether it comes from the $2\,''$uncertainty at the Herschel observations for this target, which as we mentioned before were collected under a Solar Aspect Angle conditions that may have cause this high uncertainty, or due to the fact the jet is not exactly in the position of the source but very close to it and what we are seeing is the shock of the jet in the molecular cloud from HOPS 108 which may be trigger also its star formation as the VLA data seems to suggest.

New high resolution observations with VLA are required to completely disentangle the mystery.

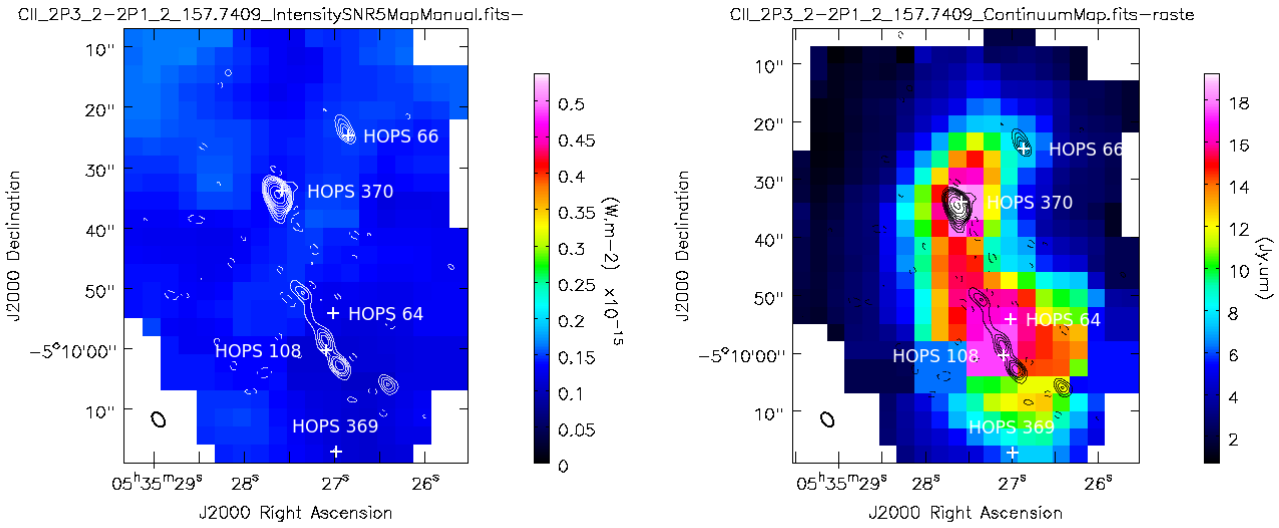

Figure 12.2: Combination of VLA 3cm data with the PACS [C II] at 157 μm line (*left*) and (*continuum*) maps. PACS data is presented in the background and the VLA as contours. Images generated by A.K.Diaz and passed as private communication.

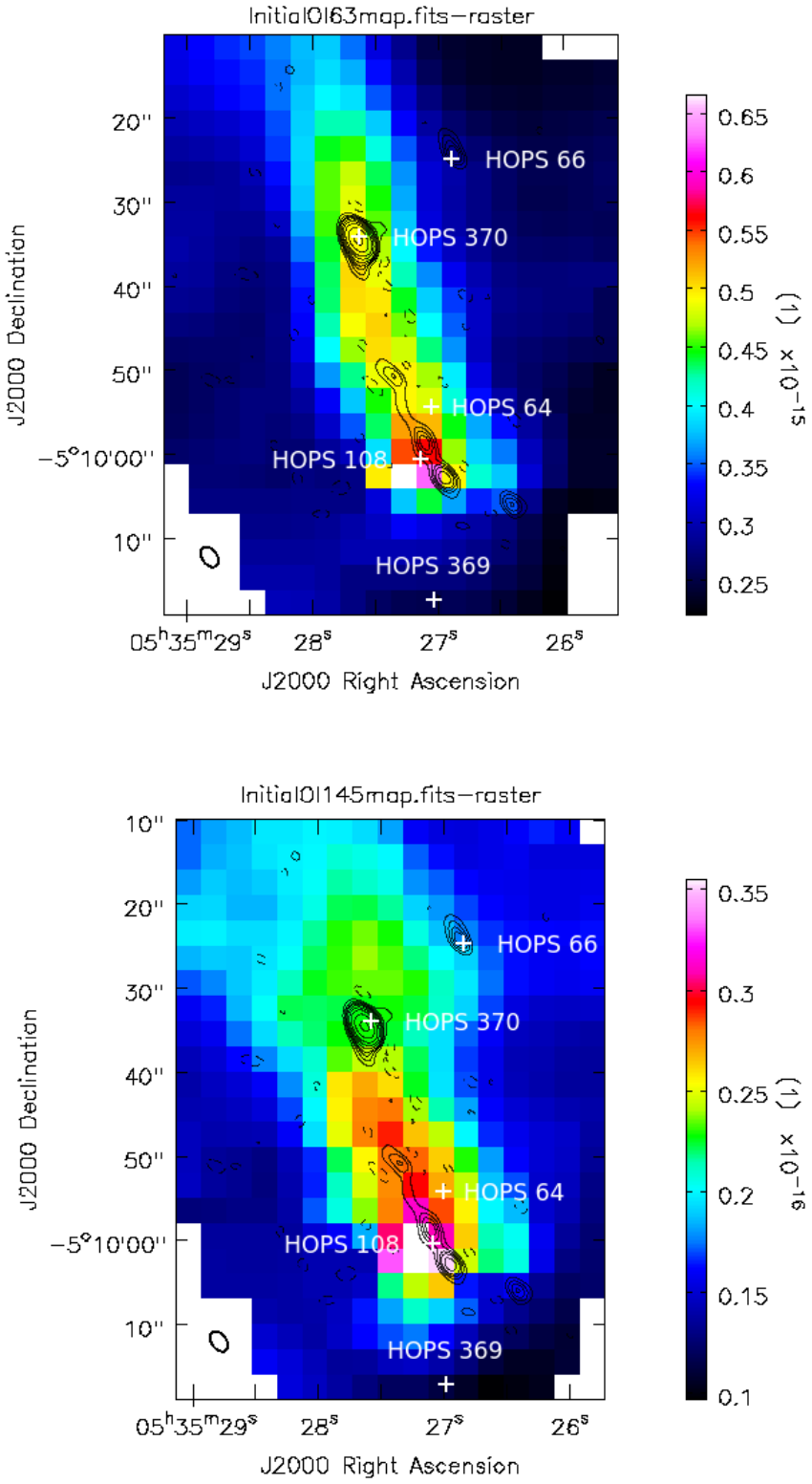

Figure 12.3: Combination of VLA 3cm data with the PACS [O I] 63 and 145 μm line maps. PACS data is presented in the background and the VLA as contours. Images generated by A.K.Diaz and passed as private communication.

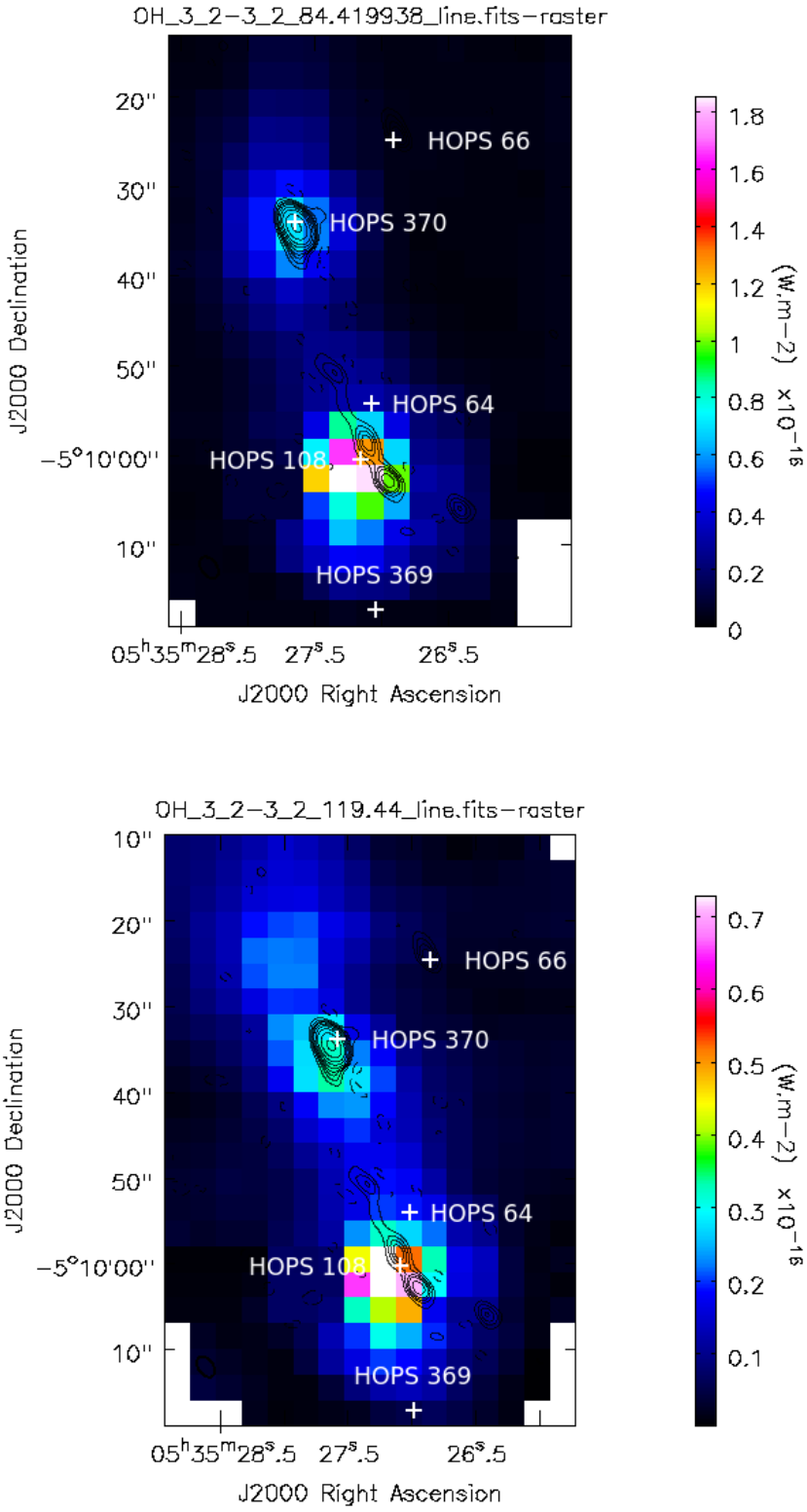

Figure 12.4: Combination of VLA 3cm data with a sample of the PACS OH line maps. PACS data is presented in the background and the VLA as contours.Images generated by A.K.Diaz and passed as private communication.

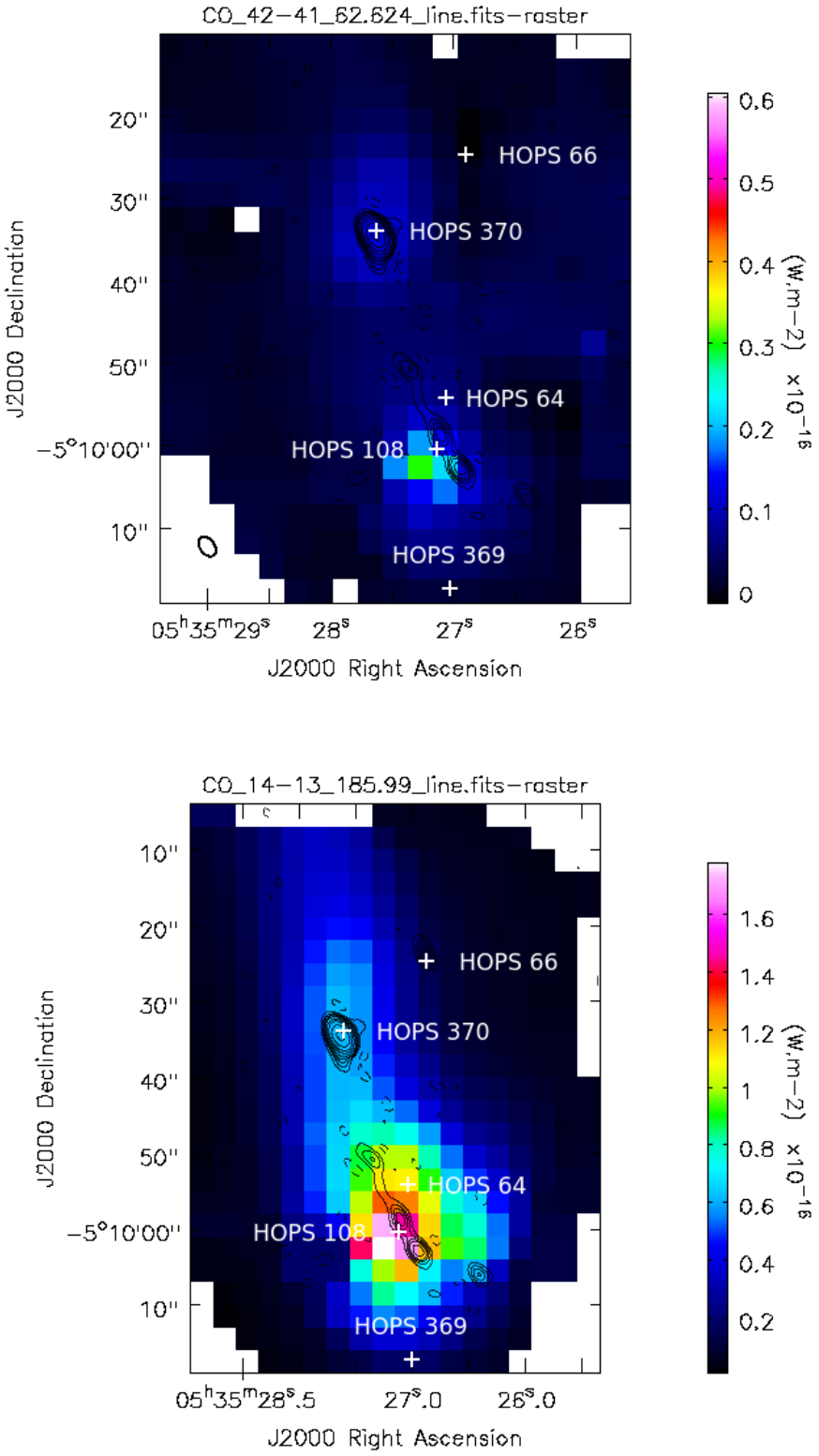

Figure 12.5: Combination of VLA 3cm data with a sample of the PACS CO and H_2O line maps. PACS data is presented in the background and the VLA as contours.Images generated by A.K.Diaz and passed as private communication.

12.3 Future Work

- Publication on the CO and H_2O water results by applying a more detail modelling from D. Neufeld.
- OH analysis
- User Provided Data Products to be delivered to the Herschel Science Archive.
- Continue with the testing of FF2, super off products and more optimal calibration source.
- GRMT proposal contribution.
- SOFIA proposal contribution.

13

Summary and Conclusions

The main conclusions of this work could be divided in two: technical achievements and scientific results.

13.1 Technical achievements

- We create validated, legacy high-quality spectral mapping products including line flux and continuum maps for all CO, water and atomic fine structure lines detected towards the OMC-2 region. The main point are:
- We optimised the creation of mosaic cubes for unchopped range observations, by removing the continuum before mosaicking.
- We compared the resultant mosaicking maps to determine the best one to use for (i) mapping , (ii) pointed and (iii) pointing plus mapping combined observations.
- We optimised spectral drizzling parameters on simulated data of oversampled spectral maps of the HOPS dataset, and these optimal parameters have been adopted by the PACS legacy pipeline.
- We estimate beam correction factors which allows one correctly measure integrated flux of point sources within a circular extraction aperture on an oversampled spectral map, a complement to the task for point sources provided within the pacs pipeline.
- We created optimally processed spectroscopy data products (cubes and maps) for the fine structure, CO, and H_2O water lines detected at the OMC-2 region at unprecedented spatial

resolution (8 ″at short wavelengths and 13″at longer wavelengths) and line sensitivity ($< 2.0 \times 10^{-17}$ Watts/m^2) in the (55-200) microns range of the far-infrared.

- Define and elaborate methodology to quantify uncertainties and confidence levels associated to line flux maps.
- Taking full advantage of the flexibility in the PACS data processing pipeline, the state-of-the-art spectral cube reconstruction algorithms are optimised for the HOPS dataset. We create hyper-spectral cubes, line flux maps, continuum maps line ratio maps, signal-to-noise maps and quality assessment of these products, combining two different type of observations.
- Validate intermediate- and final level legacy products, also including comparison to previous studies on the same region.

This PhD work started in 2011, therefore many of the current standard algorithms in recent Herschel Interactive Processing Environment versions were *drizzle* and other algorithms such as *specInterpolate* were a prototype or not developed for our scientific case jet. This thesis has combined contributed to the testing and improving to several of the current PACS spectrometer pipeline developed by PACS ICC and ourselves.

- Pointing gyro-reconstruction, a method from PACS ICC and HSC.
- Baseline Subtraction, a method which separates continuum and line with continuum cubes.
- ExtractSpectrum : A method to extract a 3D sub-cube from a 3D spectral cube.
- Drizzle: A method based on the projection of the data onto regular spatial and spectral grids taking advantage for spatially resampling spectral cubes at rasters, using the drizzle method of Fruchter & Hook (2002) coded in HIPE (Regibo 2012).
- specInterpolate: a method for spatially resampling spectral cubes, based on creating a new grid from an old one, using the Delauanay (reference) algorithm and then interpolating the spectral fluxes, at each wavelength, between the pixels of the grids. (Technical Note on Cube Interpolation Validation, E.Puga, 26 November 2014)
- Line- and continuum- map generation with the spectrum fitter and multifitter of HIPE.
- Scripts developed to convolve spectral images from a wavelength to another.

13.2 Scientific results

We modeled the star-formation processes in the OMC-2 region and possible interactions between FIR3 and FIR4 and surrounding targets using the high spatial resolution spectral line flux maps derived from PACS spectrometer observations.

- The jet driven by FIR 3 is the first to be imaged in [O I] 63 μm from an intermediate mass protostar. [O I] jets from low mass class 0 protostars observed with *Herschel*/PACS by

(Nisini et al. 2015) show mass loss rates in the range of 1-4 $\times 10^{-7}$ $M_\odot$ yr^{-1}. These mass loss rates are an order of magnitude lower than that of FIR 3. The mass loss rate for FIR 3 is higher than even the relatively high mass loss rate of 2-4 $\times 10^{-6}$ $M_\odot$ yr^{-1} found for HH 46 by (Nisini et al. 2015). Thus our results indicate that the mass loss rates in intermediate mass protostars are $\sim$ 10 times higher than that observed for most low mass class 0 protostars, consistent with the idea that they drive more powerful jets than their low-mass counterparts (A&A Letter, submitted).

- The peak [O I] emission, nevertheless, is observed close to FIR 4. All the high-excitation molecular cooling lines in the far-IR (H_2O, CO and OH) observed with *Herschel*/PACS have also their peak emission at the location of FIR 4 (Furlan et al. 2014, González-García et al. in prep). In fact, FIR 4 is one of the brightest far-IR line emitting source among all the protostars observed by HOPS. The far-IR line luminosities measured within a 9.4″aperture around FIR 4 is more than 4× higher than that observed for FIR 3 (Manoj et al. 2013). Our analysis and other studies of the region, however, do not show any evidence for FIR 4 driving a powerful outflow/jet which could excite such intense line emission (González-García, B.M, in preparation). We argue, therefore, that the bright line emission seen toward FIR 4 is the terminal shock (Mach disk) of the FIR 3 jet. Such terminal shocks are often the brightest features of YSO jets, and comprise many of the best-known Herbig-Haro objects. FIR 4 may simply lie along the line of sight and may not even be physically associated with the shocked emitting region.

- We estimated the density and physical temperature of the emitting gas along the jet by comparing the observed CO line ratios to a grid of model of rotational diagrams generated for large range of values of T (100- 5000 K), n(H2) (10^2-10^{12} cm^{-3}), and a column density (or optical depth) (Neufeld & Kaufman 1993; Neufeld 2012; Manoj et al. 2013). We then compared the model rotational diagrams with the observed ones to find the best fit solutions by minimizing the reduced-χ^2. The best fit models and physical parameters (corresponding to the minimum in reduced-χ^2) obtained for CO emitting gas for 4 positions along the jet also used for the [OI] analysis.

- We confirm the under-abundance of the H_2O at star formation regions compared to the CO abundance.

- We have contributed, in collaboration with the radioastonomer team (Osorio et al, in preparation) in better understanding the nature from the source OMC-2 FIR4.

To conclude this thesis, we show Fig. 13.1 our toy model of the OMC-2 region, develop from the findings from this work and the literature.

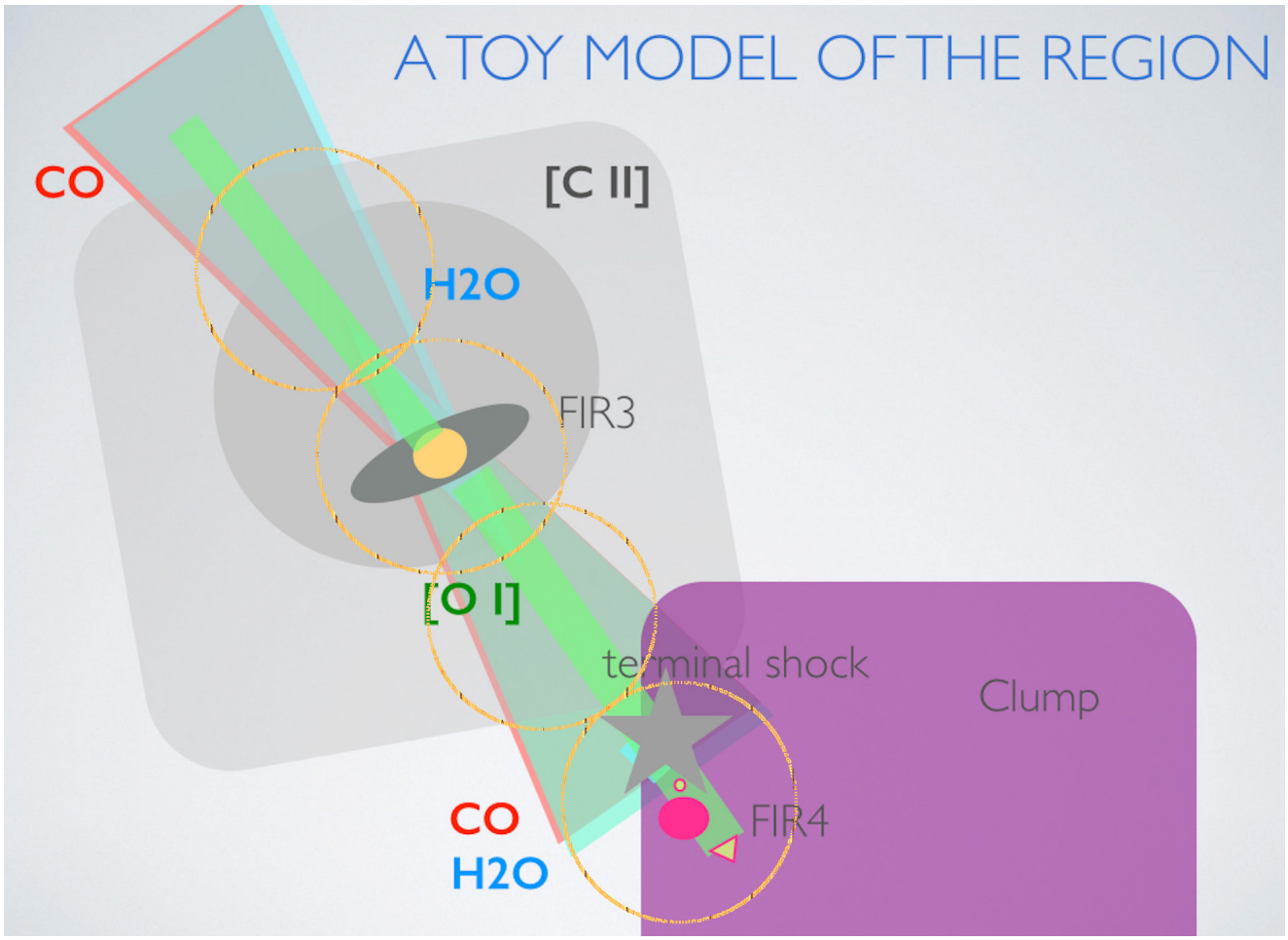

Figure 13.1: Our toy model of the OMC-2 region. In green there is the narrow jet structure, driven by FIR 3, that extends north-east and south-west. This impact with the cold cloud where FIR 4 is forming, very close to FIR 4 but maybe to exactly in the same position. Along the outflow there is detected CO and H_2O emission. The four apertures on which the fluxes were measured for the line maps generated in this work are shown. The extended emission that we see at [C II] line maps, is also shown.

A

Basic equations of star formation theory

A.1 Bonnor-Ebert mass calculation

The simplest case of a self-gravitating cloud is a static isothermal cloud with no magnetic field. For a given surface pressure $P_{th,0}$, the critical mass M_{cr} - i.e., the maximum mass for such a cloud to be in hydrostatic equilibrium (stable or unstable) - is the Bonnor-Ebert mass (McKee & Ostriker 2007).

$$M_{BE} \equiv 1.182 \frac{\sigma_{th}^4}{(G^3 P_{th,0})^{1/2}} = 1.182 \frac{\sigma_{th}^3}{(G^3 \rho_0)^{1/2}} \tag{A.1}$$

A.2 Bolometric temperature definition

Actually there is a parameter called "bolometric temperature" (T_{bol}), defined by Myers & Ladd (1993), which represent the temperature of a blackbody having the same mean frequency as the observed SED YSO, (Chen et al. 1997). The source function S_ν:

$$S_\nu = \pi \frac{R^2}{D^2} \frac{2h\nu^3}{c^2} \frac{1}{\exp(-h\nu/KT_{bol}) - 1} \tag{A.2}$$

$$L_{bol} = 4\pi\sigma T_{bol}^4 R^2 \tag{A.3}$$

where R is the radius of the source and D is the distance to the source, and h, k and σ are Planck's, Boltzmann's and Stefan-Boltzmann constants, respectively.

$$L_{bol} = 2\sigma D^2 T_{bol}^4 S_\nu \frac{c^2}{h\nu^3}[exp(-\frac{h\nu}{kT_{bol}}) - 1] \tag{A.4}$$

A.3 Luminosity of a protostar

The total luminosity of the protostars could be divided on the luminosity from the central forming star and the accretion processes. At very young object the second is the only one detected for being the central object totally embedded by the material from the envelope that is accreted onto the disk and then onto the star.

$$L_{tot} = L_{star} + L_{acc} \tag{A.5}$$

$$L_{star} = 4\pi R_{star}^2 \sigma T_{eff} \tag{A.6}$$

$$L_{acc} = G\frac{M_{star}\dot{M}_{acc}}{R_{star}} \tag{A.7}$$

A.4 Protostar envelope mass

As the thermal emission from dust is optically thin and proportional to the total particle mass, P.André and Montmerle estimated the envelope mass, measured at a wavelength (λ) by equation A.8, as the flux density measured over the entire region, at a LTE environment of temperature (T_{dust}). κ_λ is the opacity and $B_\lambda(T_{dust})$ is the blackbody spectrum at the dust temperature.

$$M_{env} = \frac{S_\lambda d^2}{j_\lambda} = \frac{S_\lambda d^2}{\kappa_\lambda B_\lambda(T_{dust})} \tag{A.8}$$

A.5 Escape velocity

Herbig Haro objects are movements of expansion but not caused by gravitational effects like rotation or collapse, therefore their velocities are higher than v_{max}. They are related to outflows.

$$\frac{mv_{max}^2}{R} - \frac{GMm}{R^2} = 0 \tag{A.9}$$

$$v_{max} = (\frac{GM}{R})^{1/2} 1 \tag{A.10}$$

A.6 Mass loss rate from [O I] 63.2 μm

From Hollenbach (1985) it has been identified that the peak of temperatures in the post-shock gas could be greater than 5000K (and outflow speed > 17 km/s will do), and the [O I] 63.2 μm cooling heavily dominates the cooling below 5000K. The intensity of [OI] 63.2 μm ($I_{[OI]}$) is related to the flux of atoms crossing the shock front: each atom bring its thermal energy to the T= 5000K point in the post-shock column, and all of this energy is radiated as [OI] photons as:

$$I_{[OI]} = \xi n_o v_s; \xi = 10^{-13} erg, \tag{A.11}$$

where n_0 is the pre shock hydrogen atom density and v_s is the shock speed. Suppose that the shock is plane parallel and travels in the *s* direction. The flux in the line in a given solid angle $\Delta\Omega$ of the shock area A seen from a distance *r*, so $\Delta\Omega = A/r^2$, therefore

$$F_{[OI]} - I_{[OI]}\Delta\Omega = \frac{\xi v_s}{r^2} n_0 A = \frac{\xi v_s}{r^2}\frac{d}{ds}(n_0 V) = \frac{\xi v_s}{m_H r^2}\frac{d}{ds}M = \frac{\xi v_s}{m_H r^2}\frac{dt}{ds}\frac{d}{dt}\dot{M} \tag{A.12}$$

so,

$$L_{[OI]} = 4\pi r^2 F_{[OI]} = \frac{4\pi\xi}{m_H}\dot{M} \tag{A.13}$$

$$\dot{M} = 8.1 \times 10^{-5} \frac{L_{[OI]}}{L_\odot}\frac{M_\odot}{year} \tag{A.14}$$

B

Optimization of Drizzle parameters

- **Validation of the optimum drizzle parameters on real data :**

  First attempt on the identification of optimum drizzle parameters at real data. Method: visual inspection.

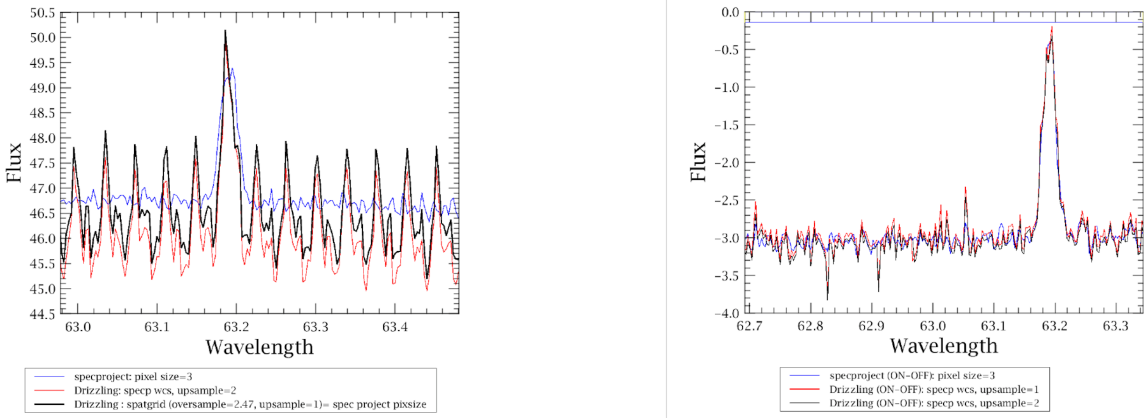

On-source unchopped raster

On-source unchopped raster, OFF flux subtracted

Figure B.1: This figure shows, two short ranges (in the blue band) of unchopped raster observation of the target HOPS85, the difficulty of identifying by visual comparison, the optimal drizzle parameters for the On-source (left) and at On-source, off subtracted (right) observations. The blue curve is the result of applying specProject to the raster observation and the black and red curves the selection of different upsample, oversample values.

Magenta (Gaussian input flux distribution evaluated for pixel centres)

Green (Gaussian rebinned to 3" pixel size) => Expected flux distribution

Blue (specProject result, peak flux scaled with pixel size)

Red (Gaussian convolved with 9.0"x9.0" effective spaxel size and rebinned to 3" pixel, peak flux scaled with pixel size)

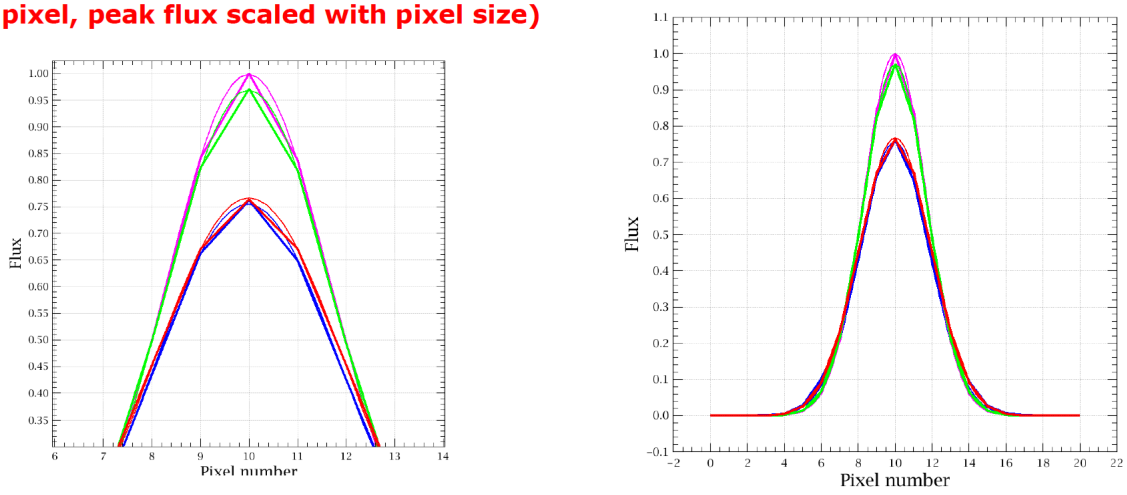

- Pixel size scale factor= ((spaxel^2.) * ((1./pixel)^2.))

Figure B.2

- **Identification of optimum drizzle parameters on simulated data :** First attempt on the identification of optimum drizzle parameters at real data with a Gaussian flux distribution. Method: Comparison of fitted FWHM at the drizzle cubes versus fitted FWHM at the beam distribution at 181 μm. Also specProject cube was compared.

  First attempt on the identification of optimum drizzle parameters at real data with a Gaussian flux distribution. Method: Comparison of fitted FWHM at the drizzle cubes versus fitted FWHM at the beam distribution at 68 μm. Also specProject cube was compared.

  Application of identified optimum parameters to two short ranges (one centred at the blue band and the other at the red band). The resultant drizzle cubes do not show the benefit of applying this method with these parameters respect to applying the specProject algorithm .

- **Identification of optimum drizzle parameters as a function of (oversample, upsample, pixfrac)** This is the result of an exhaustive testing of the drizzle input parameters for oversample raster maps in the 68 μm. The input data was a Pacs Level 1 cube from the oversample maps HOPS85 which flux was replaced by a Gaussian flux distribution. The maps show the different spatial distribution of the flux for the different input parameters selected at the generation of the spatial grids.

  This is the result of an exhaustive testing of the drizzle input parameters for oversample raster maps in the 181 μm.

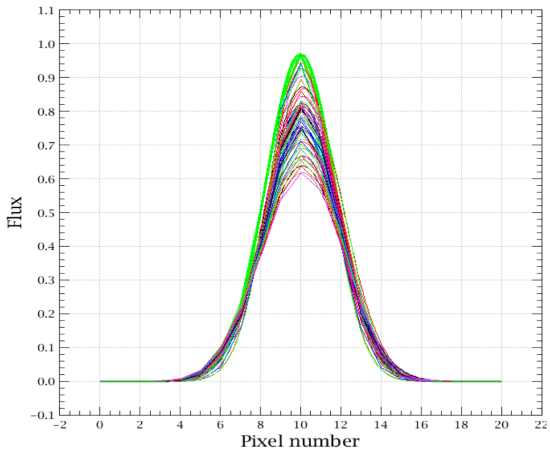

Figure B.3: This figure shows the different flux distributions along a cross section, of an input Gaussian flux distribution to which specProject and drizzle (for upsample=[1,2,3] and pixfrac=[0.1,0.2.0.3,..,0.9]) have been applied. The observation on which the simulated flux was applied is obsid xxx, and we used the pointing information from this oversample raster observation

FWHM	Upsample	Pixfrac
10.99	1	0.1
11.15	1	0.2
11.78	1	0.3
12.17	**Gaussian convolved to 3" pixel size Fit**	
12.39	1	0.4
12.63	2	0.5
12.70	2	0.6
12.71	3	0.1
12.74	2	0.4
12.78	3	0.2
12.79	1	0.5
12.82	1	0.6
12.96	1	0.8
13.00	1	0.7
13.01	2	0.3
....	..	...

FWHM	Upsample	Pixfrac
....	..	...
13.05	3	0.3
13.08	1	0.9
13.09	2	0.7
13.14	2	0.2
13.36	2	0.1
13.42	1	1.0
13.46	**specProject Fit**	
13.52	3	0.4
13.58	2	0.8
13.86	3	0.5
14.00	2	0.9
14.15	3	0.6
14.22	3	0.7
14.34	3	0.8
14.37	3	0.9
14.40	2	1.0
14.67	3	1.0

Figure B.4: This table shows the resultant FWHM obtained from fitting a Gaussian to each of the flux distributions mentioned at figure B.3. Green colour represent the Gaussian distribution at the central pixel and blue colour represent the specProject distribution (in line to Fig B.3). We identified optimum parameter those (upsample, pixfrac) parameters which flux distribution have a FWHM closer and smaller to the FWHM from the PSF at that wavelength .

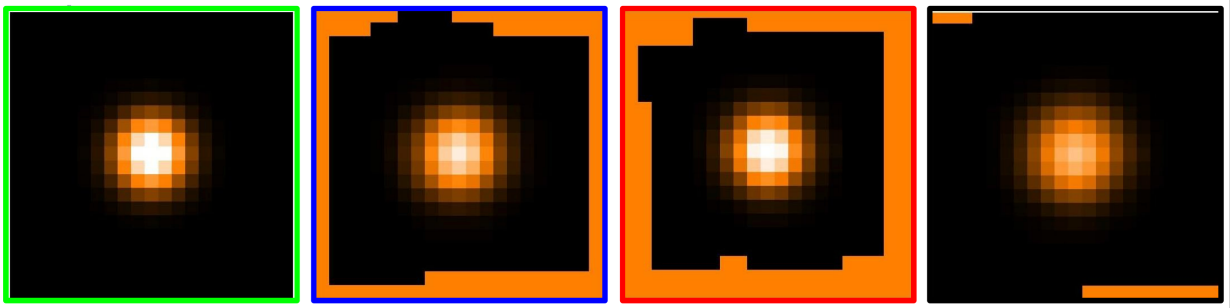

Figure B.5: This figure shows the resulting images from our simulation (Fig. B.3 and B.4) for a short range around 181 μm. From left to right they are: the expected flux distribution (green), specProject flux distribution (blue), drizzle flux distribution for those parameters that best match the FWHM of the beam (red), drizzle flux distribution for those parameters that worst match the FWHM of the beam (black) .

FWHM	Upsample	Pixfrac
7.57	1	0.1
7.63	1	0.2
8.02	1	0.3
8.44	**Gaussian convolved to 3" pixel size Fit**	
9.05	1	0.4
9.54	1	0.5
9.76	2	0.5
9.81	2	0.6
9.82	2	0.4
9.90	2	0.3
9.93	1	0.6
10.13	1	0.7
10.14	2	0.2
10.20	3	0.2
10.21	3	0.1
10.28	2	0.1

FWHM	Upsample	Pixfrac
....	..	...
10.31	1	0.8
10.38	1	0.9
10.39	2	0.7
10.40	3	0.3
10.46	**specProject Fit**	
10.76	3	0.4
10.92	1	1.0
10.98	2	0.8
11.22	3	0.5
11.57	3	0.6
11.60	2	0.9
11.75	3	0.8
11.80	3	0.7
11.96	2	1.0
12.17	3	0.9
12.51	3	1.0

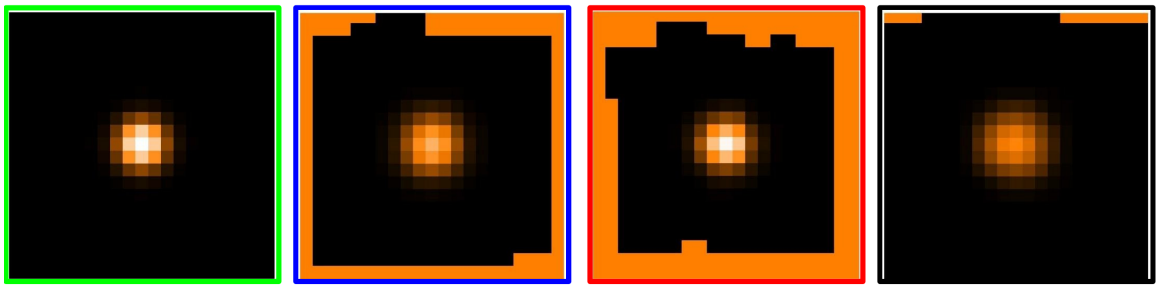

Figure B.6: This figure shows the same analysis than Fig. B.4 and B.5 for a short range around 68 μm.

FWHM	Upsample	Pixfrac
8.08	Gaussian convolved to 2.65" pixel size Fit	
~~8.47~~	~~2~~	~~0.1~~
8.67	1	0.4
8.78	2	0.2
8.83	1	0.3
8.91	1	0.5
8.92	1	0.1
9.03	1	0.2
9.08	2	0.3
9.22	1	0.6
9.45	2	0.4
9.64	2	0.5
9.73	1	0.7
9.99	2	0.6
10.00	3	0.1
10.06	1	0.8

FWHM	Upsample	Pixfrac
....	..	...
10.07	3	0.2
10.17	2	0.7
10.23	3	0.3
10.36	3	0.4
10.45	3	0.5
10.63	2	0.8
10.68	1	0.9
10.72	3	0.6
10.97	2	0.9
11.02	3	0.7
11.03	**specProject Fit**	
11.11	1	1.0
11.28	3	0.8
11.45	2	1.0
11.81	3	0.9
12.07	3	1.0

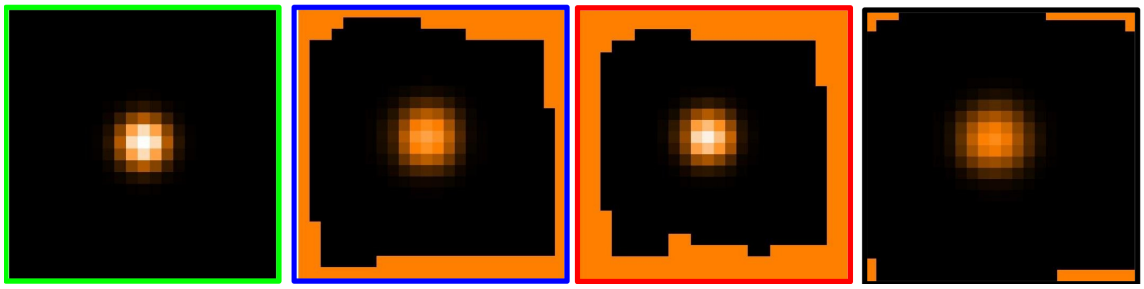

Figure B.7: This figure shows the same analysis than Fig. B.6 but for a fixed oversample factor = 3, upsample =[1,2,3] and pixfrac=[0.1,...,1.0].

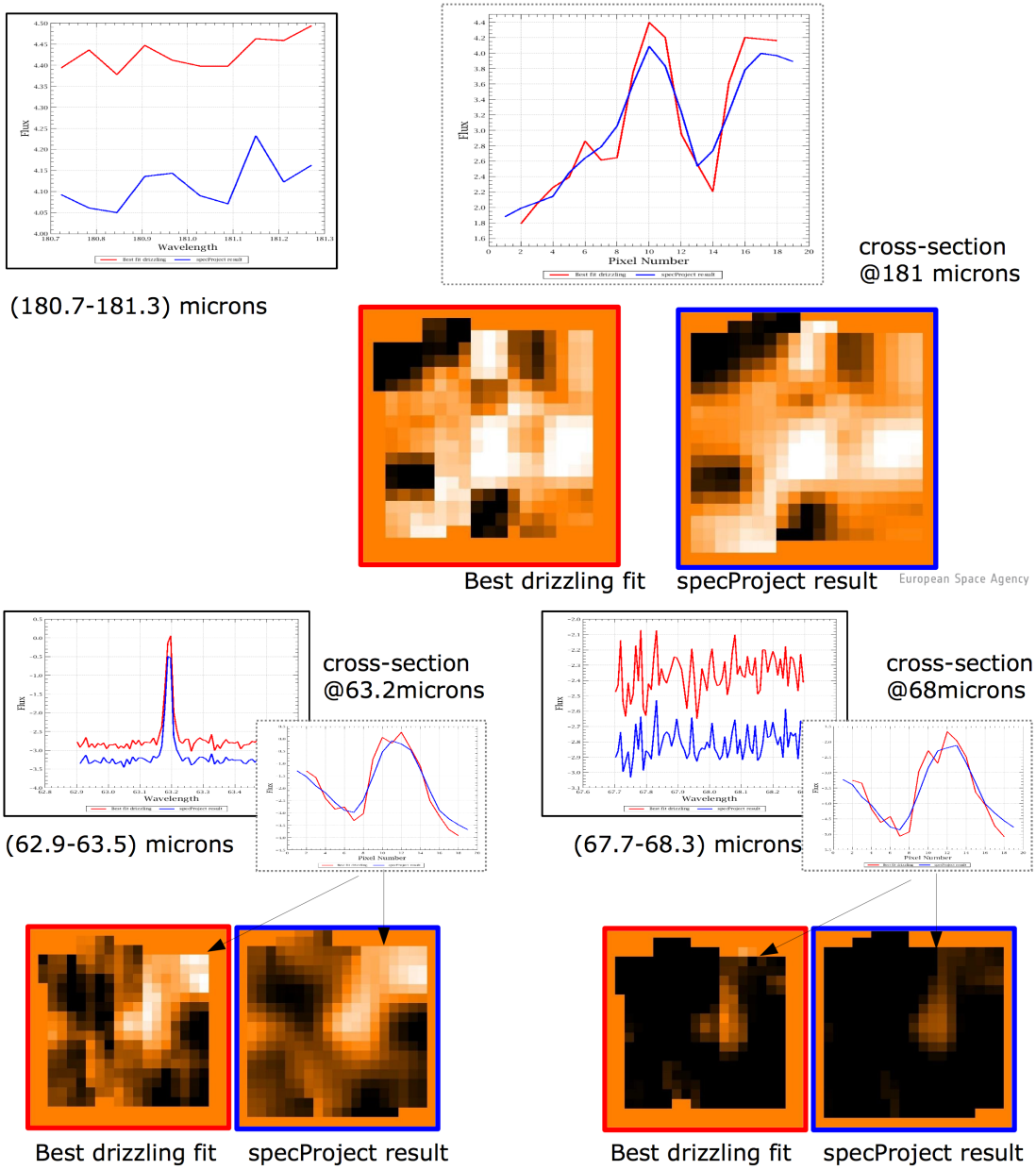

Figure B.8: This figure shows the comparison of applying drizzle (with the optimum input parameters identified at that wavelength) and specProject for two short ranges of the observation xxx ($\sim$ 2 μm centered at 181 μm (top) and 63 μm (bottom). The same WCS created by specProject (for an output pixel of 3″) was used for the generation of drizzle cubes. The continuum was not subtracted from the Pacs Level 1 cubes, and the uncertainty in the continuum for unchopped range modes did not show any obvious identification.

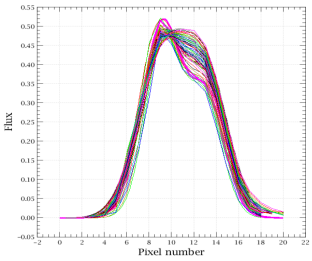

K	FWHM1	FWHM2	Upsample	Pixfrac
15.74	11.21	11.06	1	0.1
16.62	10.91	12.54	1	0.2
16.79	**12.83**	**10.82**	**Expected flux fit**	
17.16	11.64	12.61	1	0.3
17.57	13.62	11.1	1	0.4
18.03	13.91	11.48	1	0.5
18.29	13.48	12.36	2	0.4
18.36	13.62	12.32	2	0.5
18.37	12.85	13.12	2	0.1
18.42	13.42	12.62	1	0.6
18.53	14.25	11.84	2	0.6
18.56	14.39	11.72	2	0.3
18.58	14.13	12.07	1	0.7
18.6	13.97	12.27	2	0.2
18.99	14.89	11.79	1	0.8
...	..	...	..	...

K	FWHM1	FWHM2	Upsample	Pixfrac
19.05	14.56	12.29	3	0.1
19.13	14.61	12.34	1	0.9
19.19	14.85	12.14	2	0.7
19.25	14.71	12.42	3	0.2
19.47	14.95	12.47	3	0.3
19.6	14.83	12.82	1	1.0
19.63	15.12	12.53	2	0.8
19.7	15.01	12.76	3	0.4
19.95	15.34	12.76	3	0.5
20.07	15.49	12.76	2	0.9
20.6	15.58	13.47	3	0.6
20.91	15.83	13.66	2	1.0
20.92	15.92	13.56	3	0.8
20.92	15.95	13.53	3	0.7
21.11	15.86	13.93	3	0.9
21.51	16.34	13.98	3	1.0

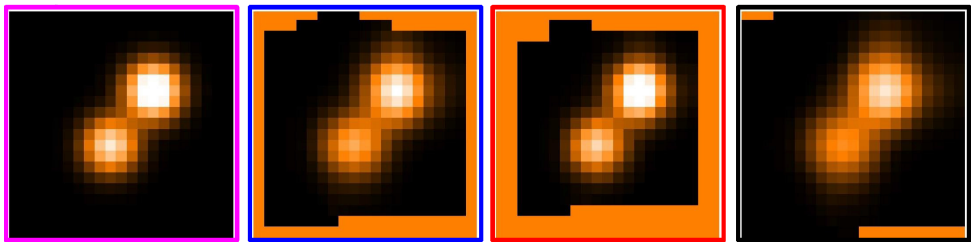

Figure B.9: This figure shows, in similar lines as previous images, the flux distribution along a cross section for 2 simulated Gaussians with different intensity levels (left image). As before, the resultant FWHM from firing the flux distribution with two Gaussians is calculated (right table). At the bottom part of this figure, there are the maps, centered at 181 μm, showing the flux distribution of the cubes from the expected flux (magenta frame), the specProject algorithm (blue frame), the drizzle cube generated with input parameters that best fit the PSF (red) and the drizzle cube generated with input parameters that worst fit the PSF (black).

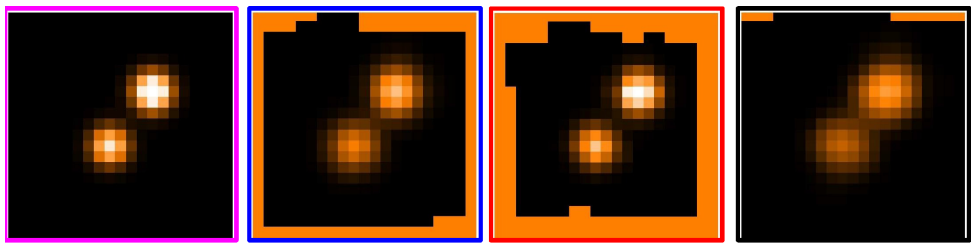

Figure B.10: The same study than Fig. B.9 have been done for 63 μm. Here there are displayed the maps, centered at 63μm, which show the flux distribution of the cubes from the expected flux (magenta frame), the specProject algorithm (blue frame), the drizzle cube generated with input parameters that best fit the PSF (red) and the drizzle cube generated with input parameters that worst fit the PSF (black).

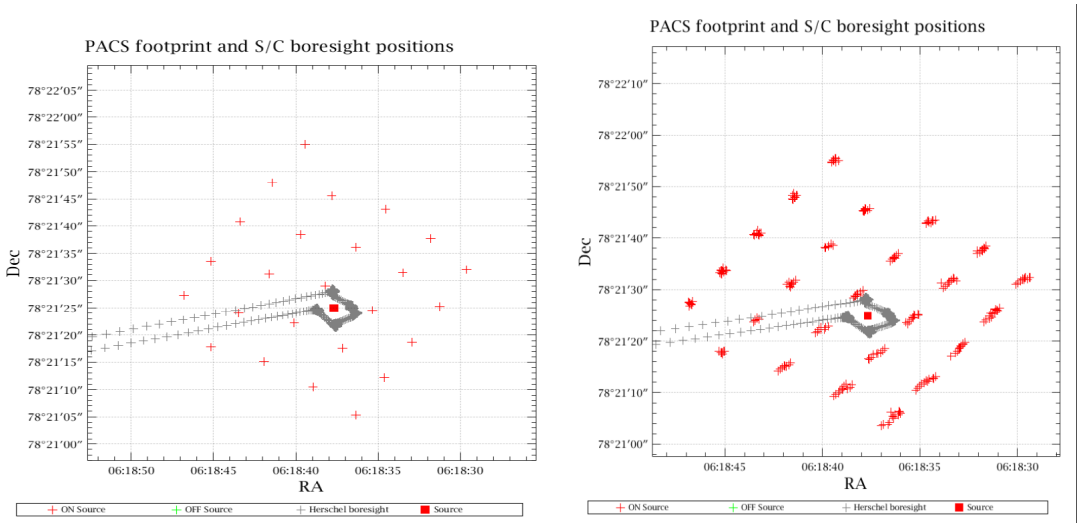

Figure B.11: Comparison of the impact on the data by using the spacecraft attitude information considering 25 sky positions (the center position of each of the 25 spaxel) or 400 sky positions (different positions for each of the 16 spectral pixels at each of the 25 spaxels).

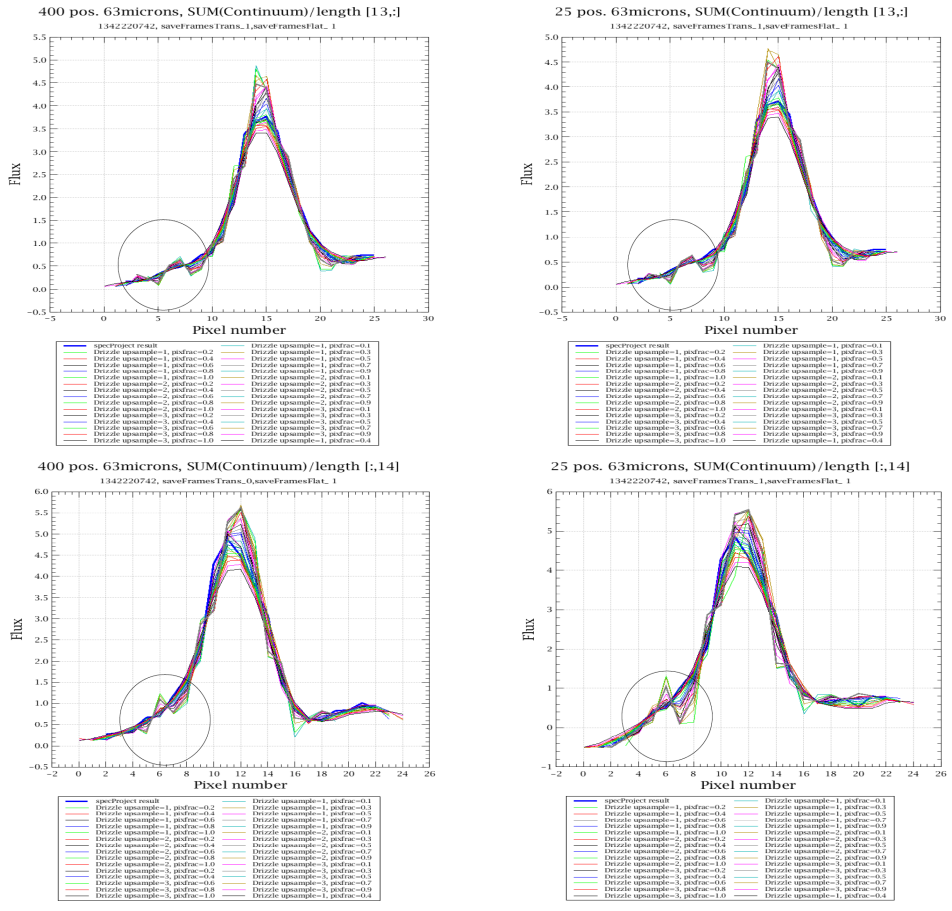

Figure B.12: Comparison of the flux distribution along the two cross sections for a single pixel position , when considering 25 or 400 positions per raster position.

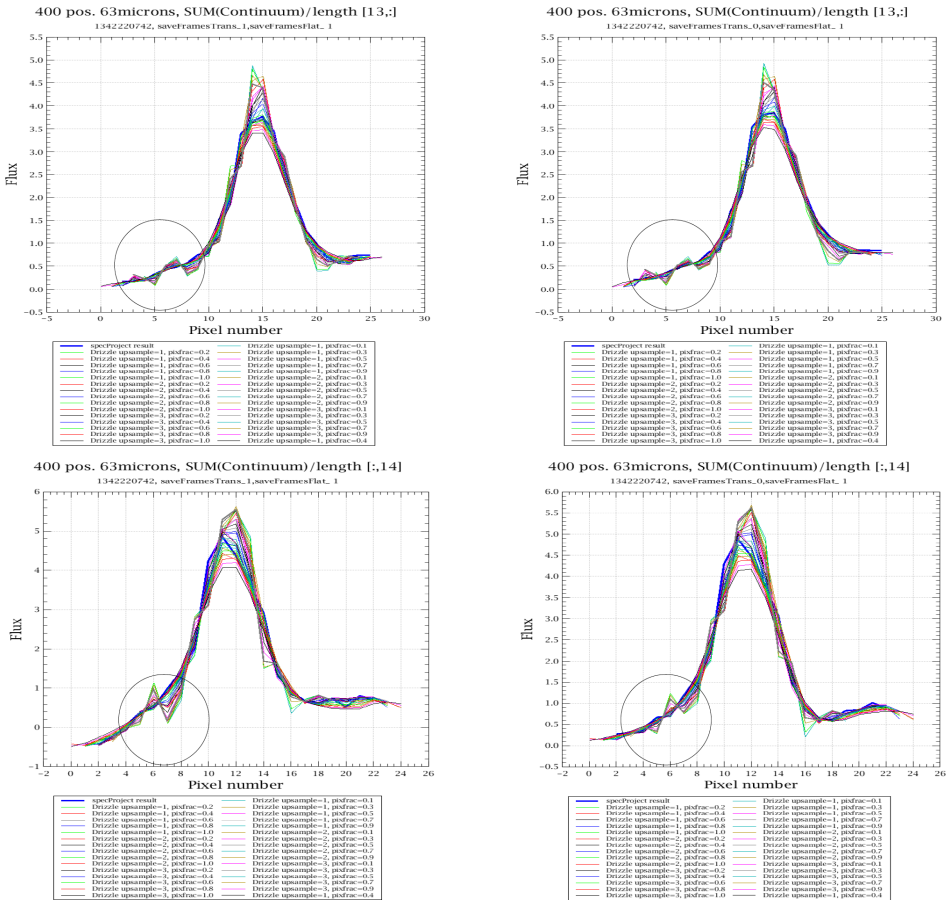

Figure B.13: Comparison of the flux distribution along the two cross sections for a single pixel position, considering the 400 positions, when applying and not applying transient corrections.

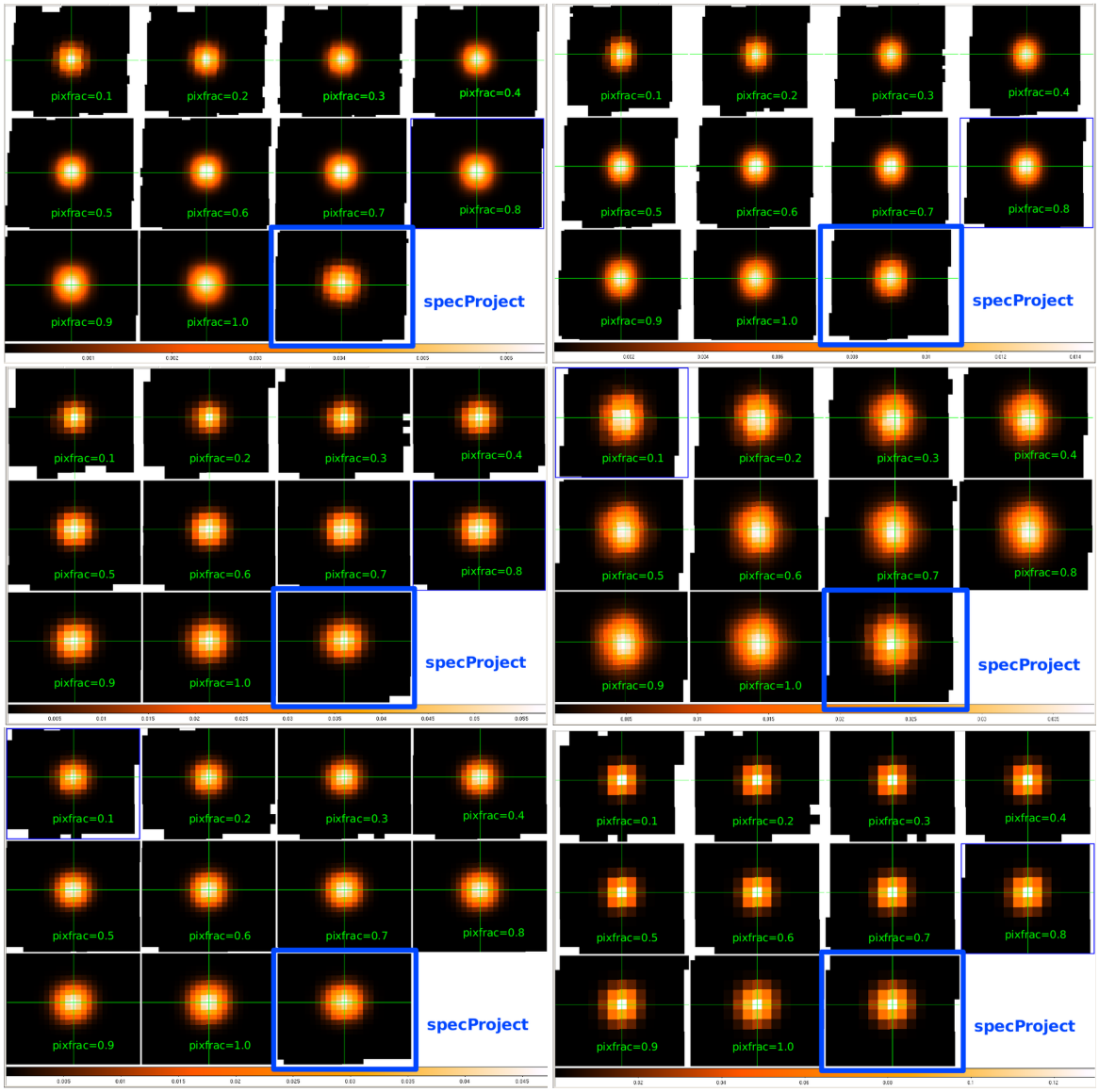

Figure B.14: Comparison of the spatial distribution of the drizzle cubes, generated at 68 μm for several (oversample, upsample) combinations and for the 9 possible pixfrac values (from 0.1 to 0.9). Also specProject, within a blue frame, generated with the same WCS is displayed for comparison. From top left to bottom right the plots represent (oversample=3, upsample=3), (oversample=3, upsample=2), (oversample=3, upsample=1), (oversample=2, upsample=3), (oversample=2, upsample=2) and (oversample=2, upsample=1) .

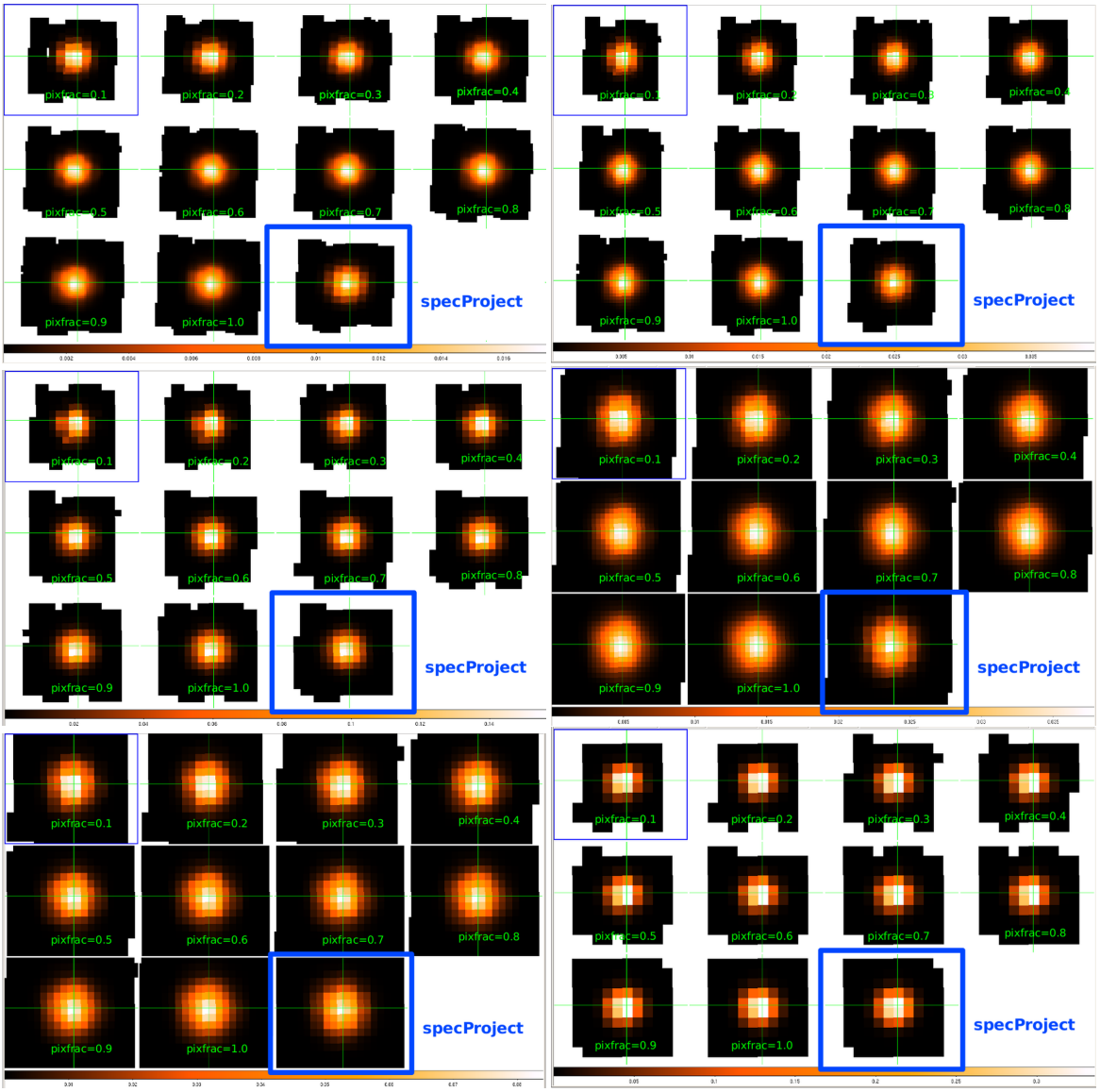

Figure B.15: Comparison of the spatial distribution of the drizzle cubes, generated at 181μm for several (oversample, upsample) combinations and for the 9 possible pixfrac values (from 0.1 to 0.9). Also specProject, within a blue frame, generated with the same WCS is displayed for comparison. From top left to bottom right the plots represent (oversample=3, upsample=3), (oversample=3, upsample=2), (oversample=3, upsample=1), (oversample=2, upsample=3), (oversample=2, upsample=2) and (oversample=2, upsample=1) .

C

Electron temperature and density

In this part there is refreshed, mainly for the student the terminology of electron temperature and how to derive it, together with the electron density from the observations. This information was mainly collected from (Gurzadyan 1997).

An electron, removed from an atom of hydrogen by photodissociation, is given an energy by the photon which follows this equation:

$$\frac{mv^2}{2} = h\nu - h\nu_0 \tag{C.1}$$

The collision of electrons follow a Maxwellian velocity distribution. From the median of the energy from free electrons it is possible to derive the electron temperature from the gas were they are and therefore from the medium.

The electron energy and the electron temperature increase when the gas is irradiated by UV radiation, for example from a close star. Two conditions should be met:

- the stationary condition: The rate of photoionizations at the hydrogen should be the same than for recombinations.
- the radiative equation condition: The amount of energy spent for the photoionizations of the hydrogen should be the same than the gain by recombinations.

In the case of planetary nebula, the lost of electronic energy could depend on the recombination of the hydrogen (what receives the name of hydrogen cooling) or by more powerful mechanisms called excitation of forbidden lines. In this second case we can derive the electron temperature

from the line ratio of intensity of transitions detected at observations. We will study this method on the [O III].

Let's consider three transition lines from [O III] among the three metastable electron levels: $^1S_0$, $^1D_2$ and ^3P, where there is an [O III] transition at 4363 μm between the levels $^1S_0$ and $^1D_2$ and the N_1 and N_2 transitions between $^1D_2$ and $^3P_1$ and $^3P_2$ respectively. With the increase of the electron temperature there will be more electrons at $^1S_0$ than at $^1D_2$ therefore the line from this transition is brighter than those called N_1 and N_2.

Therefore, measuring from the observations the intensity from the three lines we can derive the electron temperature by line ratios. The basic reasoning that the number of electrons depopulated from an electronic level should be the same than the number of electrons that populated the same level. Therefore considering previous levels as 1, 2 and 3 and their concentration of O^{++} in them as n_1, n_2 and n_3, the equation is the following:

$$n_1(q_{12} + q_{13}) = n_2(A_{21} + q_{21}) + n_3(A_{31} + q_{31}) \tag{C.2}$$

$$n_2 q_{23} + n_2(A_{21} + q_{21}) = n_3(A_{32} + q_{32}) + n_1 q_{12} \tag{C.3}$$

$$\frac{q_{ji}}{q_{ij}} = \frac{w_i}{w_j} e^{\frac{-(\varepsilon_i - \varepsilon_j)}{kT_e}} \tag{C.4}$$

$$E(N_1 + N_2) = n_2[A(^1D_2 \rightarrow ^3P_2)h\nu_{N_1} + A(^1D_2 \rightarrow ^3P_1)h\nu_{N_2}] = n_2 A_{21} h\nu_{12} \tag{C.5}$$

$$E(4363\mu m) = n_3 A_{32} h\nu_{32} \tag{C.6}$$

$$\frac{E(N_1 + N_2)}{E(4363\mu m)} = f(n_e, T_e) e^{\frac{Cte}{T_e}} \tag{C.7}$$

In cases where the density is very low ($n_e \leq 10^3\ cm^{-3}$) it could be considered $n_e = 0$ and therefore T_e could be determined from observations.

In cases of local thermalyzed equilibrium, where all the levels could be considered thermalised (at the same temperature), by assigning the electron temperature known by bibliography at those conditions it is possible to determine the electron density at the gaseous medium.

C.0.1 Calculation of electron density

Here we present the equation used for the calculation of the electron density ,(Storey et al. 1979).

$$n_e = \frac{\gamma_{01}(A_{21} + A_{20}) + \gamma_{02}(A_{21} - (R/a)A_{10})}{\gamma_{01}((R/a)\gamma_{12} - \gamma_{21} - \gamma_{20}) + \gamma_{02}((R/a)(\gamma_{12} + \gamma_{10}) - \gamma_{21})}$$

$$R = \frac{I_{10}}{I_{21}}$$

$$a = \frac{A_{10} \times \lambda_{21}}{A_{21} \times \lambda_{10}}$$

γ_{01} collisional excitation rate from level 0 to 1
γ_{02} collisional excitation rate from level 0 to 2
γ_{12} collisional excitation rate from level 1 to 2
γ_{10} collisional de-excitation rate from level 1 to 0
γ_{20} collisional excitation rate from level 2 to 0
γ_{21} collisional excitation rate from level 2 to 1
A_{10} Einstein radiative coefficien from level 1 to 0
A_{20} Einstein radiative coefficien from level 2 to 0
A_{21} Einstein radiative coefficien from level 2 to 1

where the coefficient rates used from the literature:

$$\gamma_{01} = 1.73 \times 10^{-10} cm^3 s^{-1}$$

$$\gamma_{02} = 7.46 \times 10^{-11} cm^3 s^{-1}$$

$$\gamma_{12} = 3.55 \times 10^{-12} cm^3 s^{-1}$$

$$\gamma_{10} = 3.11 \times 10^{-10} cm^3 s^{-1}$$

$$\gamma_{20} = 4.16 \times 10^{-10} cm^3 s^{-1}$$

$$\gamma_{21} = 1.10 \times 10^{-11} cm^3 s^{-1}$$

$$A_{10} = 8.542 \times 10^{-5} s^{-1}$$

$$A_{20} = 1.380 \times 10^{-10} s^{-1}$$

$$A_{21} = 1.643 \times 10^{-5} s^{-1}$$

$$\lambda_{21} = 145.5 microns$$

$$\lambda_{10} = 63.18 microns$$

D

Error budget

Here we briefly explain the error budget for the derived parameters obtained in this PhD thesis.

The initial measurements from where other parameters are derived are fluxes within apertures in line maps or line ratio maps. This aperture size (9-10 ″radius), as explained in chapter 8, were taken as a compromise: to measure as much of the various targets as possible without including other sources of emission.

As explained in chapter 8, we generated RMS and SNR maps for the cubes of line emission (continuum-subtracted) and those of continuum emission. The RMS maps are the result of subtracting from the *peak* obtained from the Gaussian line fit, the continuum p_0 term, taken from the polynomial fit to the continuum from the continuum-only cubes, divided by the above-mentioned standard deviation values within a range of 3-5 μm (a drizzleId), in a region were no lines were detected.

The flux tables in chapters 10 and 11 provide 3 σ line sensitivities, calculated from the integrated flux of an unresolved emission line centred at the observed line wavelength adjusting each line peak intensity to the 3 σ continuum noise estimate.

The value of sigma reported in these tables were computed in the following way:

$$\Sigma rms_{aperture} \times \sigma_{fit} \times \sqrt{2\pi} \times \frac{2.998^{-12}}{\lambda^2} \tag{D.1}$$

In order to be complete, to this 3 σ value we added quadratically the calibration error from the processing, which for PACS is 10-12 % (PACS Spectroscopy and Performance document) and for SPIRE is 10-15 % (SPIRE Release Note for the Spectrometer Mapping AOT).Tables 11.3 and 11.1 provide the quadratic sum of errors.

From the [O I] fluxes it was determined the [O I] luminosity and the mass-loss rate. We performed error propagation in the following way:

$$\sigma L = 4\pi \sqrt{(2rF\sigma r)^2 + (r^2\sigma F)^2} \tag{D.2}$$

$$\sigma \dot{M}_{out} = 8.1 \times 10^{-5} \sigma L \tag{D.3}$$

The error estimated for the mass-accretion rate, calculated by the equation 10.2.3, follow the same error propagation logic as equation D.3

In the case of the line ratios, the errors should be propagated following the equation D.5:

$$L_R = \frac{Flux_A}{Flux_B} \tag{D.4}$$

$$\sigma L_R = \sqrt{(\frac{1}{Flux_B})^2 \sigma Flux_A^2 + (\frac{Flux_A}{Flux_B^2})^2 \sigma Flux_B^2} \tag{D.5}$$

As the electron density is derived from the [O I] 63 to 145 μm line ratio map, see equation C.0.1, where R is given as the median value within an aperture, the error in this derived measure was calculated by standard error propagation errors for a single variable (R).

In the case of the limiting detection for the [O III] line emission, the 3-σ line sensitivities are calculated from the integrated flux of an unresolved emission line centered at the observed line wavelength and its line peak intensity is adjusted to the 3-σ continuum noise estimate. This integrated flux is a sum of all spaxels falling within the selected extraction aperture at 88.34 μm bin to generate a spectrum 1d.

The errors at the rotational diagram temperatures, where given by the covariance of the best fit to each of the three identified J_{up} ranges, defined by the PACS spectral bands.

The errors provided at the identification of the density and temperatures of the gas at shocked regions, following Neufeld (2012) models, are upper and lower limits based on the CO line ratio errors used as input values to the models.

References

Adams, F. C., Lada, C. J., & Shu, F. H. 1987, ApJ, 312, 788

Adams, J. D., Herter, T. L., Gull, G. E., et al. 2010, in Society of Photo-Optical Instrumentation Engineers (SPIE) Conference Series, Vol. 7735, Society of Photo-Optical Instrumentation Engineers (SPIE) Conference Series, 1

Adams, J. D., Herter, T. L., Osorio, M., et al. 2012, ApJ, 749, L24

André, P., Men'shchikov, A., Bontemps, S., et al. 2010, A&A, 518, L102

Andre, P., Ward-Thompson, D., & Barsony, M. 1993, ApJ, 406, 122

Andre, P., Ward-Thompson, D., & Barsony, M. 2000, Protostars and Planets IV, 59

Arzoumanian, D., André, P., Didelon, P., et al. 2011, A&A, 529, L6

Bachiller, R. 1996, ARA&A, 34, 111

Bachiller, R. & Pérez Gutiérrez, M. 1997, ApJ, 487, L93

Bally, J. 1989, in Lecture Notes in Physics, Berlin Springer Verlag, Vol. 350, IAU Colloq. 120: Structure and Dynamics of the Interstellar Medium, ed. G. Tenorio-Tagle, M. Moles, & J. Melnick, 309

Bally, J. 2008, Overview of the Orion Complex, ed. B. Reipurth, 459

Bally, J. & Lada, C. J. 1983, ApJ, 265, 824

Bally, J., O'Dell, C. R., & McCaughrean, M. J. 2000, AJ, 119, 2919

Baraffe, I., Homeier, D., Allard, F., & Chabrier, G. 2015, A&A, 577, A42

Barsony, M. & Kenyon, S. J. 1992, ApJ, 384, L53

Bate, M. R. 1998, ApJ, 508, L95

Beckwith, S., Evans, II, N. J., Gatley, I., Gull, G., & Russell, R. W. 1983, ApJ, 264, 152

Bell, K. L., Berrington, K. A., & Thomas, M. R. J. 1998, MNRAS, 293, L83

Bergin, E. A., Ciardi, D. R., Lada, C. J., Alves, J., & Lada, E. A. 2001, ApJ, 557, 209

Bergin, E. A., Neufeld, D. A., & Melnick, G. J. 1999, ApJ, 510, L145

Bianchi, S., Gonçalves, J., Albrecht, M., et al. 2003, A&A, 399, L43

Blottiau, P., Chieze, J. P., & Bouquet, S. 1988, A&A, 207, 24

Bonito, R., Orlando, S., Miceli, M., et al. 2010, A&A, 517, A68

Bonnell, I. A., Bate, M. R., Clarke, C. J., & Pringle, J. E. 1997, MNRAS, 285, 201

Bonnor, W. B. 1956, MNRAS, 116, 351

Bontemps, S., Andre, P., Terebey, S., & Cabrit, S. 1996, A&A, 311, 858

Boogert, A. C. A., Pontoppidan, K. M., Knez, C., et al. 2008, ApJ, 678, 985

Boss, A. P. & Yorke, H. W. 1995, ApJ, 439, L55

Cantalupo, C. M., Borrill, J. D., Jaffe, A. H., Kisner, T. S., & Stompor, R. 2010, ApJS, 187, 212

Carpenter, J. M. 2000, AJ, 120, 3139

Carrasco-González, C., Rodríguez, L. F., Anglada, G., et al. 2010, Science, 330, 1209

Caselli, P., Hartquist, T. W., & Havnes, O. 1997, A&A, 322, 296

Caselli, P., Walmsley, C. M., Tafalla, M., Dore, L., & Myers, P. C. 1999, ApJ, 523, L165

Chen, H., Grenfell, T. G., Myers, P. C., & Hughes, J. D. 1997, ApJ, 478, 295

Chen, H., Myers, P. C., Ladd, E. F., & Wood, D. O. S. 1995, ApJ, 445, 377

Chini, R., Reipurth, B., Ward-Thompson, D., et al. 1997, ApJ, 474, L135

Cohen, J. G. & Frogel, J. A. 1977, ApJ, 211, 178

Cohen, M., Hollenbach, D. J., Haas, M. R., & Erickson, E. F. 1988, ApJ, 329, 863

Crimier, N., Ceccarelli, C., Lefloch, B., & Faure, A. 2009, A&A, 506, 1229

Crutcher, R. M. 1999, ApJ, 520, 706

Curiel, S., Raymond, J. C., Moran, J. M., Rodriguez, L. F., & Canto, J. 1990, ApJ, 365, L85

de Graauw, T., Helmich, F. P., Phillips, T. G., et al. 2010, A&A, 518, L6

de Jong, J. A., Wieprecht, E., Schreiber, J., et al. 2012, in Astronomical Society of the Pacific Conference Series, Vol. 461, Astronomical Data Analysis Software and Systems XXI, ed. P. Ballester, D. Egret, & N. P. F. Lorente, 631

Dinerstein, H. 1995, in The Analysis of Emission Lines: A Meeting in Honor of the 70th Birthdays of D. E. Osterbrock, M. J. Seaton, ed. R. Williams & M. Livio, 134

Draine, B. T. 1980, ApJ, 241, 1021

Dunham, M. M., Arce, H. G., Allen, L. E., et al. 2013, AJ, 145, 94

Dunham, M. M., Crapsi, A., Evans, II, N. J., et al. 2008, ApJS, 179, 249

Dunham, M. M., Stutz, A. M., Allen, L. E., et al. 2014, Protostars and Planets VI, 195

Ebert, R. 1957, ZAp, 42, 263

Ehle, M., Gonzalez-Riestra, R., & Gonzalez-Garcia, B. 2004, GRB Coordinates Network, 2508, 1

Eiroa, C., Fedele, D., Maldonado, J., et al. 2010, A&A, 518, L131

Eiroa, C., Marshall, J. P., Mora, A., et al. 2011, A&A, 536, L4

Eiroa, C., Marshall, J. P., Mora, A., et al. 2013a, VizieR Online Data Catalog, 355, 50011

Eiroa, C., Marshall, J. P., Mora, A., et al. 2013b, A&A, 555, A11

Enoch, M. L., Evans, II, N. J., Sargent, A. I., & Glenn, J. 2009, ApJ, 692, 973

Ercolano, B. & Koepferl, C. 2014, Astrophysics and Space Science Proceedings, 36, 63

Evans, II, N. J. 1999, ARA&A, 37, 311

Evans, II, N. J., Allen, L. E., Blake, G. A., et al. 2003, PASP, 115, 965

Evans, II, N. J., Dunham, M. M., Jørgensen, J. K., et al. 2009, ApJS, 181, 321

Evans, II, N. J., Rawlings, J. M. C., Shirley, Y. L., & Mundy, L. G. 2001, ApJ, 557, 193

Federrath, C. & Klessen, R. S. 2012, ApJ, 761, 156

Fischer, W. J., Megeath, S. T., Stutz, A. M., et al. 2013, Astronomische Nachrichten, 334, 53

Flower, D. R. & Pineau des Forets, G. 1995, MNRAS, 275, 1049

Foster, P. N. & Chevalier, R. A. 1993, ApJ, 416, 303

Fruchter, A. S. & Hook, R. N. 2002, PASP, 114, 144

Furlan, E., Megeath, S. T., Osorio, M., et al. 2014, ApJ, 786, 26

Gatley, I., Becklin, E. E., Mattews, K., et al. 1974, ApJ, 191, L121

Gautier, III, T. N., Fink, U., Larson, H. P., & Treffers, R. R. 1976, ApJ, 207, L129

Giannini, T., Nisini, B., & Lorenzetti, D. 2001, ApJ, 555, 40

Goicoechea, J. R., Cernicharo, J., Karska, A., et al. 2012, A&A, 548, A77

Gonzalez-Garcia, B. M. & Solano, E. 2003, in IAU Joint Discussion, Vol. 20, IAU Joint Discussion, 12

González-García, B. M., Zapatero Osorio, M. R., Béjar, V. J. S., et al. 2006, A&A, 460, 799

Greene, T. 2001, American Scientist, 89, 316

Greene, T. P., Wilking, B. A., Andre, P., Young, E. T., & Lada, C. J. 1994, ApJ, 434, 614

Griffin, M. J., Abergel, A., Abreu, A., et al. 2010, A&A, 518, L3

Gurzadyan, G. A. 1997, The Physics and Dynamics of Planetary Nebulae

Haro, G. & Herbig, G. H. 1955, Boletin de los Observatorios Tonantzintla y Tacubaya, 2, 33

Hartigan, P., Edwards, S., & Ghandour, L. 1995, ApJ, 452, 736

Hartmann, L. 2009, Accretion Processes in Star Formation: Second Edition (Cambridge University Press)

Herczeg, G. J., Karska, A., Bruderer, S., et al. 2012, A&A, 540, A84

Hollenbach, D. 1985, Icarus, 61, 36

Hollenbach, D. & McKee, C. F. 1989, ApJ, 342, 306

Hollenbach, D. J. & Tielens, A. G. G. M. 1997, ARA&A, 35, 179

Hollenbach, D. J. & Tielens, A. G. G. M. 1999, Reviews of Modern Physics, 71, 173

Hunter, C. 1977, ApJ, 218, 834

Johnson, J. J., Gehrz, R. D., Jones, T. J., Hackwell, J. A., & Grasdalen, G. L. 1990, AJ, 100, 518

Jørgensen, J. K., Hogerheijde, M. R., Blake, G. A., et al. 2004, A&A, 415, 1021

Kama, M., López-Sepulcre, A., Dominik, C., et al. 2013, A&A, 556, A57

Karska, A., Herczeg, G. J., van Dishoeck, E. F., et al. 2013, A&A, 552, A141

Karska, A., Kristensen, L. E., van Dishoeck, E. F., et al. 2014, A&A, 572, A9

Kaufman, M. J. & Neufeld, D. A. 1996, ApJ, 456, 611

Kaufman, M. J., Wolfire, M. G., Hollenbach, D. J., & Luhman, M. L. 1999, ApJ, 527, 795

Keenan, F. P., Burke, V. M., & Aggarwal, K. M. 1991, ApJ, 371, 636

Kenyon, S. J., Calvet, N., & Hartmann, L. 1993, ApJ, 414, 676

Kenyon, S. J. & Hartmann, L. 1995, ApJS, 101, 117

Konigl, A. & Pudritz, R. E. 2000, Protostars and Planets IV, 759

Könyves, V., André, P., Men'shchikov, A., et al. 2010, A&A, 518, L106

Krumholz, M. R. 2011, in American Institute of Physics Conference Series, Vol. 1386, American Institute of Physics Conference Series, ed. E. Telles, R. Dupke, & D. Lazzaro, 9–57

Kryukova, E., Megeath, S. T., Gutermuth, R. A., et al. 2012, AJ, 144, 31

Kueppers, M., O'Rourke, L., Bockelee-Morvan, D., et al. 2012, LPI Contributions, 1667, 6377

Küppers, M., O'Rourke, L., Bockelee-Morvan, D., et al. 2012, in European Planetary Science Congress 2012, 417

Lada, C. J., Walker, C. K., Young, E., & Margulis, M. 1987, in Bulletin of the American Astronomical Society, Vol. 19, Bulletin of the American Astronomical Society, 758

Lada, C. J. & Wilking, B. A. 1984, ApJ, 287, 610

Larson, R. B. 1969, MNRAS, 145, 271

Lodders, K. & Palme, H. 2009, Meteoritics and Planetary Science Supplement, 72, 5154

López-Santiago, J., Bonito, R., Orellana, M., et al. 2015, ApJ, 806, 53

López-Sepulcre, A., Taquet, V., Sánchez-Monge, Á., et al. 2013, A&A, 556, A62

Manoj, P., Watson, D. M., Neufeld, D. A., et al. 2013, ApJ, 763, 83

Mardones, D. 2003, in Astrophysics and Space Science Library, Vol. 299, Astrophysics and Space Science Library, ed. J. Lépine & J. Gregorio-Hetem, 359

Marshall, J. P., Löhne, T., Montesinos, B., et al. 2011, A&A, 529, A117

McKee, C. F. & Ostriker, E. C. 2007, ARA&A, 45, 565

Megeath, S. 2014, WFC3 Spectroscopy of Faint Young Companions to Orion Young Stellar Objects, HST Proposal

Megeath, S. T., Fischer, W., Ali, B., et al. 2010, in Bulletin of the American Astronomical Society, Vol. 42, American Astronomical Society Meeting Abstracts 415, 440.13

Megeath, S. T., Flaherty, K. M., Hora, J., et al. 2005, in IAU Symposium, Vol. 227, Massive Star Birth: A Crossroads of Astrophysics, ed. R. Cesaroni, M. Felli, E. Churchwell, & M. Walmsley, 383–388

Megeath, S. T., Gutermuth, R., Muzerolle, J., et al. 2012, AJ, 144, 192

Menten, K. M., Reid, M. J., Forbrich, J., & Brunthaler, A. 2007, A&A, 474, 515

Mezger, P. G., Zylka, R., & Wink, J. E. 1990, A&A, 228, 95

Molinari, S. & Noriega-Crespo, A. 2002, AJ, 123, 2010

Mouschovias, T. C. 1991, in NATO Advanced Science Institutes (ASI) Series C, Vol. 342, NATO Advanced Science Institutes (ASI) Series C, ed. C. J. Lada & N. D. Kylafis, 449

Müller, T. G., O'Rourke, L., Barucci, A. M., et al. 2012, A&A, 548, A36

Myers, P. C. & Ladd, E. F. 1993, ApJ, 413, L47

Nadeau, D., Neugebauer, G., & Geballe, T. R. 1982, ApJ, 253, 154

Nakano, T. 1998, ApJ, 494, 587

Naylor, D. A., Gom, B. G., Schofield, I., Tompkins, G., & Davis, G. R. 2003, in Society of Photo-Optical Instrumentation Engineers (SPIE) Conference Series, Vol. 4855, Millimeter and Submillimeter Detectors for Astronomy, ed. T. G. Phillips & J. Zmuidzinas, 540–551

Neufeld, D. A. 2012, ApJ, 749, 125

Neufeld, D. A. & Dalgarno, A. 1989, ApJ, 344, 251

Neufeld, D. A., Gusdorf, A., Güsten, R., et al. 2014, ApJ, 781, 102

Neufeld, D. A. & Hollenbach, D. J. 1994, ApJ, 428, 170

Neufeld, D. A. & Kaufman, M. J. 1993, ApJ, 418, 263

Neufeld, D. A., Melnick, G. J., Sonnentrucker, P., et al. 2006, ApJ, 649, 816

Nielbock, M., Chini, R., & Müller, S. A. H. 2003, A&A, 408, 245

Nisini, B., Benedettini, M., Giannini, T., et al. 1999, A&A, 350, 529

Nisini, B., Lorenzetti, D., Cohen, M., et al. 1996, A&A, 315, L321

Nisini, B., Santangelo, G., Giannini, T., et al. 2015, ApJ, 801, 121

Ogino, S., Tomisaka, K., & Nakamura, F. 1999, PASJ, 51, 637

Ohashi, N., Lee, S. W., Wilner, D. J., & Hayashi, M. 1999, ApJ, 518, L41

O'Rourke, L., Barucci, A., Gònzalez-Garcìa, B., Dotto, E., & Küppers, M. 2012a, in European Planetary Science Congress 2012, 789

O'Rourke, L., Bockelee-Morvan, D., Groussin, O., et al. 2012b, in European Planetary Science Congress 2012, 733

O'Rourke, L., Kiss, C., Barucci, A., et al. 2012c, in European Planetary Science Congress 2012, 753

O'Rourke, L., Küppers, M., Jorda, L., et al. 2012d, LPI Contributions, 1667, 6292

O'Rourke, L., Müller, T., Altieri, B., et al. 2012e, LPI Contributions, 1667, 6299

O'Rourke, L., Müller, T., Altieri, B., et al. 2014, in Asteroids, Comets, Meteors 2014, ed. K. Muinonen, A. Penttilä, M. Granvik, A. Virkki, G. Fedorets, O. Wilkman, & T. Kohout, 400

O'Rourke, L., Müller, T., Valtchanov, I., et al. 2011, in EPSC-DPS Joint Meeting 2011, 1464

Ossenkopf, V. & Henning, T. 1994, A&A, 291, 943

Osterbrock, D. E. & Ferland, G. J. 2006, Astrophysics of gaseous nebulae and active galactic nuclei

Ott, S. 2010, in Astronomical Society of the Pacific Conference Series, Vol. 434, Astronomical Data Analysis Software and Systems XIX, ed. Y. Mizumoto, K.-I. Morita, & M. Ohishi, 139

Palla, F. & Stahler, S. W. 1991, ApJ, 375, 288

Palla, F. & Stahler, S. W. 1993, ApJ, 418, 414

Palmeirim, P., André, P., Kirk, J., et al. 2013, A&A, 550, A38

Pelletier, G. & Pudritz, R. E. 1992, ApJ, 394, 117

Peterson, D. E. & Megeath, S. T. 2008a, The Orion Molecular Cloud 2/3 and NGC 1977 Regions, ed. B. Reipurth, 590

Peterson, D. E. & Megeath, S. T. 2008b, The Orion Molecular Cloud 2/3 and NGC 1977 Regions, ed. B. Reipurth, 590

Piazzo, L., Calzoletti, L., Faustini, F., et al. 2015, MNRAS, 447, 1471

Pilbratt, G. L., Riedinger, J. R., Passvogel, T., et al. 2010, A&A, 518, L1

Podio, L., Kamp, I., Flower, D., et al. 2012, A&A, 545, A44

Poglitsch, A., Waelkens, C., Geis, N., et al. 2010, A&A, 518, L2

Pontoppidan, K. M., Boogert, A. C. A., Fraser, H. J., et al. 2008, ApJ, 678, 1005

Popesso, P., Magnelli, B., Buttiglione, S., et al. 2012, ArXiv e-prints

Rebull, L. M., Padgett, D. L., McCabe, C.-E., et al. 2010, ApJS, 186, 259

Regibo, S. 2012, PhD thesis, Institute of Astronomy, Katholieke Universiteit Leuven, Belgium

Reipurth, B., Rodríguez, L. F., & Chini, R. 1999, AJ, 118, 983

Rodriguez Pascual, P., Gonzalez Riestra, R., Gonzalez Garcia, B., et al. 2002, IAU Circ., 7821, 3

Roussel, H. 2013, PASP, 125, 1126

Sandstrom, K. M., Peek, J. E. G., Bower, G. C., Bolatto, A. D., & Plambeck, R. L. 2007, ApJ, 667, 1161

Saraceno, P., Andre, P., Ceccarelli, C., Griffin, M., & Molinari, S. 1996, A&A, 309, 827

Schartel, N., Ehle, M., Breitfellner, M., et al. 2003, IAU Circ., 8072, 3

Schilke, P., Walmsley, C. M., Pineau des Forets, G., & Flower, D. R. 1997, A&A, 321, 293

Schreiber, J., Wieprecht, E., de Jong, J., et al. 2009, in Astronomical Society of the Pacific Conference Series, Vol. 411, Astronomical Data Analysis Software and Systems XVIII, ed. D. A. Bohlender, D. Durand, & P. Dowler, 478

Schulz, N. S. 2005, From Dust To Stars Studies of the Formation and Early Evolution of Stars

Shimajiri, Y., Takahashi, S., Takakuwa, S., Saito, M., & Kawabe, R. 2008, ApJ, 683, 255

Shu, F. H., Adams, F. C., & Lizano, S. 1987, ARA&A, 25, 23

Skrutskie, M. F., Cutri, R. M., Stiening, R., et al. 2006, AJ, 131, 1163

Snell, R. L., Loren, R. B., & Plambeck, R. L. 1980, ApJ, 239, L17

Spaans, M., Hogerheijde, M. R., Mundy, L. G., & van Dishoeck, E. F. 1995, ApJ, 455, L167

Stahler, S. W. & Palla, F. 2005, The Formation of Stars

Storey, J. W. V., Watson, D. M., & Townes, C. H. 1979, ApJ, 233, 109

Storey, J. W. V., Watson, D. M., Townes, C. H., Haller, E. E., & Hansen, W. L. 1981, ApJ, 247, 136

Stutz, A. M. & Kainulainen, J. 2015, A&A, 577, L6

Stutz, A. M., Tobin, J. J., Stanke, T., et al. 2013, ApJ, 767, 36

Tafalla, M., Myers, P. C., Caselli, P., & Walmsley, C. M. 2004, A&A, 416, 191

Tayal, S. S. 2008, A&A, 486, 629

Terebey, S., Chandler, C. J., & Andre, P. 1993, ApJ, 414, 759

Terebey, S., Shu, F. H., & Cassen, P. 1984, ApJ, 286, 529

Tielens, A. G. G. M. & Hollenbach, D. 1985, Icarus, 61, 40

van Dishoeck, E. F., Herbst, E., & Neufeld, D. A. 2013, Chemical Reviews, 113, 9043

van Dishoeck, E. F., Kristensen, L. E., Benz, A. O., et al. 2011, PASP, 123, 138

Watson, D. M. 1985, Physica Scripta Volume T, 11, 33

Watson, D. M., Bohac, C. J., Hull, C., et al. 2007, Nature, 448, 1026

Watson, D. M., Genzel, R., Townes, C. H., & Storey, J. W. V. 1985, ApJ, 298, 316

Werner, M. W., Hollenbach, D. J., Crawford, M. K., et al. 1984, ApJ, 282, L81

Werner, M. W., Roellig, T. L., Low, F. J., et al. 2004, ApJS, 154, 1

Whitney, B. A., Wood, K., Bjorkman, J. E., & Cohen, M. 2003a, ApJ, 598, 1079

Whitney, B. A., Wood, K., Bjorkman, J. E., & Wolff, M. J. 2003b, ApJ, 591, 1049

Whitworth, A. & Summers, D. 1985a, MNRAS, 214, 1

Whitworth, A. & Summers, D. 1985b, MNRAS, 214, 1

Wieprecht, E., Schreiber, J., de Jong, J., et al. 2009, in Astronomical Society of the Pacific Conference Series, Vol. 411, Astronomical Data Analysis Software and Systems XVIII, ed. D. A. Bohlender, D. Durand, & P. Dowler, 531

Wilking, B. A., Lada, C. J., & Young, E. T. 1987, in Bulletin of the American Astronomical Society, Vol. 19, Bulletin of the American Astronomical Society, 1092

Williams, J. P., Plambeck, R. L., & Heyer, M. H. 2003, ApJ, 591, 1025

Zatsarinny, O. & Tayal, S. S. 2003, ApJS, 148, 575

Zuckerman, B., Kuiper, T. B. H., & Rodriguez Kuiper, E. N. 1976, ApJ, 209, L137